Development of a thermal-hydraulics/thermomechanics coupling model for the evaluation of the behavior of SFR fuel assemblies under irradiation

Francisco Acosta

Communauté
UNIVERSITÉ Grenoble Alpes

THÈSE

Pour obtenir le grade de

DOCTEUR DE LA COMMUNAUTE UNIVERSITE GRENOBLE ALPES

Spécialité : **MEP : Mécanique des fluides Energétique, Procédés**

Arrêté ministériel : 25 mai 2016

Présentée par

Francisco ACOSTA

Thèse dirigée par **Pablo RUBIOLO**, Professeur, Communauté Université Grenoble Alpes
et codirigée par **Thierry CADIOU**
et **Victor BLANC**, CEA
préparée au sein du **Laboratoire d'Etudes et de Modélisations des Systèmes (CEA/DEN/CAD/DER/SESI/LEMS)** et dans **l'École Doctorale I-MEP2 - Ingénierie - Matériaux, Mécanique, Environnement, Energétique, Procédés, Production**

Développent d'une méthodologie de couplage thermo-hydraulique et thermomécanique pour l'évaluation du comportement sous irradiation des assemblages combustibles des RNR-Na

Development of a thermal-hydraulics / thermomechanics coupling methodology for the evaluation of the behavior of SFR fuel subassemblies under irradiation

Thèse soutenue publiquement le **15 octobre 2019**,
devant le jury composé de :

Monsieur PABLO RUBIOLO
PROFESSEUR, GRENOBLE INP, Directeur de thèse
Monsieur EMILIO BAGLIETTO
PROFESSEUR ASSOCIE, INSTITUT DE TECH. DU MASSACHUSETTS - USA, Rapporteur
Monsieur FREDERIC LEBON
PROFESSEUR, UNIVERSITE AIX-MARSEILLE, Président
Madame EMILIE FERRIE
MAITRE DE CONFERENCES, GRENOBLE INP, Examinatrice
Monsieur BENOIT PERRIN
INGENIEUR, FRAMATOME, Examinateur

Résumé

Les faisceaux d'aiguilles des assemblages combustibles des réacteurs à neutrons rapides à caloporteur sodium (RNR-Na) se déforment au cours de leur irradiation, ce qui impacte l'écoulement du caloporteur et la distribution de températures dans l'assemblage, dont la connaissance est essentielle pour la démonstration de sûreté. De plus, les mécanismes à l'origine de cette déformation, à savoir le gonflement et le fluage thermique et d'irradiation, dépendent fortement de la température de la gaine du combustible, d'où l'existence d'un couplage entre les évolutions thermo-hydraulique et thermomécanique des assemblages. Par le passé, ce couplage a été négligé dans les simulations numériques, et une approche plus conservative a été privilégiée : les simulations thermo-hydrauliques étaient réalisées sans tenir compte de la déformation géométrique, et les distributions de températures résultantes étaient utilisées comme des données d'entrée pour les simulations thermomécaniques. L'objectif de cette thèse est de définir une méthodologie pour l'évaluation du comportement des assemblages combustibles de type RNR-Na sous irradiation en prenant en compte le couplage entre leurs évolutions thermo-hydraulique et thermomécanique.

A cet effet, un nouveau couplage numérique a été développé entre le code industriel de dynamique des fluides numérique (CFD) STAR-CCM+ et DOMAJEUR2, code basé sur la méthode aux éléments finis et dédié à la modélisation du comportement thermomécanique des assemblages combustibles RNR-Na sous irradiation. Ce couplage a été réalisé par l'échange de la déformation de la gaine, calculée par DOMAJEUR2, et de son champ de températures, obtenu avec le modèle CFD qui prend en compte de manière explicite la déformation géométrique des aiguilles combustibles. De plus, les conditions aux limites thermo-hydrauliques utilisées dans les simulations CFD, comme le débit massique de sodium dans le faisceau, sont ajustées pour tenir compte de cette déformation.

Cette méthodologie a été appliquée à des faisceaux respectivement de 7 et 19 aiguilles combustibles munies de fils espaceurs, avec des caractéristiques géométriques et des conditions aux limites représentatives des RNR-Na de quatrième génération, ont été analysés. Dans le cas des faisceaux combustibles fortement irradiés, les simulations couplées conduisent à une réduction significative de la déformation diamétrale des aiguilles combustibles, par rapport aux simulations non couplées, causée par la prise en compte de l'augmentation de la température de la gaine induite par la déformation. En raison de la déformation plus faible, la contrainte

maximale de la gaine a été réduite. De plus, des simulations ont été menées afin de vérifier que, en situation de fonctionnement normal, la dépendance de la neutronique à l'évolution de la thermo-hydraulique et de la thermomécanique est faible. Enfin, une contribution à la validation de cette méthodologie de simulation couplée a été réalisée avec un benchmark numérique basé sur un outil de simulation couplé existant et en simulant l'irradiation d'un assemblage combustible expérimental. Contrairement à l'approche innovante développée dans le cadre de ce travail de thèse, l'outil de simulation existant utilise un modèle thermo-hydraulique simplifié et ne tient pas compte de l'impact de la déformation sur le débit massique du caloporteur, qui, selon les résultats de l'évaluation, a une importance majeure. La simulation de l'irradiation expérimentale a conduit à une déformation maximale de la gaine et un gradient de déformations en accord avec les grandeurs mesurées, bien que des limitations liées aux lois empiriques de gonflement utilisées dans DOMAJEUR2 pour le calcul du gonflement aient été identifiées. La reformulation de ces lois à l'aide de la méthodologie de simulation couplée développée constitue une perspective à ce travail de thèse.

Abstract

The fuel pin bundles of Sodium-cooled Fast Reactors (SFR) undergo significant geometrical changes during their irradiation, which affect the coolant flow and temperature distributions in the fuel subassemblies, the knowledge of which is essential for safety assessments. Moreover, as the mechanisms responsible for the deformation of the fuel bundles, namely the swelling and creep, strongly depend on the fuel cladding temperature, a coupling between the thermal-hydraulic and thermomechanical evolutions of the fuel subassemblies exists. In the past, this coupling has been neglected in the numerical simulations, and a more conservative approach has been preferred. In this conservative approach, the thermal-hydraulic simulations are conducted without considering the geometrical deformation, and the resulting temperature distributions are used as input for the thermomechanical simulations. The objective of this thesis is to define a new methodology for the evaluation of the behavior of SFR fuel bundles under irradiation that considers the coupling between their thermal-hydraulic and thermomechanical evolutions.

To this end, a new numerical coupling has been developed between the industrial Computational Fluid Dynamics (CFD) code STAR-CCM+ and DOMAJEUR2, a finite element code dedicated to the modeling of the thermomechanical behavior of SFR fuel subassemblies under irradiation. The coupling has been implemented via the exchange of the cladding deformation, calculated by DOMAJEUR2, and its associated temperature field, obtained with a CFD model implemented in STAR-CCM+ that explicitly considers the geometrical deformation of the fuel pins. In addition, the thermal-hydraulic boundary conditions used in the CFD simulations, such as the sodium mass flow rate through the bundle, are also adjusted to account for the deformation.

Fuel bundles of 7 and 19 wire-wrapped pins, with geometrical characteristics and boundary conditions representative of fourth generation SFRs, were analyzed in order to gain insight on the effects of the coupling. For highly irradiated fuel bundles, the coupled simulations were shown to lead to a significant reduction of the diametral strain of the fuel pins, with respect to non-coupled simulations, caused by the deformation-induced cladding temperature increase. Consequence of the lower deformation, the cladding maximal stress was also significantly reduced. Additionally, neutronic simulations were conducted in order to verify that, under nominal operating conditions, its coupling with thermal-hydraulics and

thermomechanics is of minor importance. Finally, a contribution to the validation of the developed coupled simulation methodology was realized by performing a numerical benchmark against a preexisting coupled simulation tool, and by simulating the irradiation of an experimental fuel subassembly. Unlike the novel approach developed in this work, the preexisting simulation tool employs a simplified thermal-hydraulic model and does not consider the impact of the deformation on the coolant mass flow rate, which was found to be of major importance. The simulation of the experimental irradiation yielded a maximal cladding deformation and deformation gradient that are in good agreement with the measured values, although limitations related to the empirical laws employed in DOMAJEUR2 to compute the swelling were identified. The reformulation of these laws using the developed coupled simulation methodology is part of the future outlook of this work.

Acknowledgements

I would firstly like to thank the CEA for giving me the opportunity to conduct this PhD and, in particular, to Manuel Saez, head of the LEMS laboratory, for his continuous support during these three years. I am also very grateful for the dedication of Thierry Cadiou and Victor Blanc, my tutors, and Pablo Rubiolo, my thesis director. This work would not have been possible without your advice, guidance, and patience.

I would also like to thank my colleagues; I really enjoyed working with you. Special thanks to Edouard, with whom I shared the office and the PhD headaches, and to Nicolas Alpy, Vincent Pascal and Nicolas Schmidt for the many technical discussions we had.

My sincere thanks also goes to all the members of the jury for the time they spent reading this manuscript and for their valuable comments and questions.

Last but not least, I would like to thank my friends, my family, and Uta. Thank you for encouraging me to take this path, and thank you for helping me walk it. I could not have done it without your support.

Contents

List of Figures

List of Tables

List of acronyms

BOL

Beginning Of Life. 35, 124, 148, 177, 199, 200, 205, 212–214, 221, 223

CAD

Computer Aided Design. 16, 84, 90–92, 107, 123, 124, 126, 128, 129, 131, 133–135, 144, 145, 150–152, 239

CEA

Atomic and Alternative Energy Commission—or *Commissariat à l'énergie atomique et aux énergies alternatives*—. 2, 6, 7, 12, 15, 16, 20, 26, 29, 35, 37, 39, 40, 47, 64, 65, 69, 70, 73, 94, 95, 99, 101, 104, 105, 136, 138, 154, 156, 164–166, 188, 189, 210, 221, 230, 231, 239

CFD

Computational Fluid Dynamics. 14, 16, 69, 70, 73, 74, 82, 84, 89, 91–93, 97, 107–110, 112–114, 116, 117, 119, 122–124, 126, 129, 133, 135, 136, 138, 140, 142, 146–149, 151–153, 155–158, 160, 169, 170, 177, 199, 200, 203–206, 208, 214, 219, 224, 225, 229, 231, 233, 235–237, 239–243, 264, 266

CHT

Conjugate Heat Transfer. 157, 158, 160, 162

DBTT

Ductile Brittle Transition Temperature. 52, 53

EOL

End Of Life. 35, 40, 56, 57, 112–114, 116, 124, 126, 148, 155, 170, 177, 178, 180, 184, 191, 194, 195, 199–201, 203, 205, 206, 208, 210–214, 223–225, 228, 229, 235, 238, 240, 242, 243

FCCI

Fuel Cladding Chemical Interaction. 54

GEN IV

Fourth Generation of Nuclear Reactors. 1, 95, 153, 240, 241

GFR

Gas-cooled Fast Reactor. 1

GIF

Generation IV International Forum. 1, 2, 6, 15

INL

Idaho National Laboratory. 2

LBE

Lead-Bismuth Eutectic. 87, 89

LFR

Lead-cooled Fast Reactor. 1, 2

MOX

Mixed Oxide. 54, 64

MSR

Molten Salt reactor. 1

ODS

Oxide Dispersion Strengthened. 53

OS

Operator Split. 12, 14, 15, 108, 110, 112, 116, 152, 169

PCMI

Pellet Cladding Mechanical Interaction. 53, 54

PWR

Pressurized Water Reactor. 4, 6, 22, 23, 36

R&D

Research and Development. 2, 15, 95, 239

SCWR

Supercritical Water-cooled Reactor. 1

SFR

Sodium-cooled Fast Reactor. 1–3, 6, 7, 9, 12, 14–17, 19–23, 25, 26, 28–30, 32–37, 39–41, 44, 45, 47, 48, 50, 52–54, 56, 59, 63–66, 69–74, 77, 78, 84, 86, 87, 90–95, 99, 101, 104, 105, 107, 114, 135, 136, 138, 139, 151, 153–156, 163–166, 184, 187–189, 208, 209, 217, 220, 221, 223, 224, 228, 230, 231, 236, 239–243, 267

TRL

Technology Readiness Level. 2

UTS

Ultimate Tensile Stress. 51, 52

VHTR

Very-High-Temperature Reactor. 1

1. Introduction

1.1. The fourth generation of nuclear reactors

The rapidly increasing world's population has to be met with an increase in the electricity generation capacity, in order to maintain— and if possible increase—the worldwide electricity access, which is highly correlated with human development (Sušnik and Zaag 2017). Depending on the technologies employed to do so, the increase in generation capacity could conflict with the pressing need to reduce the emission of greenhouse effect gases (Jiang 2011), which is one of the reasons why nuclear energy is often considered to be a necessary contributor to the future energy mix (Brook, Alonso, Meneley, et al. 2014; MIT 2018).

It is precisely to address the need for increased nuclear energy supply that the Generation IV International Forum (GIF) has been created, in the year 2000, initially representing nine countries where nuclear was relevant and considered to be essential for the future, and currently comprising 14 members. In the year 2002, the GIF announced a selection of six advanced nuclear reactor concepts that it considered to represent the future in nuclear power plant technologies. These concepts, which constitute the Fourth Generation of Nuclear Reactors (GEN IV), were selected because they represent a substantial improvement, with respect to the existing technologies, in four main different areas, namely, Sustainability, Safety & Reliability, Economics, and Proliferation Resistance & Physical Protection. The selected technologies are:

- Gas-cooled Fast Reactor (GFR), with a closed fuel cycle;
- Lead-cooled Fast Reactor (LFR), with a closed fuel cycle;
- Molten Salt reactor (MSR), with thermal and fast neutron concepts and a closed fuel cycle;
- Sodium-cooled Fast Reactor (SFR), with a closed fuel cycle;
- Supercritical Water-cooled Reactor (SCWR), thermal and fast concepts with open and closed fuel cycles;
- Very-High-Temperature Reactor (VHTR), with thermal neutrons and an open fuel cycle.

The prevalence of closed fuel cycle concepts, in which the spent fuel is reprocessed and recycled, responds to the need of optimising the utilisation of the uranium resources and minimising the high-level nuclear waste. The choice of operating in the fast neutron spectrum is, as explained in Section 1.2.2, also in line with this goal.

Out of these six concepts, the GIF considers that the LFR and the SFR are the ones with higher Technology Readiness Level (TRL) (OECD/NEA 2018), and that the latter is the nearest-term deployable system for actinide management (OECD/NEA 2014). Recently, in the USA, the SFR was the only concept considered mature enough to support preliminary design and licensing activity before the year 2025, as established by a technology maturity assessment conducted by the Idaho National Laboratory (INL) (Gougar, Bari, Kim, et al. 2015), and it has also been the concept privileged by France since the year 2010 (Gauche and Rouault 2011).

This work is conducted in the framework of the Research and Development (R&D) efforts carried over at the Atomic and Alternative Energy Commission—or *Commissariat à l'énergie atomique et aux énergies alternatives*— (CEA) on advanced SFR prototypes, which is why this technology is described in the following section.

1.2. Sodium-cooled Fast Reactors

In this section, we firstly outline some of the SFR main characteristics. Then, the choice of the energy spectrum of the neutrons and the employed coolant are explained. Finally, the SFR subassembly and its deformation during the irradiation, which is at the core of this work, is introduced.

1.2.1. SFR system

A typical SFR is schematically presented in Figure 1.1, where its main components are indicated. This figure corresponds to a pool-type reactor, which has similar working principles than loop-type systems but, unlike the latter, integrates the main components—the primary pumps and the intermediate heat exchangers—inside the reactor vessel. In the pool-type SFR, the primary pumps take sodium from the cold plenum and make it flow through the core. After exchanging heat there and increasing its temperature, the sodium goes into the hot plenum and then through the intermediate heat exchangers to end up in the cold plenum again, thus closing the primary circuit. The intermediate heat exchangers, that protect the primary circuit from potential water-sodium reactions discussed in Section 1.2.3, allow heating up the secondary sodium, which then flows through the steam generators to produce the water vapor needed for the traditional Rankine-cycle-based

energy conversion system, which is, up to now, the reference technological solution (OECD/NEA 2018).

The upper core structure supports the required core instrumentation, and holds and guides the insertion of neutron absorbing rods, used to control the core's nuclear chain reaction and to shut it down. The core is composed of an arrangement of slender structures called subassemblies, amongst which the fuel subassemblies contain the nuclear fuel needed for the fission chain reaction. They constitute the object of this work, and are described in more detail in Section 1.2.4.

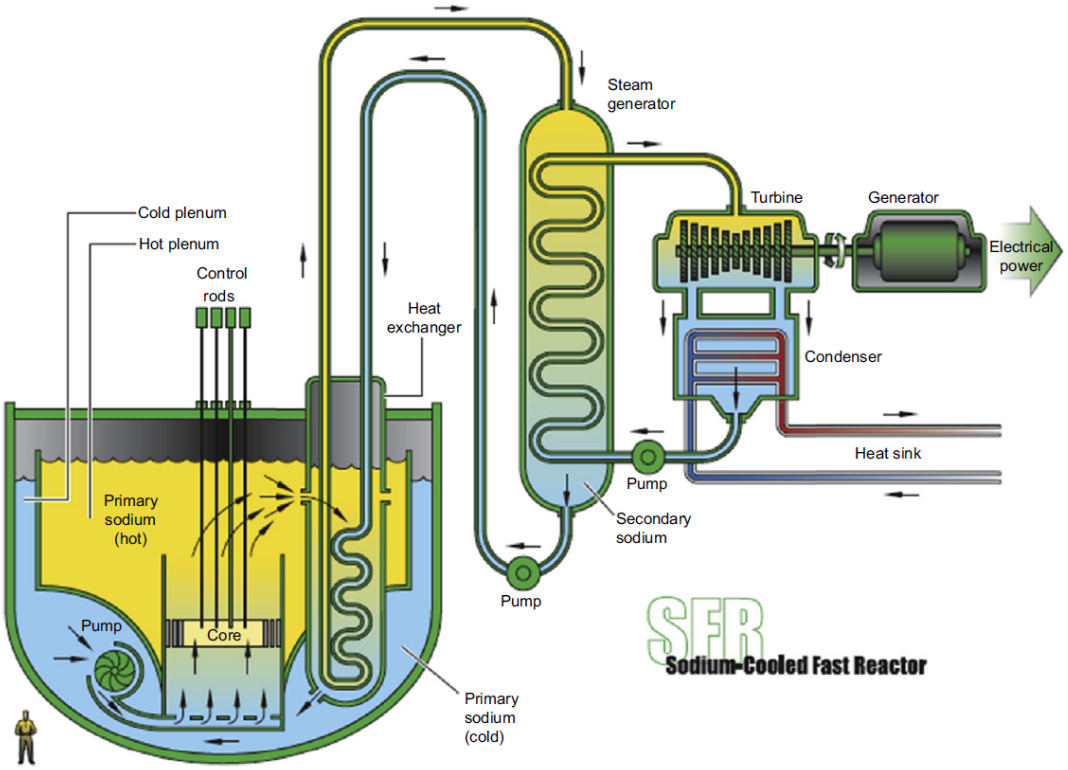

Figure 1.1.: Pool-type SFR system (H. Ohshima and Kubo 2016).

As its name suggests, the SFR technology is defined by the choice of the coolant fluid and of the neutron energy spectrum, an overview of which is given in the following sections.

1.2.2. Fast neutron energy spectrum

The neutrons produced by the fission reaction have an average energy of approximately 2 MeV and, in the context of reactor physics, they are called fast neutrons

since they have not yet lost part of their energy by scattering, process referred to as neutron slowing down. Most nuclear reactors in operation today rely on the slowing down of the neutrons to benefit from the increased fission probability that thermal neutrons, which are in thermal equilibrium with the surrounding medium at an energy of approximately 25 meV, have. This is achieved by introducing in the reactor materials of low mass number, which increase the energy loss of the neutrons with each scattering, good examples of which are graphite, beryllium, and heavy and light water. The required inventory of fissile isotopes in the reactor, which are the isotopes that can undergo a fission reaction with both thermal and fast neutrons, is decreased due to the higher fission probability associated with the thermalization of the neutron energy spectrum. This reduces the need of increasing the proportion of the fissile ^{235}U isotope with respect to the more abundant ^{238}U, by a costly process known as uranium enrichment.

However, in thermal reactors—the most popular of which is the Pressurized Water Reactor (PWR)—, the fertile isotopes, that can produce a fissile isotope by transmutation, are barely utilised as an energy source. This is the case of ^{238}U, that constitutes almost 99.3% of natural uranium but does not undergo fission when the incident neutron is not energetic enough (Joël Guidez and Bonin 2014). In a thermal reactor, ^{238}U is firstly transmuted into ^{239}Pu, and then, by successive neutron captures, into ^{240}Pu, ^{241}Pu, ^{242}Pu, and so on. Only the Pu isotopes with odd mass number are fissile, therefore the rest, just like ^{238}U, are not utilised. Moreover, they are detrimental to the fission chain reaction since they absorb neutrons. Overcoming this limitation is one of the motivations for the development of fast reactors.

In fast reactors, the nuclear chain reaction is sustained directly with the highly energetic fission neutrons, without purposely reducing their energy by scattering. A sustained fission reaction with fast neutrons requires a larger inventory of fissile isotopes, which is achieved by enriching uranium and by employing a mixture of uranium and plutonium as fuel. However, ^{238}U and all the Pu isotopes mentioned before can undergo fission with fast neutrons. Additionally, the ratio of the probability of a neutron inducing a fission to the probability of it being captured (fission-to-capture ratio) is higher in the fast spectrum, as well as the number of neutrons per fission of ^{239}Pu. This leads to an increase in the excess neutrons from ^{239}Pu fission that, in turn, can be captured by ^{238}U to breed more ^{239}Pu (Yang 2012). The breeding capability of a reactor is characterized by the average number of fissile nuclides produced per fissile nuclide consumed, which can be larger than unity in which case is called breeding ratio.

The higher fission-to-capture ratio also means that fast reactors are more efficient at burning the long lived transuranic elements, that in thermal reactors end up as high level waste. Moreover, fast reactors could even be used to transmute the long

lived actinides present in used fuel from thermal reactors.

Profiting from the enhanced economical and environmental benefits of fast reactors is only possible if the right coolant is employed, as explained next.

1.2.3. Liquid sodium as coolant

The choice of the coolant is tightly related to the choice of the neutron energy spectrum. In fast reactors, and contrary to the case of thermal reactors, elements with low mass numbers are avoided, since they contribute to the neutron slowing down process. This rules out the use of water, employed in most operating thermal reactors, as a coolant fluid. Also, the coolant should not absorb neutrons, and should be stable under irradiation.

Additionally, to increase the breeding ratio and to reduce the amount of fissile isotopes required to achieve a sustained fission chain reaction, geometrically compact cores are employed, which leads to a very high power density that calls for an efficient heat transfer from the fuel to the coolant, which is improved when the latter presents a high thermal conductivity and heat capacity. Besides, the melting and boiling points of the coolant should be compatible with the desired temperature operation range, since, if liquid, its solidification during reactor operation and its evaporation must be avoided. In addition, in order to limit the pumping power required, the coolant viscosity should be low.

Other industrial criteria also have to be considered when choosing the coolant, such as the chemical compatibility with the reactor components it is in contact with and their inspectability, its behaviour in case of leakage, potential associated fire or toxic risks, or the availability of compatible pumps, heat exchangers, and other reactor components. In view of all these requirements, it is not surprising that only a few fluids are being considered as suitable coolants for fast reactors. In Europe, these are molten salts, helium, lead[1], and sodium, the latter being the one with the largest operational experience (Joël Guidez and Bonin 2014).

Indeed, sodium has a very high thermal conductivity, and a high boiling point that allows for non-pressurized designs that eliminate the accidental scenarios related to depressurization, and for a large coolant temperature increase within the core, which increases the thermodynamic efficiency of the reactor and favours the natural convection as a passive cooling strategy. Additionally, its compatibility with the reactor materials is excellent, and corrosion can be managed by controlling impurities such as oxygen and hydrogen (H. Ohshima and Kubo 2016). It also has a relatively low density, which makes the use of gravity based passive stop systems

[1] Typically in eutectic mixture with bismuth.

possible, and low viscosity, which limits the required pumping power.

The neutronic properties of sodium are also very satisfactory, since its relatively high mass number makes it inefficient to slow down neutrons that, additionally, sodium only weakly absorbs. Besides, its activation under irradiation is low, although two radioactive isotopes produced with low probability have to be considered for maintenance and dismantling operations.

The main disadvantage of sodium as a coolant fluid is that it reacts vigorously and exothermically when in contact with water, and it can also burn when exposed to air. For these reasons, specific means have been developed to reduce the occurrence of sodium leaks, and to detect them when they occur. Concerning the risk of sodium fires, several approaches, mostly based on limiting the available oxygen for its combustion, have also been developed (Cacuci 2010). Enhancing the robustness of existing heat exchangers against sodium-water reaction, or even eliminating the risk of water-sodium reactions by employing a Brayton energy conversion cycle, are amongst the primary research and development activities envisaged by the GIF for the next years (OECD/NEA 2014).

1.2.4. SFR fuel subassemblies

The fuel subassemblies of SFR are composed of a bundle of elongated cylindrical rods called fuel pins, arranged in a triangular lattice and containing the nuclear fuel in the form of—typically—ceramic pellets. As an example, the fuel subassembly, here called subassembly for the sake of brevity, of an advanced SFR prototype being designed at the CEA is presented in Figure 1.2. The fuel bundle is enclosed by a hexagonal wrapper can—also called hexcan—, is held in place at the bottom by a core grid into which the inlet nozzle is inserted, and has a lifting head for handling purposes. In the concept illustrated in Figure 1.2, a plenum is introduced above the fuel bundle in order to favor a mechanism—described in Section 2.3.2—by which the power of the reactor is passively reduced in case of loss of coolant or coolant density, which is a desired safety feature. The coolant goes into the subassembly through a series of holes in the inlet nozzle, to then flow upwards through the fuel bundle, the plenum and the upper neutron shielding, finally exiting the subassembly through the lifting head. It should be noted that, unlike the case of the PWR, the separation provided by the hexcan makes of each subassembly an independent hydraulic channel, connected to the others only via the plenums below and above the core.

The fuel pins, illustrated schematically in Figure 1.3 together with the cross section of the fuel bundle, are constituted of hollow cylindrical claddings that contain the fuel pellets, and are separated by helically wrapped spacer wires, that also increase the coolant mixing. They have a lower and upper plenum

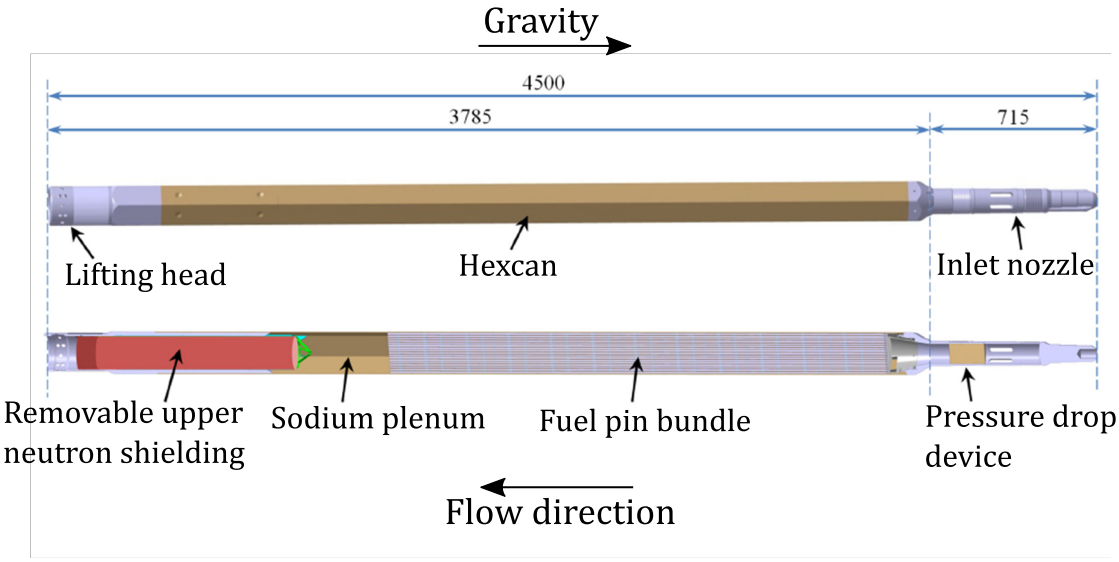

Figure 1.2.: Fuel subassembly of an advanced SFR prototype (Beck, Blanc, Escleine, et al. 2017). The dimensions are in mm.

to accommodate the gaseous fission products. As indicated in that figure, the triangular pin arrangement gives place to three distinct types of elementary channels for the coolant flow, namely the triangular, corner, and edge subchannels. Two characterizing parameters of SFR subassemblies are the ratio of the pitch P, which is the minimal distance between fuel pin centers, to the external diameter of the cladding D_{ec}, and the ratio of the helix step H of the spacer wires to D_{ec}.

Some of the innovative SFR designs currently being studied present values of these parameters that escape their experimentally validated range. This is the case, for example, of the P/D_{ec} of the SFR being designed at the CEA (Beck, Blanc, Escleine, et al. 2017) that, in order to enhance the aforementioned mechanism by which the rector power is reduced when the sodium density is reduced, has a lower P/D_{ec} than the range recommended by the subassembly design rules in France (CEA 1994). These design rules are partially based on extensive irradiation experiences—conducted in Rapsodie, Phenix, and SuperPhenix reactors (Schneider 2009)—that, a priori, cannot be extrapolated to some of these new designs, which increases the effort required to validate them.

The subject of this work is, precisely, the evolution of SFR subassemblies during irradiation, and it is therefore briefly introduced in the next section.

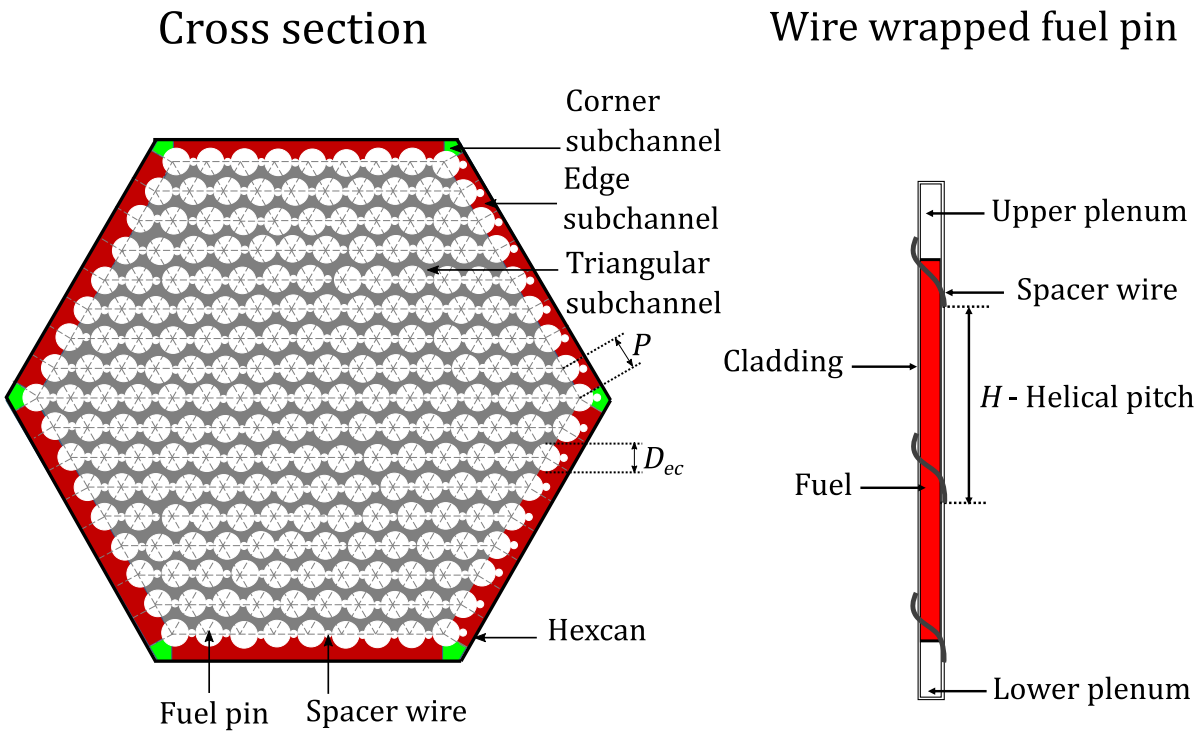

Figure 1.3.: Cross section of a SFR fuel subassembly and schematic representation of one fuel pin (adapted from Saxena 2014)

1.2.5. SFR bundle deformation

During their lifetime in the reactor core, the fuel pin claddings, the spacer wires, and the hexcan that are part of the subassemblies are exposed to high temperatures and increasing irradiation dose, which is a measure of the interaction of the radiation with the materials. Besides, the claddings are subject to an increasing internal pressure due to the accumulation of gaseous fission products, and also to external pressure exerted by the sodium, which affects the hexcan as well. Consequence of the irradiation, the swelling and irradiation creep of the materials—described in sections 2.2.2.2 and 2.2.2.3, respectively—lead, together with their thermal expansion, to the deformation of the fuel bundle (Leclere 1983).

Swelling is the isotropic increase of the material volume, and it is dependent of the irradiation dose and of the temperature, amongst other variables. Irradiation creep is the isochoric plastic strain of a material under the effect of stresses—such as the ones associated to the internal pressurisation of the claddings—and depends mainly on the irradiation dose, the temperature, and the mechanical stress level (F. Garner 2006).

These phenomena cause the diametral strain of the claddings, an example of which is presented in Figure 1.4a, which leads to the contact between fuel pins, and between pins and the hexcan. These contacts induce high mechanical stresses in the cladding, and increase the ovalisation and the helical flexion of the fuel pins, already present due to the tension of the spacer wires. Extreme examples of cladding ovalisation and helical flexion of the fuel pins are presented in Figure 1.4b and in Figure 1.4c, respectively. Additionally, the fuel pins can also exhibit an increase of their length, as well as bowing due to differential thermal expansion and swelling. The hexcan can also bow under the effects of differential deformation, and increase in length and in plate to plate distance. However, as discussed in Section 2.2.2.2, these effects are very limited when compared to the strains of the fuel pins due to the alloys employed for the hexcan, which show great irradiation stability (Beck, Blanc, Escleine, et al. 2017) but cannot be used for the claddings due to their higher operational temperature and internal pressurization (IAEA 2012).

Throughout this work, we will see that the deformed fuel bundle has a higher hydraulic resistance than the nominal one, which leads to a reduction of the coolant mass flow rate and to an associated increase in coolant outlet temperature. Besides, that the deformation induces local perturbations in the distribution of the sodium flow, which also affect its temperature distribution. These effects are traditionally not considered in the SFR subassembly simulations, which, as described next, constitute a key step in the design process of SFR.

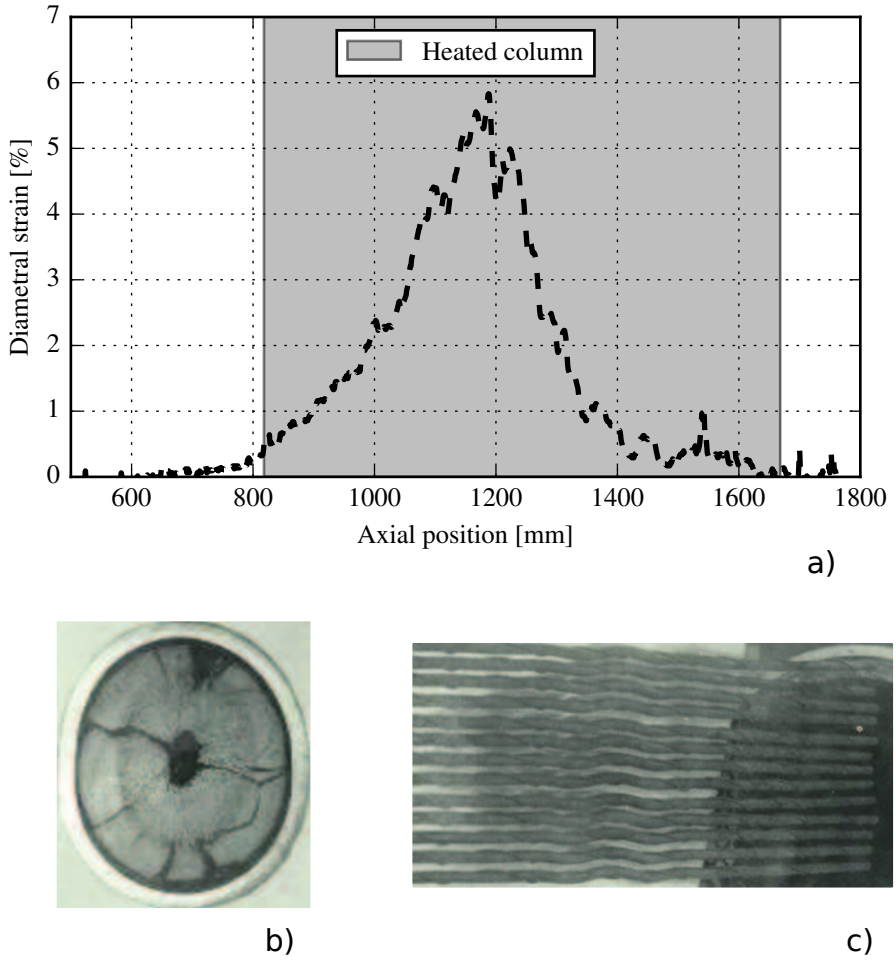

Figure 1.4.: a) Measured axial profile of diametral strain of a fuel pin irradiated in Phenix reactor. The heated column of the fuel pin—where most of the fission energy is produced—is indicated. b) Image of a highly ovalised fuel pin. c) Image of fuel pins that exhibit a very high helical flexion.

1.3. Numerical simulations and multiphysics

1.3.1. Need for comprehensive simulations

A fundamental part of the iterative design process of a nuclear reactor consists in verifying that the design choices made lead to the desired reactor behavior, both in nominal and in accidental situations. In practice, this translates to evaluating the distribution of variables of interest, such as temperature or nuclear power, as well as their evolution during the operation of the reactor, during transients deemed relevant, or even after the end of the lifespan of the component being studied. Historically, this task has been accomplished by combining the use of

experimental approaches and numerical analyses, the latter conducted—since they became available—with computers.

In an ideal scenario, one would be able to employ experimental techniques to study every case of interest, without having to make simplifying hypotheses or modelling choices as is the case with numerical simulations. However, for nuclear reactor systems, this is very often not practical, too expensive, or even not possible. The limitations come mainly from the dimensional or time scales involved; the irradiation, pressure, and temperature conditions that are difficult to reproduce and under which instrumentation becomes very challenging; or from the risks involved in the reproduction of the scenarios of interest, an extreme case of which would be a severe accident. Being able to overcome these limitations led to the widespread use of numerical simulation tools for the design and analysis of nuclear reactors.

Traditionally, the technique employed for the numerical simulations of reactor systems consisted in identifying the distinct physical components involved, i.e. phenomena responding to different governing equations, and treating them separately. This paradigm led to the development of the so called *single-physics* computer codes, that became more complex and sophisticated with the years, and that were validated individually. Some examples are the codes employed to compute the neutron flux[2] distribution within the reactor, the codes used to compute the temperature and flow characteristics of the coolant, the ones employed to evaluate the performance of the fuel pins, or the ones used to investigate the mechanical state of the components of the reactors.

However, separating the studies in different physical components responded to the need of limiting the complexity of the problem to be solved by each computer code, but neglected the interdependence between the involved phenomena. In cases when this dependence is one directional, it can be resolved by chaining the different simulations by using the output of one as part of the input of the following. On the other hand, the simple chaining of simulations is not sufficient in cases where there is a strong two-way coupling between the evolution of the variables of interest, a canonical example of which is the evolution of the fuel temperature and the nuclear power in an accidental transient; indeed, the safety of nuclear reactors is greatly dependent on the negative feedback that a temperature increase has on their power—discussed in Section 2.3.2—, and on the temperature increase immediately following a power outburst.

In order to resolve the multi-physical coupling which is relevant in many nuclear reactor applications, and motivated by the increase of computational power and the development of parallel computation techniques, the straightforward coupling of

[2]The neutron flux characterises the distribution of the neutron population in a reactor, and is discussed in Section 2.3.

the aforementioned single-physics codes was popularised. This technique, called Operator Split (OS), has become the main multi-physics paradigm in reactor analysis, and is based on the information exchange between the codes. Its development was also motivated by the preexisting verification and validation of the single-physics codes, which is not compromised by the OS coupling (Mahadevan, Elia Merzari, Tautges, et al. 2014).

OS based couplings, as well as other coupling techniques, have been extensively employed to address the interdependence between neutronics and thermal-hydraulics, which becomes particularly relevant in transient scenarios. Indeed, multiple platforms have been developed to this end, namely PARCS/TRACE (Xu, Downar, Walls, et al. 2009), DeCART/StarCD (Weber, Sofu, Yang, et al. 2004), NURESIM (Chauliac, Aragonés, Bestion, et al. 2011), RELAP5-3D (Uspuras, Kaliatka, and Bubelis 2004), among many others used to study thermal reactors. Similar tools have also been developed for or applied to SFR. Some examples are HEMERRA (Bruna, Fouquet, Dubois, et al. 2007) Nek-5000/PROTEUS (Mahadevan, Elia Merzari, Tautges, et al. 2014), MCNPX/COBRA-IV (Vazquez, Tsige-Tamirat, Ammirabile, et al. 2012), or even SHARP (E. Merzari, Shemon, Y. Yu, et al. 2015) and GeN-Foam (Fiorina, Clifford, Aufiero, et al. 2015) that also take into account the thermal deformation of some core structures. However, other relevant areas of SFR analysis have been relegated, one of these being the evolution of SFR fuel subassemblies during their irradiation. The thermal-hydraulic and the thermomechanical evolution of the SFR subassemblies are coupled due to their significant irradiation induced deformation, which both depends on and affects the coolant temperature distribution. Nevertheless, this coupling is typically neglected in the numerical simulations conducted to evaluate their evolution.

1.3.2. Traditional and multiphysical simulations of the evolution of SFR subassemblies

The numerical simulation of the irradiation of SFR subassemblies is traditionally done by sequentially conducting different single-physics calculations, and using the output of one as the input of the next one. This process is illustrated in Figure 1.5, as an example, for the particular case of the SFR simulation program of the CEA. In this scheme, a neutronic evaluation yields the power and irradiation dose distribution within the fuel bundle and their time evolution. The power distribution is used by a thermal-hydraulics code to obtain the temperature distribution within the fuel bundle. A fuel thermomechanics code—also called fuel performance code—uses the dose and power computed by the neutronic calculation, and the maximal cladding temperature obtained with the thermal-hydraulic simulation, to compute, among other variables, the evolution of the fission gas release and the associated pressure inside the claddings. Finally, a bundle thermomechanical

code is employed to compute the evolution of the strain and stress fields during the irradiation, for which the irradiation dose, internal cladding pressure, and temperature histories are needed.

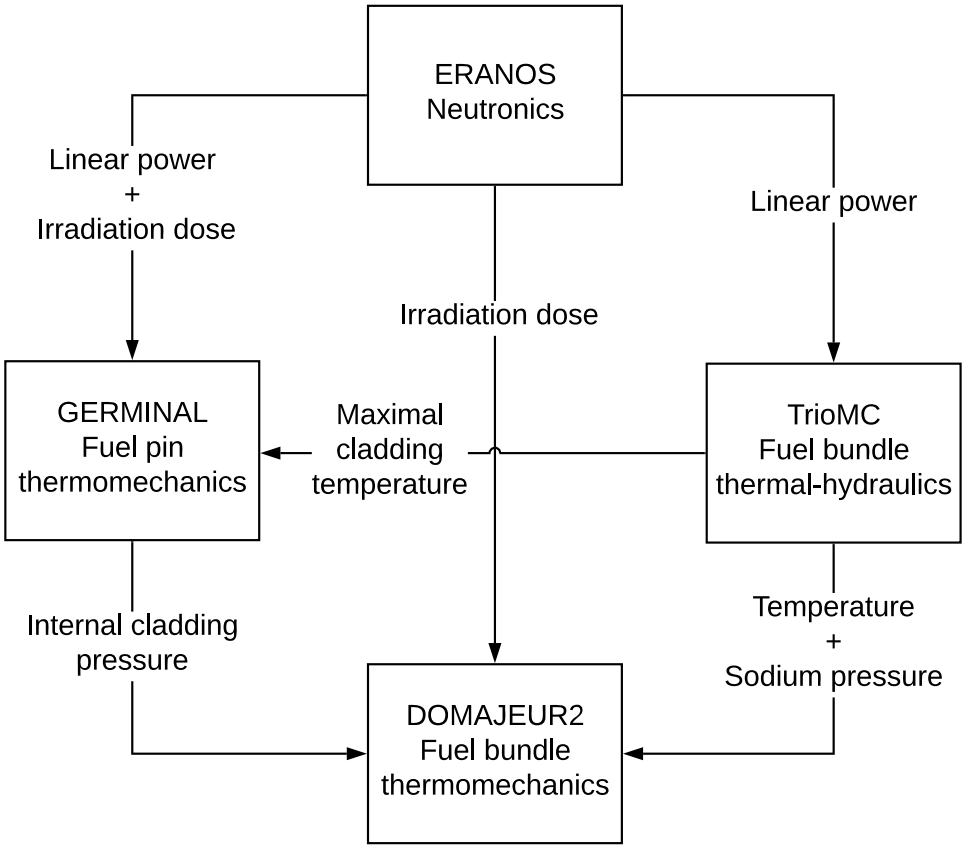

Figure 1.5.: Traditional SFR subassembly simulation scheme. Example of the strategy employed at the CEA.

With this simulation strategy, then, the effects of the deformation on thermal-hydraulics are not considered, since the simulations are conducted using the *as-fabricated* bundle dimensions. Therefore, the modification of the temperature field induced by the deformation cannot be considered for computing the evolution of the bundle's deformation, which is temperature dependent. Indeed, the most common practice is to consider a constant temperature distribution throughout the irradiation under consideration (Masoni 2016), or, at most, to take into account the temperature evolution as a consequence of the evolution of the linear power with the burn-up of the fuel, discussed in Section 2.2.1.

The impact of the bundle deformation on its thermal-hydraulics has been observed experimentally in SFR, for example in Rapsodie and Phenix reactors, for which very simple models were proposed to estimate the maximal cladding temperatures in the deformed geometries (Laubin 1982; Pol and Bourdot 1978). In addition, more detailed Computational Fluid Dynamics (CFD) simulations have been used to show the impact of arbitrarily generated bundle deformations, representative of mildly irradiated subassemblies, on its temperature and flow distributions (Baglietto, Fricano, and Sosnovsky 2014; Sosnovsky, Baglietto, Keijers, et al. 2015). However, the coupled evolution of thermal-hydraulics and thermomechanics are not addressed in these works.

Early efforts to consider this coupling were presented by (Ohmae, Morino, Nakao, et al. 1972), by (Sakai, Okubo, and Hishida 1978) and by (Miki 1979). These approaches are based on the use of very simplified thermal-hydraulic simulation tools, and on semi-analytical methods to compute the irradiation induced bundle deformation, neglecting in some cases relevant phenomena. A more comprehensive approach has been recently presented by (Uwaba, Hiroyuki Ohshima, and M. Ito 2017), in which a bundle-thermomechanics code is coupled with a thermal-hydraulic code following the OS paradigm. In that work, a more sophisticated beam-based finite element representation of the fuel bundle is employed to simulate its deformation as a consequence of thermal expansion, swelling, creep, and the mechanical contacts between fuel pins and between the pins and the hexcan. However, a low resolution thermal-hydraulic code has also been employed, which relies on empirical correlations to compute the cross flow between the different subchannels and, as discussed in Chapter 3, is outperformed by more modern CFD techniques (Fanning, W. D. Pointer, and Thomas 2009), especially in significantly deformed fuel bundles (Baglietto, Fricano, and Sosnovsky 2014).

In addition, none of the aforementioned approaches considers the impact of the deformation of the bundle on the coolant mass flow rate, even though (Uwaba, Hiroyuki Ohshima, and M. Ito 2017), (Miki 1979) and (Ohmae, Morino, Nakao, et al. 1972) acknowledge its existence. Indeed, the bundle deformation increases its hydraulic resistance which leads to a coolant redistribution within the core, since less deformed subassemblies represent a preferential coolant flow channel. As a consequence, the mass flow rate of the deformed subassembly can be significantly reduced with respect to a non-deformed one, which has already been observed experimentally (Pol and Bourdot 1978).

Overcoming some of the limitations of the existing methodologies for simulating SFR subassemblies under irradiation—namely the use of very simplified thermomechanical and/or thermal-hydraulic simulation tools, and the nonconsideration of the dependence of the coolant mass flow rate on the deformation—is one of the main goals of this work, which are outlined next.

1.4. Motivations and goals of this work

This work is conducted in the framework of the R&D activities of the CEA on an advanced SFR prototype. As in all SFR development programs, one of the main challenges is to extend the lifespan of the subassemblies, increasing their burn-up and thus improving the economic performance of the reactor, which nowadays constitutes one of the most decisive factors for determining the success of a technological solution for the energy supply problem (MIT 2018). In fact, the evaluation of high burn-up SFR subassemblies is identified by the GIF as one of the main R&D axes for the next years (OECD/NEA 2018).

The need of simulating the extended irradiation of SFR subassemblies reinforces the interest of being able to evaluate the coupling effects between the bundle deformation and its thermal-hydraulics, since they become more relevant at higher irradiation doses. However, as explained in Section 1.3.2, this coupling is traditionally neglected in the numerical simulations conducted to evaluate the evolution of the subassemblies, and the few existing coupling methodologies have significant limitations that arise, mainly, from the use of very simplified lumped parameters thermal-hydraulic codes, from ignoring the effect of the deformation on the coolant mass flow rate, and from using—in most cases—simplified thermomechanical analyses.

Besides, the coupling effects are very dependent on the geometry of the subassembly under consideration, on the temperature range at which it is operated, on the irradiation dose level and on the material properties of its constituents, among other factors, which is why the scarce existing results cannot be extrapolated to new SFR designs, of which the CEA prototype is part. Furthermore, as of the start of this work, the CEA did not possess a simulation methodology to evaluate these coupling effects.

The present work intends to address these issues by developing a methodology for the simulation of the evolution of the fuel subassemblies of SFR under irradiation, in nominal operating conditions, which takes into account the coupling between their thermal-hydraulics and thermomechanics and, if deemed necessary, their neutronics. Moreover, this methodology should be based on state-of-the art simulation techniques, in order to profit from the additional physical insight they provide with respect to the simplified approaches employed in the past, and should not interfere with preexisting code validation efforts, which indicates the adequacy of the OS coupling paradigm. Finally, this work aims to provide a first evaluation of the coupling effects during the irradiation of a SFR subassembly under conditions that are representative of the prototype being studied at the CEA.

1.5. Structure of the manuscript

The remainder of this manuscript is organized as follows.

In Chapter 2, we describe the main thermal-hydraulic, thermomechanical, and neutronic phenomena that are involved in evolution of SFR subassemblies under irradiation in nominal operating conditions. We also study their interdependence and evaluate their importance, in order to define which need to be considered in the coupled simulation methodology here developed.

In Chapter 3, we discuss the different techniques available for the numerical simulation of the thermal-hydraulics of SFR bundles, and we detail the implementation of a CFD approach done in this work to this end.

In Chapter 4, we describe a numerical tool developed at the CEA for the simulation of the thermomechanical evolution of SFR subassemblies under irradiation, which is employed in this work.

In Chapter 5, we describe the simulation methodology developed in this work, based on the coupling between the aforementioned CFD model and the thermomechanical simulation tool of the CEA. In this chapter, we also describe a model developed to take into account the effects of the bundle deformation on the coolant mass flow rate, and an algorithm implemented to generate a Computer Aided Design (CAD) representation of the deformed fuel bundles, required for the CFD simulations.

In Chapter 6, we present the coupled simulation of several study cases aimed at gaining insights on the effects of the coupling in conditions representative of the irradiation of fuel bundles of advanced SFR designs. Additionally, we present neutronic and heat-transfer simulations conducted to validate some of the main hypotheses adopted in the coupling methodology.

In Chapter 7, two application cases are presented. One is based on the simulation of an irradiation campaign conducted in Phenix reactor, while the other is a numerical benchmark performed against a preexisting coupled approach.

Finally, in Chapter 8, the conclusions and outlooks of this work are discussed.

2. SFR subassembly evolution. Phenomenology of a multiphysical system

In this chapter, we introduce the main physical phenomena involved in the evolution of the subassemblies of SFR during their irradiation under nominal conditions, presented in Figure 2.1. During their lifetime in the reactor, the swelling, the creep and the thermal expansion of the structural materials that constitute the subassemblies (I) give place to a very significant geometrical deformation of the fuel bundles (II). This deformation affects the hydraulic resistance of the subassembly under consideration (III), which leads to a coolant mass flow redistribution in the core (IV), since less deformed subassemblies offer a preferential flow channel. The core-level mass flow redistribution affects the total coolant mass flow rate of the deformed subassembly, and the distribution of this flow within the subassembly (V) is also dependant of the deformation itself. Both the coolant mass flow distribution inside the subassembly and the fuel bundle geometrical deformation affect the coolant (and cladding) temperature field (VI), which has a feedback on the temperature-dependent phenomena (I) responsible for the subassembly deformation (II). The temperature of the coolant, which is in average higher in deformed fuel bundles, affects its density and, together with the increased diameter that the deformed fuel pins exhibit, leads to a reduction of the available coolant in the subassembly cross section (VII). This has an impact on the neutron flux distribution (VII), which affects temperature because it determines the power distribution, but is also temperature dependent. Finally, the neutron distribution determines the neutron damage (IX), which is the leading cause of the phenomena (I) that lead to the subassembly deformation (II).

To introduce these concepts, this chapter is organized as follows. Firstly, in Section 2.1, we deal with the thermal-hydraulic characteristics of sodium flow in wired wrapped fuel bundles. Then, in Section 2.2, we present the main contributing factors to the thermomechanical evolution of the subassemblies, and their consequences. In Section 2.3, we outline the fundamental notions of neutron physics required to understand how it is linked to the thermal-hydraulics and the thermomechanics of SFR subassemblies. Finally, the phenomena and coupling mechanisms considered in the simulation methodology developed in this work are identified in Section 2.4.

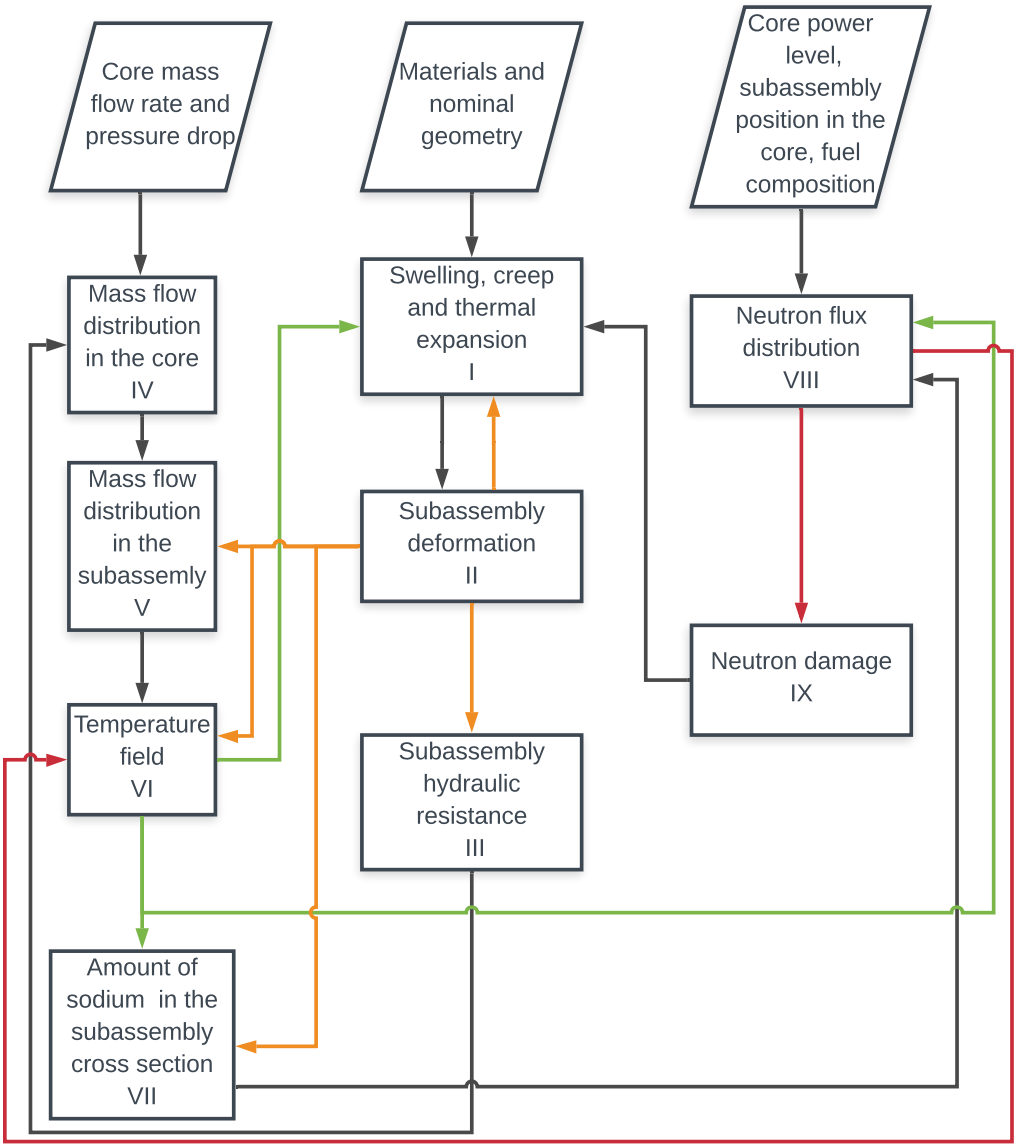

Figure 2.1.: Main physical phenomena involved in the evolution of SFR subassemblies under irradiation in nominal operating conditions.

Table of Contents

2.1. Thermal-hydraulics

2.1.1. Generalities

In nominal operation of SFR, liquid sodium flows through the subassemblies that constitute the core under a forced convection regime. It is injected by the primary pumps into the reactor vessel lower plenum that communicates the inlet nozzles of all subassemblies and, after flowing through them, it enters the upper reactor plenum that connects their outlets. In pool-type designs, this plenum is only pressurized above atmospheric pressure by the column of sodium above the

subassemblies (∼5m). Within each subassembly, the sodium goes firstly through the inlet nozzle and then through the wire-wrapped fuel pin bundle, identified in Figure 1.2 where the subassembly of the advanced SFR designed at the CEA is presented as an example.

In this advanced SFR, with the objective of homogenizing the core outlet sodium temperature and of respecting the design limits imposed on the maximal cladding temperature, the coolant mass flow rate of each subassembly is regulated according to its position within the core. This is achieved by introducing a pressure loss device between the inlet nozzle and the fuel bundle. Also in this reactor, after flowing through the fuel bundle, the coolant goes into a subassembly plenum, still within the hexcan, that separates the outlet of the fuel bundle from the upper neutronic shielding, that typically takes the shape of a wire-wrapped pin bundle of fewer pins and with larger diameter and shorter length than the fuel pins.

The sodium inlet temperature is close to 400°C, while the average outlet temperature is typically close to 550°C. The sodium heating takes place within the active length of the bundle, which contains the fuel pellets where the fission reactions take place, also called heated column. The length of the heated column is around 1 m, while the total length of the bundle is close to 2 m. This difference is mainly determined by the length of the plenum inside the fuel pins needed to accommodate the gaseous fission products, as discussed in Section 2.2.1.2.

The sodium velocity through the subassembly greatly determines the flow regime and its characteristics, as discussed next.

2.1.2. Turbulent flow regime

Fluid flows can be generally classified in three different regimes, namely laminar, transition and turbulent, according to their Reynolds number, which represents the ratio of inertial to viscous forces and can be defined for internal flows as:

$$Re = \frac{\rho U D_h}{\mu} \tag{2.1}$$

where ρ is the density of the fluid, U its average velocity, μ its dynamic viscosity, and D_h the hydraulic diameter of the flow channel, which can be expressed as:

$$D_h = \frac{4A}{P_w} \tag{2.2}$$

with A being the cross sectional area available for the fluid flow and P_w the wetted perimeter of the cross section.

At low velocities (i.e. low Re), the fluid flows in an ordered way following smooth

streamlines, and is called laminar flow. Under these conditions, it is dominated by viscous forces that damp out any velocity fluctuations that might arise. As the Re increases, disturbances appear within the flow leading to magnitude and direction variations in velocity that are no longer damped out by the fluid's viscosity, rendering the flow turbulent. A transition regime exists for intermediate Re, in which the velocity perturbations start manifesting gradually.

The transition to the turbulent regime is defined by a critical Reynolds number Re_c, which depends on the geometry of the problem. For wire-wrapped fuel bundles, Cheng and Todreas (Cheng and Neil E. Todreas 1986) proposed the following expression dependent on the fuel pin pitch to diameter ratio P/D_{ec}:

$$log(Re_c/10000) = (0.7(P/D_{ec}) - 1.0) \tag{2.3}$$

which yields Re_c from 12,000 to 19,000 as P/D_{ec} varies from 1.1 to 1.4, range that includes most SFR designs. In nominal operating conditions, the sodium flow in a SFR subassembly is characterized by a Re between 40000 and 60000, and is therefore well within the turbulent regime.

In turbulent flows, swirling structures with irregular velocities, called eddies, are formed, destroying the smooth streamlines of laminar flows. These eddies enhance the rate at which momentum and energy is transferred within the fluid, which is why turbulent flows are often preferred for industrial heat transfer applications. However, as discussed in Section 2.1.4, the turbulent contribution to heat transfer in liquid metals is limited due to their high thermal conductivity.

In most internal flows, the fluid velocity on the solid surface that confines it can be considered null, since the adhesive molecular forces between the fluid particles and the wall are greater than the cohesive forces between fluid particles, and this is referred to as no-slip condition. Then, if we consider the velocity in the axial direction (flow direction), it is seen to increase, in the direction perpendicular to the wall, from zero to its maximal local value. The enhanced momentum transfer of turbulent flows makes this increase more rapid than in laminar flows, as illustrated in Figure 2.2 for the canonical example of the flow in a circular tube, considering a time-averaged velocity. For incompressible and isotropic Newtonian fluids (valid hypotheses for liquid sodium), the viscous shear forces exerted by the wall to the fluid are proportional to the wall normal velocity gradient, and are thus increased in the turbulent case with respect to the laminar flow. These forces lead to the pressure loss of the flowing fluid, which is thus higher in turbulent flows and is discussed in Section 2.1.6.

The sodium physical properties not only intervene in the definition of Re, but also define other relevant flow characteristics, which is why they are discussed next.

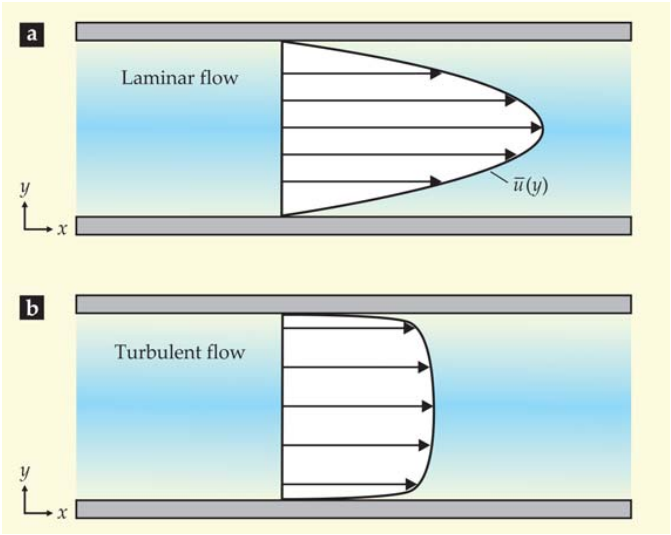

Figure 2.2.: Laminar (a) and turbulent (b) time-averaged axial velocity ($\overline{u}$) profiles for the flow in a circular pipe (Smits and Marusic 2013).

2.1.3. Sodium properties

As explained in Section 1.2.3, liquid sodium is chosen as coolant fluid mainly for its compatibility with a fast neutron spectrum and for its physical properties, which are compared to those of water—the coolant employed in most operating nuclear reactors—in Table 2.1, for representative coolant temperatures and pressures of SFR and PWR.

Property	Units	Sodium (1 atm, 475°C)	Water (15.5 MPa, 315°C)
Kinematic viscosity (ν)	m^2/s	2.92e-7	1.19e-7
Heat capacity (C_p)	J/kg/K	1268	5920
Thermal conductivity (k)	W/m/K	68	5.39e-1
Thermal diffusivity (α)	J/kg/K	6.4e-5	1.3e-7
Boiling point	°C	882	345
Density (ρ)	kg/m^3	838	694
Prandtl number ($Pr = \frac{\nu}{\alpha}$) (See Section 2.1.4)	-	4.56e-3	0.91

Table 2.1.: Sodium (Sobolev 2011) and water (Clément and Bardet 2017) physical properties at representative SFR and PWR coolant temperatures and pressures.

The high boiling point of sodium allows to operate the reactor close to atmospheric pressure, while still being able to have a temperature increase within

the core of about 150°C and having a margin to boiling of more than 300°C in nominal operating conditions. Besides, while the viscosity of sodium is of the same order of magnitude as that of water, its thermal conductivity and diffusivity are about 130 and 500 times larger, respectively. This means that sodium is comparatively much better at conducting heat, and that this heat conduction takes place at a higher rate. As a consequence, the Prandtl number of sodium, which represents the ratio of momentum to thermal diffusivities, is about 200 times smaller than that of water in the operational conditions of PWR. The consequences that this has on the heat transfer properties of sodium are explained in Section 2.1.4.

In the temperature operational range of SFR subassemblies, the temperature dependence of the physical properties of sodium is not very significant. The most sensitive property is the viscosity that, for example, decreases by about 6% with respect to its value at 475°C when temperature is increased by 50°C. This variation is comparable to the uncertainty of the correlations employed to compute the physical properties of sodium (Sobolev 2011).

2.1.4. Low Prandtl flows

The Prandtl number is a non dimensional parameter that depends exclusively on the physical properties of the fluid, and it can be expressed as:

$$Pr = \frac{\nu}{\alpha} = \frac{C_p \mu}{k} \tag{2.4}$$

where ν is the kinematic viscosity of the fluid, α its thermal diffusivity, μ its dynamic viscosity, k its thermal conductivity, and C_p its isobaric heat capacity. Physically, it weights the diffusion of momentum and heat, and it is $<< 1$ for liquid metals such as sodium. This has consequences on the heat transport mechanisms that are particularly relevant near solid surfaces where heat exchange takes place.

To illustrate this, we can consider, for example, the flow of a Newtonian fluid with free stream temperature T_0 on a semi infinite plate at temperature T_W. As presented in Figure 2.3, both the velocity and the temperature profiles develop in the direction perpendicular to the wall, to reach the flow's free stream temperature and velocity. This development takes place in the so called momentum and thermal boundary layers, where the effects of viscosity and of the wall temperature, respectively, are relevant. The boundary layers have a characteristic thickness, typically defined as the distance from the wall when the velocity or the temperature reach 99% of the free stream values. In the case of fluids with $Pr << 1$, the thermal energy diffusion from the wall is larger than the momentum diffusion, and thus the thermal boundary layer thickness (δ_{th}) is larger than the momentum boundary layer thickness (δ_v). For $Pr \sim 1$, which is the case of water for example, the momentum and temperature boundary layers have similar thickness, which motivated

the development and widespread use of the Reynolds analogy between momentum and heat transport to compute the turbulent contribution to heat transfer. However, this analogy, which is described in Section 3.2.2, does not hold for sodium.

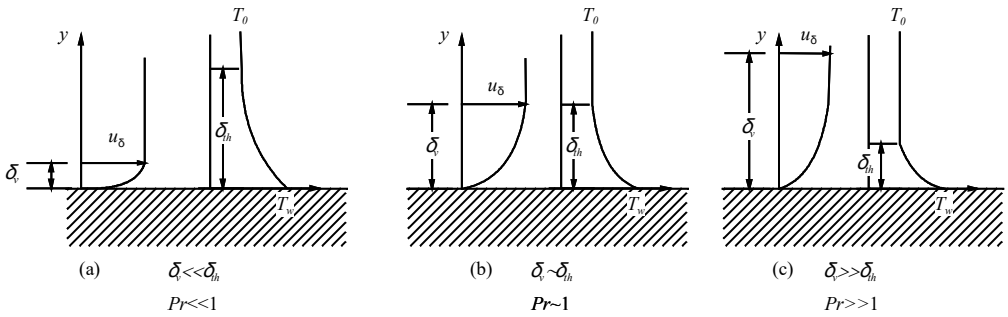

Figure 2.3.: Effect of Pr number on the thickness of the thermal and momentum boundary layers in the case of a flow with free stream temperature T_0 over a semi infinite plate at temperature T_w (OECD/NEA 2015).

For laminar flows of liquid metals under forced convection, the difference between the velocity and temperature profiles does not induce fundamentally different behaviours than those of other fluids, since the heat away from the bounding walls is transported mainly by molecular conduction, and is thus not affected by the velocity distribution. Due to this, the heat transfer correlations developed for fluids with Pr close to unity still hold for liquid metals.

In turbulent flows, on the other hand, heat transport is determined both by the molecular conductivity and the eddy conductivity, discussed in Section 3.2.2, which refers to heat transported by the turbulent eddies and can be the dominant mechanism in fluids for which $Pr \sim 1$ holds. In fluids with $Pr << 1$, however, the molecular conductivity dominates and its effects are not only concentrated on a thin layer close to the wall but also in the turbulent core of the fluid, which is why specific liquid metal heat transfer correlations had to be determined (OECD/NEA 2015).

It is then interesting to compare heat transfer correlations developed for liquid metals to those of fluids with higher Pr. For internal forced convection, a relevant parameter is the heat transfer coefficient h, which relates the heat flux q'' from a solid surface into the fluid to temperature difference between the two, and can be written as:

$$h = \frac{q''}{T_w - T_b} \tag{2.5}$$

where T_w is the temperature of the solid surface and T_b a representative temperature

of the fluid, called bulk temperature, often taken to be the average on the considered cross section. A traditional way of nondimensionalizing the heat transfer coefficient is by defining the Nusselt number Nu that represents the ratio of the convective to conductive heat transport in the direction perpendicular to the flow. Based on the hydraulic diameter D_h, it can be expressed as:

$$Nu = \frac{hD_h}{k} \tag{2.6}$$

For a fluid with $0.7 \leq Pr \leq 120$ flowing with $2500 \leq Re \leq 1.24 \times 10^5$ while being heated, Dittus and Boelter (Dittus and Boelter 1985) developed the following correlation:

$$Nu = 0.023 Re^{4/5} Pr^{0.4} \tag{2.7}$$

while, for liquid metals, one of the most accurate formulas (Bejan 1993) is that of Notter and Sleicher (Notter and Sleicher 1972):

$$Nu = 6.3 + 0.0167 Re^{0.85} Pr^{0.93} \tag{2.8}$$

which is valid for $0.004 \leq Pr \leq 0.1$, $10^4 \leq Re \leq 10^6$, and constant wall heat flux, and is based on experimental and computational data (Bejan 1993). Unlike the case for $Pr \sim 1$, Nu for low Pr fluids was observed to depend on the type of thermal boundary condition (fixed T_w vs fixed q'') as well as on the geometry of the problem (Neil E. Todreas and Mujid S. Kazimi 1990).

Comparing equations 2.7 and 2.8 reveals some key characteristics of liquid metal flows. Firstly, Nu grows with the increasing Re in both cases, since the convective heat exchange is increased by turbulent eddies at increasing flow velocities. However, this dependence is greatly reduced in the case of liquid metals due to the multiplication by their very low Pr. Additionally, the additive constant of Equation 2.8 reveals that significant heat transfer occurs for low Pr fluids even at low Re, due to the high contribution of their conductivity.

Indeed, as discussed in (G. Grötzbach 2013), in a fluid of $Pr = 0.007$—so, slightly higher than that of sodium at SFR operating temperatures—the eddy heat transport exceeds the molecular transport only for $Re > 214000$. It then follows that, at the typical $Re \sim 50000$ of the sodium flow in SFR subassemblies, the contribution of turbulence to the heat transport in the wall normal direction is low. As discussed in Section 3.2, this is relevant because it reduces the relative importance of the model employed to compute the eddy conductivity, and it implies that the uncertainties on the velocity field have a lesser impact on the temperature field than for higher Pr flows.

The flow characterization cannot be complete without considering, besides the

turbulent regime and the low Prandtl effects, the particularities of the geometry of SFR subassemblies, which are discussed next.

2.1.5. Characteristics of sodium flow in wire-wrapped fuel pin bundles

The bundle of wire-wrapped fuel pins is characterized by the following geometrical parameters:

- The external diameter of the fuel pins D_{ec} and of the spacer wires D_w;
- The minimum distance between pin centers, or pitch P;
- The winding step H of the helically wrapped spacer wires;
- The gap g_H between the center of a peripheral pin and the hexcan;
- The side length L_H of the cross section of the hexcan, with an associated plate to plate distance E;
- The number of fuel pins N_{pins};
- The length of the fuel bundle L_{bundle}.

The value of the parameters that describe the cross section of the fuel bundle of the advanced SFR being designed at the CEA are presented, as a representative example, in Figure 2.4. In this case, the local hydraulic diameter of the corner and edge subchannels are significantly larger than the triangular inner subchannels, which is also the case for other SFR designs. Besides, the heat input per unit length is lower in the peripheral subchannels than in the inner subchannels, since the first are next to the hexcan while the latter are surrounded by fuel pins. For these reasons, there are two distinct flow zones within the cross section of the bundle. The peripheral region presents higher axial velocity values, and the fuel pins there are colder than the pins from the inner (or central) region, although the first are subject to higher temperature gradients around their circumferences. As we will see in Section 2.2.2, the differences between central and peripheral pins have direct consequences on their thermomechanical evolution under irradiation.

A recent review on existing pin bundle experiments identified, besides the aforementioned peripheral/central differences, the following key flow characteristics (Saxena 2014):

- There is significant circular flow and wake downstream of the spacer wires. This creates a low velocity zone that leads to cladding hot spots.

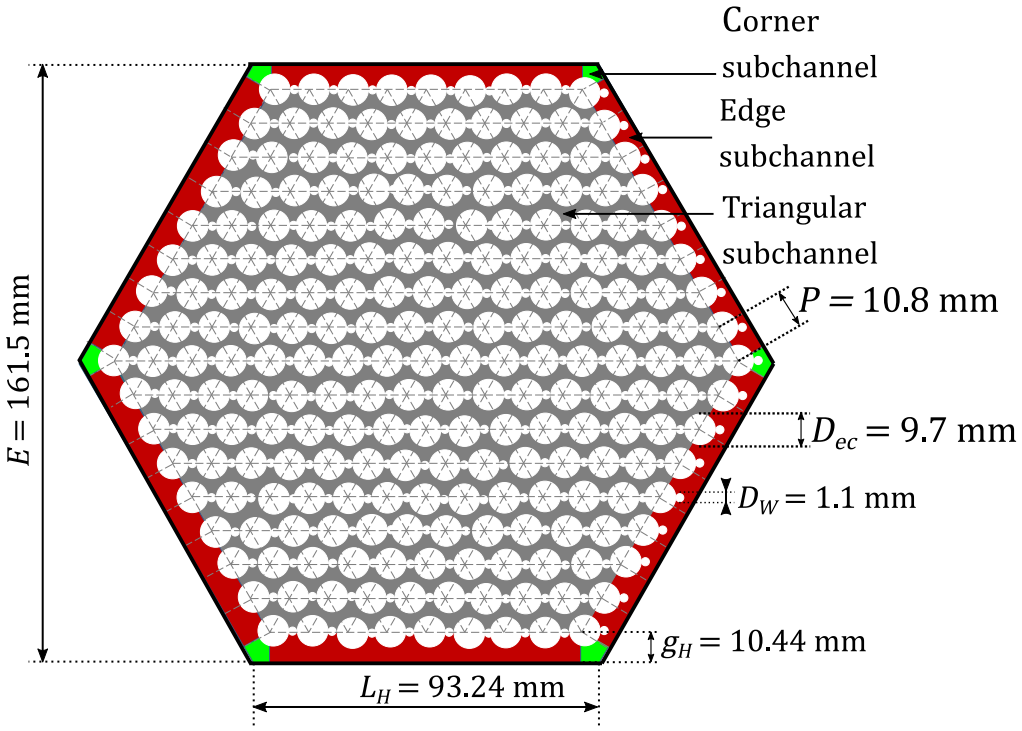

Figure 2.4.: Cross section of the fuel bundle of the advanced SFR designed at the CEA. Adapted from (Saxena 2014).

- The axial velocity of a given subchannel and its cross flow are cyclic along the axial direction, with a spacial periodicity given by the helical pitch H of the spacer wire.

In complement with the experimental campaigns, significant efforts have been done in the last years in terms of numerical simulations, in order to improve our understanding of the thermal-hydraulics of wire-wrapped pin bundles. Some relevant findings are summarized below:

- The spacer wires induce very significant secondary flows, with tangential velocities representing up to about 15% of the axial velocity, which are stronger in the edge and corner subchannels than in the central ones (J.-H. Jeong, Song, and Lee 2017b; Cadiou and Saxena 2015). One of the reasons for this is that, following the length of the bundle, the gap between peripheral pins and the hexcan is always interrupted by the wire in the same angular direction; however, the gaps between fuel pins are interrupted by spacer wires in alternating rotation directions, and thus their effects cancel out partially (Zhao, J. Liu, Ge, et al. 2017). Besides, the force exerted by the wires on the fluid is dependent on the axial velocity, but also heavily dependent on

the angular position between the wire and the pin, and the relative position between the wire and the hexcan (J.-H. Jeong, Song, and Lee 2017a).

- Increasing the winding step H (in the range 100 mm $< H <$ 300 mm) leads to a lower sodium cross flow and significantly decreases the friction factor (Natesan, Sundararajan, Narasimhan, et al. 2010; Gajapathy, Velusamy, Selvaraj, et al. 2015), and it has very little effect on the Nusselt number (Natesan, Sundararajan, Narasimhan, et al. 2010). However, completely eliminating the twist does have a noticeable impact, as shown by (Gajapathy and Velusamy 2016) who computed a Nu 15% larger for helically wrapped spacer wires than with straight spacers, which was explained by the increased sodium mixing.

- Increasing the number of pins of the bundle does not have a large influence on the main flow features (Natesan, Sundararajan, Narasimhan, et al. 2010), although larger fuel bundles lead to a higher mass exchange between central subchannels (Brockmeyer, Carasik, Elia Merzari, et al. 2017) and to slightly larger friction factors (Rolfo, Péniguel, Guillaud, et al. 2012).

The determining role of the geometrical parameters of SFR bundles on the sodium flow characteristics suggests the need of a detailed thermal-hydraulic model in order to capture these effects in a numerical simulation. The geometry of the subassembly also determines its pressure loss due to friction, which is linked to the coolant mass flow rate and is discussed next.

2.1.6. Pressure drop in SFR subassemblies

In a viscous fluid, internal shear stresses arise due to its resistance to move with uniform velocity when only one portion of it is subjected to an externally imposed velocity. For incompressible flows of Newtonian fluids, the components τ_{ij} of the shear stress tensor τ can be expressed as (Neil E. Todreas and Mujid S. Kazimi 1990):

$$\tau_{ij} = \mu(\frac{\partial v_i}{\partial x_j} + \frac{\partial v_j}{\partial x_i}) \tag{2.9}$$

where $v_{i,j}$ and $x_{i,j}$ are the i, j components of the velocity and position, respectively, and μ the dynamic viscosity of the fluid. For internal flows, the wall shear stress τ_w acting against the fluid motion is of particular engineering interest since it leads to its pressure loss due to friction. Under the no-slip condition discussed in Section 2.1.2, one can see from Equation 2.9 that τ_w can only depend on the velocity gradient in the wall normal direction. As discussed in that section, the wall normal velocity gradient is higher in turbulent than in laminar flows, which

causes the frictional energy loses to be higher in the first[1].

It is customary to nondimentionalize τ_w by employing the Darcy-Weisbach friction factor f_D as follows:

$$f_D = \frac{8\tau_w}{\rho U^2} \tag{2.10}$$

where U is the mean flow velocity. Then, the pressure drop ΔP due to friction at the wall over a length L can be written as:

$$\Delta P = \frac{f_D L U^2 \rho}{2D_h} = \frac{f_D L Q^2}{2\rho D_h A^2} \tag{2.11}$$

where D_h is the hydraulic diameter of the channel under consideration, A its cross sectional area, and Q the mass flow rate of the fluid.

Over the last six decades, over a hundred experimental investigations of the pressure drop in wire-wrapped pin bundles have been conducted worldwide, resulting in about 10 empirical correlations between the friction factor, the Reynolds number, and the geometrical parameters of the bundle (S. Chen, N. Todreas, and Nguyen 2014; S. K. Chen, Y. M. Chen, and N. E. Todreas 2018). One of these correlations is that developed by Rehme (Rehme 1973), that can be expressed as:

$$f_D = ((64/Re)F^{0.5} + (0.0816/Re^{0.133})F^{0.9335})N_{pins}\pi(D_{ec} + D_w)/P_w) \tag{2.12}$$

where

$$F = (P/D_{ec})^{0.5} + 7.6(P/D_{ec})^2(D_{ec} + D_w)/H^{2.16} \tag{2.13}$$

As indicated by Equation 2.13, and as discussed in the previous section, increasing the pitch of the wire, H, leads to a lower friction factor. This is illustrated in Figure 2.5, where the normalized friction factor is presented as a function of H, as computed with Equation 2.12 using the dimensions of the advanced SFR designed at the CEA and taking $Re = 50000$.

Additionally, equations 2.12 and 2.13 evidence the dependence of f_D on the diameter D_{ec} of the fuel pins. Increasing D_{ec} only slightly reduces the friction factor, as can be observed in Figure 2.6a, where Rehme's correlation and $Re = 50000$ were also employed[2]. However, as illustrated in Figure 2.6b, it significantly reduces the

[1] The velocity fluctuations of turbulent flows add an additional contribution to the shear stress (see Section 3.2.2), not considered in this analysis based on mean velocity profiles. However, the importance of these additional stresses is low close to the wall, and they vanish on the wall surface (Kundu, Cohen, and Hu 2001), and thus the qualitative conclusion remains valid.

[2] Virtually the same result is obtained if the mass flow rate is kept constant, instead of Re.

hydraulic diameter of the bundle. Therefore, the reduction of D_h overcomes the reduction of f_D, so that increasing D_{ec} leads to an increase in the bundle pressure drop, if the coolant mass flow rate is not modified, or to a reduced flow rate, if the pressure drop is kept constant, as can be deduced from Equation 2.11. This is of particular relevance in the context of evaluating the coolant mass flow rate in deformed fuel bundles, which is discussed in Section 5.3.2. In Section 5.3.2, we will show that the coolant mass flow rate of a deformed subassembly—in which D_{ec} is increased—is lower than that of a non-deformed one. This is because all subassemblies are connected at their inlets and outlets by plenums, so the coolant can be diverted from the deformed subassembly towards the non-deformed ones, which provide a preferential flow path with less hydraulic resistance. This flow redistribution according to the hydraulic resistance of the subassemblies is the same principle that allows homogenizing the outlet temperature of the core of SFR by introducing pressure drop devices in their inlet nozzles, as mentioned in Section 2.1.1.

A reduction of the coolant mass flow rate would be of little importance if it was not for its impact on the temperature distribution within the subassembly, which is discussed next.

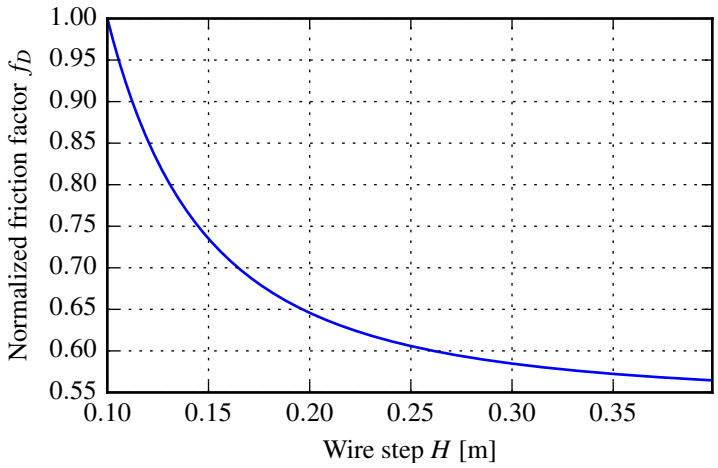

Figure 2.5.: Normalized friction factor as a function of H, computed with Rehme's correlation.

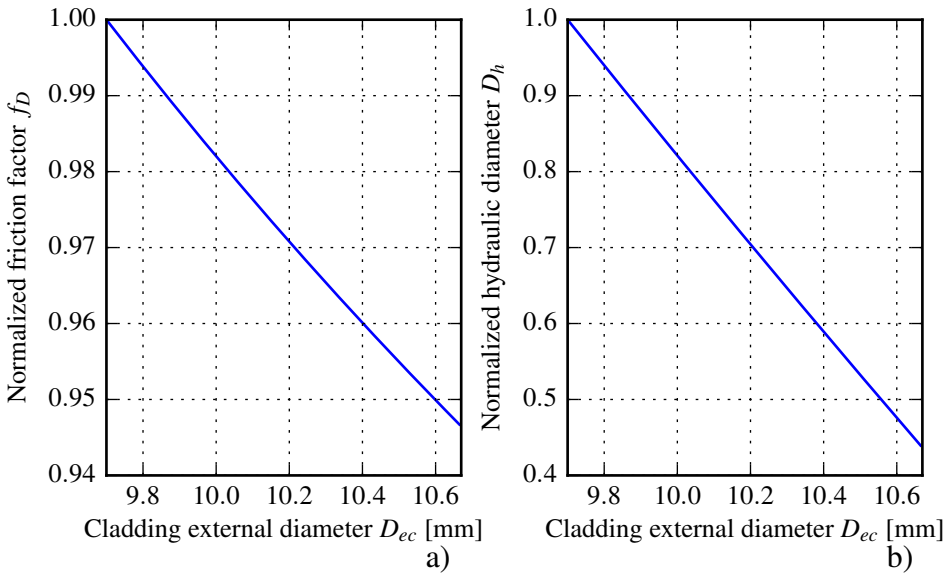

Figure 2.6.: Normalized friction factor computed with Rehme's correlation (a) and normalized hydraulic diameter (b) as a function of the cladding external diameter.

2.1.7. Axial distribution of sodium temperature

The steady state axial distribution of the average sodium temperature $\overline{T}_{Na}(z)$ within the subassembly cross section (sodium bulk temperature) can be computed from a known temperature $\overline{T}_0$ at an axial position z_0 (e.g. the inlet sodium temperature) and the axial distribution of the subassembly linear power $q'(z)$ by considering an energy balance. This yields:

$$\overline{T}_{Na}(z) = \overline{T}_0 + \frac{1}{QCp}\int_{z_0}^{z} q'(\tilde{z})d\tilde{z} \tag{2.14}$$

where Q is the mass flow rate of the coolant in the subassembly, which is assumed to remain in liquid state, and Cp the coolant's specific heat capacity, considered constant here. Then, the axial profile of coolant's bulk temperature is proportional to the integral of the linear power profile.

Equation 2.14 allows to evaluate the increase of the sodium bulk temperature $\delta\overline{T}_{Na}(z)$ as a consequence, for example, of the mass flow rate reduction δQ mentioned in Section 2.1.6. Then, if we consider the length of the heated column (i.e. where $q'(z) \neq 0$), we have that $\delta\overline{T}_{Na}(z)$ is null at its inlet, and grows monotonically with the axial position to reach, at the outlet, a value $\delta\overline{T}_{out}$ given by:

$$\delta\overline{T}_{out} = \frac{P_{SA}}{CpQ}\frac{\delta Q}{Q-\delta Q} = \Delta\overline{T}^{0}_{Na}\frac{\delta Q}{Q-\delta Q} \tag{2.15}$$

where P_{SA} is the total subassembly power and $\Delta\overline{T}^{0}_{Na} = \overline{T}_{Na} - \overline{T}_{0}$ the difference between the inlet and outlet sodium bulk temperature before the mass flow rate Q is reduced.

2.1.8. Section summary

In this section, we firstly define some of the general characteristics of the sodium flow in SFR subassemblies, including its turbulent nature and the implications that this has. Then, the sodium physical properties are introduced, and its very high conductivity is highlighted. These properties give place to a very low Pr number, the consequences of which are then discussed. Out of these, one of the most relevant is that, in nominal operating conditions, the heat transfer from the claddings to the sodium is dominated by conduction. As discussed in Section 3.2, this reduces the relative importance of the error introduced in the modelling of the turbulent contribution to the heat exchange.

Finally, the parameters that characterize the SFR fuel bundles and the main resulting flow characteristics are summarized. It results that the external diameter of the cladding is a key parameter, and that it plays a major role in the pressure drop characteristic of the bundle. In this work, this is of upmost importance, since—as we will see in Section 2.2.5—the cladding diameter increases as a consequence of the irradiation, and this leads to a reduction of the coolant mass flow rate, evaluated in Section 5.3.2. As discussed at the end of this section, this causes a sodium temperature increase.

Such a temperature variation would have an impact on the temperature-dependent thermomechanical evolution of the fuel bundle, which is discussed in the next section.

2.2. Thermomechanics

In this section, we show how the fuel pin claddings, the spacer wires and the hexcan of SFR subassemblies evolve during their irradiation, from a thermomechanical point of view. The main external loads that lead the evolution of the stress and strain states of these components are:

- The high temperatures they are subject to;
- The internal pressurization of the claddings due to the accumulation of gaseous fission products, and, to a lesser extent, the sodium pressure which acts both

on the claddings and on the hexcan;

- The exposure to highly energetic neutrons produced in the fission chain reaction, which interact with the materials inducing microscopic changes that have macroscopic consequences.

Then, we begin by describing the evolution and magnitude of these loads.

2.2.1. Evolution of the external loads

2.2.1.1. Temperature

The steady state heat conduction within the cladding can be described in terms of Fourier's law, which relates the heat flux vector $\boldsymbol{q''}(\boldsymbol{r})$ to the temperature gradient $\boldsymbol{\nabla} T(\boldsymbol{r})$ and can be expressed as (Incropera 2007):

$$\boldsymbol{q''}(\boldsymbol{r}) = -\lambda_c \boldsymbol{\nabla} T(\boldsymbol{r}) \tag{2.16}$$

where $\boldsymbol{r}$ is the position vector and λ_c the cladding thermal conductivity, assumed constant here. By considering only the conduction in the radial direction, the cladding temperature at any point of its thickness can be computed from the linear power q' and the temperature at its external wall. Under these conditions, the cladding temperature at a radius r, $T_c(r)$, can be written as (Bailly 1999):

$$T_c(r) = T_c(r_{ec}) + \frac{q'}{2\pi\lambda_c} \ln\left(\frac{r_{ec}}{r}\right) \tag{2.17}$$

where r_{ec} is the external cladding radius. The cladding temperature difference between its external and internal radii ($r_{ec} - r_{ic} \sim 0.5$ mm) is typically between 20°C and 40°C.

The cladding surface temperature $T_c(r_{ec})$ is the same as the temperature of the sodium it is in contact with, so both the cladding and the sodium average temperatures have a similar axial distribution. To illustrate this, the axial profiles of sodium and cladding temperatures within the active length an SFR subassembly are presented in Figure 2.7. In this figure, the cladding temperature is computed at its mid-thickness and averaged in its circumference, while the sodium temperature is averaged in the subchannel being considered. The distribution of linear power and neutron flux[3] are also presented in this figure, as calculated for a Phenix subassembly by the code employed to follow the operation of the reactor. In this case, the neutron flux and the linear power have a chopped cosine shape with a maximum close to the center of the active length of the subassembly. Therefore,

[3]The (scalar) neutron flux indicates—at a given position and for all energies and directions—the number of neutrons moving per unit surface and per unit time. As discussed in Section 2.3, it is the main variable used to describe the neutron distribution in the reactor.

as predicted by Equation 2.14, the sodium and cladding temperatures present a sinusoidal axial distribution that grows until reaching its maximum at the upmost part of the heated column. It should be noted that the temperature fluctuations induced by the spacer wires are not considered in the simplified thermal-hydraulic calculations conducted to generate the curves of Figure 2.7. These effects could be understood as temperature perturbations acting on the baseline cladding temperature illustrated in that figure, and, as we will see in Section 6.5, they can be very significant.

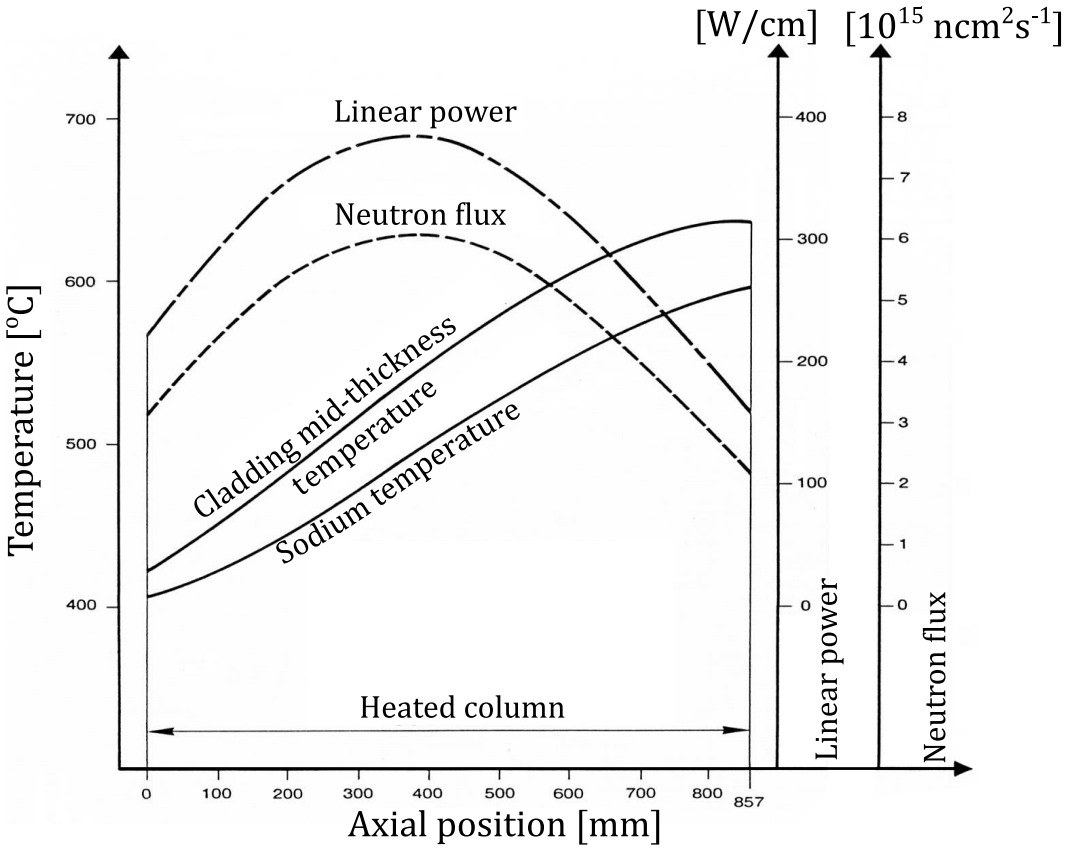

Figure 2.7.: Axial distribution of cladding temperature for a central pin of a Phenix subassembly, of the sodium temperature within a subchannel in contact with the cladding, and of the linear power and neutron flux, as computed by the code employed to follow the operation of the reactor (Pelletier 2018).

The temperature range of the fuel cladding presented in Figure 2.7, given approximately by a temperature of 400°C at the bottom of the heated column and 620°C at its upper part, is representative of an inner pin of a SFR fuel bundle. It

is to be noted that the upper limit of this range represents, expressed in Kelvin (K), approximately 50% of the melting point of the cladding steel in K, which has consequences on the behaviour of the materials under irradiation, discussed in Section 2.2.2. Additionally, it leads to a thermal expansion of the claddings that can reach up to close to 1%. As explained in Section 2.1.5, the cladding temperature is lower for the peripheral pins of the bundle, and the magnitude of this temperature difference can be as high as 100°C (Cadiou and Saxena 2015). This temperature difference has significant consequences on the thermomechanical behaviour of the fuel bundle, as we will see in Section 6.6.

If we consider a subassembly under irradiation at constant total reactor power and with constant mass flow rate and geometry, the evolution of its temperature distribution is determined by the evolution of the subassembly power distribution. Without considering the perturbations induced by the neutron absorbing control rods that are partially inserted in different positions within the core, the subassembly power time evolution depends on the fuel utilisation, or burn-up.

In axially homogeneous fuel concepts, the depletion of the fissile atoms within the fuel leads to a reduction of the subassembly power and thus to a reduction of its temperature over time. On the other hand, in axially heterogeneous concepts where fertile and fissile blankets are intercalated, the generation of fissile isotopes in the first might outbalance the fuel depletion of the latter. In this case, the power distribution inside the subassembly would change, and the total subassembly power would increase during the irradiation. As a result of the subassembly power increase, the sodium outlet temperature would also increase during the irradiation. This power evolution is illustrated in Figure 2.8, that shows the Beginning Of Life (BOL) and End Of Life (EOL) power distribution of the advanced SFR designed at the CEA, as calculated by neutronic simulations conducted during its conceptual design stages. In this case, a large power increase is observed in the central fertile blanket during the irradiation. The power of the lower fertile blanket also increases but it has a smaller contribution to the total power, both at BOL and at EOL. Due to the increased power in the fertile blankets, the average sodium temperature at the outlet of the fuel column is, in this case, approximately 10°C higher at EOL than at BOL.

Independently of the evolution of the linear power, the sodium and the cladding temperature distribution within the fuel bundle depend on the evolution of its geometry and of the coolant mass flow rate, the determination of which is at the core of this work. The evolution of the bundle geometry is discussed in Section 2.2.5, and its numerical simulation is described in Chapter 4. The evaluation of the deformation-induced coolant mass flow rate reduction is discussed in Section 5.3.2.

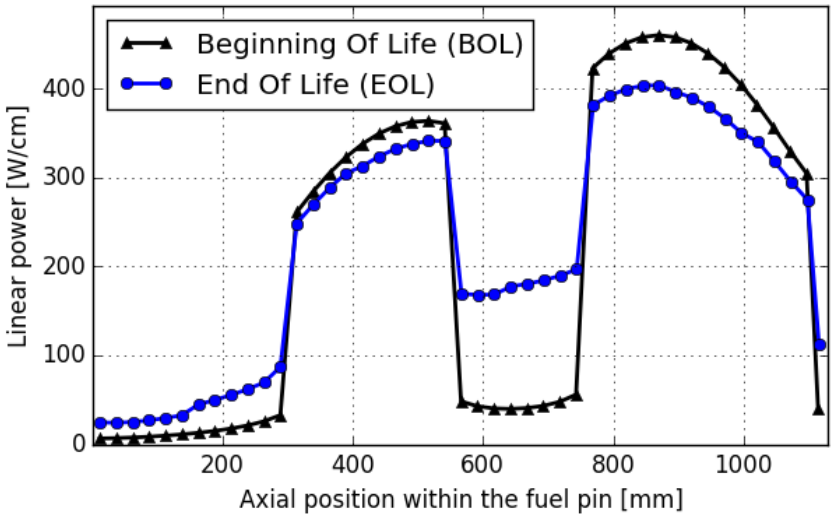

Figure 2.8.: BOL and EOL linear power profile of an axially heterogeneous fuel pin.

2.2.1.2. Pressure

Some of the isotopes produced by the fission reactions are in gaseous form, and a fraction of the gases are trapped inside the fuel pellets where they are produced, thus contributing to their swelling. However, the high operational temperature of SFR fuels favours their diffusion against the temperature gradient (i.e. towards the external surface of the pellet), leading to their release into the free volume within the fuel cladding. The percentage of the fission gases that escape the fuel pellets increases with burn-up, as illustrated in Figure 2.9 for a Phenix fuel pin. At high burn-up, the fission gas release typically reaches 80-90% in SFR[4], leading to internal cladding pressures that can reach several MPa (Yang 2012).

By considering Dalton's law of partial pressures and the ideal gas law, the internal cladding pressure P_{fg} due to the gaseous fission products can be expressed as:

$$P_{fg} = \frac{\sum_i n_i RT}{V} \tag{2.18}$$

where V is the free volume inside the cladding, R the ideal gas constant, T the temperature of the gas mixture, and n_i the number of moles of each fission gas. The working temperature being fixed, the main design variable available to limit the internal cladding pressure, and thus its associated stress, is the available volume inside the fuel cladding. Therefore, a large free volume is achieved by including a

[4]In PWR, the fission gas release is $\sim$ 10%.

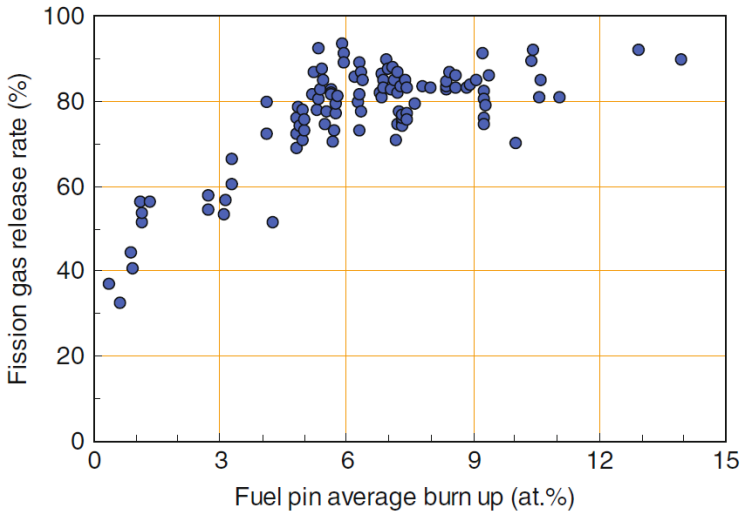

Figure 2.9.: Fission gas release rate as a function of burn-up for a standard Phenix fuel (Cacuci 2010).

large plenum below the fuel column, and a shorter plenum above it. The fuel pin of the advanced SFR designed at the CEA is characterized by a relatively large pin internal diameter of 8.7 mm and a large lower plenum of almost half the total pin length. For this reason, the expected fission gas pressure at high burn-up is close to 4 MPa, significantly lower than that of Phenix fuel pins (internal diameter of 5.5 mm and lower plenum of $\sim 1/3$ of the pin length) that could exceed 8 MPa.

With longer lower plenums, most of the fission gases accumulate below the heated length of the fuel pins, and they are thus affected by the sodium inlet temperature and less so by the sodium outlet temperature and its changes during the irradiation. This is particularly relevant in the context of this work, since it implies that the cladding internal pressure is not significantly affected by the temperature increase induced by the deformation of the bundle, which—as discussed in Section 6.5—is maximal towards the outlet of the heated column of the fuel bundle and does not affect the lower gas plenum.

In addition to the inner pressure due to the fission gases, the claddings are also subject to sodium pressure, that acts on their external surface and affects also the hexcan. This pressure is maximal at the bottom of the fuel bundle, since the coolant looses pressure due to friction as it moves up and the hydrostatic pressure is also reduced in that direction. Finally, the sodium flowing in the small gaps between subassemblies also acts on the hexcan, and the associated sodium external pressure is also maximal at the bottom. Representative values of maximal sodium internal and external pressures are 0.4 MPa and 0.2 MPa, respectively, and thus

the hexcan is subject to a maximal net pressurization of 0.2 MPa.

Under the load imposed by the internal pressure P_{fg}, the cladding may be conveniently approximated by a thin-walled cylindrical tube closed at both ends (Waltar, Todd, and Tsvetkov 2012). Under this approximation, the cladding circumferential (hoop) stress $\sigma_{\theta\theta}$ is given by[5]:

$$\sigma_{\theta\theta} \cong P_{fg}\overline{r}_c/e \tag{2.19}$$

where $\overline{r}_c = (r_{ec} + r_{ic})/2$ and e is the thickness of the cladding. Under the same approximation, in which the ends of the claddings are considered to be closed and thus subject to the same pressure level, the longitudinal stress σ_{zz} is half of the hoop stress:

$$\sigma_{zz} \cong P_{fg}\overline{r}_c/2e \tag{2.20}$$

The radial stress is equal to the internal pressure at the inner radius of the cladding, and null (or equal to the external pressure if it is considered) at its outer radius. Since $\overline{r}_c/e \sim 10$, we can see from equations 2.19 and 2.20 that the radial stress is significantly smaller than the hoop and longitudinal stresses. For thin-walled cylinders, and neglecting the external pressure, the radial stress can be approximated by:

$$\sigma_{rr} \cong -P_{fg}/2. \tag{2.21}$$

where the negative sign indicates it is a compressive stress.

In order to predict the yield of metals, which is the onset of plastic—permanent—deformation, based on the results of uniaxial tensile tests, it is customary to define an equivalent stress σ_{eq}. Considering that ductile materials start yielding when the elastic energy associated to their deformation reaches a critical value (Hill 1998) motivates the definition of the von Mises equivalent stress, which can be written as:

$$\sigma_{eq} = \sqrt{\frac{(\sigma_1 - \sigma_2)^2 + (\sigma_2 - \sigma_3)^2 + (\sigma_3 - \sigma_1)^2}{2}} \tag{2.22}$$

where σ_i $(i = 1, 2, 3)$ are the principal stresses, which are the components of the stress tensor when it is expressed in a basis such that the non-diagonal components (shear stresses) are null. In a cylinder under axisymmetric loading, the principal stresses are the normal stresses in the radial, circumferential and longitudinal

[5] In this analysis, we have neglected the external cladding pressure P_{ext} since, as discussed in this section, it is significantly lower than P_{fg}. Its effects can be taken into account by simply replacing P_{fg} by $P_{fg} - P_{ext}$ in the expressions given to compute the stresses, noting that—unlike P_{fg}—P_{ext} depends on the axial position within the cladding.

directions, and thus the equivalent stress is given by:

$$\sigma_{eq} = \sqrt{\frac{(\sigma_{\theta\theta} - \sigma_{rr})^2 + (\sigma_{rr} - \sigma_{zz})^2 + (\sigma_{zz} - \sigma_{\theta\theta})^2}{2}} \tag{2.23}$$

Employing Equation 2.23 and the cladding dimensions of the advanced SFR designed at the CEA, and considering an internal pressure of 8 MPa, a conservative[6] approximation of the equivalent stress induced by the pressurization of $\sigma_{eq} = 63.8$ MPa is obtained. The equivalent stress thus computed corresponds to the primary equivalent stress associated to the cladding internal pressure, averaged in the thickness of the cladding. Primary stresses are those that result from internal forces and moments required to satisfy the mechanical equilibrium with the external forces and moments and body forces, and they cannot be relaxed by a small plastic deformation. Then, the $\sigma_{eq} = 63.8$ MPa is significantly lower than the limit of approximately 100 MPa—as calculated for a very penalizing temperature of 650°C—considered for the primary cladding stresses during the operation of the advanced SFR designed at the CEA.

It should be noted that the secondary stresses, which appear as a consequence of internal or boundary constraints and can be relaxed by plastic strain, are not taken into account in this analysis. Examples of secondary stresses are the ones caused by the differential thermal expansion within the cladding, or by a non-uniform swelling distribution, phenomenon that is described in Section 2.2.2.2. To guarantee the mechanical integrity of the cladding, another design limit is imposed to the total equivalent stress, which takes into account both the primary and secondary stresses, and is evaluated locally, as opposed to being averaged in the thickness of the cladding. This limit is approximately 200 MPa, for the advanced SFR designed at the CEA and for a temperature of 650°C.

2.2.1.3. Irradiation dose

The irradiation dose quantifies the interaction of the irradiation field with the materials, and it is customary to express it in Displacements Per Atom (dpa). Expressed in this way, the irradiation dose represents the average number of times that each atom of the material is displaced from its original position as a consequence of the interaction with energetic particles that, in the case of interest of this work, are the fast neutrons produced by the fission chain reaction.

As will be further explained in Section 2.3.3, the irradiation dose increases with increasing neutron flux integrated over time, also called fluence. However, unlike

[6] Conservative because a Phenix pressure level was employed, which is higher than the pressure estimated for this new reactor.

the fluence, it is also a function of the probability of an incident neutron of inducing a given number of atom displacements in the irradiated material, which is very dependent on the neutron energy and on the material itself. This difference makes the irradiation dose correlate well with the irradiation effects on the material properties[7], which is not the case with neutron fluence. This can be seen in Figure 2.10 where the yield stress (a relevant mechanical property discussed in Section 2.2.2.4) change of irradiated stainless steel samples in three reactors with very different neutron energy spectra are plotted as a function of fluence and of irradiation dose in dpa.

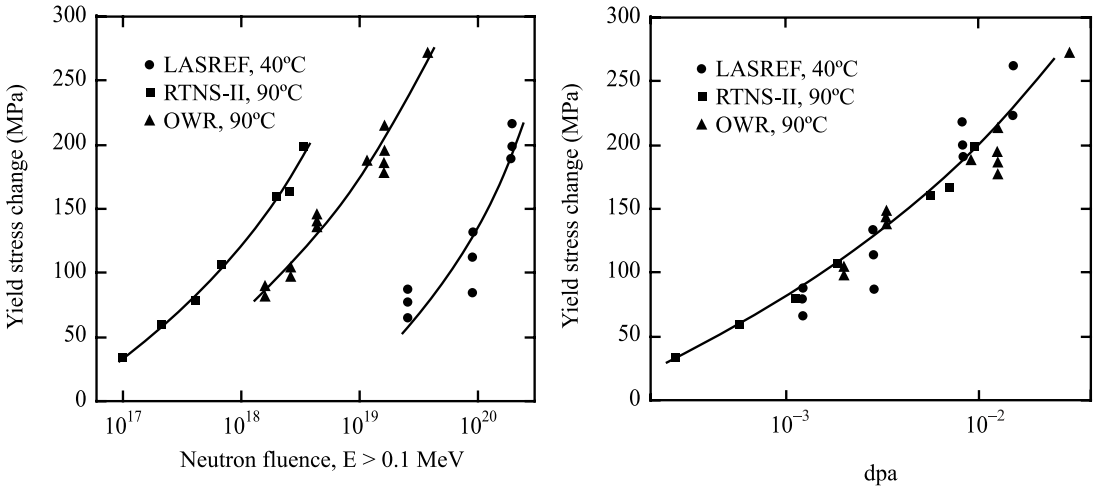

Figure 2.10.: Yield stress change of stainless steel irradiated in three reactors with different neutron energy spectra, as a function of fluence and of irradiation dose in dpa (Gary S. Was 2007).

The axial distribution of irradiation dose at EOL follows closely the fast neutron flux profile. Therefore, it has a maximum close to the core mid-plane for axially homogeneous fuel bundles, while two distinct maxima—one below and one above the core mid-plane—are present in fuel pins that include a fertile blanket between two fissile columns. This effect can be observed in Figure 2.11, where the normalized EOL axial dose distributions are presented as computed for a Phenix fuel cladding and for a cladding of the advanced SFR designed at the CEA. In this reactor, the maximal dose currently being considered is close to 100 dpa. However, in Phenix reactor, subassemblies have been irradiated up to doses close to 160 dpa (Pelletier 2018). At this dose level, the effects of swelling and irradiation creep, described in Section 2.2.2, lead to a significant geometrical deformation of SFR fuel bundles, described in Section 2.2.5, which compromises the mechanical integrity

[7]Provided that the displacement based damage dominates over transmutation effects. As discussed in Section 2.2.2, this is indeed the case for the structural materials of fast reactors.

of the subassemblies and thus limits their lifespan. Being able to increase the maximal dose up to which the integrity of the subassemblies is guaranteed is one of main research lines in SFR development programs, since it would lead to a higher burn-up and thus to a more efficient utilisation of the fuel (OECD/NEA 2018).

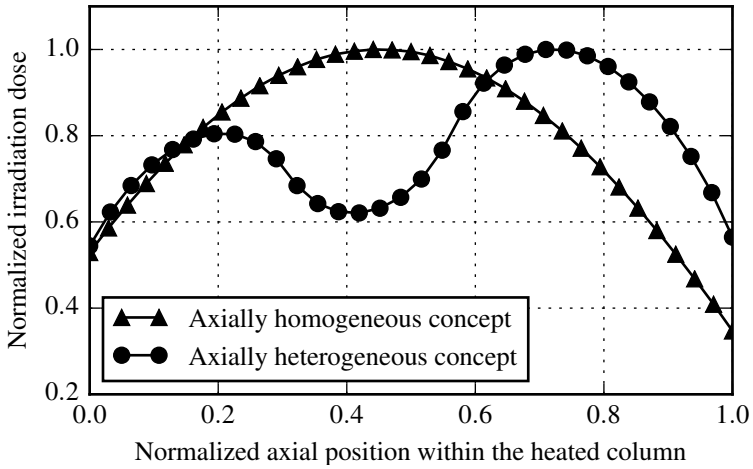

Figure 2.11.: Axial profiles of normalized cladding irradiation dose for an axially homogeneous and an axially heterogeneous fuel concept.

2.2.2. Irradiation effects on the subassembly materials

2.2.2.1. Irradiation damage

Metals have a crystal structure, which means that their atoms are arranged in an ordered lattice that can be described by the periodic repetition of a unit cell, consisting of a defined number of atoms arranged in a fixed geometrical pattern. However, this lattice is not perfect, and has a series of crystallographic defects that have an effect on the macroscopic behaviour of the metal. These defects can be a consequence of, for example, the presence of impurities, the thermal vibration of atoms, the thermomechanical treatment employed in the metal manufacturing, or the interaction with a radiation field. The main crystallographic defects can be classified as (Mouritz 2012; Bailly 1999; Gary S. Was 2007; Frank 1957):

- **0D.** Point defects, which involve one atom or a pair of atoms. The three main types of point defects are missing atoms from the lattice (vacancies), atoms placed in a position normally not occupied (interstitial), or atoms in the lattice replaced by an atom of a different element (substitutional defect). Point defects form the foundation for all observed effects of irradiation on the physical and mechanical properties of materials (Gary S. Was 2007);

- **1D.** Dislocations, which can be in the form of a line that forms a boundary between a region of the crystal that has slipped and one that has not, and can also form closed loops. They act as sources and sinks of point defects, and some attract more interstitials than vacancies, which is characterised by the dislocation bias.
- **2D.** Grain boundaries, which limit two crystals (within which the lattice is continuous) with different orientations.
- **3D.** Volume defects, such as voids and bubbles.

The predominant effect of the irradiation on the metals employed on fast reactor subassemblies comes from the displacement of atoms of their crystalline structure (F. Garner 2012). This generates some of the defects mentioned above, whose migration and clustering is responsible for the macroscopic effects of the irradiation on these materials (Bailly 1999). In stainless steels irradiated in water cooled reactors, the transmutation of elements produced by neutron capture reactions—and the generation and precipitation of helium in particular—can have a significant importance. However, transmutation is only a second-order contribution to the damage process when these steels are irradiated in fast reactors. Indeed, the helium production rate in highly thermalized neutron spectra has been observed to reach $\sim$ 100 atomic parts per million (appm) He/dpa, while typical values for fast neutron spectra are $\sim$ 0.1-0.3 appm He/dpa (F. A. Garner 2004). It should be noted, however, that the transmutation-induced helium clusters serve as nucleation sites for voids that, as discussed below, have a major role in the evolution of steels under irradiation (F. Garner 2012).

In fast reactors, the metal atom displacements come predominantly from the elastic collision with high energetic neutrons. When a neutron collides with an atom in the metal, the latter can be displaced from its original position in the lattice if the neutron energy is high enough. This first atom impacted by the neutron, called PKA (Primary Knocked-on Atom), can come to rest in an interstitial position or displace other atoms, thus generating a displacement cascade, the probability of which increases with increasing energy of the incident neutron. This cascade is concentrated in a very small volume, and results in the creation of a collection of point defects (vacancies and interstitials) and clusters of these defects in the crystal lattice. After they are created, these defects do not remain static but migrate due to diffusion and coalesce with a kinetics that depends on factors such as temperature, neutron flux, irradiation dose, and concentration of alloying elements.

The irradiation generates interstitials and vacancies in pairs, called Frenkel Pairs, that increase the volume of the material. If these point defects are sufficiently close to each other, they recombine and disappear, undoing the volume increase. At high enough temperatures, they can migrate within the crystalline lattice and recombine,

and can also be annihilated by defect sinks—which are surfaces, grain boundaries and dislocations—, process that also removes part of the volume increase associated with the defect. Alternatively, defects of the same type can be agglomerated in clusters. Interstitial clusters of a given size collapse into dislocation loops, which removes a large part of the associated volume increase. Clusters of vacancies, on the other hand, can either collapse into a loop, which also removes the associated volume increase, or form a void. In this case, the volume increase of the material is preserved (Bailly 1999).

The processes described above lead to several mechanisms that induce dimensional changes of the irradiated materials. These are void swelling, swelling due to the formation of helium bubbles, irradiation induced growth, and irradiation creep. In the materials employed in fast reactors, swelling due to helium bubbles is minor (Lauritzen, Withop, and Wolff 1969), and they do not exhibit growth since they do not have a crystallographic texture[8], required for growth to manifest (Adamson, Griffiths, and Patterson 2017). Therefore, only void swelling and irradiation creep are addressed next.

2.2.2.2. Void swelling

Void swelling can be defined as a macroscopic increase in volume of a material caused by the formation, growth, and coalescence of microscopic voids, consequence of irradiation induced atom displacements. This happens if the flow of vacancies towards the voids is higher than the flow of interstitials, which is possible since the latter are preferentially attracted and annihilated by the dislocations present in the metal structure.

The first models developed to describe the swelling process rely on the formalism of rate theory, and take into account the generation, recombination and annihilation of defects on the different types of sinks, and, eventually, the interactions between defects and impurities. These models allowed to determine some general characteristics of swelling, summarized below (Bailly 1999):

- In most metals and alloys, swelling occurs at temperatures between 0.3 and 0.6 T_M, where T_M is the metal melting temperature in K. The swelling g depends on the void density N_{void} and on their average volume V_{void}, such that it can be expressed as $g = N_{void}V_{void}$. For $T << 0.2\ T_M$, no swelling occurs since the defects are annihilated by mutual recombination. At the lower end of the temperature range where swelling occurs, the defects are in high concentration and thus the void nucleation rate is high but, since the

[8] Radiation-induced growth is a volume-conservative, anisotropic distribution of strains that does not require the action of stresses, and affects materials in which the crystals have a preferential orientation, also called texture.

defect diffusion is slow, the volume of the voids remains very small. On the other hand, for temperatures close to the upper limit of the range, the defect diffusion rate is high, and they are therefore annihilated at sinks at a high rate. In this scenario, the void nucleation is very low, and there are only few voids with a large volume, with practically no contribution to the macroscopic swelling. In between, there is a temperature that maximizes swelling, which typically lies between 0.4 T_M and 0.5 T_M.

- Swelling increases with the irradiation dose, but is characterized by an incubation period during which, in spite of the increasing dose, the volume change remains very small. At sufficiently high doses, the swelling rate reaches a steady state value, also called stationary swelling. The dose from which swelling becomes noticeable, called incubation dose, is strongly dependent on the characteristics of the material and on the irradiation conditions.

- Swelling is highly dependent on the dislocation density. If it is sufficiently high, their role as defects annihilators overcome the effects of their preference for interstitials, and thus swelling is reduced.

However, the simplified models used to derive the characteristics described above only represent some of the processes that contribute to the swelling of irradiated metals. An exhaustive review on the subject was conducted by Garner (F. Garner 2006; F. Garner 2012), who highlighted the contribution of the following factors:

- **Crystal structure.** For example, austenitic steels present higher stationary swelling rate than ferritic/martensitic steels.

- **Base composition**. It affects swelling mainly by modifying its incubation dose. In Fe-Cr-Ni ternary alloys (which are the base of the industrial steels adopted for the SFR fuel claddings), increasing the nickel content reduces swelling, although the trend is reversed at high nickel contents (∼35 to 60 Ni wt%). On the other hand, swelling increases monotonically with increasing chromium content. The effects of the base composition are also dependent on the irradiation temperature.

- **Solutes**. The addition of solutes also affects almost exclusively the incubation dose. Out of the solutes studied, phosphorus and then silicon are the most effective suppressors of void growth over the entire temperature regime of swelling. Some additives, such as Ti and C—the effects of which are linked due to the formation of TiC—greatly suppress swelling in some temperature ranges, but increase it in others. In cold worked steels, however, the addition of Ti is beneficial in the whole temperature range of interest.

- **Thermomechanical Treatment**. Cold working increases the dislocation density and thus delays the stationary swelling phase. The temperature of

the thermal annealing done to keep the additives in solid solution also has a significant impact on the swelling behaviour of the materials, and thus needs to be carefully controlled.

- **Displacement Rate**. An increase in the displacement rate (i.e. dpa per unit time) has been shown to produce, in different materials, longer incubation periods.

- **Temperature**. As mentioned before, it affects the tendency of vacancies and interstitials to recombine, and also the formation and dissolution rates of both interstitial clusters and vacancy clusters. It affects the steady state swelling, although there is a large temperature plateau where it is approximately constant. In addition, it influences the swelling through the modification of the behavior of the solutes.

- **Stress.** Swelling has been observed to increase with increasing stresses.

Besides the undesired effects of the dimensional changes induced by swelling, discussed in Section 2.2.5, this phenomenon has been shown to lead to an excessive embrittlement of the steels employed for the fuel claddings and the hexcan when it exceeds a value of approximately 6% Vol (Fissolo, Cauvin, Hugot, et al. 1990; Schmidt 1992), which is currently on of the limiting factors for the lifespan of SFR subassemblies. For these reasons, being able to predict the swelling of these components during their irradiation is essential from a safety point of view. However, the complex dependence of swelling on the numerous factors mentioned above makes it very difficult to develop a consistent theoretical model to predict it. To overcome this difficulty, the solution adopted by the different SFR development programs around the world is based on determining empirical swelling laws from samples of known composition and thermomechanical treatment irradiated under controlled conditions.

These empirical swelling laws aim to capture its dependence on temperature and irradiation dose. For the austenitic steels employed for the fuel claddings in the French SFR development program, the volume swelling rate per dpa, $\dot{g}$, is expressed as follows:

$$\dot{g} = \frac{\dot{g}_0}{1 + e^{\frac{\Delta_g - D}{\delta_g}}} \tag{2.24}$$

Under this formulation, Equation 2.24 indicates that at sufficiently high irradiation dose D, the swelling rate tends to the stationary swelling rate per dpa, $\dot{g}_0$. Additionally, the swelling rate is very low for doses inferior to the incubation dose Δ_g, and the transition between the swelling incubation period and the stationary swelling rate is ruled by the transition dose δ_g. This is schematically illustrated in Figure 2.12a for the swelling rate and on Figure 2.12b for the cumulated swelling

g, that results from integrating Equation 2.24 with respect to the irradiation dose. Due to its isotropy, the linear swelling strain ε_{swe} can be expressed as:

$$\varepsilon_{swe} = (1+g)^{1/3} - 1 \approx \frac{1}{3}g \tag{2.25}$$

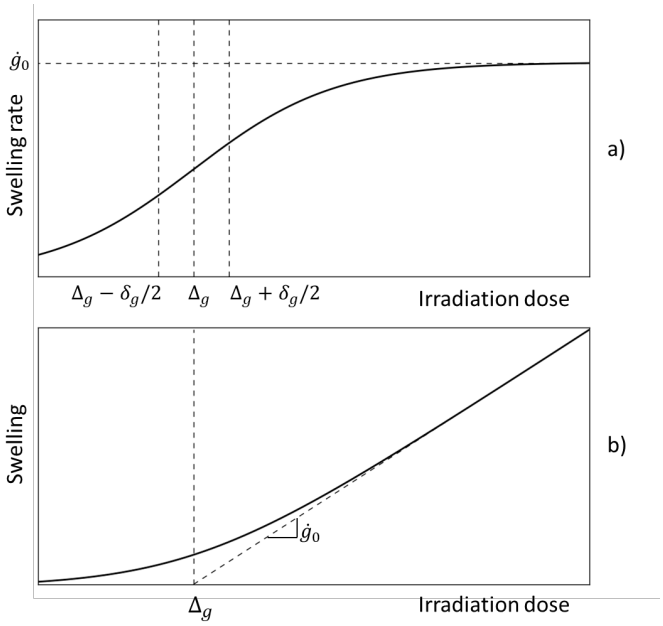

Figure 2.12.: Schematic representation of swelling rate (a) and of the cumulated swelling as a function of the irradiation dose, as determined by an empirical law.

The dependence of the steady swelling rate, the incubation dose, and the transition dose on temperature T is considered, and they are expressed as follows.
Stationary swelling:

$$\dot{g}_0 = \beta_1 e^{-\left(\frac{T-\beta_2}{\beta_3}\right)^2} \tag{2.26}$$

Incubation dose:

$$\Delta_g = \beta_4 e^{-\left(\frac{T-\beta_5}{\beta_6}\right)^2} + \beta_7 \tag{2.27}$$

Transition dose:

$$\delta_g = \beta_8 + \beta_9 T \tag{2.28}$$

where β_i $(i = 1, ..., 9)$ are constants that depend on the material being irradiated (H. Touron 1988).

For the reference austenitic steel for the fuel claddings of the advanced SFR designed at the CEA, equations 2.24 to 2.28 lead to the behavior illustrated in Figure 2.13. The steady state swelling rate is presented in Figure 2.13a, for different irradiation doses, as a function of temperature. In Figure 2.13b, the cumulated swelling for different irradiation doses and the swelling incubation dose are presented as a function of temperature. It can be observed that, for this steel, the steady state swelling rate is maximal for a temperature close to 520°C—which, in K, represents approximately 50% of the steel's melting point—, while the maximal cumulated swelling is shifted to lower temperatures (460°C to 485°C for the dose range considered) due to the temperature dependence of the incubation dose. At higher temperatures, the partial derivative of swelling with respect to temperature, $\partial g/\partial T$, is negative. It is important to note that, as can be observed in Figure 2.7, a significant part of the heated length of SFR fuel pins operate in this range, in which a temperature increase would lead to a reduction of the swelling strain. This temperature dependence is the main reason—together with the creep temperature dependence discussed in Section 2.2.2.3—for the coupling between the thermal-hydraulic and thermomechanical evolution of SFR fuel bundles, and it explains why, as we will see in Section 6.5, the deformation-induced temperature increase has a negative feedback on deformation.

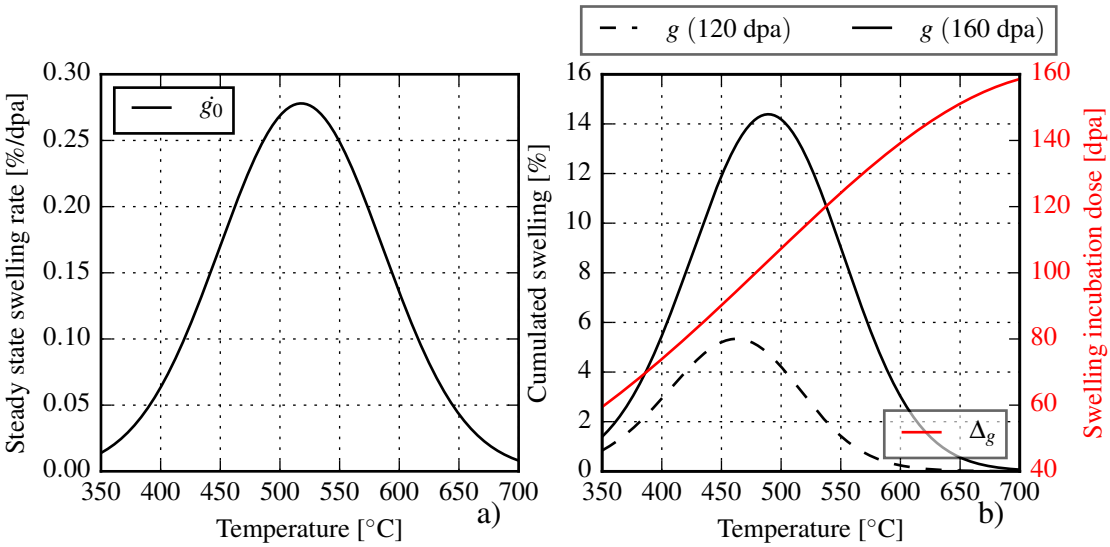

Figure 2.13.: Steady state swelling rate as a function of temperature (a), and temperature dependence of the swelling incubation dose and, for two different irradiation doses, of the cumulated swelling (b). These results correspond to the reference austenitic steel for the fuel claddings of the advanced SFR designed at the CEA.

As mentioned before, the ferritic/martensitic alloys exhibit low swelling rates, and, for this reason, they have been retained as the material for the hexcans, which therefore exhibit great irradiation stability even at high doses (J. L. Séran, Lévy, Gilbon, et al. 1992). Indeed, the empirical law developed for the swelling of the reference hexcan steel of French SFR considers a constant swelling rate of about 2.5e-5 1/dpa, which is two orders of magnitude lower than the maximum swelling rate of the cladding steel. However, the creep resistance (see Section 2.2.2.3) of these steels drops drastically above a temperature of about 550°C, which is why they cannot be employed for the claddings that operate at higher temperature and under a much higher internal pressurisation than the hexcan (Bailly 1999).

The empirical swelling laws presented in this section have been determined by measuring the diametral strain of irradiated fuel claddings and correlating it with the calculated irradiation dose and temperature. To isolate the swelling contribution to the total strain, density measures were performed in some cases (we will see in Section 2.2.2.3 that the other major contributing mechanism to the cladding permanent strain is volume conservative) and, in others, the computed contribution of other mechanisms was simply deducted from the measured strain. The temperature and swelling gradients in the circumference of the claddings—evaluated in this work and discussed in sections 6.5 and 6.6, respectively—were not taken into account, since the simplified thermal-hydraulic codes available when these laws were determined did not allow to have this kind of detail in the temperature distribution.

If the swelling distribution within the material is not homogeneous, secondary internal stresses arise from the differential strain. These stresses, that also appear as a consequence of differential thermal expansion, are relaxed—during nominal reactor operation—as the material undergoes plastic deformation under the effect of irradiation creep, which is described next.

2.2.2.3. Irradiation induced creep

Creep can be defined as the time-dependent deformation of a metal under constant load and at high temperature ($T/T_m > 0.3$). This deformation is characterized for being irreversible and volume conservative, and is caused by the generation and diffusion of vacancies and dislocations. The irradiation increases the production of excess defects and modifies microstructure of the irradiated metal, and thus it significantly increases the creep rate over that due to thermal creep alone, and induces creep in temperature ranges where thermal creep is negligible (Gary S. Was 2007).

Unlike thermal creep, which has a high order dependence on the applied stress given by σ^n, with n generally between 4 and 7, irradiation creep is characterized by

a first stage where an initially high strain rate decreases until a steady state strain rate is reached, which exhibits a linear dependence on stress and is accelerated with the appearance of swelling[9]. The steady state creep is typically reached within the first hundreds of hours of irradiation in fast reactors, and it is thus the most relevant stage (Borodin, J.-C. Chen, Sauzay, et al. 2014). Even though irradiation creep is not considered damaging, and has the beneficial effect of relaxing stresses within the material, it can lead to unacceptably high strains (Bailly 1999; F. Garner 2012). It is then of engineering interest to express the strain induced by steady state irradiation creep in terms of the main loads of the materials under irradiation, as is done with swelling. The most widely used approach to do so considers 3 different creep mechanisms, summarized in what follows (Bailly 1999; Gary S. Was 2007; Borodin, J.-C. Chen, Sauzay, et al. 2014; F. Garner 2006).

The Stress Induced Preferred Absorption (SIPA) mechanism describes the contribution of dislocation climb to the creep strain. Dislocation climb is the process by which a dislocation goes over an obstacle—such as a void or a loop—, and it is required for it to then move (glide), leading to the permanent deformation of the material. The SIPA mechanism reflects the fact that some dislocations are more efficient at climbing these obstacles, depending on their orientation relative to the direction of the applied stress, and its effects can be expressed as a function of the equivalent applied stress σ_{eq} as:

$$\dot{\varepsilon}^{SIPA}_{irr.creep} = K\sigma_{eq} \tag{2.29}$$

where $\dot{\varepsilon}_{irr.creep}$ is the irradiation creep strain rate per dpa, and K the creep compliance modulus.

While SIPA relates to the increased dislocation climbing, other mechanisms are related to the climb-enabled gliding of dislocations. One of these is the Preferred Absorption Glide (PAG), which is a consequence of SIPA. In this mechanism, climbing enables the gliding of pinned dislocations—that is, blocked by an obstacle—and thus the material can deform beyond the elastic strain that occurs if the dislocations remain pinned. The contribution of PAG to the irradiation creep strain has been observed to depend on the square of the stress, and can be expressed as:

$$\dot{\varepsilon}^{PAG}_{irr.creep} = 2K\alpha{\sigma_{eq}}^2 \tag{2.30}$$

where α is a constant further described below. The third mechanism is the creep strain caused by the climb and glide of dislocations due to their interstitial bias. This term is linked to swelling, since, as the material swells, more and more

[9] As discussed in this section, some of the mechanisms that contribute to the irradiation creep have a quadratic dependence on the stress. However, these are of minor importance in most of the stress range of interest.

vacancies precipitate in voids, leading to a higher interstitial absorption in the dislocations. It is then expressed as:

$$\dot{\varepsilon}^{g}_{irr.creep} = \alpha \sigma_{eq} \dot{g} \tag{2.31}$$

where α is the creep swelling coupling coefficient. For the austenitic steels employed for the fuel claddings, it is customary to consider a constant value of α close to 10^{-3} MPa^{-1}, even though it has been observed to decrease with increasing swelling at high swelling levels. This behaviour, called creep damping, is not yet fully understood (F. Garner 2012).

In practice, the contributions of these three mechanisms are added, such that the empirical equation employed for the macroscopic evaluation of irradiation creep is given by:

$$\dot{\varepsilon}_{irr.creep} = K\sigma_{eq} + 2K\alpha {\sigma_{eq}}^2 + \alpha \sigma_{eq} \dot{g} \tag{2.32}$$

In the absence of swelling, the balance between the SIPA and PAG contributions depends on the applied stress and on the cold working of the material. For the Ti stabilized austenitic steels employed for the claddings of the French SFR, PAG has been shown to have a negligible contribution up to at least 180 MPa (Maillard, R. Touron, J L Séran, et al. 1992)[10]. For these steels, the value of K is considered to depend of temperature and is written as:

$$K = \gamma_1 e^{-\left(\frac{T-\gamma_2}{\gamma_3}\right)^2} + \gamma_4 \tag{2.33}$$

where γ_i $(i = 1, ..., 4)$ are experimentally determined constants. Unlike the swelling empirical law given by equations 2.24 to 2.28, whose coefficients need to be determined for each different alloy—or even for a production batch of a given alloy—, the creep compliance has been observed to have roughly the same value for austenitic steels of different composition (F. Garner 2012), and gives place to the behaviour presented in Figure 2.14. In this figure, the irradiation creep strain rate is presented, for different stress levels, as a function of temperature, and the steady state swelling strain rate used to compute it is also presented. It can be seen that, like with swelling, the irradiation creep strain has a maximum for a temperature close to 500°C, after which it monotonically decreases. As presented in Figure 2.13, the maximum cumulated swelling—this is, integrated up to a given dose—is shifted to slightly lower temperatures due to the effects of the incubation dose, which grows with temperature in the range of interest. This shift also affects the cumulated irradiation creep strain, since it has a term proportional to the swelling rate, though to a lesser extent.

[10] This implies that, up to 90% of the maximal stress design limit discussed in Section 2.2.1.2, the irradiation creep term that is linear in stress dominates.

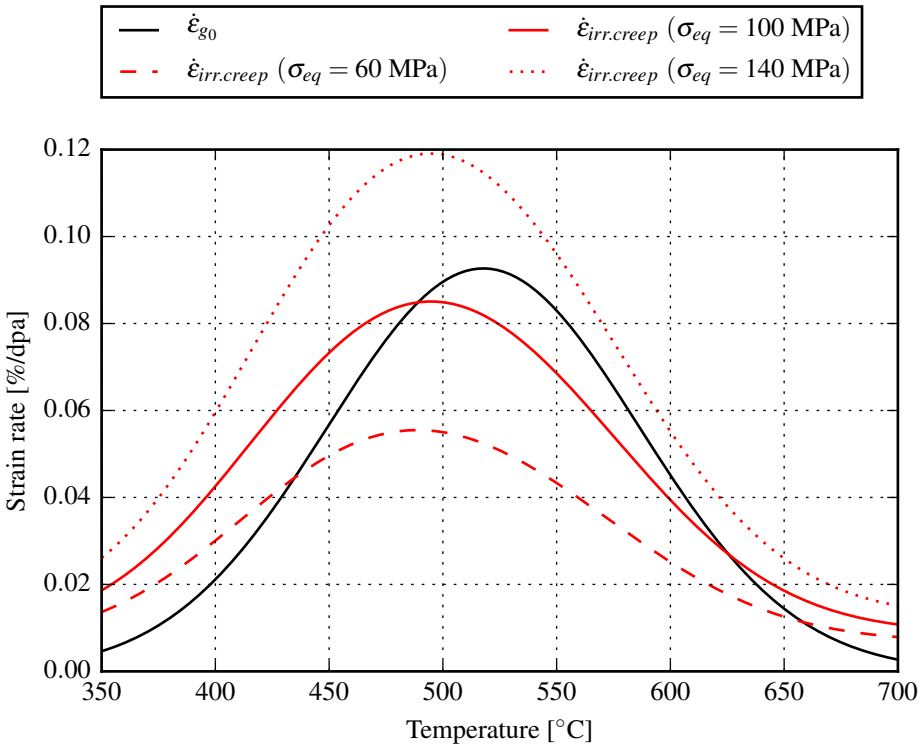

Figure 2.14.: Strain rates induced by the steady state swelling and by irradiation creep for different stress levels, as a function of temperature. These rates represent the asymptotic behaviour predicted by the empirical laws, since the steady state swelling rate was considered to compute the irradiation creep strain rate. These results correspond to the reference austenitic steel for the fuel claddings of the advanced SFR designed at the CEA.

2.2.2.4. Irradiation effects on the mechanical properties of steels

The main consequence of the irradiation on the mechanical properties of austenitic steels is a modification on their mechanical strength and their ductility, and these effects depend on the irradiation temperature, as well as on the thermomechanical treatment of the steels. It is customary to analyze the irradiation effects in terms of the results of a tensile test and, in particular, the Ultimate Tensile Stress (UTS), which is the maximal engineering stress[11] reached during the test, and the yield stress, defined as the stress when 0.2% plastic strain is reached.

The evolution under irradiation of the mechanical properties of the cold worked austenitic steels employed for the fuel claddings exhibits three different phases.

[11] The engineering stress σ_{en} under a load F is given by $\sigma_{en} = F/A_i$, where A_i is the initial cross sectional area of the loaded specimen. The real stress is computed using the real area, that is reduced as the tensile test proceeds, and most noticeably if necking occurs.

During a first short phase, the mechanical properties change at a high rate to then stabilize during a second phase. For temperatures below approximately 450°C to 480°C, an increase of the UTS and the yield stress is observed; at higher temperatures, the tendency is inverted. This low temperature hardening and high temperature softening is illustrated in Figure 2.15, where the stabilized (i.e. values during the second phase) UTS and the yield stress of samples irradiated in Phenix reactor are presented as a function of their irradiation temperature (equal to the test temperature), and are compared to the tensile properties of unirradiated samples. As the irradiation proceeds, a third phase in the evolution of the mechanical properties manifests with a marked reduction in the steel ductility, induced by the increase of void swelling. Indeed, as mentioned in Section 2.2.2.2, a swelling of about 6% has been shown to lead to excessive embrittlement of the cladding steel.

It is also important to mention that the irradiation also lowers the Ductile Brittle Transition Temperature (DBTT), which is the temperature at which the material transitions from ductile to brittle, and it is most relevant for the evaluation of the mechanical integrity of the claddings at handling or room temperatures.

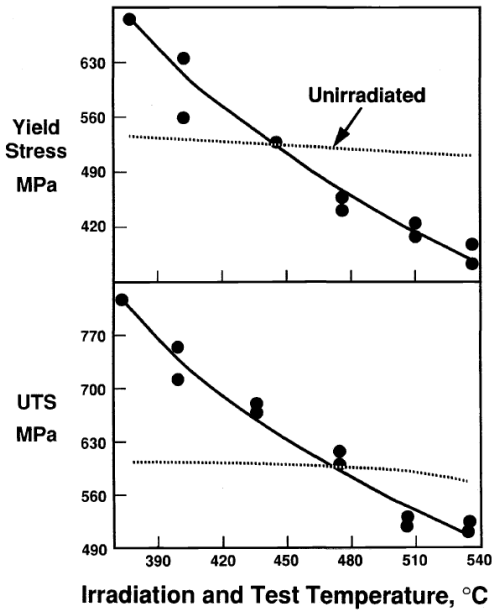

Figure 2.15.: Irradiation-induced changes in the tensile properties of cold-worked, Ti-stabilized steel samples irradiated in Phenix reactor, as a function of temperature (F. Garner 2006).

The reference martensitic steel for the hexcan of French SFR, on the other hand, presents almost no evolution of its tensile properties with the irradiation. However,

an increase of the DBTT is observed when irradiated at temperatures below 450°C approximately (J. L. Séran, Lévy, Gilbon, et al. 1992).

2.2.3. Materials employed for the cladding and the hexcan

The materials employed for the fuel claddings and the hexcan of SFR subassemblies were originally selected based on their compatibility with the fuel and the sodium, their stability under irradiation and their resistance to swelling, their high temperature mechanical strength and ductility (mainly the cladding), and their corrosion resistance.

The leading factor in the evolution of the employed materials has been the swelling resistance, and different strategies have been employed to improve it. In the French SFR program, successive improvement from the austenitic stainless steel of type 316 first employed have been achieved by increasing the Ni content, adding swelling retarding additives such as Ti, and by performing specific thermomechanical treatments such as cold working. The current reference material for the fuel claddings of French SFR is the 15-15Ti Austenitic Improved Material 1 (AIM1) steel.

As mentioned before, the ferritic/martensitic steels exhibit a significantly superior swelling resistance than the austenitic steels. However, they cannot be used for the claddings due to their low creep resistance at temperatures above 550°C approximately, which is not compatible with the operational temperature of the claddings and their high internal pressurization. However, they are employed for the hexcans since they are not subject to such solicitations. In the French SFR program, the reference material for the hexcan is the martensitic steel EM10.

While the ferritic/martensitic steels employed for the hexcan seem to be a satisfactory long term solution which would allow the very high doses of $\sim$ 200 dpa envisaged for SFR, the poor swelling resistance of austenitic steels of the cladding makes reaching those dose levels unlikely. The most promising solution is based on ferritic/martensitic steels with increased high temperature creep resistance induced by a fine dispersion of oxides, called Oxide Dispersion Strengthened (ODS) steels (Pelletier 2018).

2.2.4. Pellet cladding interaction

During their irradiation, the fuel pellets can come in contact with the cladding by closing the small, helium filled, fabrication gap that separates them. This gives place to the so called Pellet Cladding Mechanical Interaction (PCMI). During operation at full power, PCMI is often negligible compared to the pressure exerted by the fission gases, although it can become relevant during fast power transients and induce a high cladding strain (Cacuci 2010). The main mitigating factors for

the PCMI are the capacity of the Mixed Oxide (MOX)[12] fuel pellets of accommodating their swelling due to their porosity and the formation of a central hole (if not already present from fabrication) (Pelletier 2018), and, at high burn-up, the formation of a chemical compound between the pellet and the cladding, called JOG (from the French *Joint Oxyde Gaine*), that is easily deformable (Uwaba, M. Ito, and Maeda 2011; Yang 2012).

A more relevant phenomena for fast reactors in nominal operating conditions is the Fuel Cladding Chemical Interaction (FCCI). Indeed, some of the fission gases can destroy the passive layer of the stainless steels employed for the fuel claddings and react with their main components, leading to the cladding corrosion. The main corrosive mechanisms attack the cladding on the upper part of the fissile column, which is at higher temperatures, and at the interfaces between the fertile and fissile blankets. The corrosion of the cladding, which was observed to increase with increasing cladding maximal temperature (Pelletier 2018), can significantly reduce its load bearing thickness, and thus compromise its mechanical integrity. However, since its effects are very localized, they do not significantly affect the evolution of the geometry of the cladding during its irradiation.

2.2.5. Deformation of SFR fuel bundles during irradiation

During their irradiation in nominal operating conditions, the SFR fuel bundles undergo significant deformation caused by the aforementioned swelling and irradiation induced creep of the fuel claddings, the spacer wires and the hexcan, and, to a lesser extent, by their thermal expansion. There are several distinct macroscopic deformation mechanisms that manifest progressively during the irradiation. The resulting evolution of the geometry of the fuel bundle and its interaction with the hexcan can be divided in three different phases, described below.

During a first phase, the fuel pins are not in contact with each other. The main deformation mechanisms involved are their bowing due to differential thermal and swelling strains, the diametral strain of the claddings and the spacer wires, and the helical flexion of the claddings under the tension of their wires, caused by the differential deformation between the two. During this phase, the gap between the fuel pins and between the peripheral fuel pins and the hexcan (initially of about 0.1 mm), is continuously reduced. The start of the second phase of the bundle deformation, schematically represented in Figure 2.16a, is marked by the closing of this gap, which gives place to the mechanical interaction between pins and between the pins and the hexcan.

[12] MOX—$(U, Pu)O_{2-x}$, with the subscript 2-x signaling an oxygen deficiency—are the reference fuel materials for SFR programs around the world (Waltar, Todd, and Tsvetkov 2012).

The contact between the fuel pins is established through the spacer wires, while the contact between fuels pins and the hexcan can be established either through the spacer wires or, if the helical flexion is high enough, directly between the cladding and the hexcan. The first of these two cases—which, given the relatively low helical flexion under the tension of the wire alone, is the most commonly encountered—is illustrated in Figure 2.16a. In practice, since not all the fuel pins deform equally, not all the gaps are closed at the same time in a given cross sectional plane. In particular, the peripheral pins exhibit higher levels of deformation, which is caused by their lower operational temperature, discussed in Section 2.1.5, and by the fact that lower temperatures induce higher swelling and irradiation creep strains in the temperature range of interest, as explained in sections 2.2.2.2 and 2.2.2.3.

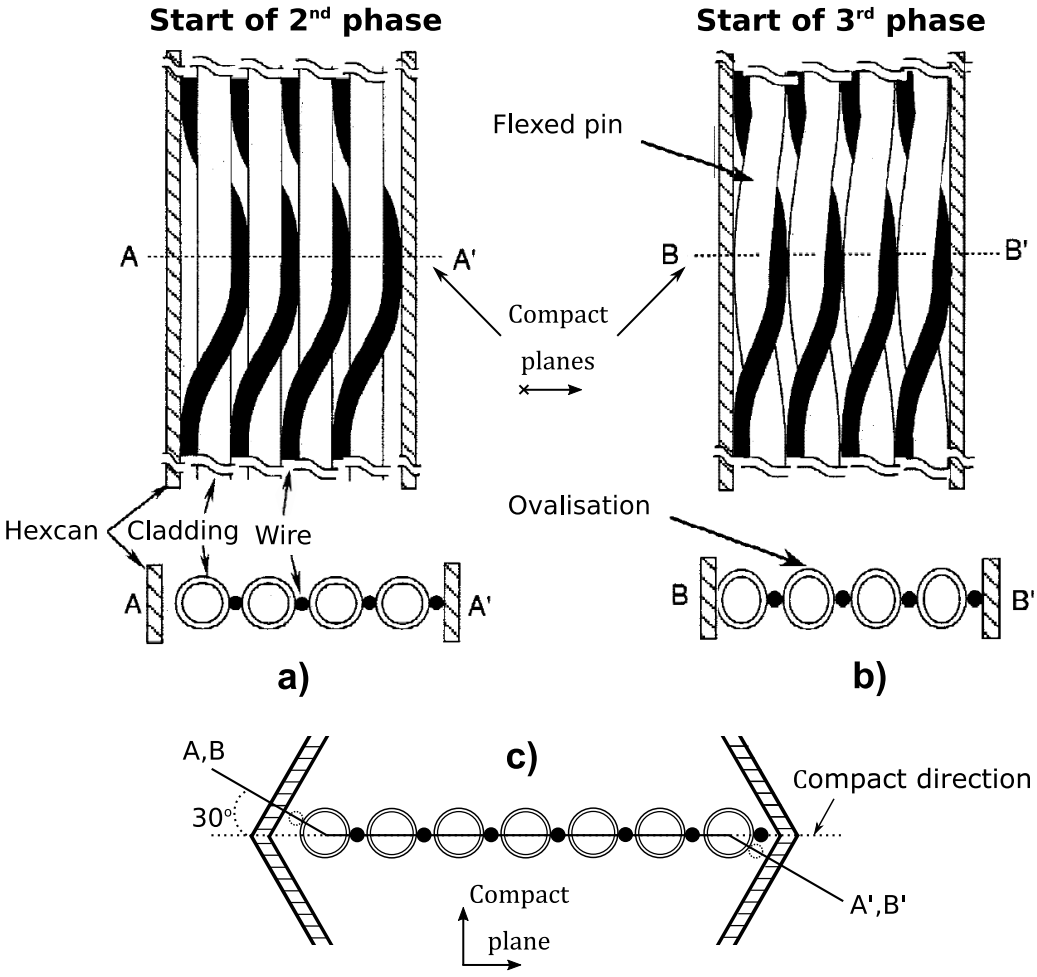

Figure 2.16.: Schematic representation of the start of the 2^{nd} (a) and 3^{rd} (b) phases of interaction between the fuel pins, and between the pins and the hexcan. Adapted from (Uwaba and K. Tanaka 2001). c) Scheme of a compact plane.

During the second phase of bundle deformation, the fuel pins will continue accommodating the growing diametral strain by occupying the available space within the cross section. If the pins' contact with the hexcan had been through the spacer wires, their helical flexion increases during this phase, under the effects of the contact forces. If, on the other hand, the contact had been established directly between the claddings and the hexcan, the helical flexion is reduced. In both cases, the cross section of the cladding is ovalised both due to the helical flexion and under the contact forces. The contacts between pins through the spacer wires are produced in the so called compact planes, in which, as indicated in Figure 2.16c, the centers of the wires and the claddings are aligned following one of the diagonals of the hexagonal pin arrangement, called compact direction. The contacts between the pins and the hexcan, also through the wires, are shifted in the vertical direction by 1/12th of the wire step (so a 30° shift from the compact direction).

As the irradiation proceeds, there might come a point where both the claddings and the spacer wires make contact with the hexcan, as illustrated in Figure 2.16b. This marks the start of the third phase of bundle deformation, characterized by a sudden increase in the stresses associated to the contact-induced cladding ovalisation. This sudden increase on the mechanical stresses might lead to the failure of the claddings, which is why the third phase of interaction is not allowed during nominal operation of SFR, and it is avoided in practice by limiting the lifetime of the subassemblies.

Of the aforementioned deformation mechanisms, the bowing is the least stiff (i.e. has the lower associated stresses), since it acts over the whole length of the fuel pins. It is followed by the helical flexion of the cladding, while the ovalisation of the cladding cross section is the stiffest mechanism, which is why—as discussed in Section 6.6—the contact-induced stresses grow rapidly in the third phase of interaction where only this mechanism can accommodate the increasing diametral strain of the claddings.

The numerous post irradiation examinations conducted on Phenix and Rapsodie subassemblies have evidenced EOL cladding diametral strains of up to about 10%, as shown in Figure 2.17a, and that this deformation is concentrated in the heated length of the fuel pins, as observed in the example presented in Figure 2.17b. Also, significant helical flexion of the fuel pins has been observed, an extreme case of which is presented in Figure 2.18 where the helical flexion progression during the irradiation is also schematically represented. In BOITIX9—the most irradiated Phenix subassembly—, for example, the helical flexion induced a maximal local deflection[13] of ∼0.5 mm, while the maximal cladding ovalisation (difference between maximal and minimal cladding diameter at a given axial position) was ∼0.5 mm.

[13]Obtained after deducting the bowing involving the entire length of the fuel pins.

An example of a highly ovalised cladding is presented in Figure 2.19, where the progression of this mechanism, led by the contact forces and countered by the fission gas pressure, is schematically illustrated as well. It is to be noted that, out of these deformation mechanisms, only the diametral deformation of the claddings affects the hydraulic diameter of the subassembly, which, as discussed in Section 2.1.6, affects the pressure drop characteristics of the fuel bundle and thus the coolant mass flow rate.

In addition, the hexcan can also deform during the irradiation—mainly by increasing its plate to plate distance—which would reduce the mechanical interaction with the fuel pins and increase the cross section available for the sodium flow. However, as mentioned in sections 2.2.2.2 and 2.2.3, the materials currently employed for the hexcan present a very high swelling resistance. For example, the hexcan of the most irradiated Phenix subassembly presented an EOL swelling of only 0.5% (Beck, Blanc, Escleine, et al. 2017). Additionally, as discussed in Section 2.2.1.2, the hexcan is subject to a low pressure that, considering its wall thickness of a few mm, leads to very low creep strains in nominal operating conditions.

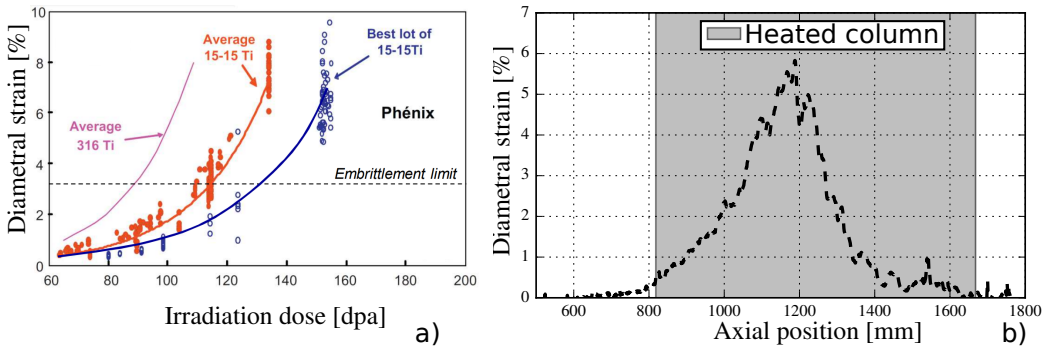

Figure 2.17.: a) Maximal diametral strain of fuel pins fabricated with different steels (see Section 2.2.3) irradiated in Phenix reactor, as a function of the irradiation dose (Yvon, Le Flem, Cabet, et al. 2015). The embrittlement limit discussed in Section 2.2.2.2 is shown, assuming a dominant contribution of swelling to the total diametral strain. b) Axial profile of diametral strain of a Phenix fuel pin showing that the strain is concentrated in the heated column.

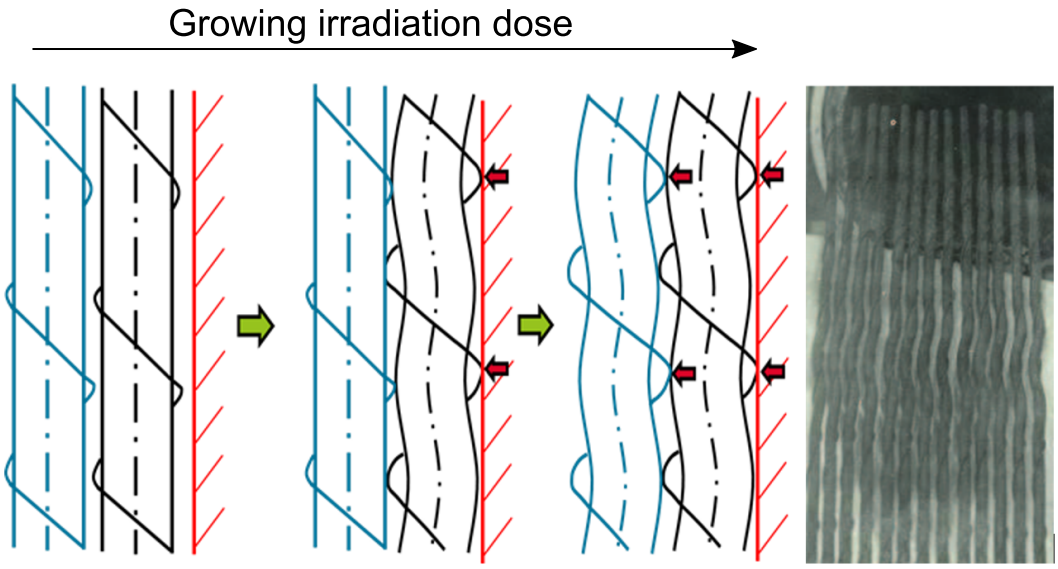

Figure 2.18.: Schematic representation of the progression of the helical flexion of the fuel pins during their irradiation, and image of irradiated fuel pins presenting an extremely high helical flexion (Cadiou and Acosta 2018).

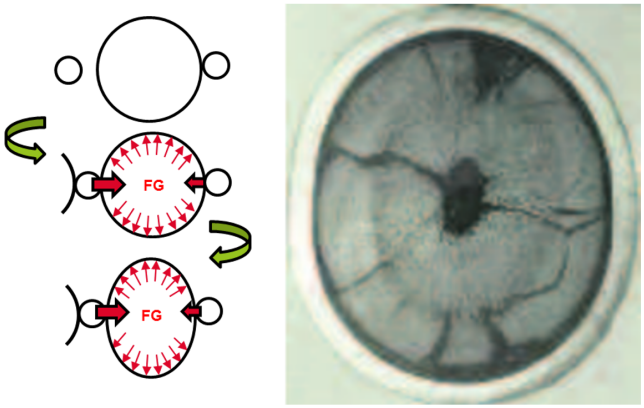

Figure 2.19.: Schematic representation of the progression of the cladding ovalisation under the contact forces and countered by the internal fission gas pressure (FG), and image of a highly ovalised fuel cladding (Cadiou and Acosta 2018).

2.2.6. Section summary

In this section, we firstly describe the magnitude and evolution of the main external loads responsible for the thermomechanical evolution of SFR subassemblies, namely the high pressure and temperature, and the growing irradiation dose. During nominal SFR operation, these loads lead to a change in the mechanical properties of the steels used for the claddings and the hexcan—which we present—, and to a significant swelling and irradiation creep of the claddings. We then describe these two phenomena and show that they have a complex dependence on multiple variables, although the empirical laws employed to evaluate them, which we then describe, consider only the temperature, irradiation dose, and, in the case of the irradiation creep, the equivalent mechanical stress. It results that swelling is characterized by an incubation period during which it remains very low in spite of the growing irradiation dose. Also, that both swelling and irradiation creep are maximal for temperatures in the [450°C, 520°C] range—which is comprised in the operational temperature range of SFR fuel bundles—above which they monotonically decrease. As we will see in Section 6.6, this temperature dependence is the main coupling mechanism with thermal-hydraulics.

Then, we briefly describe the interaction between the fuel pellets and the claddings, that has a mechanical and a chemical component. For SFR under nominal operating conditions, the chemical component is more relevant, and it is embodied by the cladding corrosion under the influence of the fission products. However, given that its effects are very localized, corrosion does no significantly influence the geometrical evolution of the cladding during its irradiation.

Finally, we describe how the swelling, the irradiation creep, and the thermal expansion lead to a very significant deformation of the fuel bundle, while the hexcan—fabricated with a swelling resistant steel—exhibits an excellent dimensional stability under irradiation. In this context, we explain how the diametral strain of the fuel pins leads to the contact between pins and between the pins and the hexcan, leading to the ovalisation of the claddings—which, as discussed in Section 6.6, is associated to high mechanical stresses—and to their helical flexion, consequence of the position of the contact points determined by the helical path of the spacer wires. Out of these mechanisms, only the diametral strain of the fuel pins affects the hydraulic diameter of the bundle, which determines its pressure drop characteristics and thus the subassembly coolant mass flow rate. This dependence, discussed in Section 5.3.2, is an essential factor to characterize the impact of the bundle deformation on its thermal-hydraulics.

2.3. Neutronics

2.3.1. Generalities

In reactor physics, a frequently used magnitude to describe the neutron behaviour is the scalar neutron flux $\phi(\mathbf{r}, E, t)$, where $\mathbf{r}$ is the position vector, E the neutron energy, and t the time. It can be interpreted as the total distance travelled at time t by all the neutrons at $(\mathbf{r}, E)$, per unit volume, energy, and time. The neutron flux distribution within a reactor depends on the materials employed and their interaction with neutrons, and on their geometric arrangement.

The material properties are characterized in terms of their probability interaction with neutrons. For a given material, the probability of a neutron moving with energy E of undergoing a reaction of type x per unit distance traveled is given by the macroscopic cross section $\Sigma_x(\mathbf{r}, E)$ [14]. With this definition, the rate of a reaction of type x per unit volume and energy can be computed from the scalar neutron flux as:

$$R_x(\mathbf{r}, E) = \phi(\mathbf{r}, E, t)\Sigma_x(\mathbf{r}, E) \tag{2.34}$$

Of particular interest in nuclear reactors is the energy production rate P, that can be expressed as:

$$P(\mathbf{r}, t) = \int_0^\infty \epsilon(\mathbf{r})\phi(\mathbf{r}, E, t)\Sigma_f(\mathbf{r}, E)dE \tag{2.35}$$

where the subscript f stands for fission reaction, and $\epsilon(\mathbf{r})$ is the energy released per fission.

The main reactions induced by neutrons in a reactor can be classified as absorption reactions, which include the fissions and radiative captures (that yield a new isotope), and scattering reactions, which re-emit a neutron (or more than one if (n,2n) reactions are considered). If all the possible reaction types x_i are considered, the intervening cross section Σ is called the total macroscopic cross section, and it can be computed by adding the contribution of each reaction, which gives:

$$\Sigma(E) = \sum_i \Sigma_{x_i}(E) \tag{2.36}$$

The total macroscopic cross section can be employed to compute the neutron mean free path λ_n in a material as:

$$\lambda_n(E) = \frac{1}{\Sigma(E)} \tag{2.37}$$

The mean free path represents the average distance travelled by the neutrons before

[14] The dependence on the neutron direction is typically neglected because materials are generally isotropic on the scale of the neutron mean free path ($\sim$ cm), defined in this section.

colliding with a nuclei within the material and undergoing a reaction of any type. The probability of a neutron escaping a system of finite dimensions increases with increasing mean free path. In fast reactors, the absorption cross section within the fast spectrum of the reactor materials being low, the mean free path is of the order of 10 cm, while in thermal reactors it is closer to 1 cm. Besides the increased neutron leakage, the long mean free path reduces the importance of local heterogeneities, such as the geometrical parameters of the fuel pins (at constant mass of all isotopes). However, when local perturbations are important (e.g. when the coolant density is drastically reduced due to boiling in a part of a subassembly), the long mean free path allows for their impact on the entire core (Yang 2012; Waltar, Todd, and Tsvetkov 2012).

For a material composed of N different isotopes, the total cross section can be written in terms of their numerical densities N_i as:

$$\Sigma(E) = \sum_{i=1}^{N} N_i \sigma_i(E) \tag{2.38}$$

where $\sigma_i(E)$ represents the likelihood for an isotope i to undergo a reaction with a neutron of energy E, and it is called microscopic cross section. Its dimensions are surface per nucleus, and it can be therefore understood as the effective surface that a given nucleus offers to the neutrons with energy E to undergo a reaction.

The reactions between neutrons and their surrounding media can either produce more neutrons (fission, (n,2n), etc), keep the total number of neutrons constant (e.g. elastic and inelastic neutron scattering[15]), or reduce it (e.g. neutron captures). Additionally, the neutrons can also escape the system. The operation of nuclear reactors is based on carefully balancing these factors to maintain a stable fission chain reaction, process characterized by the effective multiplication factor k given by:

$$k = \frac{Neutron\ productions}{Neutron\ absorptions + Neutron\ leakage} \tag{2.39}$$

The effective multiplication factor can be understood as ratio between the number of neutrons in two successive generations, with the fission process separating these generations. If $K = 1$, the system is called critical and the neutron population is constant over time. In subcritical systems ($K < 1$), the neutron population decays over time leading to the end of the fission chain reaction, while in supercritical systems ($K > 1$), this population—and the associated nuclear power given by Equation 2.35—grow with time. To quantify the departure from the critical

[15] In an elastic scattering reaction, the kinetic energy of the particles is conserved, which is not the case in inelastic scattering.

equilibrium, the reactivity ρ of the system is usually defined as:

$$\rho = \frac{k-1}{k} \tag{2.40}$$

The relevance of ρ can be further understood by considering the point kinetics approximation (Reuss 2008), in which the neutron flux is considered to vary in amplitude, $n(t)$, without changing its shape $\psi(\mathbf{r}, E)$, and is thus written as:

$$\phi(\mathbf{r}, E, t) = n(t)\psi(\mathbf{r}, E) \tag{2.41}$$

Within this approximation, the evolution of $n(t)$ is computed taking into account the contribution of the neutrons emitted instantly with the fission reaction (prompt neutrons), and the neutrons emitted later on following a radioactive decay. The latter are called delayed neutrons, and represent a β fraction of the total emitted neutrons. It is customary to regroup the delayed neutron precursors in different families of concentration C_i, that decay with a time constant λ_i to emit delayed neutrons representing a fraction β_i of the total emitted neutrons. Then, in the absence of an external neutron source, the evolution of n and C_i is expressed as:

$$\frac{dn}{dt} = \frac{\rho - \beta}{\Lambda} n + \sum_i C_i \lambda_i \tag{2.42}$$

$$\frac{dC_i}{dt} = \frac{\beta_i}{\Lambda} n - C_i \lambda_i \tag{2.43}$$

where Λ is the mean generation time between the birth of a fission neutron and the subsequent absorption leading to another fission. If a reactivity ρ is introduced in a critical reactor and then remains constant in time, the resulting evolution of the neutron population can by approximated by:

$$n(t) \approx a e^{\omega t} \tag{2.44}$$

where a is a constant. When the absolute value of ρ is low, one can approximate:

$$\omega \approx \frac{\rho}{\bar{\Lambda}} \tag{2.45}$$

where $\bar{\Lambda}$ is the mean neutron generation time that takes into account the contribution of the delayed neutrons, such that:

$$\bar{\Lambda} = (1 - \beta) + \sum_i \beta_i (\frac{1}{\lambda_i} + \Lambda) >> \Lambda \tag{2.46}$$

On the other hand, for high reactivities such that $\rho > \beta$, one can write:

$$\omega \approx \frac{\rho - \beta}{\Lambda} \tag{2.47}$$

In this case, the prompt neutrons alone are sufficient to achieve critically and the time constant of the neutron population increase is dramatically reduced, which in power reactors constitutes the start of an accidental situation. Computing the evolution of $n(t)$ for varying $\rho(t)$ is less straightforward, but, much like in the simple cases illustrated above, ρ and β play a major role.

It should be noted that the preceding analysis holds only if the delayed neutrons induce fission with the same probability than prompt neutrons. In general, this is not true mainly because delayed neutrons are typically produced at lower energies than prompt neutrons. To take these effects into consideration, effective kinetic parameters ${\beta_i}^{eff}$,β_{eff} and $\bar{\Lambda}_{eff}$ are defined and used instead, and they depend on the space and energy distribution of the neutron flux and of the adjoint neutron flux, which quantifies the effectiveness of neutrons at different energies and positions of increasing the neutron population (e.g. by inducing a fission reaction)(Stacey 2007). In SFR, β_{eff} is typically about 370 pcm, and it is customary to report reactivity values normalized with β_{eff} in a unit called dollar \$.

2.3.2. Reactivity feedbacks

In view of the dominating effect of the reactivity on the reactor kinetics, it is important to quantify the dependence of ρ to changes in the system. This is typically done by defining reactivity feedback coefficients, computed for specific geometric and material configurations by analysing the response to a variety of perturbations. Two of the most relevant reactivity feedbacks for SFR are related to the sodium void effect and to a fuel temperature related phenomenon called Doppler effect, and they are briefly discussed next.

In large fast reactors, the loss of sodium or the reduction of sodium density can result in a large positive reactivity effect. The voiding or change in sodium density could be caused, for example, by a leak in the reactor tank, by sodium boiling, or by the diametral expansion of the fuel claddings that, at the deformed plane, reduces the cross section occupied by sodium. This reactivity feedback is very space dependent, and involves four different phenomena (Waltar, Todd, and Tsvetkov 2012):

- **Spectral hardening**. The loss of sodium reduces the scattering interaction with the neutrons and thus their slowing down. This results in an increase in the average neutron energy, which has a positive reactivity effect, mainly

because the average number of neutrons released per fission increases with the energy of the incident neutron.

- **Increase neutron leakage**. The reduced interaction with the sodium reduces the total neutron cross section and thus increases the neutron mean free path, which increases the probability of neutrons of escaping the reactor, which reduces the reactivity. This phenomenon is more relevant in the periphery of the core.
- **Elimination of neutron captures in sodium**. As sodium density is reduced, so are the parasitic neutron captures in it. Since the sodium captures are relatively low, this results in a small positive reactivity effect.
- **Change in self-shielding**[16]. The reduced scattering with sodium modifies the fission cross section, leading to a small reactivity effect.

The first two phenomena, of opposite sign, are largely dominating. Their effect have also a different spatial dependence: the first is most relevant in the central region of the core, while the second is higher in its periphery. In order to reduce the positive overall reactivity feedback caused by a loss of sodium, this spatial dependence led to the development of the heterogeneous core concept (CFV) of the advanced SFR designed at the CEA. The reactivity contribution of sodium void in each different zone of this heterogeneous core is presented in Figure 2.20. It is important to note that the high positive reactivity ($> \beta_{eff}$) effect of sodium voiding in the fissile and fertile blankets are the result of voiding all the subassemblies of the inner core, of which this reactor has 180. Then, if we interest ourselves in the consequences of the sodium voiding of one subassembly—for example, due to the diametral deformation of a highly irradiated subassembly within the core—the resulting reactivity effect should be $<< \beta_{eff}$. The quantitative evaluation of this effect, however, requires the consideration of the spatial dependence of the void reactivity feedback.

The other reactivity feedback mentioned above, the Doppler effect, is related to the fuel temperature. A net increase in the neutron capture cross section, caused by an increase in fuel temperature, introduces a negative reactivity feedback, while the contrary is true when the fuel temperature is reduced. This is caused by a broadening of the resonances of the neutron capture cross section—which are very high cross section values over a narrow energy range—of some isotopes, consequence of the temperature increase. MOX fuels posses a relatively strong Doppler feedback effect, which is a desired feature to counter an overpower transient, in which fuel temperature initially rises, but a liability in other transient scenarios where the

[16] Self-shielding refers to a process by which a neutron flux local (in space or energy) reduction due to a very high local cross section leads to a reaction rate significantly lower than what Equation 2.34 would give for non-depressed neutron flux.

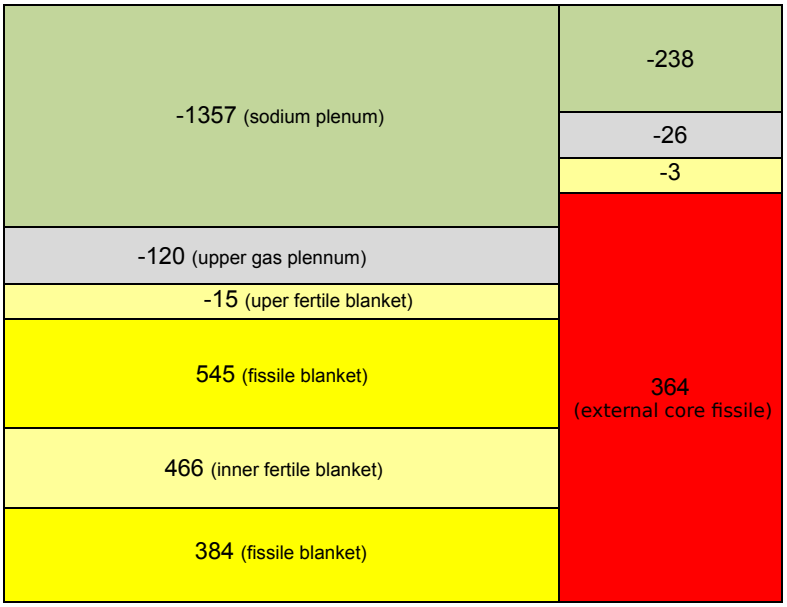

Figure 2.20.: Reactivity effect of sodium voiding in the different regions of the core of the advanced SFR designed at the CEA, expressed in pcm (Coquelet-Pascal, Venard, Sciora, et al. 2017).

fuel temperature is initially reduced, such a loss of primary coolant flow.

For a uniform change in fuel temperature from T_1 to T_2 (in K), the reactivity change can be computed as (Waltar, Todd, and Tsvetkov 2012):

$$\Delta\rho_D = K_D \ln(T_2/T_1) \tag{2.48}$$

where K_D is the so called Doppler coefficient. For the advanced SFR designed at the CEA, $K_D \sim -650$ pcm, which allows to estimate—by means of Equation 2.48—a negative reactivity of 20 pcm when the fuel temperature of the entire core is increased, for example, by 50 K from its nominal value, showing its relatively low importance in this range of temperature variations.

2.3.3. Irradiation dose calculation

The damage rate produced by the irradiation with a neutron flux with energy distribution $\phi(E)$ on a material of atomic density N, can be computed as:

$$R_d = N \int_E \int_{T_E} \phi(E)\nu(T_E)\sigma_d(E, T_E)dT_E dE \tag{2.49}$$

where $\sigma_d(E, T_E)$ is the displacement cross section, which quantifies the probability of an incident particle of energy E of transferring an energy T_E to the first atom it encounters (PKA), and $\nu(T_E)$ is the number of atom displacements that the PKA then generates in the solid. The damage rate given by Equation 2.49 can be integrated over the duration of the irradiation under consideration to compute the total irradiation dose in dpa.

The transferred energy T_E is a growing function of the energy of the incident particle, and the number of displaced atoms $\nu(T_E)$ grows with T_E and has a minimum energy threshold (∼20-25 eV) bellow which it is null (Doligez, Bouneau, David, et al. 2017). These factors contribute to the higher radiation damage rate present in fast reactors when compared to thermal reactors. However, the main reason for this is the higher neutron flux, which is ∼100 times higher in fast reactors than in thermal reactors (IAEA 2012).

2.3.4. Section summary

In this section, we introduce the main concepts of neutron and reactor physics required to understand how they are linked to the thermal-hydraulic and thermomechanical evolution of SFR subassemblies under irradiation. We firstly introduce the scalar neutron flux, which characterizes the neutron population in the reactor and determines its power distribution. Then, we introduce the concept of reactivity, which is a measure of the departure from a perfect balance between neutron productions and neutron losses, and determines the time evolution of the neutron population. Given the importance of the reactivity, we discuss how it is affected by a fuel temperature change and by a loss of sodium density, which are of interest to us since both can arise as consequence of the deformation of a SFR fuel bundle. A first estimation indicates that, following the bundle deformation, the reactivity change caused by these effects would be minor. However, considering the spatial dependence of the reactivity feedback related to a change in sodium density is required for a precise quantification of this effect. Finally, we show how the damage induced by the neutrons on a material—quantified by the irradiation dose—can be computed using the scalar neutron flux.

2.4. Phenomenological summary and simulation assumptions

The main phenomena discussed in this chapter are included in Table 2.2, where their importance for the coupled thermal-hydraulic/thermomechanical evolution of SFR subassemblies under nominal operating conditions is indicated, together with

the main associated simulation requirements.

Phenomenon (related chapter section)	**Importance**	**Simulation requirements**
Swelling (2.2.2.2)	High	Subassembly TM model[17] + Swelling law
Irradiation creep (2.2.2.3)	High	Subassembly TM model + Irradiation creep law
Thermal expansion (2.2.5)	High	Subassembly TM model
Thermal Creep (2.2.2)	Moderate	Subassembly TM model + Thermal creep law
Fuel pin diametral strain (2.2.5)	High	Subassembly TM model + Material laws
Fuel pin flexion (2.2.5)	High	Subassembly TM model + Material laws
Fuel pin ovalisation (2.2.5)	Potentially high	Subassembly TM model + Material laws
Neutronic feedbacks (2.3.2)	Low	Neutronic model
Temperature and dose dependent mechanical properties of steel (2.2.2.4)	Moderate	Subassembly TM model + Dose and temperature dependent properties
Temperature dependence of the fission gas pressure (2.2.1.2)	Low	Temperature dependent gas law
Pellet-cladding chemical interaction (2.2.4)	Potentially high	Subassembly TM model + Fuel pellet TM and thermodynamic model
Pellet-cladding mechanical interaction (2.2.4)	Low	Subassembly TM model + Complex fuel pellet TM model
Hexcan deformation (2.2.5)	Low	Subassembly TM model + Material laws
Turbulent coolant flow in a deformed bundle (2.1.2)	High	Detailed TH model + deformation representation
Temperature dependent physical properties of the coolant (2.1.3)	Low	TH model + Temperature dependent properties

Table 2.2.: Importance of the main phenomena involved in the thermal-hydraulic (TH) and thermomechanical (TM) evolution of SFR subassemblies in nominal operating conditions.

This work focuses on the evaluation of the thermomechanical evolution of the structural components of the fuel bundle—namely the fuel claddings, the spacer wires and the hexcan—, coupled to the evolution of its thermal-hydraulic behavior. Concerning the impact of thermal-hydraulics on thermomechanics, the most relevant

[17] In all cases, the TM model requires as input the temperature distribution, computed with a TH model.

phenomena are swelling and irradiation creep, because they lead to large cladding strains and they strongly depend on temperature. Consequently, this coupling source is considered in this work. The thermal expansion contributes to the bundle deformation—although to a significantly lesser extent—, and it induces secondary stresses, so it is also considered here. The magnitude and consequences of these stresses depend on the mechanical properties of the cladding and hexcan materials, whose temperature and irradiation dose dependence are taken into account.

The impact of the bundle deformation on its thermal-hydraulics has a global and a local component. The global effect is a generalized temperature rise, which is maximal at the outlet of the heated column, consequence of the reduction of the coolant mass flow rate. As discussed in Section 2.1.6, this is mainly caused by a reduction of the hydraulic diameter of the bundle. The local effects arise from the reduction of the minimal distance between fuel pins, and between the hexcan and the pins, and from the modification of the local hydraulic diameter of the subchannel under consideration. All the deformation mechanisms responsible for these effects, discussed in Section 2.2.5, are relevant from a mechanical point of view and are therefore taken into consideration in the thermomechanical simulations conducted in this work. However, the deformed bundle geometry is simplified in the thermal-hydraulic simulations, as discussed next.

Out of the fuel cladding deformation mechanisms discussed in Section 2.2.5, only their diametral strain affects the hydraulic diameter of the bundle. Additionally, it induces all of the local effects mentioned in the preceding paragraph. For this reason, it is taken into account in this work both for the calculation of the coolant mass flow rate and for the calculation of the temperature and velocity distributions in the deformed fuel bundles. For a prediction of the local effects that the bundle deformation has on its thermal-hydraulics, a detailed thermal-hydraulic model that considers the turbulent nature of the flow is required.

The helical flexion does not change the hydraulic diameter of the fuel bundle, but it could have an effect on its pressure drop characteristics. However, this effect is not expected to be very significant since, after almost a decade of operation, it had not been observed in Phenix reactor (CEA 1981). Additionally, if the helical flexion of neighbouring pins is similar, it does not modify the hydraulic diameter of the triangular subchannel defined between them, as can be qualitatively inferred from Figure 2.16b; the center of the subchannel is simply displaced on the plane perpendicular to the flow direction. Only the peripheral subchannels are reduced—and exclusively at the axial positions where the spacer wire does not separate the pin from the hexcan—which could lead to a reduction of the peripheral coolant flow and an increase in the flow through the central subchannels. This peripheral mass flow reduction was observed experimentally in a 7-pin mock-up deformed bundle with a high helical flexion, but the velocity of the triangular

subchannels was not significantly modified in that experiment (Lahaye, Cognet, Mertens, et al. 1988). This is in agreement with preliminary CFD simulations we conducted, in which the flexion of the fuel pins, representative of irradiated SFR bundles, led to only 1% change in the pressure drop within the heated column of the fuel bundle. Considering these results, and motivated by a preexisting study that predicted a very low helical flexion of the fuel pins of the advanced SFR designed at the CEA (Masoni 2016)—the development of which is the framework of this thesis—, the global effects of the pin flexion on the total subassembly coolant mass flow rate are not considered in this work. However, considering the local flow redistribution caused by the flexion of the pins is possible with the developed methodology, and it is done for the application case presented in Section 7.2.

The ovalisation of the claddings does not affect the hydraulic diameter of the fuel bundle, it does not change the minimal distance between pins—since for it to become significant the contact needs to be already established—, and it has very little effect on the hydraulic diameter of any particular subchannel. For this reasons, it is not taken into account in the thermal-hydraulic simulations conducted in this work. However, the ovalisation of the fuel pellet could lead to a significant modification on the heat flux distribution in the circumference of the cladding. Considering this effects would require the modelling of the fuel pellets, their deformation, and the heat conduction within them, which exceeds the modelling scope of this work and would lead to an excessively high computational cost.

Finally, considering the very high dimensional stability of the hexcan under irradiation—as mentioned in Section 2.2.5—its very low deformation is not represented in the thermal-hydraulic simulations conducted in this work, with the exception of the cases in which the flexion of the pins is considered. In cases with high pin flexion, considering an undeformed hexcan could lead to a geometrical incompatibility in the thermal-hydraulic model (i.e. the fuel pins could *go through* the hexcan).

Concerning neutronics, it should be clear from the previous sections that it is an essential component of the evolution of SFR subassemblies under irradiation, since it provides the heat source that determines their temperature distribution and it is responsible for the radiation damage that induces their geometrical evolution. However, as discussed in Section 2.3, the feedback mechanisms that make the neutronic behaviour of the reactor depend on temperature (mainly Doppler and sodium density change) and on the deformation of the fuel bundle (displaced sodium) are not strong enough to make this effects significant for the evolution of a given subassembly. For this reason, these feedbacks are not taken into account in this work, hypothesis that is verified by means of neutronic simulations presented in Section 6.3.

Concerning the interaction between the fuel pellets and the cladding, as discussed in Section 2.2.4, the effects of the mechanical interaction on the cladding stresses are very limited under nominal, steady state conditions. The chemical interaction that leads to the cladding corrosion, on the other hand, could lead to a considerable localised reduction of the load bearing thickness of the cladding. Given its local character, the effects of corrosion do not significantly affect the global thermomechanical evolution of the fuel bundle, and are therefore not explicitly considered in this work. Nevertheless, a conservative assessment of these effects could be done by simply modelling a thinner cladding. However, by doing so, a potential coupling source linked to the influence of the cladding temperature on the corrosion thickness would be ignored. This dependence has been observed experimentally (Pelletier 2018), but it is not well represented even in the most advanced codes that model a single fuel pin—including the fuel pellets—, an example of which is the CEA code GERMINAL (Lainet, Michel, Dumas, et al. 2019)[18]. The local coupling between a fuel pellet model and a thermodynamic code would be necessary to evaluate correctly the effects of corrosion and their temperature dependence, which is out of the scope of this work.

Another potential coupling source between thermal-hydraulics and thermomechanics is the temperature dependence of the internal cladding pressure, that leads to its deformation due to creep. However, as discussed in Section 2.2.1.2, the use of a large gas plenum below the active length of the fuel pin—notably in the advanced SFR designed at CEA—makes the pressure little sensitive to potential sodium temperature variations consequence of the bundle deformation, which do not affect the lower plenum. This effect is therefore neglected in this work.

The main conclusion that can be drawn from Table 2.2 and from the preceding paragraphs is that, in order to simulate the evolution of SFR subassemblies under irradiation, characterized by a coupling between thermal-hydraulics and thermomechanics evidenced by Figure 2.1, a coupled approach is required. In particular, the evolution of the geometry of the fuel pin bundle under the effects of irradiation needs to be computed taking into account the temperature distribution which is affected by the deformation. To this end, in this work we develop a simulation methodology based on the coupling between a CFD model of the coolant flowing in a deformed bundle—implemented in the commercial code STAR-CCM+—, and DOMAJEUR2, a finite element based code—developed at the CEA—for the modelling of the thermomechanical evolution of SFR fuel bundles under irradiation. The implementation of the CFD model is described in Chapter 3, while DOMAJEUR2 is presented in Chapter 4. The implementation of the coupling between the two is discussed in Chapter 5.

[18] In GERMINAL, only a temperature threshold of 550°C, below which no corrosion is modeled, is considered.

3. Numerical simulation of the thermal-hydraulics of SFR subassemblies

This chapter is dedicated to the numerical simulation of the thermal-hydraulics of SFR subassemblies and, in particular, of their wire-wrapped fuel pin bundles. Firstly, in Section 3.1, we introduce the main simulation techniques available to do so, to then describe the one retained in this work, in Section 3.2. Finally, the implementation of the selected technique realized in this work is presented in Section 3.3.

Table of Contents

3.1. Available methods for simulating the thermal-hydraulics of SFR subassemblies

3.1.1. Subchannel analysis

In the subchannel analysis, the fuel bundle is represented as a set of parallel flow channels that are connected to each other by crossed flow mixing. The axial length is divided into a number of *slices* so that for each of them there is one control volume per subchannel, as illustrated in Figure 3.1. Then, the conservation of mass, momentum and energy is solved for the defined control volumes, which are coupled by the exchange of these quantities between adjacent control volumes.

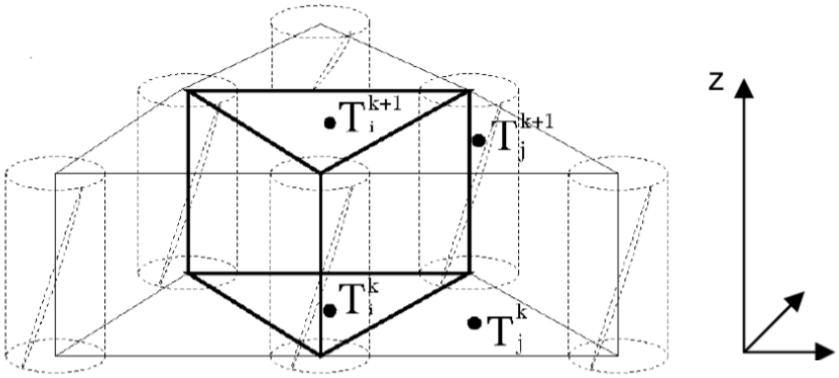

Figure 3.1.: Example of a control volume in subchannel analysis. T_i^k represents the temperature in the node k of the subchannel i.

In this approach, the particular geometrical characteristic of wire-wrapped fuel pin bundles are not explicitly considered, and they result only in a modification of the hydraulic diameter and of the wetted perimeter of the cross section of each subchannel. In addition, the momentum, energy and mass exchanges between subchannels are computed by means of empirical mixing laws, which in the case of SFR bundles have to account for the effects of the spacer wires. For the pressure loss due to friction, correlations are employed as well.

Subchannel analysis allows to reproduce the general flow characteristics, and is an essential tool for the thermal-hydraulic design of nuclear reactors since it has a low computational cost, and it can be practically employed to study the entire core of the reactor, which is still extremely challenging with the more sophisticated approaches described in the next section (Roelofs, Gopala, Jayaraju, et al. 2013). However, computing the variables of interest in only one point within the cross section of each subchannel limits the detail of their calculated distribution, as can

be noted in the case of temperature in the example presented in Figure 3.2.

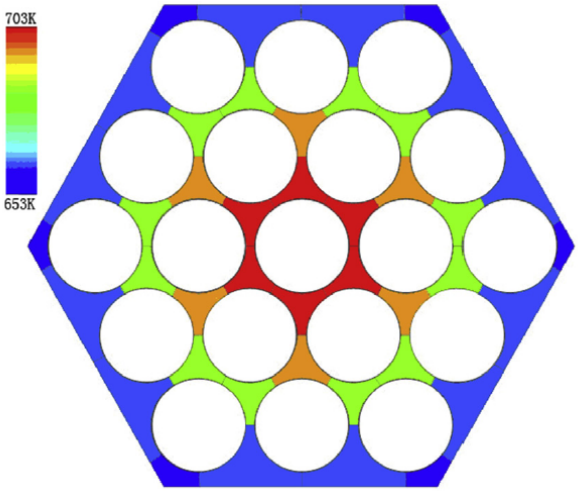

Figure 3.2.: Example of the sodium temperature distribution computed with subchannel analysis (Wu, Li, X. Yu, et al. 2013).

Additionally, the definition of the coefficients that describe the mixing between subchannels varies between different codes, which leads to large discrepancy between the results obtained with them (H.-Y. Jeong, Ha, Kwon, et al. 2007; X. Liu and Scarpelli 2015). These coefficients are, besides, often considered axially independent in subchannel codes (Fanning, W. D. Pointer, and Thomas 2009), in which case they are not able to correcly reproduce the periodicity of the flow induced by the spacer wire discussed in Section 2.1.5. As a result, they tend to perform poorly when compared to other more detailed methods in the prediction of the temperature of the peripheral subchannels in particular, where the position and the phase of the wire has great impact. This limitation has been evidenced, for example, in (Fanning, W. D. Pointer, and Thomas 2009), where the simulations of a 217-pin SFR subassembly using a subchannel method and a more sophisticated CFD-RANS approach—described in Section section 3.2—were compared. This comparison showed that the temperatures of the inner subchannels of the bundle were slightly overpredicted by the subchannel method, but differences of up to 25°C were observed for the peripheral subchannels. These results are in agreement with a similar comparison recently conducted at the CEA, which showed good agreement in the axial temperature profile of the central subchannel of a 217-pin bundle, but differences of up to about 20°C in a peripheral one, results yet to be published. Also in this line, (X. Liu and Scarpelli 2015) showed that a subchannel approach consistently overpredicted the temperature in the inner subchannels of a 19-pin wire-wrapped bundle, while the tendency was reversed only in a corner

subchannel. In that work, the authors also highlight the very high sensitivity of the temperature of the peripheral subchannels on the choice of the mixing model, and show that the choice of the pressure drop correlation has very significant effects in the temperature of the inner subchannels, since it affects the flow distribution amongst them.

Furthermore, the mass flow between subchannels computed by a subchannel approach was compared to the one obtained with CFD-RANS simulations in (Emilio Baglietto, Joseph William Fricano, and Eugeny Sosnovsky 2014). The authors of that work showed that, while both approaches were in good qualitative agreement in non-deformed wire-wrapped pin bundles, large discrepancies were observed in the impact of a mild bundle deformation (expansion of the hexcan, 1% maximal diametral strain of the pins, and helical flexion) on the crossflow, and concluded that the CFD-RANS approach provided more physically consistent results.

For the reasons exposed above, and unlike preexisting efforts to simulate the coupling between thermal-hydraulics and thermomechanics in the evolution of SFR subassemblies—discussed in Section 5.1—, in this work we employ a more detailed approach for the thermal-hydraulic simulations, which belongs to a broader family of methods introduced next.

3.1.2. Computational Fluid Dynamics

Computational Fluid Dynamics (CFD) refers to the numerical approximation of the behaviour of fluid flows based on their conservation laws, which can be written for a fluid control volume as described next (Moukalled, Mangani, and Darwish 2016).

3.1.2.1. Governing equations

Continuity equation, or mass conservation equation

$$\frac{\partial \rho}{\partial t} + \boldsymbol{\nabla} \cdot \rho \mathbf{u} = 0 \tag{3.1}$$

Where ρ is the density and $\mathbf{u}$ the velocity of the fluid. By defining the material derivative operator as:

$$\frac{D}{Dt} \equiv \frac{\partial}{\partial t} + \mathbf{u} \cdot \boldsymbol{\nabla} \tag{3.2}$$

the continuity equation can be expressed in the following form:

$$\frac{D\rho}{Dt} + \rho \boldsymbol{\nabla} \cdot \mathbf{u} = 0 \tag{3.3}$$

If the flow is considered to be incompressible ($\frac{D\rho}{Dt} = 0$), the mass conservation equations reduces to:

$$\boldsymbol{\nabla} \cdot \mathbf{u} = 0 \tag{3.4}$$

Linear momentum conservation equations

$$\frac{\partial(\rho \mathbf{u})}{\partial t} + \boldsymbol{\nabla} \cdot (\rho \mathbf{u}\mathbf{u}) = \boldsymbol{\nabla} \cdot \boldsymbol{\sigma} + \mathbf{f_b} \tag{3.5}$$

where $\boldsymbol{\sigma}$ is the stress tensor, which characterizes the surface forces, and $\mathbf{f_b}$ the body forces, or forces per unit volume. The linear momentum conservation equations, also called Navier-Stokes equations, indicate that the change in the linear momentum of a considered fluid control volume is given by the net momentum flow through its boundaries, and by the action of forces on its surface and body forces on its volume. It is customary to express the stress tensor as follows:

$$\boldsymbol{\sigma} = -p\mathbf{I} + \boldsymbol{\tau} \tag{3.6}$$

where $\mathbf{I}$ is the identity tensor of size (3x3), p the pressure, and $\boldsymbol{\tau}$ the deviatoric or viscous stress tensor. The first term on the right hand side of Equation 3.6 quantifies the stresses that would exist if the fluid was static, while the second term represents the additional stresses that arise due to the motion of a viscous fluid. For Newtonian fluids, the viscous stress tensor is assumed to be a linear function of the velocity gradient, and is written as:

$$\boldsymbol{\tau} = \mu\{\boldsymbol{\nabla}\mathbf{u} + (\boldsymbol{\nabla}\mathbf{u})^T - \frac{2}{3}(\boldsymbol{\nabla} \cdot \mathbf{u})\mathbf{I}\} \tag{3.7}$$

where μ is the molecular viscosity of the fluid. This expression reduces, in the incompressible case, to:

$$\boldsymbol{\tau} = \mu\{\boldsymbol{\nabla}\mathbf{u} + (\boldsymbol{\nabla}\mathbf{u})^T\} \tag{3.8}$$

Then, combining equations 3.5 to 3.8 gives:

$$\frac{\partial(\rho \mathbf{u})}{\partial t} + \boldsymbol{\nabla} \cdot (\rho \mathbf{u}\mathbf{u}) = -\boldsymbol{\nabla} p + \boldsymbol{\nabla} \cdot \left(\mu\{\boldsymbol{\nabla}\mathbf{u} + (\boldsymbol{\nabla}\mathbf{u})^T\}\right) + \rho \mathbf{g} \tag{3.9}$$

where only the body forces under the gravitational acceleration $\mathbf{g}$ were considered. In terms of the material derivative given by Equation 3.2, and using the incompressibility hypothesis, the conservation of linear momentum can be written as:

$$\rho \frac{D\mathbf{u}}{Dt} = -\boldsymbol{\nabla} p + \boldsymbol{\nabla} \cdot \left(\mu\{\boldsymbol{\nabla}\mathbf{u} + (\boldsymbol{\nabla}\mathbf{u})^T\}\right) + \rho \mathbf{g} \tag{3.10}$$

Energy conservation equation

$$\frac{\partial(\rho e)}{\partial t} + \boldsymbol{\nabla} \cdot (\rho e \mathbf{u}) = \mathbf{f_b} \cdot \mathbf{u} + \boldsymbol{\nabla} \cdot (\mathbf{u} \cdot \boldsymbol{\sigma}) - \boldsymbol{\nabla} \cdot \mathbf{q} + Q_v \tag{3.11}$$

where e is the total energy per unit mass, $\mathbf{q}$ the heat flux, and Q_v an energy source per unit volume. In the case of incompressible flow of Newtonian fluids, and neglecting the temperature increase caused by viscous dissipation, the energy conservation equations can be expressed in terms of the temperature T as follows:

$$\rho C_p \frac{DT}{Dt} = -\boldsymbol{\nabla} \cdot \mathbf{q} + Q_v \tag{3.12}$$

where C_p is the specific heat of the fluid. Finally, considering the Fourier's law given by:

$$\mathbf{q} = -k\boldsymbol{\nabla} T \tag{3.13}$$

where k is the thermal conductivity of the fluid, the energy equation can be written as:

$$\rho C_p \frac{DT}{Dt} = \boldsymbol{\nabla} \cdot (k\boldsymbol{\nabla} T) + Q_v \tag{3.14}$$

3.1.2.2. Methods for the resolution of the conservation equations

The equations presented in the previous section describe the behaviour of the three types of flows discussed in Section 2.1.2, namely laminar, transition, and turbulent flows. In laminar cases and in simple geometries, analytical solutions might be obtained, but this is no longer possible as the Reynolds number increases or the geometries become more complex. In these cases, the conservation equations are discretized in space and time and solved numerically. The main techniques to do so differ mainly in the treatment of turbulence in the resolution of the Navier-Stokes equations, and are introduced next.

Direct Numerical Simulations (DNS)

The most straightforward approach, called DNS, consists on solving the discretized Navier-Stokes equations without further approximations, which implies resolving the various time and space scales of the turbulent flow, thus making this approach intrinsically 3D and time dependent. In turbulent flows, there is a flux of energy from large scale eddies towards smaller eddies that end up dissipating their kinetic energy into heat by viscous action, in a process called the energy cascade which is illustrated in Figure 3.3. The main practical limitation of this approach comes then from the need of a mesh fine enough to resolve the smallest eddies in the flow, characterized by the Kolmogorov length scale η (Kolmogorov 1941). It can be shown that the ratio between this scale and the length scale l_0 of the largest eddies, which is comparable with the characteristic dimension of the flow, follows (Pope 2000):

$$\frac{\eta}{l_0} \sim Re^{-3/4} \tag{3.15}$$

For a 3D simulation, this results in the number of calculation points required

to resolve turbulence growing with $Re^{9/4}$. Due to this, DNS of the flow in SFR fuel bundles typically characterized by $Re \sim 50000$ are still beyond the currently available computational power, even though simulations on reduced domains (e.g. a section of one subchannel) and at lower Re have been conducted and employed to validate and improve the simulation methodologies described next (Ranjan, Pantano, and Fischer 2010; Baglietto, Ninokata, and Misawa 2006).

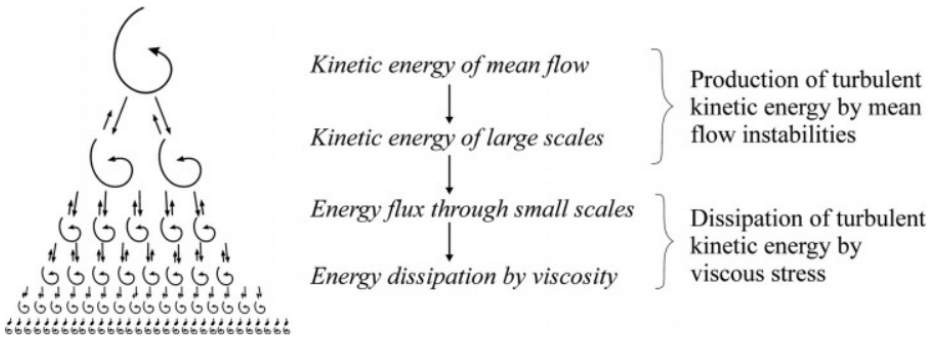

Figure 3.3.: Energy flux from large to small scales (Andersson 2012).

Large-Eddy Simulations (LES)

LES techniques are based on the observation that the larger eddies exhibit more anisotropy and dependence on the geometry of the problem considered than smaller eddies. Then, the dynamics of larger eddies is explicitly computed, while the smaller eddies are modeled. This is done by applying a spatial filtering given by a convolution integral that takes the following general form:

$$\overline{\mathbf{u}}(\mathbf{x},t) = \int G(\mathbf{x}-\xi;\Delta)\mathbf{u}(\mathbf{x},t)d\xi \tag{3.16}$$

where $\overline{\mathbf{u}}(\mathbf{x},t)$ is the filtered velocity at a position $\mathbf{x}$ that results from the action of the convolution kernel $G(\mathbf{x}-\xi;\Delta)$, which depends on the filtering width Δ. Various different functions are proposed as the convolution kernel, and time filtering of the higher frequencies can also be conducted. The instantaneous velocity is then decomposed as follows:

$$\mathbf{u}(\mathbf{x},t) = \overline{\mathbf{u}}(\mathbf{x},t) + \mathbf{u}'(\mathbf{x},t) \tag{3.17}$$

where the sub-grid scale velocity $\mathbf{u}'(\mathbf{x},t)$ has, in general, a not null filtered residual (i.e. $\overline{\mathbf{u}'}(\mathbf{x},t) \neq 0$). Filtering the linear momentum conservation Equation 3.10 gives:

$$\rho\frac{\overline{D}\overline{\mathbf{u}}}{\overline{D}t} = -\boldsymbol{\nabla}\overline{p} + \boldsymbol{\nabla}\cdot\left(\mu\{\boldsymbol{\nabla}\overline{\mathbf{u}} + (\boldsymbol{\nabla}\overline{\mathbf{u}})^T\}\right) + \rho\mathbf{g} + \boldsymbol{\nabla}\cdot\boldsymbol{\tau}^{\boldsymbol{SGS}} \tag{3.18}$$

where the mean material derivative defined as:

$$\frac{\overline{D}}{\overline{D}t} \equiv \frac{\partial}{\partial t} + \overline{\mathbf{u}} \cdot \boldsymbol{\nabla} \tag{3.19}$$

has been used. It can be observed that a new term given by the divergence of the so called sub-grid scale stress tensor $\boldsymbol{\tau}^{SGS}$ appears, while in all other terms of Equation 3.10 the instantaneous velocity and pressure are simply replaced by their filtered components. This new term represents the effects of the interaction of the eddies of all scales, including the unresolved ones, on the larger resolved eddies, and is written:

$$\boldsymbol{\tau}^{SGS} = \rho(\overline{\mathbf{u}} \cdot \overline{\mathbf{u}} - \overline{\mathbf{u}\mathbf{u}}) \tag{3.20}$$

To close the problem, $\boldsymbol{\tau}^{SGS}$ needs to be expressed as a function of the filtered velocity $\overline{\mathbf{u}}$ only, for which several different models exist.

It should be noted that the filtered velocity is still a random, unsteady field, even when the flow can be considered statistically steady. Therefore, LES techniques are also intrinsically time dependent. Additionally, in high Re, wall bounded flows often found in engineering applications, resolving the near wall behaviour implies the use of a small filtering width Δ, which in turn imposes a fine space discretization. This results in a computational cost estimated by (Spalart 2000) to be only 10 times lower than DNS, and in grid-requirements more recently shown by (Choi and Moin 2012) to be comparable to those of DNS. As a consequence, LES studies are also limited to very restricted domains of SFR subassemblies, unless a supercomputer is employed (Roelofs, Dovizio, Uitslag-Doolaard, et al. 2018).

In this work we intend to develop a simulation methodology that can be practically applied to full scale subassemblies (up to over 200 fuel pins), and thus we shift our attention to a different technique that does not explicitly resolve the turbulent eddies. This technique, which is currently the most widely used approach for the simulation of wire-wrapped fuel bundles (Roelofs, Gopala, Jayaraju, et al. 2013; Roelofs, Dovizio, Uitslag-Doolaard, et al. 2018), is called Reynolds-Averaged Navier-Stokes, and it is described in more detail in the next section.

3.2. Reynolds-Averaged Navier-Stokes

3.2.1. RANS conservation equations

In the Reynolds-Averaged Navier-Stokes (RANS) method, the variables of interest such as velocity, pressure and temperature, are split into time averaged and fluctuating components in the so called Reynolds decomposition. The averaged component $\overline{\Phi}(\mathbf{x})$ of a variable $\Phi(\mathbf{x}, t)$ is given by:

$$\overline{\Phi}(\mathbf{x}) = \lim_{\mathcal{T}\to\infty} \frac{1}{\mathcal{T}} \int_0^{\mathcal{T}} \Phi(\mathbf{x}, t)dt \tag{3.21}$$

Then, the decomposition reads:

$$\Phi(\mathbf{x}, t) = \overline{\Phi}(\mathbf{x}) + \Phi'(\mathbf{x}, t) \tag{3.22}$$

where the fluctuating component $\Phi'(\mathbf{x}, t)$ has a null time averaged value, i.e.:

$$\overline{\Phi'(\mathbf{x}, t)} = 0 \tag{3.23}$$

When the time averaging given by Equation 3.21 is applied to the mass, momentum and energy conservation equations presented in Section 3.1.2.1, one obtains the so called RANS equations, given below for the incompressible flow of a Newtonian fluid:

Mass conservation

$$\boldsymbol{\nabla} \cdot \overline{\mathbf{u}} = 0 \tag{3.24}$$

Linear momentum conservation

$$\rho \frac{\overline{D}\overline{\mathbf{u}}}{\overline{D}t} = -\boldsymbol{\nabla}\overline{p} + \boldsymbol{\nabla} \cdot \left(\mu\{\boldsymbol{\nabla}\overline{\mathbf{u}} + (\boldsymbol{\nabla}\overline{\mathbf{u}})^T\} - \rho\overline{\mathbf{u}'\mathbf{u}'}\right) + \rho\mathbf{g} \tag{3.25}$$

Energy conservation

$$\rho C_p \frac{\overline{DT}}{\overline{D}t} = \boldsymbol{\nabla} \cdot \left(k\boldsymbol{\nabla}\overline{T}\right) - \rho C_p \overline{\mathbf{u}'T'} + Q_v \tag{3.26}$$

It can be noted that averaged momentum and energy conservation equations have the same form than equations 3.10 and 3.14 with the exception of the terms that appear on the right hand side of each equation and depend on the product of fluctuating variables. These terms are, for the momentum equation:

$$-\boldsymbol{\nabla} \cdot \rho\overline{\mathbf{u}'\mathbf{u}'} \equiv \boldsymbol{\nabla} \cdot \boldsymbol{\tau}^{\boldsymbol{R}} \tag{3.27}$$

and for the energy equation:

$$-\rho C_p \overline{\mathbf{u}'T'} \equiv \boldsymbol{q}^{\boldsymbol{R}} \tag{3.28}$$

where the Reynolds stress tensor $\boldsymbol{\tau}^{\boldsymbol{R}}$ and the turbulent heat flux $\boldsymbol{q}^{\boldsymbol{R}}$ have been defined.

Note that with the definition given by Equation 3.21, the averaged variable $\overline{\Phi}(\mathbf{x})$ is time independent and thus $\frac{\overline{D}\overline{u}}{\overline{D}t} = \overline{\mathbf{u}} \cdot \boldsymbol{\nabla}\overline{\mathbf{u}}$ and $\frac{\overline{DT}}{\overline{D}t} = \overline{\mathbf{u}} \cdot \boldsymbol{\nabla}\overline{T}$, which makes the RANS equations time independent. However, the time dependence is considered in the Unsteady RANS (URANS) methods, that replace the limit given by Equation 3.21 by an averaging over a finite time period $\mathcal{T}_0$ such that it is significantly larger

than the time scale of the turbulence induced oscillations of the flow variables. In this work we only deal with statistically steady flows, so the time independent RANS equations are considered.

3.2.2. Closure problem

The Reynolds stress tensor $\boldsymbol{\tau}^{\boldsymbol{R}}$ and the turbulent flux $\boldsymbol{q}^{\boldsymbol{R}}$ introduce new unknowns that need to be expressed in terms of mean flow quantities in order to close the problem. To do so, the most widely employed methods rely on the Boussinesq and on the gradient diffusion hypotheses. The Boussinesq hypothesis proposes, by analogy to the stress-strain rate relation of Newtonian fluids (see Equation 3.7), that the deviatoric Reynolds stresses are proportional to the mean strain rate, which for the incompressible case gives:

$$\boldsymbol{\tau}^{\boldsymbol{R}} = \mu_t\{\boldsymbol{\nabla}\overline{\mathbf{u}} + (\boldsymbol{\nabla}\overline{\mathbf{u}})^T\} - \frac{2}{3}\rho k\mathbf{I} \tag{3.29}$$

where μ_t is the turbulent or eddy viscosity and k is the turbulent kinetic energy defined as:

$$k = \frac{1}{2}\overline{\mathbf{u}' \cdot \mathbf{u}'} \tag{3.30}$$

For incompressible flows, the term $-(2/3)\rho k\mathbf{I}$ can be incorporated in a turbulent pressure defined as:

$$\overline{p} \leftarrow \overline{p} + \frac{2}{3}\rho k \tag{3.31}$$

reducing the additional unknowns to μ_t only. Similarly, by analogy to Fourier's law of heat conduction, the gradient diffusion hypothesis assumes that the turbulent heat flux is proportional to the mean temperature gradient and can be written as:

$$\mathbf{q}^R = k_t\boldsymbol{\nabla}\overline{T} \tag{3.32}$$

where k_t is the turbulent or eddy thermal conductivity.

An additional hypothesis is typically employed to relate the turbulent thermal conductivity to the turbulent viscosity by assuming similarity between the turbulent momentum and heat transport mechanisms. This assumption, called Reynolds analogy, introduces the dimensionless turbulent Prandtl number Pr_t:

$$Pr_t = \frac{C_p\mu_t}{k_t} = \frac{\nu_t}{\alpha_t} \tag{3.33}$$

where the turbulent momentum diffusivity $\nu_t = \mu_t/\rho$ and turbulent thermal diffusivity $\alpha_t = k_t/(\rho C_p)$ have been used. Then, only μ_t needs to be computed to close the problem, which is done by defining turbulence models.

3.2.3. Turbulence models

The turbulent viscosity can be expressed in terms of characteristic length (l^*) and velocity (u^*) scales, such that:

$$\mu_t = \rho l^* u^* \tag{3.34}$$

The models that aim to calculate these scales to then obtain μ_t can be grouped in the following general categories:

- Algebraic models
- One equation models
- Two equation models

The algebraic models, such as the mixing length model, compute μ_t by deriving l^* from the geometry of the flow, without solving any additional partial differential equation. The one and two equation models, on the other hand, require the resolution of one and two additional transport equations, respectively, to compute μ_t. Other approaches exist—called second order closure models—that are not based on the Boussinesq hypothesis and thus, unlike all previously mentioned approaches, are able to account for the anisotropy of turbulence. However, they are more computationally expensive since they involve the resolution of one partial differential equation for each of the six different components of the Reynolds stress tensor.

For industrial applications, the two equation models are the most widely used, the $k-\epsilon$ and the $k-\omega$ being the most popular families. The standard $k-\epsilon$ model solves one transport equation for the turbulent kinetic energy k, exactly derived from the definition of the Reynolds stresses, and one empirically constructed equation for its dissipation rate ϵ. Then, the turbulent viscosity is written as follows

$$\mu_t = \frac{\rho C_\mu k^2}{\epsilon} \tag{3.35}$$

where C_μ is a constant coefficient of the model. In the derivation of the transport equations of the standard $k-\epsilon$ model, the effects of molecular viscosity are neglected, which is why it yields good results in the bulk of the wall-bounded turbulent flows but it is not valid close to the wall, where the effects of viscosity become dominant. Indeed, in this formulation, ϵ becomes singular at the wall (Perot and De Bruyn Kops 2006). One way of overcoming this problem is damping the turbulent kinetic energy by using a function that tends to zero as the distance to the wall goes to zero; in some cases, similar damping is applied to some coefficients of the transport equation of ϵ as well. The models that employ these damping functions are called low-Re models, as opposed to the high-Re models that do not employ any damping and cannot be applied in the viscous dominated layer near the wall. Alternatively, a two-layer approach can be used. In this case, in the cells

close the the wall, both ϵ and μ_t are prescribed as a function of the wall distance. The values thus obtained are smoothly blended with the quantities computed by a high-Re formulation as the distance from the wall grows.

Further improvements of the standard $k-\epsilon$ model were introduced by rigorously deriving the ϵ transport equation from the equation of the transport of the mean-square vorticity fluctuation, and from considering a coefficient C_μ that is no longer constant and depends on the mean flow and turbulence properties. This last modification allows the model to avoid nonphysical results linked to the violation of the realizability, which requires the normal Reynolds stresses to be positive as well as the fulfilment of the Cauchy-Schwarz' inequality given by $\left(\overline{\mathbf{u}' \cdot \mathbf{u}'}\right)^2 > \overline{\mathbf{u}'^2 \cdot \mathbf{u}'^2}$. The model that implements these improvements is called realizable $k-\epsilon$ and is often used in combination with the two-layer formulation.

In the second most popular family of two equation turbulence models, the transport of a new quantity ω is solved instead of the transport of ϵ, such that:

$$\omega = \frac{\epsilon}{C_\mu k} \tag{3.36}$$

This formulation has the advantage that the ω transport equation can be integrated in the viscous sub-layer, so it performs well in this region without the need of using damping functions. It also outperforms the $k-\epsilon$ models in presence of adverse pressure gradients, but one of its major drawbacks is that it is highly sensitive to the specification of the free stream value of ω, and it often fails to provide good predictions in the bulk of wall bounded flows. This motivated the development of models such as the $k-\omega$ SST, which switch between the $k-\omega$ and the $k-\epsilon$ formulations depending on the distance to the wall.

As discussed in Section 3.3.3, in this work we employ a two-layer realizable $k-\epsilon$ model, in combination with a mathematical description of the mean flow quantities near the walls that is called wall law and is introduced next.

3.2.4. Near wall modeling

As discussed in Section 2.1.2, the molecular dissipative forces that dominate near the wall lead to large gradients in the flow variables in this region, which should be correctly captured in a CFD simulation since they account for relevant flow phenomena such as the pressure loss due to friction. The most straightforward approach to do so is to use a very fine spatial discretization near the wall, and to numerically solve the transport equations of the selected turbulent model in the whole simulation domain, which can only be done with the models that are valid near the wall. Additionally, the mesh resolution required to do so leads, in many cases, to a number of computational cells that is too high for its practical

application and that increases with the Re number as the viscous dominated region becomes thinner. To overcome this problem, the near wall region can be modeled by a so called wall function instead of being explicitly resolved, which is used to compute the wall shear stress and the turbulent quantities in the computational cells adjacent to the wall, that need to be placed at a distance where the wall law is valid.

The formulation of the wall laws is based on the boundary layer description first given by von Karman (Kármán 1931), in which the a non-dimensional mean velocity u^+ is expressed as a function of a non dimensional wall normal distance y^+. These non dimensional variables are defined as:

$$u^+ = \frac{u}{\sqrt{\tau_w/\rho}} \tag{3.37}$$

where τ_w is the wall shear stress and u the velocity parallel to the wall, and:

$$y^+ = \frac{y\sqrt{\tau_w/\rho}}{\nu} \tag{3.38}$$

where y is the distance from the wall and ν the kinematic viscosity of the fluid. In this description, the inner region of the boundary layer is separated into three distinct layers given by:

- **A viscous sub-layer** $(0 < y^+ < 5)$, where the viscous effects dominate and the flow is almost laminar. In this region the non dimensional velocity is given by:

$$u^+ = y^+ \tag{3.39}$$

- **A buffer sub-layer** $(5 < y^+ < 30)$, where the turbulent and viscous effects are comparable.

- **A logarithmic layer** $(30 < y^+ <\sim 400)$, where turbulence dominates. The non dimensional velocity is:

$$u^+ = \frac{1}{k_{VK}} ln(y^+) + B \tag{3.40}$$

  where $k_{VK} \approx 0.42$ is the von Karman constant and $B \approx 5.0$

The resulting velocity profile is illustrated in Figure 3.4.

A similar classification can be done with the thermal boundary layer by defining a non-dimensional temperature. It can be shown that a conductive sub-layer, in which the effects of molecular conduction dominate, extends up to $y^+ \sim 3/Pr$ which

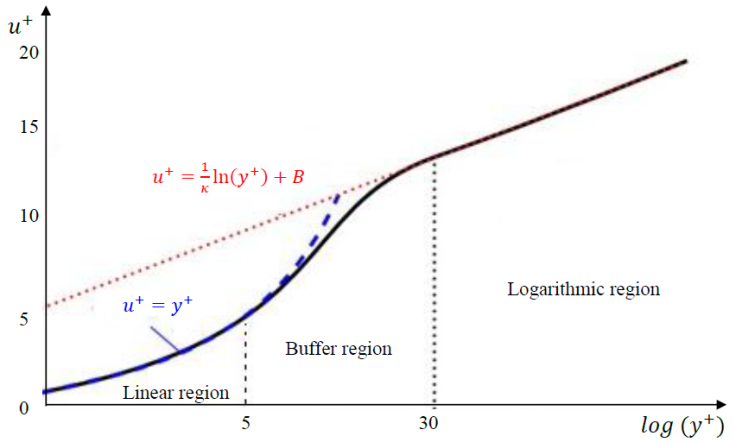

Figure 3.4.: Non-dimensional velocity profile in the inner boundary layer (Saxena 2014).

in the case of sodium gives $y^+ \sim 750$. It is clear then that the conduction dominated layer is significantly larger than the momentum viscous sub-layer in this case.

By using such a description of the near wall velocity and temperature non-dimensional profiles, the inner boundary layer does not need to be resolved in the CFD simulation. Analytical solutions can be derived for the turbulent equations for the viscous sub-layer and the logarithmic region, but the intermediate buffer layer is problematic. For this reason, this approach leads to more accurate results when the first computational cell is not placed in the buffer region (Kalitzin, Medic, Iaccarino, et al. 2005).

3.3. Implemented CFD-RANS model

In this work, the thermal-hydraulic simulations of SFR fuel bundles are conducted using a RANS approach implemented in the commercial CFD code STAR-CCM+ (*STAR-CCM+ v12.02 Users Manual* 2017), and it is described in what follows.

3.3.1. STAR-CCM+

STAR-CCM+ is a multi disciplinary simulation tool, developed by Siemens, that allows to conduct all the required steps for a CFD simulation, namely the construction of the representation of the modeled geometry (CAD model), its spatial discretization (meshing), the resolution of the discretized governing equations, and the post-processing of the results. This is a desired feature in the framework of the development of a coupled methodology in which all these steps need to be

conducted automatically, and information is exchanged with a thermomechanical simulation tool, since it reduces the number of code to code interfaces that need to be developed. Added to this, powerful user scripting capabilities, based on macros coded in JAVA language, allow to modify the behaviour of any of these steps.

In addition, STAR-CCM+ has been extensively used for the simulation of liquid-metal-cooled subassemblies with satisfactory results ((Hamman and Berry 2010; Baglietto, Fricano, and Sosnovsky 2014; E. Merzari, Fischer, Yuan, et al. 2016; Brockmeyer, Carasik, Elia Merzari, et al. 2017; Pacio, Wetzel, Doolaard, et al. 2017), among many others), which is a challenging task, among other reasons, due to their complex geometry which is difficult to mesh. Indeed, as discussed in Section 3.3.5, its versatile and robust meshing tool is a key feature, and even more so when meshing fuel bundles that present irregular deformation patterns consequence of their irradiation.

STAR-CCM+ employs the finite volume method to approximate the solution of the partial differential equations, described in Section 3.1.2.1, that define the conservation laws. To do this, the simulation domain is firstly divided into non-overlapping finite volumes (or cells), over which the conservation equations are integrated to yield a set of algebraic equations with the values of the dependent variables in each of them as unknowns, which is solved iteratively. In the discretization process, volume integrals in the finite volumes are converted into surface integrals over their faces. Then, since the flux leaving a volume through a given face is the same as the flux entering a neighbor volume that shares that face, the finite volume method is strictly conservative. A second order upwind scheme is employed for the discretization of the conservation equations. The reader is referred to the user manual of STAR-CCM+ for details on the discretization scheme and numerical methods employed, which are not the focus of this work and are thus not discussed here.

3.3.2. Selected fluid models

For the thermal-hydraulic simulations conducted in this work, the sodium flow is considered to be incompressible, and constant fluid thermophysical properties are employed. These properties are evaluated from (Sobolev 2011) at the average temperature between the inlet and the outlet of the simulation domain, described in Section 3.3.4. As discussed in Section 2.1.3, the properties of sodium do not vary strongly with temperature in the range of interest to us, so this simplification was considered adequate for the simulations here conducted. The possibility of employing polynomial expressions to consider their temperature dependence was also implemented, but this option increases the computational cost of the simulation since it couples the momentum and energy equations, and because the polynomials need to be evaluated for each cell and iteration. In all cases, the effects of gravity

were not considered, which implies that the small buoyancy effects present in the forced convection regime in nominal conditions are neglected.[1]

The steady state, Reynolds-Averaged Navier-Stokes and energy equations (see Section 3.2.1) are solved employing the segregated flow and fluid temperature models, which are based on a SIMPLE-type algorithm (Patankar and Spalding 1972) and a Rhie-and-Chow-type (Rhie and Chow 1983) pressure-velocity coupling, implemented in a collocated variable arrangement.

3.3.3. Turbulence model and wall treatment

Numerous RANS studies of SFR subassemblies or representative geometries have shown very good agreement between different turbulence models, and particularly so regarding the sodium temperature distribution (see, for example, (Chandra, Roelofs, Houkema, et al. 2009; Fricano and Baglietto 2014; Roelofs, Dovizio, Uitslag-Doolaard, et al. 2018; E. Merzari, Fischer, Yuan, et al. 2016; Smith, Babin, W. David Pointer, et al. 2008; Smith, Tokuhiro, W. David Pointer, et al. 2009; Natesan, Sundararajan, Narasimhan, et al. 2010; Rolfo, Péniguel, Guillaud, et al. 2012). There are two main reasons for this behaviour. Firstly, as discussed in Section 2.1.4, the very low Pr of sodium implies, in the range of Re of SFR subassemblies in nominal operation, that the heat exchange process is dominated by conduction, and the turbulent contribution has thus a lower importance. Additionally, the fuel bundle geometry is such that the wall has a dominant effect on the flow, which is modeled by the wall laws when this approach is adopted.

In this work, we employ a two-layer realizable $k-\epsilon$ turbulence closure model, in a so called *All* y^+ formulation (*STAR-CCM+ v12.02 Users Manual* 2017). This formulation employs a blending approach between a two-layer and a high-Re model. In this approach, for the wall-adjacent cells with low y^+ ($<\sim 1$), the turbulent kinetic energy k is computed by solving its transport equation, while the dissipation rate ϵ is prescribed as:

$$\epsilon = \frac{k^{3/2}}{l_\epsilon} \tag{3.41}$$

where l_ϵ is a characteristic length depending on the wall distance and calculated using Wolftein's model (Wolfshtein 1969). Similarly, the turbulence viscosity μ_t of the wall-adjacent cells is also prescribed as a function of the wall distance. On the other hand, when y^+ is higher ($>\sim 30$) and the viscous sub-layer is not resolved, all relevant turbulent quantities are derived from the wall laws, namely Reichardt's

[1] This hypothesis may lose validity for partial flow regimes with significantly lower velocities, in which cases the buoyancy effects might become significant. In this case, the body forces can be approximated by $\rho_0 \mathbf{g}\beta(T_0 - T)$, where ρ_0 and T_0 are a reference density and temperature of the fluid, respectively, and β is its thermal expansion coefficient.

(Reichardt 1951) and Kader's (Kader 1981) for momentum and temperature, respectively. It is important to note that Kader's law depends on the Pr of the fluid, and it is in good agreement with experimental observations on fluids of a wide range of Pr, including liquid metals (Kader 1981). A smooth blending between the two cases ($y^+ <\sim 1$ and $y^+ >\sim 30$) is achieved by using an exponential weighting function, which is designed to provide reasonable results for wall-adjacent cells with intermediate y^+. This formulation is recommended when having a mesh fine enough to resolve the viscous sub-layer in the whole simulation domain is not practical, but having $y^+ > 30$ everywhere is also difficult to achieve. The complex SFR bundle geometry is a good example of this situation, since small wall-adjacent cells near the contact between the spacer wires and the cladding, discussed in Section 3.3.6, are difficult to avoid.

As discussed in Section 3.2.2, the turbulence model computes the turbulent momentum diffusivity, while the turbulent thermal diffusivity is computed from Equation 3.33 using the turbulent Prandtl number, according to the Reynolds analogy. This technique has been shown to provide good results for fluids with Pr close to unity, but, as anticipated in Section 2.1.4, it presents significant limitations for fluids with $Pr << 1$, specially in natural and mixed convection regimes (G. Grötzbach 2013). More sophisticated turbulent heat flux closure models exist, including variable Pr_t models, and both isotropic and anisotropic models that solve for additional transport equations of turbulent quantities. Even though these approaches seem promising, they need further calibration for low Pr fluids and in complex geometries, and they are still being actively developed (Shams 2018). The Reynolds analogy with constant $Pr_t = 0.85 - 0.9$ is still the most widely employed approach, even though the available correlations for Pr_t yield values between 1.5 and 4.2 for sodium at a $Re = 50000$ (Saxena 2014).

In this work, however, we employ the default value of $Pr_t = 0.9$ since, using the wall law approach, minimal effects on the temperature distribution were observed in preliminary simulations employing $Pr_t = 2$ (maximal temperature variations of $\sim 2°C$). These results are in agreement with the simulations conducted with $Pr_t = 1$ and $Pr_t = 3$ and presented in (Rolfo, Péniguel, Guillaud, et al. 2012), that showed differences in the Nusselt number (see equations 2.6 and 2.5) of under 3% even at a lower $Re = 25000$. For $Pr = 0.007$, experimental measurements in a heated pipe showed that the eddy diffusivity becomes larger than the molecular diffusivity only for $Re = 214000$, and the ratio between the two is approximately $\alpha_t/\alpha \sim 0.2$ for $Re \sim 40000$ (Günther Grötzbach 1981). Sodium has an even lower $Pr \sim 0.004$ so, in nominal flow conditions in a SFR subassembly, the effect of the turbulent heat flux model is not expected to have major importance. It should be noted that this is not the case for other liquid metals used as fast reactor coolants, such as Lead-Bismuth Eutectic (LBE) that has $Pr \sim 0.025$ for which the same experiment showed that $\alpha_t/\alpha \sim 1$ for $Re = 60000$.

3.3.4. Simulation domain and boundary conditions

The simulation domain is circumscribed to the coolant within the heated column of the fuel bundle. That is to say, the sodium surrounding the wire-wrapped fuel pins and enclosed by the hexcan, which external and internal surfaces, respectively, are part of the boundaries of the domain; this is schematically represented in Figure 3.5 for a 7-pin fuel bundle, where the pin naming system adopted in this work is also indicated.

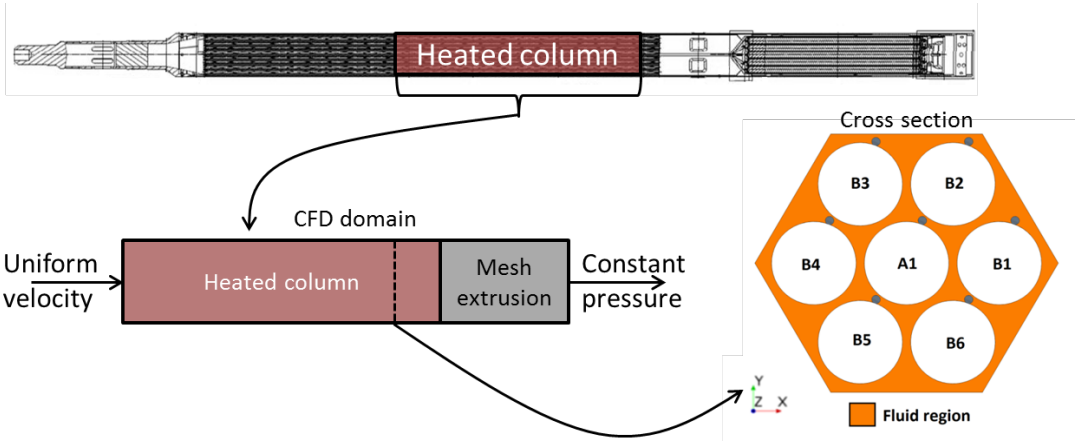

Figure 3.5.: Representation of the CFD simulation domain. The hydraulic boundary conditions at the entrance and outlet of the domain are indicated, as well as the fuel pin naming system.

The mesh of the fluid domain within the heated column is generated following the procedure indicated in Section 3.3.5, the results of which are discussed in Appendix A. A 20 cm long extrusion is added at its exit, which allows setting a constant pressure boundary condition downstream the region of interest and improves the convergence rate of the simulations. No-slip boundary conditions are used for all solid walls, and the hexcan is considered to be adiabatic, as well as the surface of the spacer wires. Finally, the heat source is provided by an axial profile of heat flux per fuel pin, which is considered uniform in the circumference of the cladding.

The simplification of considering only the fluid domain and imposing a circumferentially uniform heat flux on the cladding external surface, which greatly reduces the computational cost of the simulations, was motivated by the sodium conductivity being ~ 3 times higher than the cladding's. In this case, the heat conduction in the cladding is not expected to significantly *smooth out* the temperature gradients

caused by the uneven sodium temperature distribution, which would not be the case if the conductivity of the cladding was significantly higher, or that of sodium significantly lower. This simplification was evaluated by computing a conjugate heat transfer case in which the thickness of the cladding was represented. In this simulation, presented in more detail in Section 6.2, the heat conduction in the cladding and the convection in the fluid are solved simultaneously, and are coupled by the heat exchange in the solid-fluid interface. The temperature distribution thus obtained is in very good agreement with the results obtained considering only the fluid domain. Similar results were recently presented in (Pacio, Wetzel, Doolaard, et al. 2017), where maximum differences in the cladding temperature of less than 3 °C ($< 2\%$ change in Nu) were obtained when considering the conjugate heat transfer in an electrically heated, 19-pin bundle cooled by LBE, which has a thermal conductivity similar to that of steel.

The coolant mass flow rate is imposed at the entrance of the domain, where uniform sodium temperature and velocity profiles are considered. The latter approximation was evaluated by means of a CFD simulation of a 217-pin fuel bundle, where a developed velocity profile was also essayed as inlet hydraulic condition. The maximum local temperature difference observed between the simulations using a flat and a developed inlet velocity profile was 2°C, the first yielding a higher temperature. The total pressure drop within the bundle was not affected by the inlet profile.

Additionally, at the inlet, the turbulence viscosity ratio (μ_t/μ) and the turbulence intensity ($\sqrt{\overline{\mathbf{u}'^2}}/U$ with U the mean flow velocity) are set respectively to 61.5 and 0.056, values obtained from the outlet of a preliminary simulation. The developed temperature and velocity fields were observed to be independent of these magnitudes[2], so the same values were employed for all the cases analyzed in this work.

Out of the boundary conditions discussed above, the coolant mass flow rate at the inlet of the bundle and the wall heat flux profile of the fuel claddings depend on the bundle deformation. The first is due to the modification of the hydraulic resistance caused by the deformation, while the latter is a consequence of the increased heat exchange surface that, at constant linear power distribution, modifies the heat flux imposed in the CFD simulations. These effects are taken into account when simulating deformed bundles, and the boundary conditions are calculated as indicated in sections 5.3.2 and 5.3.3.

[2] Additionally, these magnitudes, computed at the outlet of the fuel bundle, had similar values in the different simulations we conducted.

3.3.5. Meshing

After the construction of the CAD model, a volume mesh is generated using STAR-CCM+'s automated meshing tool, which, based on global parameters such as a target cell size, allows creating a good quality mesh even in the complex geometry of SFR bundles. In this case, polyhedral cells are employed for the core of the fluid volume, and one or two layers of prismatic cells are placed on the solid boundaries of the domain. One of the main advantages of polyhedral cells is that they typically have a large number of neighbors when compared to, for example, tetrahedral or hexahedral cells, which is beneficial for the approximation of the gradients of the flow variables. Additionally, to achieve equivalent accuracy, approximately 5 times fewer cells are required when using polyhedral cells when compared to tetrahedral cells (*STAR-CCM+ v12.02 Users Manual* 2017). The prismatic cells allow to more accurately compute the wall distance of the near-wall cells, and to better control the y^+ at which the wall laws employed in this work are evaluated. For the *All* y^+ approach, the thickness of the prism layer should be defined aiming to achieve wall-adjacent cells that have $y^+ < 5$ or $30 < y^+ < 150$ or higher.

To reduce the number of computational cells, the CAD model is contracted, before the meshing procedure, by a factor of 4 in the flow direction. Afterwards, the mesh of the contracted geometry is re-scaled up by the same factor. This procedure, with an expansion factor of up to 8, was found to not significantly affect the results (Ulrich Bieder, Valérie Barthel, Frederic Ducros, et al. 2010; Smith, Tokuhiro, W. David Pointer, et al. 2009), since the gradients of the variables of interest are much smaller in the direction of the flow than in the perpendicular direction.

Besides the target cell size and the prism layer thickness, a relevant parameter of the automated meshing tool is the minimum number of cells placed in a gap, defined as the distance between two CAD surfaces. In our problem, this gap is the distance between the surfaces of two neighboring claddings, or between a spacer wire and a cladding. In the deformed fuel bundles simulated in this work, the fuel pins increase their diameter and thus these gaps are reduced. Defining a minimum number of cells in them allows then to limit the degradation of the mesh in deformed geometries.

The parameters required by the meshing tool were defined as to have a y^+ distribution adequate for the turbulence model employed, and aiming to have a total cell count in large subassemblies (> 200 pins) so that the simulations could be conducted in a personal computer with less than 128GB of Random Access Memory (RAM). To do so, a mesh convergence study, presented in Appendix A, was conducted based on a 7-pin study case, the resulting mesh of which is presented as an example in Figure 3.6 where the bundle inlet is shown. The chosen parameters

resulted in approximately 2 million cells for the 7-pin bundle of 0.8 m in length, and about 60 million for a 217-pin bundle of the same length, the largest evaluated in this work.

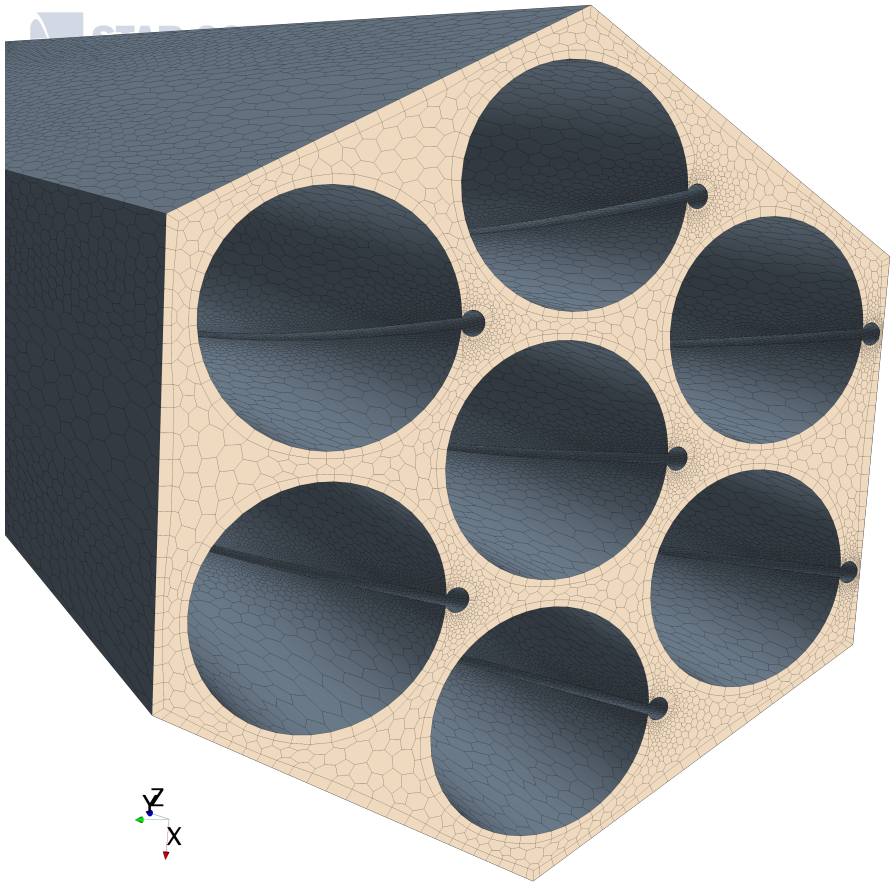

Figure 3.6.: Example of the mesh obtained for a 7-pin bundle.

3.3.6. Wire-cladding contact representation

Te tangential contact between the spacer wires and the fuel claddings they wrap poses severe difficulties for the CAD managers and the meshing tools, that fail to handle them robustly. With very few exceptions ((J.-H. Jeong, Song, and Lee 2017a) for example), the geometry of the contact is simplified in the CFD studies of SFR bundles found in literature. A widely used approach consists in introducing a slight interpenetration ϵ_{inter} between the wire and the cladding, as indicated in Figure 3.7a, and it has been shown to not significantly affect the velocity or temperature fields in the bundle (Natesan, Sundararajan, Narasimhan, et al. 2010; Zhao, J. Liu, Ge, et al. 2017). Additionally, the edges defined by the contact

between the cladding and the wire can be rounded by applying circular fillets of small radius, as indicated by Figure 3.7b, still leading to good quality results (E. Merzari, Fischer, Yuan, et al. 2016). These two approaches were identified by (Ulrich Bieder, Valérie Barthel, Frederic Ducros, et al. 2010) as the ones with less impact on the results, outperforming several others that simplify the contact even further.

In this work, an algorithm for the automatic generation of the CAD model of nominal and deformed bundles was developed and it is presented in Section 5.3.1. This algorithm applies the wire cladding interpenetration systematically, with ϵ_{inter} as a user defined value, and the possibility of filleting the contact edges was also implemented. Both simplifications led to bundle pressure drop values differing in about 1%, and to very similar sodium temperature distributions. The filleting reduces the overall cell count by about 10% but, in the conditions of the simulations conducted in this work, it increases the proportion of cells with $5 < y^+ < 30$, which is undesired. Additionally, as discussed in Section 5.3.1.3, it compromises, in some cases, the robustness of the CAD generation algorithm. For this reasons, only the first simplification is employed in the simulations here presented, and a value of $\epsilon_{inter} = 5\text{x}10^{-5}$ m is adopted.

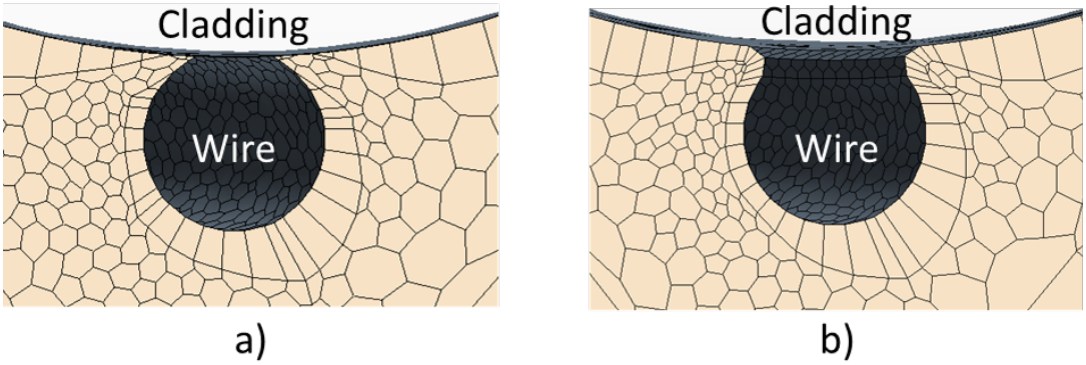

Figure 3.7.: Wire cladding interpenetration (a) and circular filleting of the contact edges (b)

3.4. Summary

In this chapter, we described the model implemented in this work in order to simulate the thermal-hydraulics of SFR subassemblies. Firstly, we overviewed the main approaches available to do so, namely subchannel analysis and CFD. The latter was chosen because it provides more detail on the temperature and velocity fields of the coolant, and because it allows to explicitly consider the complex

geometry of the fuel bundle and the changes it undergoes during irradiation. This leads to a higher predictive capability than that achievable using a subchannel model, particularly in the peripheral subchannels of the fuel bundle and in deformed geometries. Out of the CFD methods available, that we briefly described, a RANS model was chosen because, for the purposes of this work, it represents a good compromise between performance and computational cost. Then, we gave a general description of the RANS simulation approach and, finally, we defined the particular model implemented in this work in the commercial CFD code STAR-CCM+ to simulate the coolant flowing through a SFR fuel bundle.

4. Numerical simulation of the thermomechanics of SFR subassemblies

This chapter is dedicated to the numerical simulation of the thermomechanical evolution of SFR subassemblies under irradiation. Firstly, in Section 4.1, two different modelling approaches—one based on representing a single pin and the other on representing the entire pin bundle and the interaction between pins—are introduced. Then, in Section 4.2, we present DOMAJEUR2, the finite element based code—representative the second type of modelling approach and developed at the CEA—employed in this work, the main input data and boundary conditions of which are described in Section 4.3. DOMAJEUR2 has two different finite element models to describe the SFR fuel bundle and the hexcan, namely a 1D beam based model and a fully 3D model, which are described in Section 4.4.

Table of Contents

4.1. Single fuel pin and entire fuel bundle simulation approaches

A key part of the design process of the SFR fuel subassemblies consists on conducting numerical simulations to verify that the design criteria—that typically take the form on limits on the maximal strain, stress, and temperature of the constituents of the subassembly—are respected both during nominal and accidental situations. A widely adopted approach consists on the use of finite element

based methods to model the thermomechanical evolution of one isolated fuel pin, including the cladding and the fuel pellets it contains, as well as the pellet cladding interaction. Such simulations are typically conducted with a 1D1/2 axisymmetric representation of the fuel pin, which means that it is divided into several axial slices whose thermal evolutions are coupled by the heat transported by the coolant. This modelling strategy is employed, for example, in the fuel performance code GERMINAL currently under development at the CEA (Lainet, Michel, Dumas, et al. 2019).

Restricting the domain to a 1D1/2 representation of one fuel pin allows to consider the evolution of the fuel pellets and the cladding during the irradiation, including their mechanical and chemical interaction. Besides, the temperature and swelling radial gradients within the thickness of the cladding, which can cause high secondary stresses (Uwaba and Ukai 2002), can be considered by employing a fine mesh that would be very computationally expensive in larger scale simulations. However, this approach cannot take into account the variation of these variables within the circumference of the claddings. Moreover, since only one fuel pin is simulated, the contact with other pins and with the hexcan cannot be predicted.

For these reasons, different and complementary approaches exist to model the entire fuel bundle, in order to include the effects of the mechanical interactions between fuel pins, and between pins and the hexcan. In these approaches, in order to avoid an excessively high computational cost, the mechanical interaction between the fuel pellets and the cladding— as discussed in Section 2.2.4, usually very limited during normal operation— are typically not considered. Additionally, the meshing employed is either less refined, or a beam-based representation of the bundle is adopted. A representative example of this alternative approach is DOMAJEUR2, a simulation tool developed by the CEA and employed in the present work, which is described next.

4.2. General presentation of DOMAJEUR2

In the context of the R&D efforts for GEN IV SFR, DOMAJEUR2, which is a specialized numerical tool for the 3D simulation of the thermomechanical behavior of SFR subassemblies, is under development at the CEA. It is based on the in-house finite element analysis code Cast3M (Le Fichoux 2011; Combescure, Hoffman, and Pasquet 1982), and it belongs to a class of computer codes that, motivated by the increase of the available computational power, aim to simulate the fuel bundle as a whole, including the interaction between its components. Worth noting members of this code class, which represents a step-up in complexity when compared to traditional codes dealing with one single pin, are, for example, BAMBOO (Uwaba, M. Ito, Ukai, et al. 2005), ETOILE (Nakagawa and Tsuboi 1990), and MARSE

(Itoh, Kinjo, and Mimura 1994), aimed to study fast breeder reactor fuel bundles, and a model developed in COMSOL (Bell and Lewis 2012), dedicated to study CANDU[1] fuel bundles.

DOMAJEUR2 calculates the time evolution of the strain and stress distributions within the fuel pin bundle and the hexcan during their irradiation, under a quasi-static hypothesis. To do so, the irradiation period under consideration is divided into multiple time steps specified by the user. The PASAPAS procedure of Cast3M (Charras and Di Paola 2011) is employed to solve, for each time step, the nonlinear mechanical equilibrium problem adopting a Lagrangian formulation. This means that, for the description of state transformation of the system, all variables are determined in material points which are identified by their initial position vector $\boldsymbol{X_0}$ in the undeformed state. This problem can be formulated for a domain Ω as:

$$\begin{cases} \nabla_0 \cdot \boldsymbol{\sigma_{PK1}} + \boldsymbol{f_0} = 0 & (4.1) \\ \boldsymbol{\sigma} = C(\boldsymbol{Y}, \boldsymbol{\varepsilon}) & (4.2) \\ \boldsymbol{\varepsilon} = \frac{1}{2}(\nabla_0 \boldsymbol{u} + (\nabla_0 \boldsymbol{u})^T + (\nabla_0 \boldsymbol{u})^T \nabla_0 \boldsymbol{u}) & (4.3) \end{cases}$$

where $\nabla_0 \cdot$ and ∇_0 are the divergence and the gradient with respect to $\boldsymbol{X_0}$, respectively. Equation 4.1 is the linear momentum balance expressed in terms of the divergence of the first Piola-Kirchhoff stress tensor $\boldsymbol{\sigma_{PK1}}$ and of the vector field $\boldsymbol{f_0}$ of body force per unit undeformed volume. The constitutive Equation 4.2 expresses the stress tensor as a function C of the strain tensor $\boldsymbol{\varepsilon}$ and of the internal variables $\boldsymbol{Y}$ of the model (e.g. temperature, irradiation dose, etc.). Finally, Equation 4.3 is the definition of the Green-Lagrange strain tensor $\boldsymbol{\varepsilon}$ in terms of the gradient of the displacement vector field $\boldsymbol{u}$. Boundary conditions need to be specified at the boundary $\partial\Omega$ of the domain and initial conditions on Ω to completely define the problem.

Following the finite element formulation, the domain Ω is divided into finite elements connected by nodes. Under this spatial discretization, the problem can be written in the form of an algebraic equation system, with the nodal displacements as unknowns, of the form:

$$[K(\boldsymbol{u})]\{\boldsymbol{u}\} = \{F(\boldsymbol{u})\} \tag{4.4}$$

where $[K(\boldsymbol{u})]$ is the stiffness matrix of the system, $\{u\}$ the vector of nodal displacements, and $\{F(\boldsymbol{u})\}$ the vector of nodal forces. The dependence of K and F on the displacement field, absent in the linear case, renders Equation 4.4 nonlinear, thus the need for an iterative procedure to solve it. In our particular problem,

[1] CANDU (Canada Deuterium Uranium) is a type of pressurized, heavy water cooled reactor originally designed in Canada.

the main sources of nonlinearities are the behaviour of the materials subject to swelling, irradiation creep and thermal creep—in this case, in the constitutive law given by Equation 4.2, C is a nonlinear function of $\boldsymbol{\varepsilon}$—and the contact between the fuel pins, and between the fuel pins and the hexcan. Indeed, the existence and the position of contacts points depend on the displacement of the fuel pins, and they globally modify the stiffness of the system. Also, the local stiffness of the claddings crushed under contact forces are modified by their ovalisation.

To account for the temperature effects, the PASAPAS procedure includes a thermal module that solves the heat equation within the domain Ω—or it considers a prescribed temperature distribution, which is our case since it is externally computed by the CFD model described in Section 3.3—, and uses this result to update the thermal loading (e.g. to consider thermal expansion or temperature dependent mechanical properties). The mechanical solver then deals with Equation 4.4 within each time step.

Within each time step, the mechanical solver performs iterations to obtain the increment of the displacement field that minimizes the residual, defined as the difference between internal and external nodal forces, within a given tolerance. Inside each finite element, the displacement field is approximated by polynomial basis functions supported by the nodes of the element. Within each iteration, the strains are computed from the displacement field, and then the stresses are calculated from the strains by explicit integration of the constitutive laws, employing a fourth order Runge-Kutta method with error control and adaptive time step. The strain and stresses are computed in the so called integration points of each element—Gauss points in our case, since the Gauss quadrature is employed to approximate the definite integrals within each element—, in which the required numerical integration of functions of the displacement field are most accurate.

The constitutive laws employed for the materials of the fuel pin and the hexcan take into account the thermal and irradiation induced creep. The irradiation induced volume swelling is also considered, and results, like the thermal expansion, in an additional strain. Finally, the contacts between the different elements of the subassembly (fuel pins, spacer wires and the hexcan) are also treated, as described later in this chapter.

4.3. Input data and boundary conditions

At the beginning of a simulation, DOMAJEUR2 loads, from a series of text input files, the time evolution of the spatial distribution of the following variables:

- The irradiation dose of the claddings and of the hexcan.

- The temperature of the claddings and of the hexcan.
- The internal pressure of the claddings, and the sodium pressure.

In the input files, the distributions of these variables are defined for a series of times within the irradiation period under consideration. Generally, these times do not match the time discretization of the thermomechanical simulation. Therefore, for each calculation time, DOMAJEUR2 computes their spatial distribution by linearly interpolating the spatial distributions given in the input files for the closest lower and larger times. For each calculation time, the values of the input variables at the nodes of the model—and, if needed, at the integration points—are also interpolated from the distribution defined in the input files. This process defines the so called *history* of the variable of interest (e.g. the cladding temperature history).

In the simulations presented in this work, unless otherwise specified, the fuel claddings and the hexcan were considered to be fixed at their base and free at their upper ends. By default, the material properties and behaviour laws of the 15-15Ti AIM1 steel and of the EM10 steel (see Section 2.2.3) are used for the claddings and spacer wires, and for the hexcan, respectively.

4.4. 3D and 1D finite element representation

Within DOMAJEUR2, several models with different levels of simplification are available to represent the fuel bundle and the hexcan. In this section, we describe the two employed in this work, namely the *detailed* 3D model and the *project* 1D model.

4.4.1. Detailed 3D model

The *detailed* model, relies on a volumetric finite element representation of the fuel pin claddings and the hexcan, whereas the spacer wires can be either represented by volumetric finite elements or by 1D beam elements. In this work, the latter option was retained after verifying an excellent agreement, in the strain and stress distributions, with simulations employing 3D elements to represent the wires. Brick and wedge elements[2] with quadratic basis functions are employed for the cladding and the hexcan. An example of the spatial discretization of a section of a 7-pin fuel bundle and of a hexcan are presented in Figure 4.1.

It can be noted in Figure 4.1 that, at each axial position, there are 13 finite elements (11 bricks and 2 wedges) in the circumference of each cladding and that

[2]These are prismatic elements that, when undeformed, have rectangular and triangular bases, respectively.

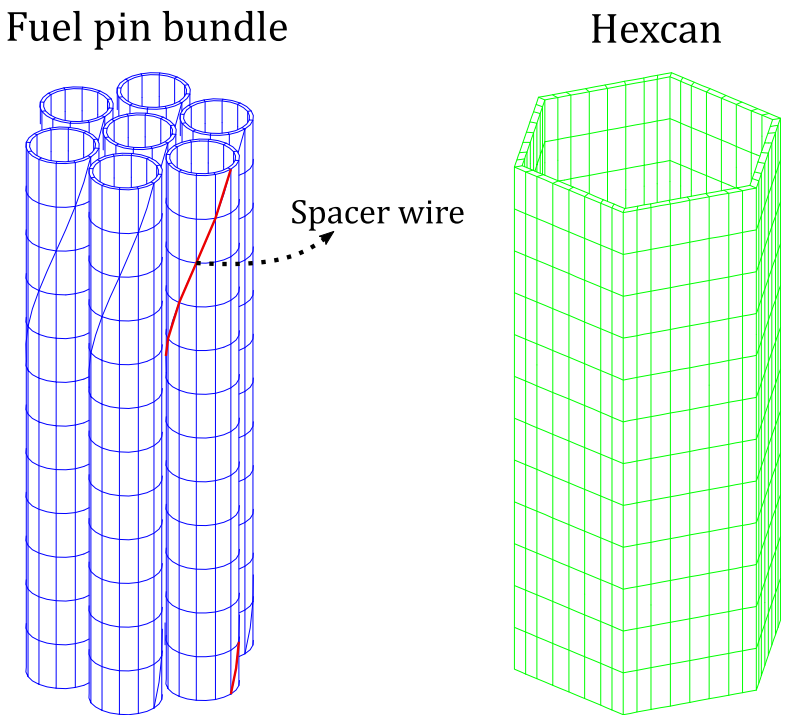

Figure 4.1.: 7-pin fuel bundle and hexcan representation with 3D volumetric finite elements. The spacer wires, one of which is highlighted in red, are represented with 1D beam elements.

there are 12 layers of elements in the length of the presented segment, which corresponds to the step of the helical path of the spacer wires. The choice of this discretization was motivated by preexisting CEA experience with the use of DOMAJEUR2 to simulate SFR subassemblies (Locatelli, Di Paola, Leturcq, et al. 2016), and it was verified by conducting preliminary mesh sensitivity studies based on the deflection and diametral strain profiles of the claddings, which, as described in Section 5.3.1, are the magnitudes on which the coupling with the STAR-CCM+ is based. It should be noted that only one element is used in the thickness of the cladding, so the radial gradients of the variables of interest will no be captured. This is done in order to limit the computational cost of the simulations conducted with this 3D model, and because the detailed analysis of the cladding stress and strain radial gradients—evaluated at the CEA with GERMINAL—is the not the goal of this work. The discretization of the hexcan, also defined based on CEA experience, was varied according to the size of the simulated fuel bundle, and between 2 and 6 elements were used per side. Given the very low deformation of the hexcan—and considering that its stress state is less relevant than that of the claddings when evaluating the mechanical integrity of the subassembly in nominal

conditions—, the problem is little sensitive to the choice of its spatial discretization.

Consequence of the fuel bundle deformation, adjacent fuel pins are susceptible of becoming in contact with each other and with the hexcan. In the 3D model of DOMAJEUR2, these potential contact points, depicted in Figure 4.2, are linked by elastic bar elements with almost null traction stiffness, and extremely high compression stiffness. Therefore, in the absence of contact, these bars have a negligible effect on the elements they link, but they rigidly connect them when contact occurs. The nonlinear viscoplastic nature of the crushing of the claddings in contact is therefore reproduced by the models of the volumetric finite elements employed to represent them, and not by the link bars. These models, or constitutive laws, consider the effects of thermal expansion, swelling (equations 2.24 to 2.28), irradiation creep (equations 2.32 to 2.33) and thermal creep, which is generally negligible in our simulations. The equivalent stress employed to evaluate the behaviour of the material is the von Mises stress, given by Equation 2.22.

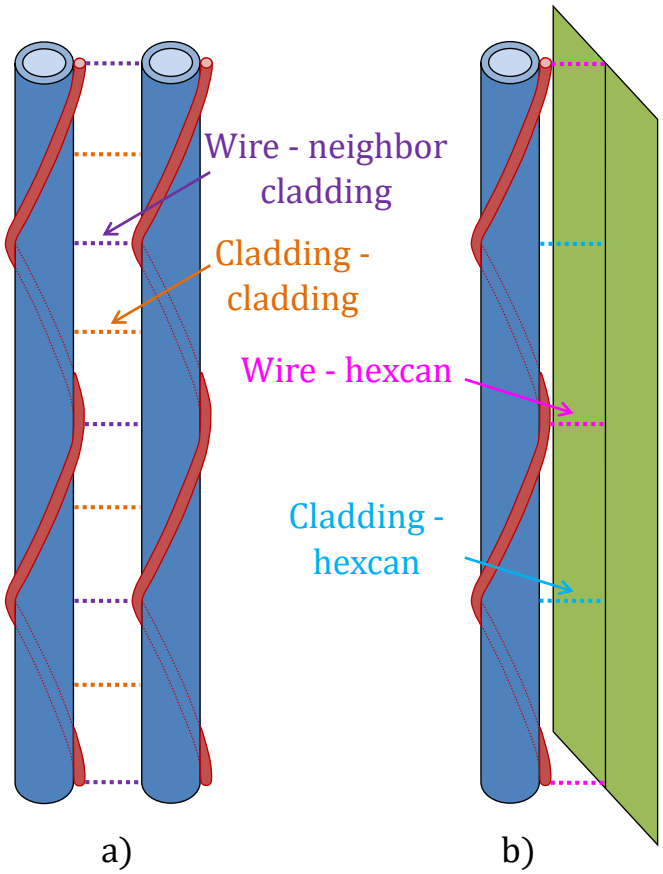

Figure 4.2.: Potential mechanical contacts between adjacent fuel pins (a) and between a fuel pin and the hexagonal can (b).

The thousands of potential contact points between fuel pins in a typical 217-pin SFR fuel bundle, and the current limitations on computational power, make the use of this 3D model extremely challenging for fuel bundles of more than 7 fuel pins. However, a simplified approach, referred to as *project* 1D model, is also available, and it can be employed for the simulation of a full-scale fuel subassembly comprising up to a few hundred fuel pins.

4.4.2. Project 1D model

In the 1D model, each fuel pin is represented by a series of 1D modified Euler-Bernoulli beam elements of annular cross section—pipe element with 1 node in the cross section—, which allow considering the effects of the internal fission gas pressurization, while shell elements are used for the hexcan. The resulting representations of a 217-pin bundle and of a hexcan are presented in Figure 4.3. As illustrated in this figure, 12 beam elements are employed per wire step length, which ensures that there is one node at each point where the contact with other pins is susceptible of occurring. Once again, this choice is based on preexisting CEA experience with the use of the 1D model of DOMAJEUR2 (Masoni 2016), and it was verified by performing a mesh sensitivity analysis based on the diametral strain and flexion of the fuel pins.

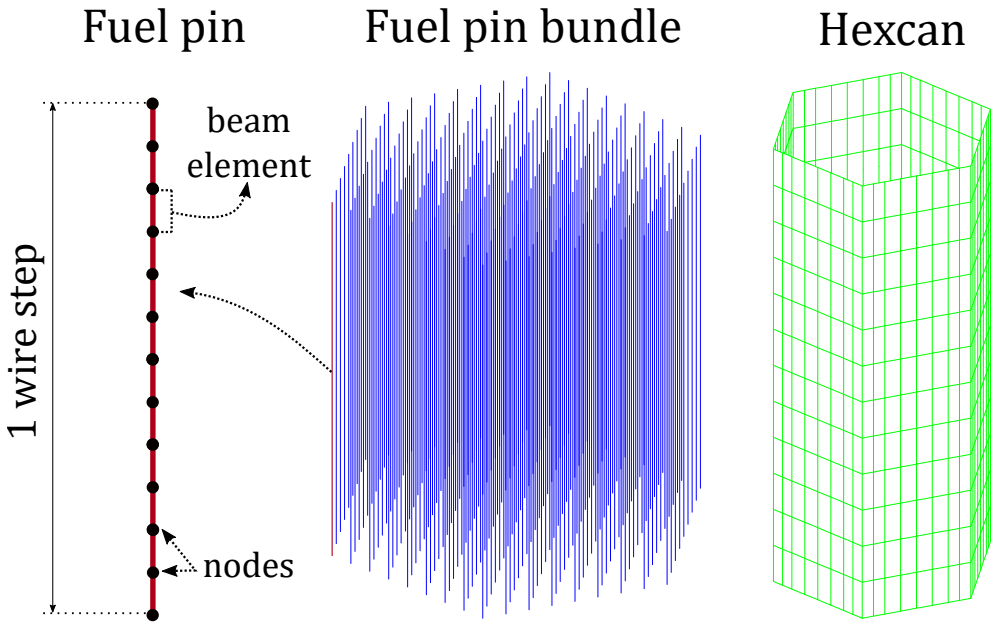

Figure 4.3.: 217-pin fuel bundle and hexcan representation with beam and shell elements, respectively. A detail of the 12 beam elements present in one wire step is shown.

In the 1D model, the increment of the fuel pin cladding external radius r_{ec} is an internal variable of the pipe elements employed to represent it, and it is calculated from the total cumulated strain in the tangential direction, $\varepsilon_{\theta\theta}$, according to:

$$\Delta r_{ec} = r_{ec}\varepsilon_{\theta\theta} \tag{4.5}$$

The different contributions to $\varepsilon_{\theta\theta}$ can be expressed as:

$$\varepsilon_{\theta\theta} = \varepsilon^{e}_{\theta\theta} + \varepsilon^{irr.creep}_{\theta\theta} + \varepsilon^{th.creep}_{\theta\theta} + \varepsilon^{swe} + \varepsilon^{th} \tag{4.6}$$

where the right hand side terms correspond, respectively, to the elastic strain, the irradiation and thermal creep strains, the swelling strain, and the thermal expansion. The cladding hoop stress induced by the internal pressure P is calculated according to the thick walled cylinder formalism (Timoshenko and Young 1956), and is given by:

$$\sigma_{\theta\theta} = \frac{2Pr^2_{ic}}{r^2_{ec} - r^2_{ic}} \tag{4.7}$$

where r_{ic} is the internal radius of the cladding. The radial stress—as discussed in Section 2.2.1.2, significantly lower than the hoop or the axial stresses in this case—is neglected here.

The stress in the axial direction, σ_{zz}, is calculated from the geometrical parameters of the pipe and the axial force it is subject to (mostly due to the internal pressure P acting on the end plugs of the fuel pin). Under these conditions, the elastic strain in the tangential direction is given by:

$$\varepsilon^{e}_{\theta\theta} = \frac{1+\nu}{E}\sigma_{\theta\theta} - \frac{\nu}{E}\left(\sigma_{\theta\theta} + \sigma_{zz}\right) \tag{4.8}$$

where ν is the Poisson coefficient and E the Young modulus of the material of the cladding. The total creep hoop strain is obtained by integrating the total creep hoop strain rate, given by:

$$\dot{\varepsilon}^{creep}_{\theta\theta} = \dot{\varepsilon}^{irr.creep}_{\theta\theta} + \dot{\varepsilon}^{th.creep}_{\theta\theta} = \frac{3}{2}\frac{\dot{\varepsilon}^{creep}_{eq}}{\sigma_{eq}}\left(\sigma_{\theta\theta} - \frac{\sigma_{\theta\theta} + \sigma_{zz}}{3}\right) \tag{4.9}$$

where $\dot{\varepsilon}^{creep}_{eq}$ is the equivalent creep strain rate, computed from the equivalent von Mises stress σ_{eq} using Equation 2.32[3]. The definition of the equivalent stress employed for the pipe elements is:

$$\sigma_{eq} = \sqrt{\sigma^2_1 + \sigma^2_4 + \sigma^2_5 + \sigma^2_6 + \sigma^2_P} \tag{4.10}$$

[3] As in the case of the 3D elements, the equivalent creep strain rate also includes the contribution of thermal creep, but it is negligible in nominal irradiation conditions, including the simulations conducted in our work.

where the contributing stresses are given in Table 4.1.

Stress	Expression for pipe element	Effort
σ_1	F_z/A	Traction
σ_4	$M_z r_{ec}/(I_y + I_x)$	Torsion
σ_5	$M_y r_{ec}/I_y$	Flexion
σ_6	$M_x r_{ec}/I_x$	Flexion
σ_P	$2Pr_{ic}^2/(r_{ec}^2 - r_{ic}^2)$	Pressure

Table 4.1.: Definition of the stresses involved in the calculation of the equivalent stress in the pipe elements. F_z is the axial force and A the cross section of the beam; M_z,M_y,M_x the bending moments with respect to the z (axial direction), x, and y axis; I_x and I_y the moments of inertia with respect to the x and y axis.

Finally, like in the 3D model, the swelling strain is computed using equations 2.24 to 2.28, and the thermal expansion is computed from the temperature T and the thermal expansion coefficient α of the material as[4]:

$$\varepsilon^{th} = \alpha(T - T_0) \tag{4.11}$$

with $T_0 = 293$ K.

It should be noted that, contrary to the 3D model in which a circumferential cladding temperature gradient can be represented, only one temperature value at each axial position is considered in the 1D model. As a consequence, the pin bowing due to differential thermal expansion cannot be represented. Additionally, the spacer wires are not explicitly represented so, in this model, the flexion of the fuel pins is only due to the contacts between them and with the hexcan. Preliminary simulations we conducted using the 3D model showed that the pin flexion induced by the tension of the wire and by the thermal gradients is minor when compared to the flexion induced by the contact between pins.

All potential contact points indicated in Figure 4.2 are linked by modified bar finite elements with an *ad hoc* model that allows estimating the stress and strain state of the internal surface of the cladding under the contact point, where the maximal tensile stress is most likely located (Leturcq, Minne, and Di Paola 2017). These elements aim to represent the 3D crushing of the cladding under contact forces, depicted in Figure 4.4a, by a 1D model, represented in Figure 4.4b, that considers, among other internal variables, the contact force and the internal

[4]The same expression is used in the 3D model.

pressure. To do so, for each time step of the thermomechanical simulation, the following main steps—described in detail in (Leturcq, Minne, and Di Paola 2017) and (Leturcq, Minne, and Di Paola 2016)—are followed in each iteration performed by the mechanical solver:

1. Compute the diametral strain of the cladding and of the spacer wire in the unrestrained condition. That is, without considering the contact with other pins or with the hexcan.

2. Compute the gap at the end of the time step—depending on the type of contact being modeled, this gap could be between a wire and a neighboring cladding, between a wire and the hexcan, between two claddings, or between a cladding and the hexcan—, which could be negative if contact occurs. This is a prediction phase.

3. If the gap is closed, compute the increment in the crushing of the cladding (δ), defined as the reduction of its diameter in the direction of contact.

4. Compute the increment in the strain tensor at the inner surface of the cladding, in the line of contact, based on:
   a) The crushing of the cladding.
   b) Strain concentration factors at the inner surface of the cladding, identified using detailed 3D elastic simulations of the crushing of a cladding[5] (see Figure 4.4a). The strain concentration factor is assumed to be the same in presence of creep. This is motivated by the observation that the irradiation creep is preponderant in normal irradiation conditions, and that its term linear on stress (see Equation 2.32) is strongly dominant.
   c) The increase of the internal diameter of the cladding, obtained without considering the contact.

5. Compute the stress tensor at the inner surface of the cladding by integration of its behaviour law, employing a thick shell formalism.

6. Compute the contact force in the bar element based on:
   a) The stress state computed in the internal surface of the cladding, stress (de)localisation factors obtained in the same detailed 3D simulation employed to obtain the strain concentration factors, and on the computed bending moments of the pipe element;
   b) The internal pressure of the cladding, which counters its ovalisation.

[5] The strain concentration factors previously identified using the fuel pin geometry of the advanced SFR designed at the CEA are used by default by DOMAJEUR2. If a different geometry is defined, DOMAJEUR2 conducts the required 3D crushing simulation once at the beginning of the thermomechanical simulation of the fuel bundle.

7. Update the internal variables at the end of the time step, including:
   a) For the sake of numerical stability, the use of a $C1$ function[6] to describe the contact force in the transition from open to closed gap. The same approach is employed for the crushing δ.
   b) The update of the ovalisation of the cladding taking into account its flexion and the contact force computed in the previous step.

Underlying hypothesis of the contact model of the modified bar elements include:

- The claddings and the spacer wires involved in the contact have the same material and geometrical properties. For example, when the contact between two claddings is represented, both are considered to be equally deformed.
- The temperature, the irradiation dose, and the internal pressure are uniform in the contact, so they take only one value in the bar element.
- The cladding flexion and ovalisation due to the tension of the spacer wire is neglected, as well as the tension itself.
- The fuel pellet does not interact with the cladding.

4.5. Summary

In this chapter, we described DOMAJEUR2, a finite element based code for the simulation of the thermomechanical evolution of SFR subassemblies under irradiation, developed at the CEA and employed in this work. The main input data required by DOMAJEUR2 to simulate the irradiation of a subassembly is the evolution of the temperature and irradiation dose distribution of its constituents, as well as the evolution of the pressure they are subject to. Two different finite element models available in DOMAJEUR2, namely a beam based 1D model and a fully 3D model, were described in this chapter. The 3D model has a significantly higher associated computational cost, which limits its practical use to small bundles of about 7 fuel pins. However, it is the only model that can capture the gradients of the variables of interest in the circumference of the claddings. Both models employ the same empirical laws to compute the swelling and irradiation creep strains, although the stresses are computed differently. Finally, we described the technique used by both models to treat the contacts between pins and between the pins and the hexcan, based on the use of contact finite elements.

[6] $C1$ functions are differentiable functions whose derivative is continuous.

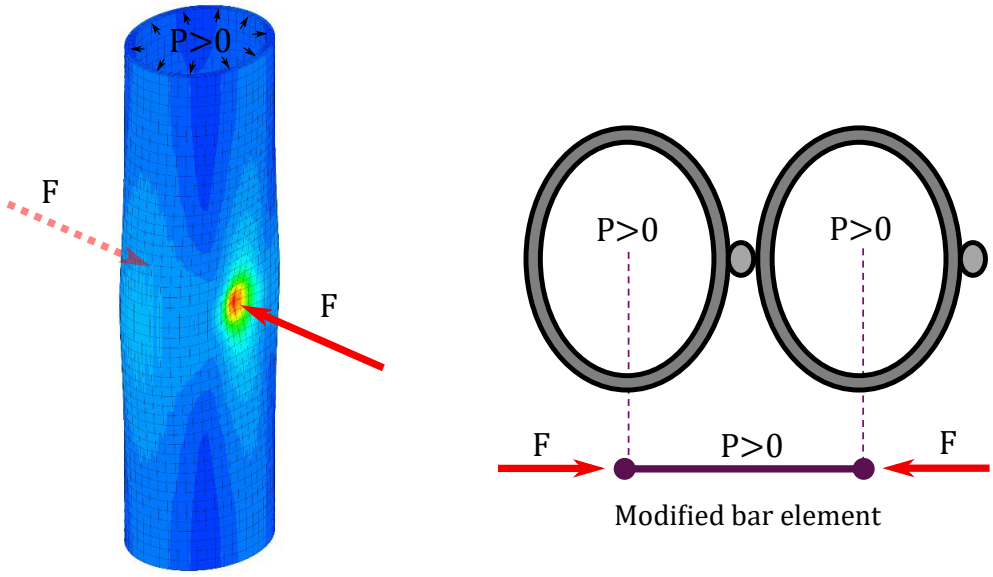

Figure 4.4.: a) 3D simulation of the crushing of a fuel cladding under contact forces of magnitude F and an internal pressure P. b) Scheme of the modified bar element, linking the neutral axis of the pipe elements that represent the claddings, employed to simulate the crushing of the cladding.

5. Coupling Methodology

This chapter is dedicated to the methodology developed in this work for the coupled thermal-hydraulic/thermomechanical simulation of SFR fuel bundles under irradiation. The few preexisting coupled simulation approaches are discussed in Section 5.1, and the new approach proposed in this work is introduced in Section 5.2.

A fundamental stage of this methodology requires conducting CFD simulations in deformed fuel bundles, which involves the generation of their CAD representation, the definition of deformation dependent boundary conditions, and the post-processing of the CFD simulations. These subjects are discussed in Section 5.3, where a brief description of the measures taken to increase the robustness of the coupled simulation methodology is also given.

A second key step involves conducting the thermomechanical simulation of the irradiation of the studied fuel bundle, for which boundary conditions based on the results of the aforementioned CFD simulations need to be defined. This step is addressed in Section 5.4, where the automatic post-processing of the thermomechanical simulations is also described.

Table of Contents

5.1. Preexisting coupled approaches

Early efforts to consider the coupling between the deformation of the fuel bundles of fast reactors and their thermal-hydraulics were presented by (Ohmae, Morino, Nakao, et al. 1972), by (Sakai, Okubo, and Hishida 1978) and by (Miki 1979). In these works, the equilibrium of the bundle deformation and its temperature distribution is evaluated employing low resolution lumped parameters thermal-hydraulic codes that, despite being the state-of-the-art at the time, as discussed in Section 3.1.1, perform poorly when compared to currently available CFD techniques (Fanning, W. D. Pointer, and Thomas 2009), especially in significantly deformed fuel bundles (Baglietto, Fricano, and Sosnovsky 2014). Furthermore, Ohmae and Sakai conduct the thermal hydraulic evaluations in some angular sectors of the bundle only, even though the bundle does not exhibit such a symmetry. Additionally, the methodology developed by the Ohmae is applicable only to bundles with spacer grids instead of spacer wires, which makes the treatment of the mechanical contacts more straightforward. In all cases, simplified models to compute the bundle deformation and its effects on thermal-hydraulics were employed. For example, Sakai only considers the effects of pin flexion, and Miki employs an analytical method that ignores the effects of irradiation creep. Besides, Ohmae and Miki compute only the static equilibrium between strains and thermal-hydraulics for one given instant. Sakai considers the temporal progression of the irradiation but, like the others, computes the swelling induced strains as instantaneous magnitudes depending only on the last computed temperature. However, as discussed in Section 2.2.2, they actually depend on the time evolution of the temperature during the irradiation, since the deformation rate is temperature dependent.

A more comprehensive approach has been recently presented by (Uwaba, Hiroyuki Ohshima, and M. Ito 2017), in which a bundle-thermomechanics code, BAMBOO (Uwaba, M. Ito, Ukai, et al. 2005; Uwaba and K. Tanaka 2017) is coupled with a thermal-hydraulic subchannel code, ASFRE (Kikuchi, Hiroyuki Ohshima, M. Tanaka, et al. 2016), following the OS paradigm. In that work, a more sophisticated beam-based finite element representation of the fuel bundle is employed to simulate its deformation as a consequence of thermal expansion, swelling, creep, and the mechanical contacts between fuel pins and between the pins and the hexcan. Besides, as opposed to the aforementioned couplings, the total cumulated irradiation induced strains are computed based on the time integration

of the instantaneous strain rates. However, as in the approaches mentioned above, a low resolution thermal-hydraulic code was employed, which relies on empirical correlations to compute the cross flow between the different subchannels and, as stated before, is outperformed by more modern CFD techniques. Additionally, the impact of the deformation of the bundle on the coolant mass flow rate has been ignored, which is also the case in the previously mentioned approaches even though Uwaba, Miki and Ohmae acknowledge its existence (Uwaba, Hiroyuki Ohshima, and M. Ito 2017; Miki 1979; Ohmae, Morino, Nakao, et al. 1972). Indeed, the bundle deformation increases its hydraulic resistance which leads to a coolant redistribution within the core, since less deformed subassemblies represent a preferential coolant flow channel. As a consequence, the mass flow rate of the deformed subassembly can be significantly reduced with respect to a non-deformed one, which has already been observed experimentally (Pol and Bourdot 1978, Pol and Bourdot 1979).

Finally, some of the results presented in the aforementioned publications are contradictory. For example, while Miki, Sakai and Ohmae predict an increase in the coolant temperature at the outlet of a deformed fuel bundle, the opposite is predicted by Uwaba; in this case, the coolant flow redistribution in the deformed bundle—while keeping the total coolant mass flow rate constant—is such that the temperature at its central region decreases with deformation, while the temperature at the periphery increases. In addition, Miki finds that changing the step of the spacer wires has almost no effect on the deformation of the fuel pins and on the thermal-hydraulics of the deformed bundle while, once again, the contrary is found by Uwaba. These inconsistencies indicate that the complexity of the problem is such that it is very difficult to draw general conclusions on the bundle behaviour, independent from the specific geometry of the bundle and the boundary conditions that apply. However, besides the complexity of the problem, the use of very simplified models, specially for the calculation of the coolant flow and temperature distribution, certainly contributes to the observed discrepancies. Indeed, as discussed in Section 3.1.1, the choice of the mixing coefficients and pressure drop correlations employed in subchannel codes greatly affects the results of the simulations conducted with them, and the prediction of the coolant temperature in the periphery of the bundle tends to be poor, even in non-deformed geometries. Predicting the flow redistribution in a deformed bundle using this approach is therefore very challenging.

Motivated by this, and as discussed in sections 1.4 and 3.1, in this work we have developed a methodology based on the coupling between a RANS approach implemented in STAR-CCM+, described in Section 3.3, and a finite element based thermomechanical simulation tool, DOMAJEUR2, described in Chapter 4. This methodology is described next.

5.2. Developed coupling methodology

For a simulation with DOMAJEUR2, the temperature history $T(\mathbf{r}, t)$ of the different components of the subassembly—that is, the time evolution, during the irradiation, of their spatial temperature distribution—must be specified. Traditionally, the temperature distribution corresponding to the non-deformed fuel bundle would be used for the whole irradiation period under consideration. In reality, as the irradiation proceeds, the bundle deformation affects the temperature distribution, generally inducing a gradual overall increase. This temperature increase, in turn, has a feedback effect on the deformation that is caused by the swelling and creep of the materials, which are temperature dependent phenomena.

To take this coupling into account, we consider the OS technique, which constitutes the main multi-physics paradigm in reactor analysis and is based on the input-output exchange between mono-disciplinary codes (Keyes, McInnes, Woodward, et al. 2013; Mahadevan, Elia Merzari, Tautges, et al. 2014), in this case DOMAJEUR2 and STAR-CCM+. This technique allows to profit from the advanced modelling capabilities of these codes and does not require their modification, which would compromise preexisting validation efforts.

5.2.1. Basis of the coupling methodology

Applying the traditional explicit OS technique would imply recalculating the temperature field in the deformed geometry obtained at each time step of the thermomechanical simulation, and, then, using this field to calculate the deformation within the next time step. In this case, illustrated in Figure 5.1a, iterations are not performed within each step of the thermomechanical simulation (TM in this figure, where TH represents a CFD simulation), so the nonlinearities due to the coupling between the two physics are not resolved within the step—i.e. the temperature and the deformation fields are not converged within the step—, which is why this approach is called loose OS coupling. Given its slow evolution, one could consider a larger time step for updating the temperature distribution than the one employed in the thermomechanical simulation but, since the temperature would be constant within each of these larger time steps[1], they would still need to be small enough to capture the temperature time evolution during the irradiation.

Alternatively, a nonlinear iterative scheme could be applied within each time step to converge the evolution of temperature and of deformation within it, in a so called tight or strong OS coupling, as in the example illustrated in Figure

[1]Note that, in this approach, no information about the temperature at the end of a time step is available at the start of that time step, which is why it is considered to be constant within the time step.

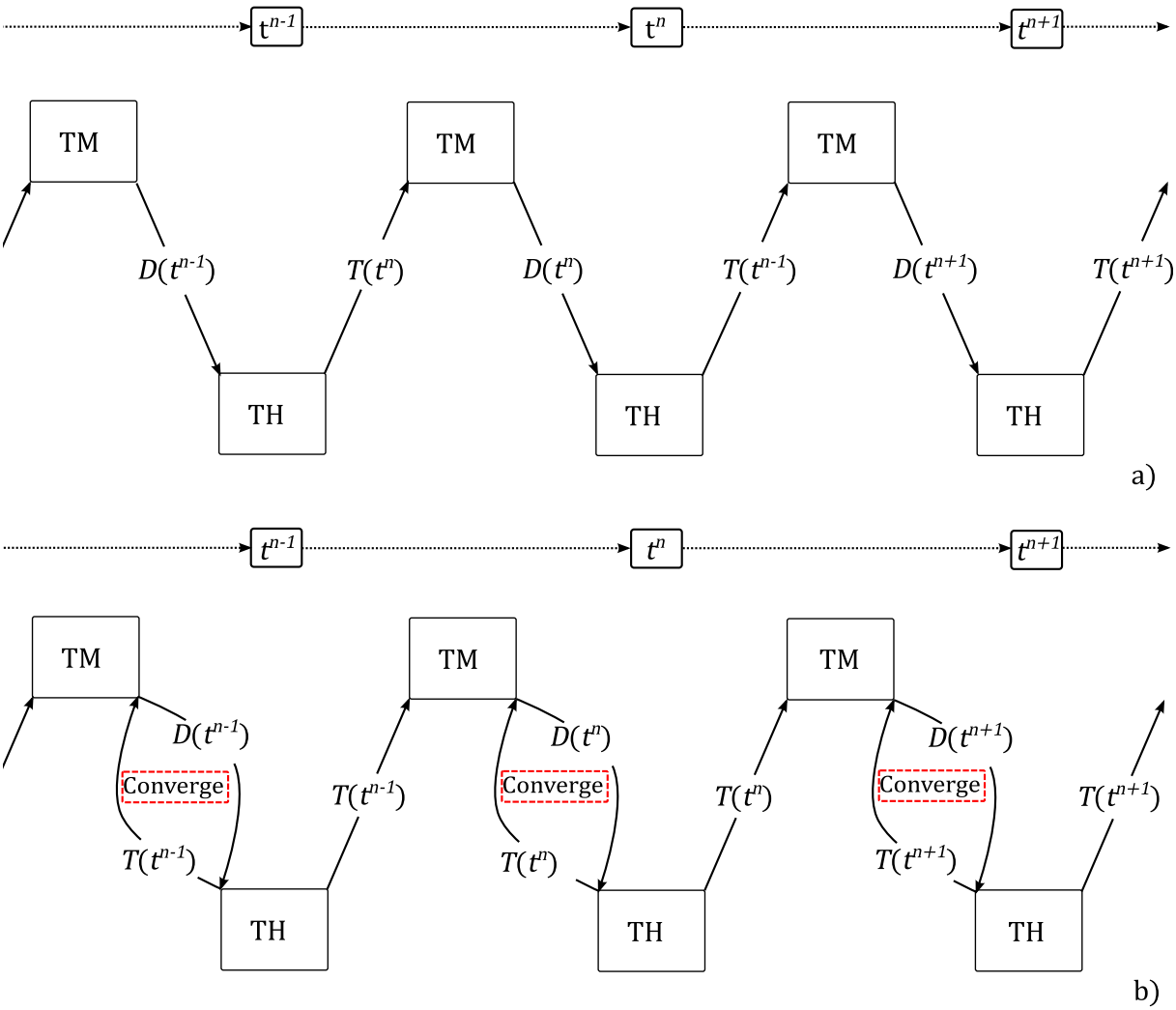

Figure 5.1.: a) Scheme of the algorithm of a non-iterative explicit OS coupling. **TM** represents one time step of the thermomechanical simulation, which computes the deformation distribution D at the end of the step. Each thermal-hydraulic simulation, which yields the temperature distribution T, is denoted by **TH**. The dependence of the position **r** of these distributions is here dropped for simplicity. b) Scheme of the algorithm of an OS coupling in which the deformation computed at the end of a given time step and the temperature distribution obtained in a geometry characterized by that deformation are converged by performing iterations.

5.1b. Note that, in this scheme, the thermomechanical simulation within each time step considers both the temperature at its beginning and at its end, unlike the non-iterative scheme in which the temperature within the step is constant and equal to the temperature at its beginning. One of the preferred techniques to implement such an iterative scheme is the Picard iteration, which favours the OS implementation since it does not require the modification of the mono-physics solvers (Mahadevan, Elia Merzari, Tautges, et al. 2014). In this case, as we will see in Section 5.2.2, the iterative procedure within each time step can be written in terms of an operator Φ as follows:

$$\mathbf{y}^{k+1} = \Phi(\mathbf{y}^k) \tag{5.1}$$

where $\mathbf{y}^k$ is the solution vector obtained in the k^{th} iteration. This procedure converges to the fixed point solution $\mathbf{y}^* = \Phi(\mathbf{y}^*)$ provided that the operator Φ is a contractor, that is:

$$\frac{\|\Phi(\mathbf{x}) - \Phi(\mathbf{y})\|}{\|\mathbf{x} - \mathbf{y}\|} \leq \gamma \tag{5.2}$$

with $\gamma \in (0, 1)$, $\forall(\mathbf{x}, \mathbf{y}) \in \mathbb{S}$, where $\mathbb{S}$ is a closed set containing $\mathbf{y}^*$. Under these conditions, the iterative process converges independently of the choice of the initial iterate $\mathbf{y}^0 \in \mathbb{S}$ (Kelley 1995).

However, performing one CFD calculation per time step of the thermomechanical simulation—or more than one if Picard iterations within the time step are considered—can lead to prohibitively high computational costs that, additionally, are not justified if, for example, the deformation within the time step is not high enough to induce a significant perturbation on the temperature field, which is indeed the case at least until the swelling incubation dose is exceeded. Preliminary simulations we conducted (Acosta 2017) indicated that considering the coupling between thermomechanics and thermal-hydraulics had a significant impact on the EOL deformation of the bundle. However, the magnitude of this impact was not found to be too dependent on the precise temperature time evolution, but rather depended on the temperature level towards the end of the irradiation, which—as discussed in Section 6.8—determines the deformation rate during the period of significant deformation.

For these reasons[2], an alternative approach has been adopted in this work, with the goal of studying the coupling effects and of obtaining an estimation of the impact of the coupling on the behavior of the bundle, while limiting the associated computational cost. This approach is based on prescribing a fuel cladding temperature history, employed for the thermomechanical simulation of

[2]Additionally, as of the start of this work, DOMAJEUR2 did not yet have the capability of updating, between successive time steps, the temperature history that, instead, is loaded from an input file at the beginning of the simulation.

the irradiation, given by:

$$\tilde{T}(\mathbf{r}, t) = f(\{T(\mathbf{r}, t^i) : t^i \in \mathbb{K}\}, t) \tag{5.3}$$

where f denotes an interpolation function, and $\{T(\mathbf{r}, t^i) : t^i \in \mathbb{K}\}$ the set of temperature distributions $T(\mathbf{r}, t_i)$, obtained with CFD simulations in deformed geometries computed by DOMAJEUR2 at the calculation times t^i in the set $\mathbb{K}$, itself a subset of the set $\mathbb{T}$ of all the calculation times. The temperature history $\tilde{T}(\mathbf{r}, t)$ thus defined is employed as input for the thermomechanical simulation of the entire irradiation period under consideration, which constitutes a global iteration, and it is repeated until convergence of the deformation field at EOL. In each global iteration, $\tilde{T}(\mathbf{r}, t)$ is modified considering the last computed bundle deformation history[3].

A scheme of the resulting algorithm is presented in Figure 5.2, where $D(t^i)$ and $T(t^i)$ represent the deformation and temperature distributions computed at a time t^i, and the dependence on $\mathbf{r}$ was dropped for simplicity. The superscript k refers to the value of a variable computed in the k^{th} global iteration. We will see, in Section 5.2.2, that the choice of $\mathbb{K}$—i.e. the choice of the calculation times for which CFD simulations are conducted and then interpolated to compute the temperature history—allows to approximate the reference solution given by the algorithm presented in Figure 5.1b, which iterates until convergence within each step of the thermomechanical simulation, as much as one desires. However, the main idea behind the developed methodology is to keep the number of elements of $\mathbb{K}$ as low as possible, while still being able to correctly represent the physics of the problem.

To illustrate the developed methodology, we firstly consider the case in which only the temperature distribution obtained in the non-deformed bundle at $t = 1$ FPD $= t_{BOL}$, $T(\mathbf{r}, t_{BOL})$, and the distribution obtained in the fully deformed bundle at the end of the irradiation, $T(\mathbf{r}, t_{EOL})$, are used for the temperature interpolation, such that $\mathbb{K} = \{t_{BOL}, t_{EOL}\}$ and $\tilde{T}(\mathbf{r}, t) = f(\{T(\mathbf{r}, t_{BOL}), T(\mathbf{r}, t_{EOL})\}, t)$. The coupled simulation can be divided into one initialization stage, represented schematically for given point in the fuel bundle in Figure 5.3, and an iterative stage, similarly illustrated in Figure 5.4.

In the initialization stage, a CFD calculation is carried over in the non-deformed geometry, and only the temperature distribution $T(\mathbf{r}, t_{BOL})$ thus obtained[4]—called

[3]Note that the impact of the deformation on the hexcan temperature is not considered here, so the coupling implemented is based on the modification of the cladding temperature history $\tilde{T}(\mathbf{r}, t)$ according to the deformation level of the bundle. As discussed in sections 2.2.5 and 2.4, the deformation of the hexcan is very low compared to the deformation of the fuel bundle, and it is not expected to have a significant impact on thermal-hydraulics. The coupling feedbacks on this very low deformation are thus neglected.

[4]It should be noted that, at t_{BOL}, the deformation is not strictly null, due to thermal expansion.

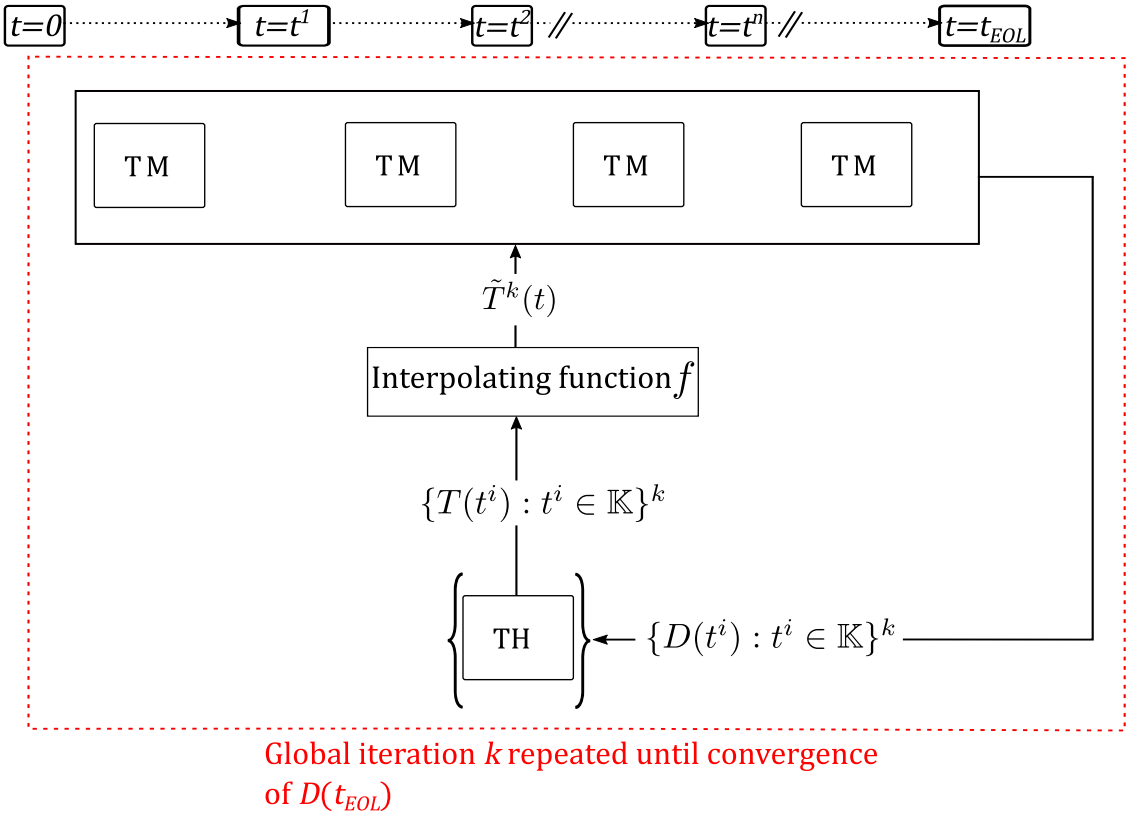

Figure 5.2.: Scheme of the algorithm of the OS coupling developed in this work, in which the thermomechanical simulation of the entire irradiation period is conducted in each global iteration, using as input a prescribed temperature history $\tilde{T}^k(t)$ which is updated in each iteration.

nominal temperature distribution—is used to construct a first temperature history, since at this point of the simulation $T(\mathbf{r}, t_{EOL})$ is not yet known. In this history, the temperature distribution is considered to remain constant, and equal to $T(\mathbf{r}, t_{BOL})$, after 1 FPD of heating up from an isothermal state, denoted by T_{cold}. The initialization stage ends when the temperature history thus defined is used as input for a first thermomechanical simulation of the irradiation period under consideration. This stage is equivalent to the traditional practice for the non-coupled subassembly simulations, and provides a first estimation of the strain and stress states of the fuel bundle at the end of the irradiation, referred to as nominal deformation or stress state.

However, considering the very low feedback it has on the bundle deformation and to avoid an additional CFD simulation that would be required to take it into account, it is here neglected. At EOL, however, thermal expansion is considered, as to improve the accuracy of the $T(\mathbf{r}, t_{EOL})$, employed to verify SFR design criteria.

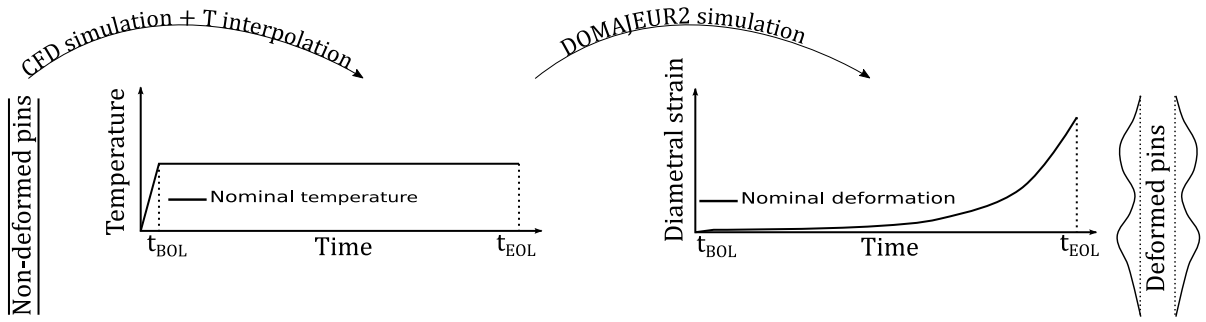

Figure 5.3.: Schematic representation of the initialization stage of the coupled simulation, which corresponds to the traditional practice for simulating SFR fuel subassemblies. The temperature time evolution corresponds to a given point within the fuel bundle, and the diametral deformation of the cladding at that point is used to represent the evolution of the geometry of the bundle. A reactor heating up phase between $t = 0$ and $t = t_{BOL}$ is represented.

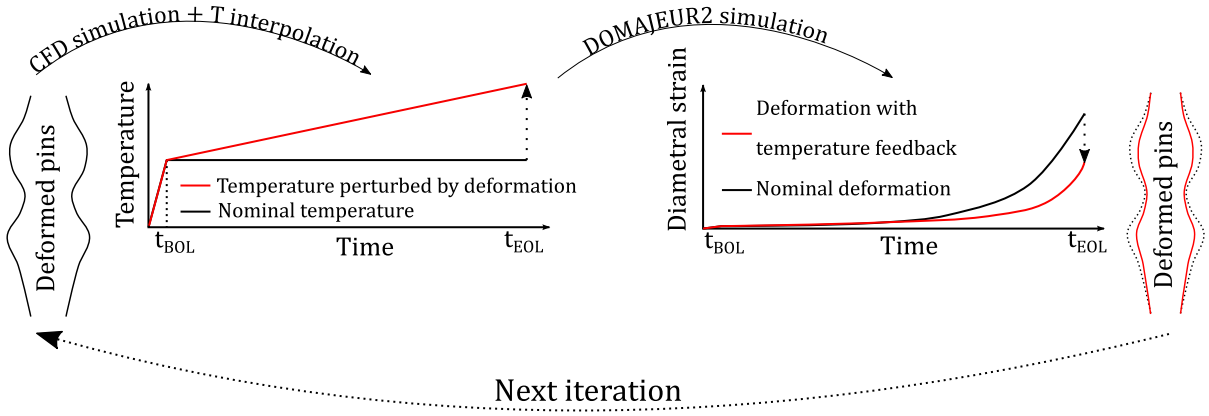

Figure 5.4.: Schematic representation of the iterative stage of the coupled simulation. The trends observed for the temperature and deformation distributions in the coupled calculations are represented in red, and correspond to a given point within the fuel bundle. In this example, a linear temperature evolution between BOL and EOL is considered after the initial heating up phase.

The second, iterative stage starts with an EOL deformed geometry previously obtained. A CFD simulation is carried over in this deformed geometry, and the resulting temperature field $T^k(\mathbf{r}, t_{EOL})$, where k indicates the iteration number, is employed to construct a new temperature history $\tilde{T}^k(\mathbf{r}, t)$ that is used next as input for a new thermomechanical simulation. In the example presented in Figure 5.4, $\tilde{T}^k(\mathbf{r}, t)$ is computed by considering a uniform temperature T_{cold} at $t = 0$, the nominal temperature distribution $T(\mathbf{r}, t_{BOL})$ at $t = 1$ FPD $= t_{BOL}$, the distribution in the fully deformed bundle $T^k(\mathbf{r}, t_{EOL})$ at the end of the irradiation, and by linearly interpolating the temperature distribution between those times[5]. This gives:

$$\tilde{T}^k(\mathbf{r}, t) = \begin{cases} T_{cold} + \frac{t}{t_{BOL}}(T(\mathbf{r}, t_{BOL}) - T_{cold}), & \text{for } 0 \leq t \leq t_{BOL} \\ T(\mathbf{r}, t_{BOL}) + \frac{(t - t_{BOL})}{t_{EOL} - t_{BOL}}(T^k(\mathbf{r}, t_{EOL}) - T(\mathbf{r}, t_{BOL})), & \text{for } t_{BOL} \leq t \leq t_{EOL} \end{cases} \tag{5.4}$$

Evidently, the modified temperature history used for the new thermomechanical calculation might lead to a different EOL deformation level, so the second stage is repeated iteratively until two successive iterations yield the same deformed geometry, within a specified tolerance. Even though the impact of the coupling is dependent on the operational conditions of the subassembly, the generally observed tendency is indicated in Figure 5.4 with red lines. Namely, a temperature increase in the deformed geometries that leads to a reduction of the bundle deformation, explained by the temperature dependence of creep and swelling discussed in Section 2.2.2.2. In all cases evaluated in this work, only a few iterations were needed for reaching convergence (< 5), as illustrated by the example discussed in Section 6.5.

To summarize, the traditional OS technique of updating the temperature distribution at regular time intervals during the thermomechanical simulation—for every one of which at least one CFD simulation in a partially deformed bundle would be required—is here replaced by prescribing the time evolution of the temperature distribution. This temperature history is given as input to DOMAJEUR2 at the beginning of the thermomechanical simulation, which is iteratively repeated until convergence. At each iteration, the temperature history is modified to take into account the evolution of the bundle deformation computed in the previous iteration.

This means that the thermomechanical simulation of the entire irradiation is repeated with each iteration (therefore called global iteration here), as opposed

[5] This implies that the variation in subassembly power, which is a consequence of its burn-up and affects the temperature distribution, is not considered in this case. We will see in Section 5.4.1 that a slightly different treatment is done when the variation of power is taken into account.

to only simulating the irradiation over one time step, updating the temperature distribution, and continuing with the next step. The latter approach would require more CFD computations, but the thermomechanical simulation could be conducted only once, if iterations within each time step are not done.

As explained before, other than reducing the number of CFD simulations required, the main motivation for adopting the global iteration strategy is based on preliminary assessments of the sensitivity of the final state of the bundle to the accurate representation of the evolution of temperature, especially early within the irradiation. However, considering the computational cost of each simulation further encourages the adoption of the approach that iterates over the whole irradiation. Indeed, to simulate a 217-pin fuel bundle, less than 5 hours were required to run the thermomechanical simulation, while meshing and running a CFD simulation required, with the same computer, up to two days. Considering that the thermomechanical simulation of the irradiation of a subassembly is divided into ~ 100 time steps, a first estimation of the total computational time of a coupled simulation yields 200 days for the explicit, non-iterative coupling illustrated in Figure 5.1a, and 9 days with the methodology here developed.

5.2.2. Algorithm

Evidently, a defining choice in this methodology is the temperature interpolating function f. We firstly consider the limiting case in which $\mathbb{K} = \mathbb{T}$ and the interpolation is linear, which means that $\tilde{T}(\mathbf{r}, t)$ is computed by linearly interpolating the temperature distributions obtained with CFD simulations in every deformed geometry computed by DOMAJEUR2. The resulting algorithm is presented in Figure 5.5.

In this case, we can show that iterating until convergence within each time step Δt of the thermomechanical simulation and then proceeding to the next time step (Method A, reference algorithm illustrated in Figure 5.1b) leads to the same result than iterating over the whole irradiation period (Method B, a particular case of the methodology developed in this work and illustrated in Figure 5.5). Here, the reference Method A is assumed to converge, and the goal of the following paragraphs is therefore to show its equivalence to Method B, and not to prove the convergence of the latter. The convergence of the coupled simulations conducted in this work is discussed in Section 6.4.

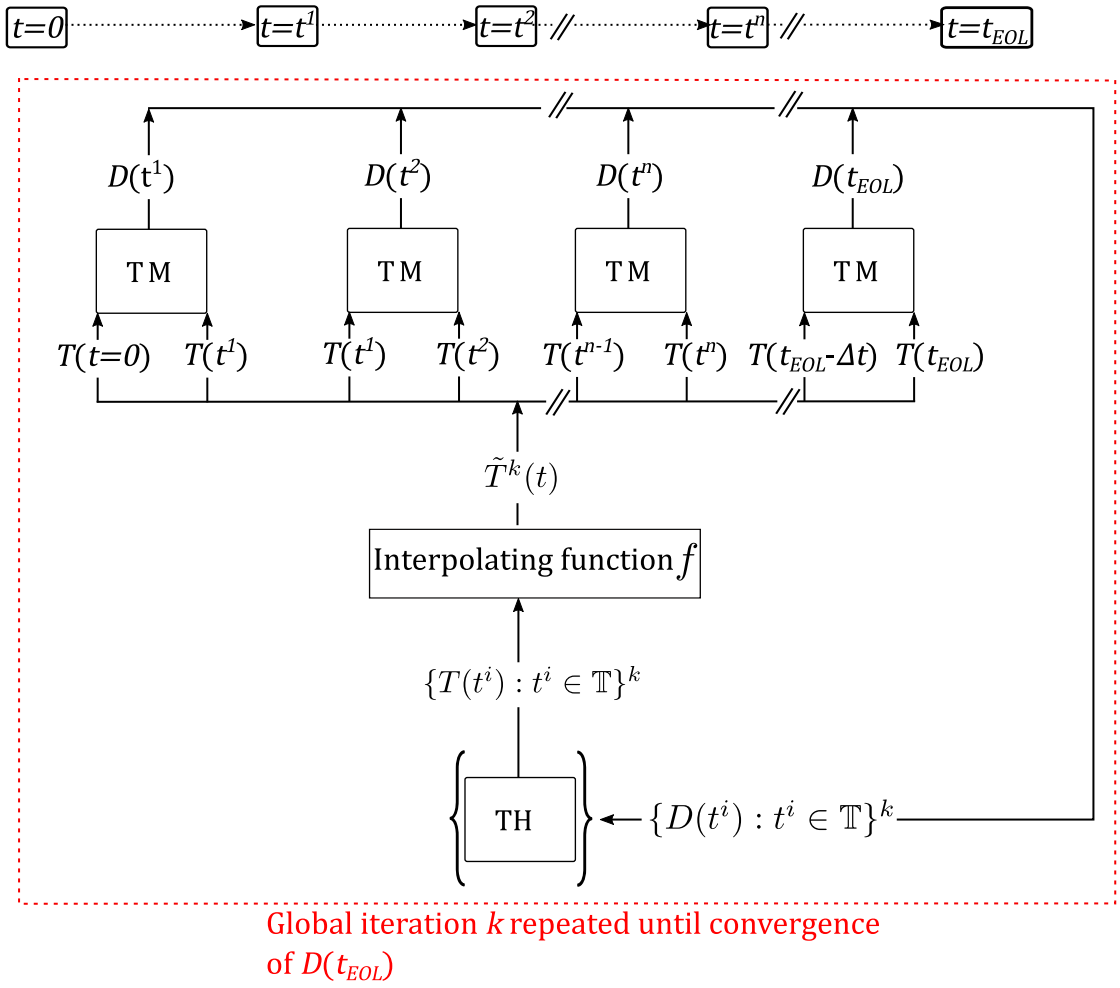

Figure 5.5.: Scheme of the algorithm of the OS coupling developed in this work, for the particular case of $\mathbb{K} = \mathbb{T}$. In this case, every temperature distribution $T(t^i)$ is obtained with a CFD simulation in the geometry characterized by the deformation $D(t^i)$. The dependence on $\mathbf{r}$ of these distributions is here dropped for simplicity.

Equivalence between global and local iterative methods

To show this equivalence, in what follows, we evaluate a time step of the thermomechanical simulation from a time $t = t^i$ up to a time $t = t^i + \Delta t = t^{i+1}$, where the temporal discretization for the thermomechanical simulation is assumed to be the same in both methods, as well as all the loadings other than temperature[6]. We represent the thermomechanical simulation within this time step with an operator Φ, such that:

$$D(\mathbf{r}, t^i + \Delta t) = \Phi(D(\mathbf{r}, t^i), T(\mathbf{r}, t^i), T(\mathbf{r}, t^i + \Delta t)) \tag{5.5}$$

where $D(\mathbf{r}, t^i + \Delta t)$ is the deformation distribution at time $t = t^i + \Delta t$, which depends on the deformation and temperature at the beginning of the time step, $D(\mathbf{r}, t^i)$ and $T(\mathbf{r}, t^i)$, but also on the temperature distribution at its end, $T(\mathbf{r}, t^i + \Delta t)$. The dependence of $T(\mathbf{r}, t^i + \Delta t)$ arises from the need of integrating the constitutive laws within the time step, which depend on temperature. This integration is done by considering a linear temperature evolution between $t = t^i$ and $t = t^i + \Delta t$. Additionally, the CFD simulation in a geometry characterized by a deformation $D(\mathbf{r}, t^i)$ is represented by an operator Ψ, such that:

$$T(\mathbf{r}, t^i) = \Psi(D(\mathbf{r}, t^i)) \tag{5.6}$$

Employing these definitions, we can describe the iterative processes of Method A and of Method B as follows.

Method A: iterations within each time step of the thermomechanical simulation.

Step $t_i \rightarrow t_i + \Delta t$:

—— Initial Values:

$D_A(\mathbf{r}, t^i)$ and $T_A(\mathbf{r}, t^i)$

These distributions are obtained after the convergence of the iterative process in the previous time step, or, if the first time step is considered, they correspond to the initial deformation $D(\mathbf{r}, t = 0)$ and temperature $T(\mathbf{r}, t = 0)$.

—— First iteration:

[6] These loadings include the irradiation dose, the subassembly power distribution, the fission gas pressure, etc., and they are not explicitly considered here since they are inputs for the simulations conducted in our work, and they are not modified in the implementation of the coupling here developed.

$$D^1(\mathbf{r}, t^i + \Delta t) = \Phi(D_A(\mathbf{r}, t^i), T_A(\mathbf{r}, t^i), T_A(\mathbf{r}, t^i))$$
$$T^1(\mathbf{r}, t^i + \Delta t) = \Psi(D^1(\mathbf{r}, t^i + \Delta t))$$

Note that, in this first iteration, the temperature at the end of the time step is initially not know, so it is assumed to be the same as at the beginning of the step.

—— Iteration k, with $k > 1$:

$$D^k(\mathbf{r}, t^i + \Delta t) = \Phi(D_A(\mathbf{r}, t^i), T_A(\mathbf{r}, t^i), T^{k-1}(\mathbf{r}, t^i + \Delta t)) \tag{5.7}$$

$$T^k(\mathbf{r}, t^i + \Delta t) = \Psi(D^k(\mathbf{r}, t^i + \Delta t))$$

Finally, using Equation 5.6, Equation 5.7 can be re-written in terms of the deformation only:

$$D^k(\mathbf{r}, t^i + \Delta t) = \Phi(D_A(\mathbf{r}, t^i), \Psi(D_A(\mathbf{r}, t^i)), \Psi(D^{k-1}(\mathbf{r}, t^i + \Delta t))) \tag{5.8}$$

Method B: global iterations over the entire irradiation period.

Step $t^i \rightarrow t^i + \Delta t$:

—— Starting values:

$T^0(\mathbf{r}, t^i)$ and $D^0(\mathbf{r}, t^i)$

$T^0(\mathbf{r}, t^i)$ is the temperature distribution prescribed at the beginning of the considered time step (i.e. $\tilde{T}^0(\mathbf{r}, t^i)$), and it is independent of the preceding steps since no iterations were conducted before this point to take them into account. The deformation $D^0(\mathbf{r}, t^i)$ is computed in the previous time step of the thermomechanical simulation. Unlike the case of Method A, in which the deformation at the start of the time step is the converged value from the previous step, $D^0(\mathbf{r}, t^i)$ is here only a first guess. If the first time step is considered, $D^0(\mathbf{r}, t^i) = D(\mathbf{r}, t = 0)$ and $T^0(\mathbf{r}, t^i) = T(\mathbf{r}, t = 0)$.

In Method B, the thermomechanical simulation of the entire irradiation is done in each global iteration. For this reason, up to a given iteration $k = j$, both $D^k(\mathbf{r}, t^i)$ and $D^k(\mathbf{r}, t^i + \Delta t)$ are modified in each iteration. Considering

Equation 5.6, we can see that the same applies for $T^k(\mathbf{r}, t^i)$ and $T^k(\mathbf{r}, t^i + \Delta t)$. In other words, both the states at the start and at the end of the time step are evolving with each global iteration. At iteration $k = j$, the state at the start of the time step, $\{T^k(\mathbf{r}, t^i), D^k(\mathbf{r}, t^i)\}$ converges to $\{T_B(\mathbf{r}, t^i), D_B(\mathbf{r}, t^i)\}$. Note that, since the state at the end of the time step, $\{T^k(\mathbf{r}, t^i\Delta t), D^k(\mathbf{r}, t^i\Delta t)\}$, depends on the state at its beginning, the first cannot converge before the second. Considering this, we divide the iterative process in two, as follows:

—— Iteration k with $k \leq j$:

$$D^k(\mathbf{r}, t^i + \Delta t) = \Phi(D^{k-1}(\mathbf{r}, t^i), T^{k-1}(\mathbf{r}, t^i), T^{k-1}(\mathbf{r}, t^i + \Delta t))$$

$$T^k(\mathbf{r}, t^i + \Delta t) = \Psi(D^k(\mathbf{r}, t^i + \Delta t))$$

—— Iteration k with $k > j$:

$$D^k(\mathbf{r}, t^i + \Delta t) = \Phi(D_B(\mathbf{r}, t^i), T_B(\mathbf{r}, t^i), T^{k-1}(\mathbf{r}, t^i + \Delta t)) \tag{5.9}$$

$$T^k(\mathbf{r}, t^i + \Delta t) = \Psi(D^k(\mathbf{r}, t^i + \Delta t))$$

Here again, using Equation 5.6, Equation 5.9 can be re-written in terms of the deformation only:

$$D^k(\mathbf{r}, t^i + \Delta t) = \Phi(D_B(\mathbf{r}, t^i), \Psi(D_B(\mathbf{r}, t^i)), \Psi(D^{k-1}(\mathbf{r}, t^i + \Delta t))) \tag{5.10}$$

Comparing equations 5.8 and 5.10, we can see that both methods will converge to the same fixed point of the operator Φ if $D_A(\mathbf{r}, t^i) = D_B(\mathbf{r}, t^i)$, i.e. if the deformation at the beginning of the time step under consideration is the same in both cases. For the first time step, both methods start with the same $D(\mathbf{r}, t = 0) = D_A(\mathbf{r}, t = 0) = D_B(\mathbf{r}, t = 0)$[7], so both converge to the same $D(\mathbf{r}, t = \Delta t)$. Then, for the second

[7] The initial deformation distribution—as the initial temperature distribution—is part of the initial conditions of the coupled simulation, assumed to be the same for both methods. In practice, the initial deformation is always null, since the starting point of the simulation is the nominal, non-deformed bundle geometry.

time step $\Delta t \to 2\Delta t$, we have $D_A(\mathbf{r}, t = \Delta t) = D_B(\mathbf{r}, t = \Delta t) = D(\mathbf{r}, t = \Delta t)$ and therefore both methods converge to the same $D(\mathbf{r}, t = 2\Delta t)$. The same reasoning can be applied sequentially to all time steps to conclude that both methods converge to the same $D(\mathbf{r}, t_i)$ $\forall t_i \in \mathbb{T}$.

Reducing the computational cost of the simulations

From the discussion of the previous section, it should be clear that setting $\mathbb{K} = \mathbb{T}$ to obtain the temperature history $\tilde{T}(\mathbf{r}, t)$ is practically non feasible due to the very high computational cost associated with performing one CFD simulation in the deformed geometry computed at every step of the thermomechanical simulation, per global iteration. The idea behind the methodology developed in this work is therefore to use a reasonable approximation of $T(\mathbf{r}, t)$ while limiting the number of CFD simulations employed to obtain it. This approximation is detailed in Section 5.4.1, where we will see that the deformation at every time step of the thermomechanical simulation is taken into account in its definition. In this case, we can expand the definition of the interpolating function given by Equation 5.3 and write:

$$\tilde{T}(\mathbf{r}, t) = f(\{T(\mathbf{r}, t^i) : t^i \in \mathbb{K}\}, \{D(\mathbf{r}, t^i) : t^i \in \mathbb{T}\}, t) \tag{5.11}$$

When the deformation computed in a given iteration is used to define the temperature history $\tilde{T}(\mathbf{r}, t)$ to be used as input for the thermomechanical simulation of the next iteration, the resulting iterative algorithm can be represented as in Figure 5.6.

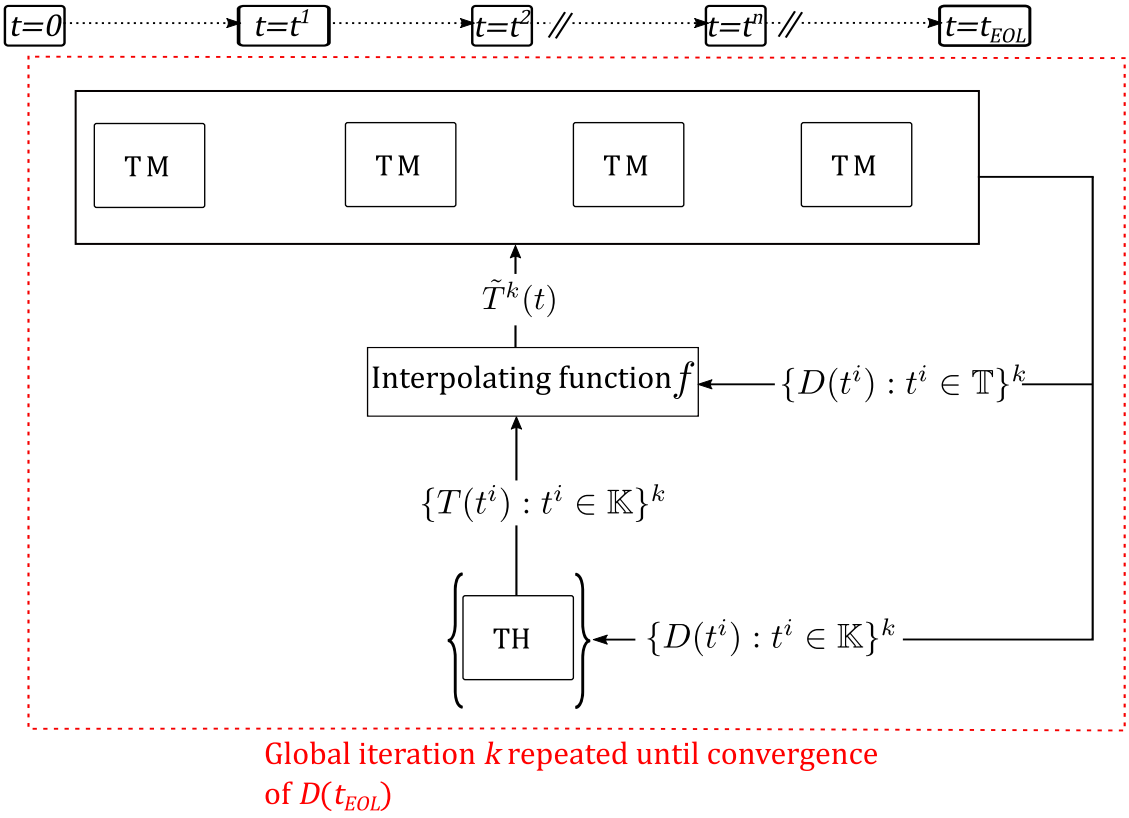

Figure 5.6.: Scheme of the algorithm of the OS coupling developed in this work, in the general case where the deformation computed at every time step of the last thermomechanical simulation is also used as input of the interpolation function f, used to compute the temperature history $\tilde{T}^k(\mathbf{r}, t)$ used as input for the next thermomechanical simulation.

5.2.3. Implementation

To implement the methodology outlined in the previous sections, an ad hoc numerical platform has been developed. Traditionally user intensive tasks been automated in this platform, including:

1. The preparation and execution of the required CFD simulations, described in Section 5.3. This includes the generation of the CAD representation of the fuel bundle, the prescription of boundary conditions that depend on the deformation, and the post-processing of the simulations.

2. The preparation and execution of the required DOMAJEUR2 simulations, described in Section 5.4, including the construction of the bundle temperature history $\tilde{T}(\mathbf{r}, t)$ based on the CFD results, as well as the post-processing of these simulations.

The main steps of the resulting iterative algorithm are schematically represented in Figure 5.7, where the initialization and the iterative stages described in Section 5.2.1 are indicated. These steps are summarized below.

At the beginning of a coupled simulation, the CAD model of the nominal bundle is generated from its non-deformed dimensions (IN1 in Figure 5.7), and it is used to conduct two CFD simulations; one with the BOL power distribution (IN2), and one with the EOL power distribution (IN3), affected by the burn-up of the subassembly. Then, these two simulations are post-processed (IN4), as detailed in Section 5.3.4, to obtain the fuel cladding temperature profiles needed to construct the temperature history used, later on, as input for a first thermomechanical simulation.

Since only the fluid domain is represented in the CFD simulations, only the temperature at the external surface of the claddings is readily available. However, the more representative cladding mid-thickness temperature is used as input by DOMAJEUR2. Then, this temperature is computed from the cladding surface temperature and the linear power profile by considering the heat conduction in the radial direction, as described in Section 5.3.4 (IN5). The resulting cladding temperature distribution is used to construct the nominal temperature history (IN6), as detailed in Section 5.4.1. Finally, this temperature history is used as input for a first DOMAJEUR2 (DMJ2) simulation of the subassembly irradiation (IN7).

The iterative stage of the simulation starts by post-processing the DOMAJEUR2 simulation (IT1), with a procedure described in Section 5.4.2. The computed deformation is employed to construct the CAD model of the deformed bundle (IT2), as detailed in Section 5.3.1.

The bundle deformation leads to a reduction of the coolant mass flow rate, and the model developed to take this into account (IT3) is described in Section 5.3.2. Additionally, the diametral strain of the claddings modifies their heat exchange surface. Then, the deformed geometry is taken into account to compute the surface heat flux profile employed as thermal boundary condition for the CFD simulations (IT4), as detailed in Section 5.3.3.

After generating the deformed CAD and computing the deformation dependent boundary conditions, a CFD simulation of the deformed fuel bundle is conducted (IT5) and afterwards post-processed (IT6), which includes the computation of the heat conduction in the thickness of the claddings (IT7). We will see in Section 5.4.1 that the temperature distributions computed in the deformed and non-deformed geometries—as well as, in some cases, the last computed evolution of the deformation of the bundle—are employed by the interpolating function f in order to compute a bundle temperature history (IT8), which is employed as input for a new thermomechanical simulation (IT9).

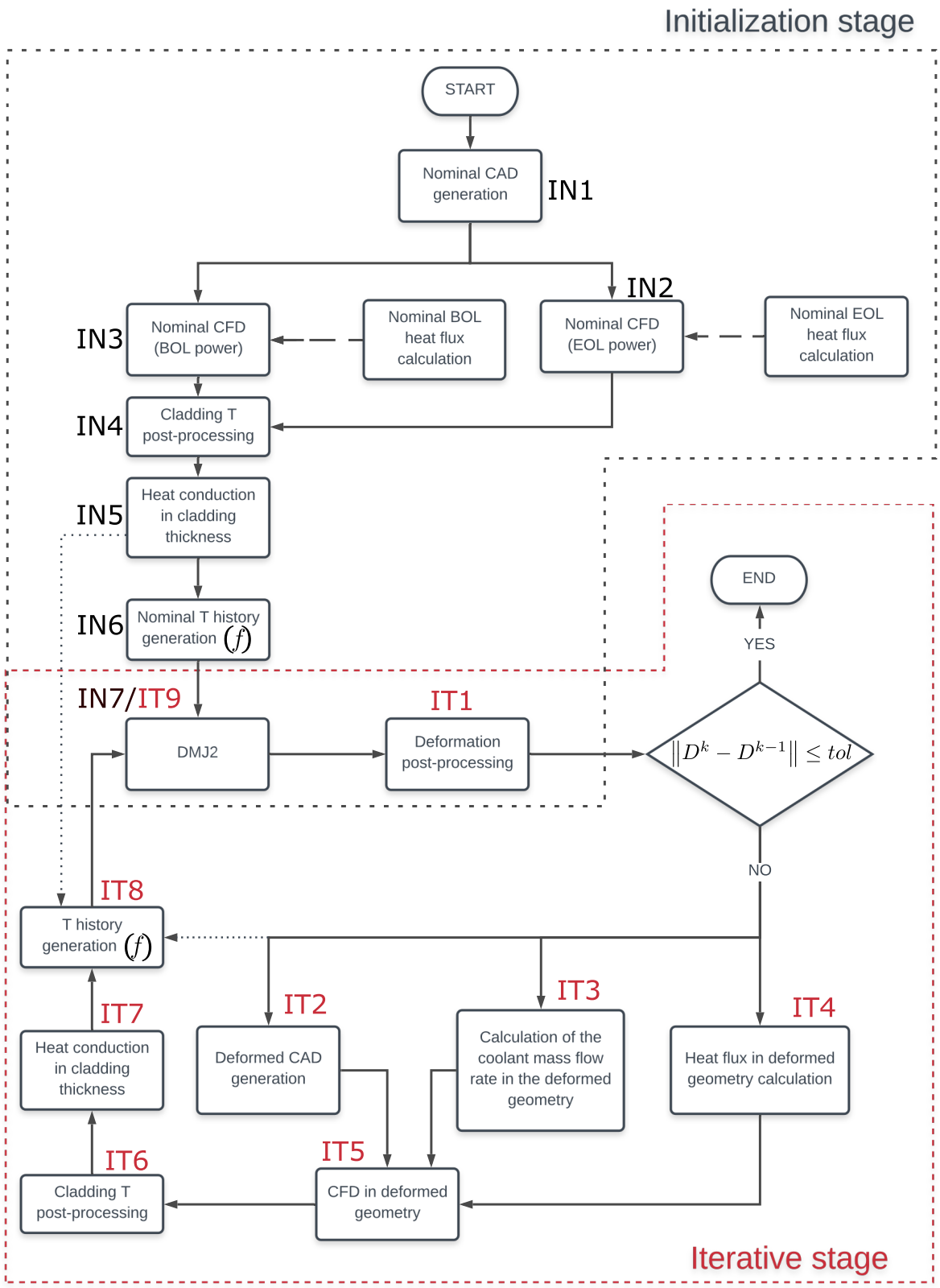

Figure 5.7.: Scheme of the main steps of the coupled simulation algorithm.

This iterative stage is repeated until the difference between the EOL deformation distribution computed by two successive iterations falls below a specified tolerance or, alternatively, after a prescribed number of iterations is reached.

The main program that implements all the procedures required for a coupled simulation has been written in the PYTHON coding language. The post-processing routines of the CFD simulations and the algorithm that generates the CAD representations of the fuel bundle have been coded in JAVA, the language employed for STAR-CCM+'s macros. Finally, the post-processing routines of the DOMAJEUR2 simulations were coded in GIBIANE, the Fortran based programming language in which both Cast3M and DOMAJEUR2 are written.

5.3. CFD of deformed fuel bundles

5.3.1. Generation of the CAD model of a deformed bundle

In order to conduct CFD simulations of deformed fuel bundles, their CAD representations have to be firstly defined. To do so, the strains and displacements computed by DOMAJEUR2, and post-processed as described in Section 5.4.2, are employed. Two different procedures have been implemented to this end using the CAD modeler of STAR-CCM+. The first takes into account the axially non-uniform diametral strain of each fuel pin, while the second considers their helical flexion as well. These two procedures are described next.

5.3.1.1. Considering the diametral deformation only

If only the diametral deformation is considered, the cross section of the cladding is circular at any given axial position, and the fuel pin—without considering its spacer wire—has rotational symmetry around its longitudinal axis. To generate the CAD representation of a given pin, the axial profile of its deformed radius, computed with DOMAJEUR2 and post-processed as described in Section 5.4.2, is employed. This profile describes the entire length of the fuel pin, while only an axial section—typically the heated column—between the axial positions z^0_{CFD} and z^1_{CFD}, measured from the base of the pin, might be represented in the CFD simulations. Then, only the section of the profile between z^0_{CFD} and z^1_{CFD} is imported into STAR-CCM+. This profile is then rotated around the longitudinal axis of the pin to generate a solid revolution body, as illustrated in Figure 5.8.

To represent the spacer wire that is helically wrapped around the fuel pin, a sweep body is generated. A sweep body is a 3D body generated by displacing a 2D sketch along a path defined by a curve. In this case, the 2D sketch is the circular

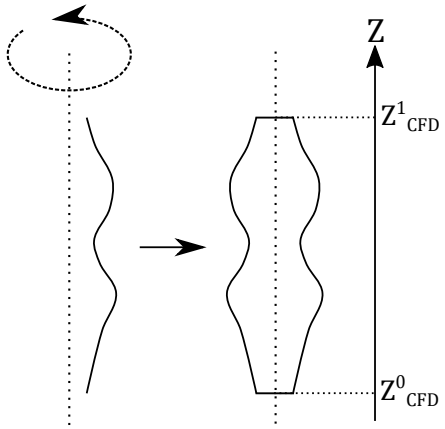

Figure 5.8.: Rotation of the axial profile of cladding external radius that produces a solid body with rotational symmetry, which represents the fuel pin.

cross section of the wire at the base of the pin—which is assumed constant since the wire deformation is not represented—, while the path is the helix defined by the centerline of the wire as it goes around the cladding.

The helical path is generated by defining points with a helix radius r_i^h, measured from the axis of the pin, at each axial position z_i and azimuthal angle θ_i^h. At z_{CFD}^0, the initial angle of the wire θ_0^w is prescribed. Then, θ_i^h is computed as:

$$\theta_i^h = \theta_0^w + 2\pi \frac{z_i}{H} \tag{5.12}$$

where H is the prescribed step of the helix. The radius r_i^h of the helix depends on the deformed cladding radius at that altitude, r_i^c, which is given by:

$$r_i^c = r_{ec} + \Delta r_{ec}(z_i) \tag{5.13}$$

where r_{ec} is the nominal external radius of the cladding, and $\Delta r_{ec}(z_i)$ the increase in the cladding external radius computed by DOMAJEUR2 at the axial position z_i, for the calculation time under consideration. The radius r_i^h is then computed as:

$$r_i^h = r_i^c + r^w - \epsilon_{inter} \tag{5.14}$$

where r^w is the radius of the wire, and ϵ_{inter} the small interpenetration introduced between the wire and the cladding to avoid the line contact that leads to meshing issues, as discussed in Section 3.3.6. To produce a smooth helical path, essential to obtain a good representation of the spacer wire, its needed axial discretization was found to be superior to that of the axial profiles of the cladding radius, which depends on the discretization employed in DOMAJEUR2. Therefore, the values r_i^c

are linearly interpolated between the values computed by DOMAJEUR2.

To create the circular sketch needed for sweeping the wire, a sketch plane needs to be defined. If a plane normal to the axis of the pin is chosen, the circular cross section of the wire would be, all along its length, perpendicular to this axis instead of being perpendicular to the helical path. Given the small angle of the helix with respect to the axis of the pin ($\sim 10°$), this approximation is not expected to have a significant impact on the thermal-hydraulics of the bundle. However, it was observed to give place, in some highly deformed pins, to an irregular contact between the wire and the cladding that induced the failure of the CAD generation. For this reason, this approximation was only retained as an option, while the default wire generation procedure uses a tilted plane to sketch the wire cross section.

To define the normal of the tilted plane, the vector $\mathbf{n_w} = \overline{\mathbf{P_1^h P_2^h}}$ is considered, where $\mathbf{P_1^h}$ and $\mathbf{P_2^h}$ are the first two points in the helical path with $z \geq z^0_{CFD}$, as illustrated in Figure 5.9. The origin of the plane is set at the center of the wire cross section at the base of the pin, i.e. at $\mathbf{P_1^h}$. The circular wire cross section is then sketched in the tilted plane thus defined, and it is used for the sweep operation. This procedure results on a solid body representing the wire-wrapped fuel pin as illustrated in Figure 5.10. It can be observed that the wire extends below and above the length of the cladding, since some points of the helical path are defined for $z < z^0_{CFD}$, and some for $z > z^1_{CFD}$. The purpose of this will become apparent later in this section.

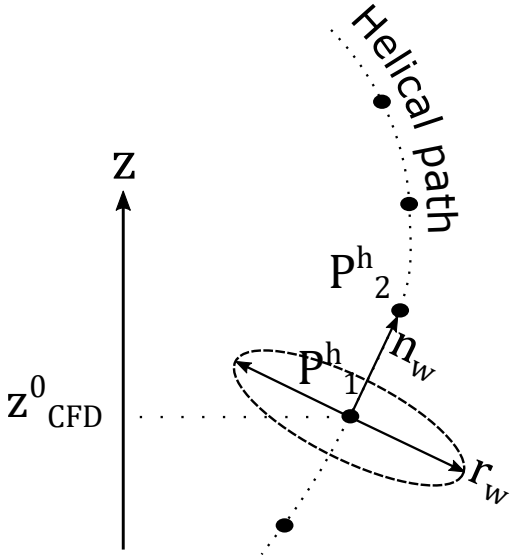

Figure 5.9.: Sketch of the tilted cross section of a spacer wire, normal to the helical path that defines the position of its center along its length.

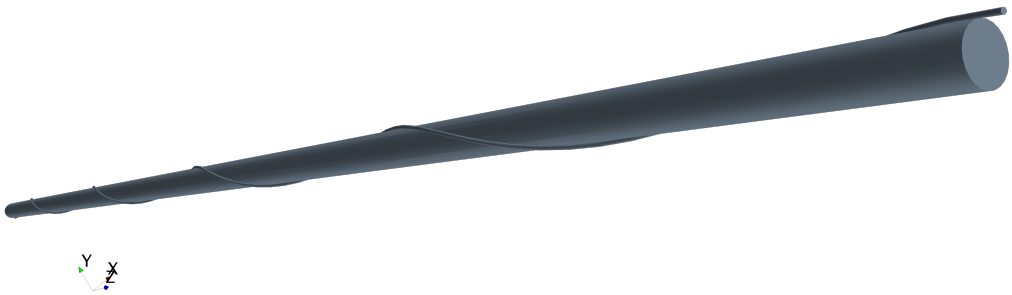

Figure 5.10.: CAD representation of a fuel pin and its spacer wire.

After the wire-wrapped pin is generated, it is displaced laterally to place it in its corresponding position in the hexagonal arrangement. Then, the procedure described above is repeated for every pin of the fuel bundle, each of which might have a different deformation profile.

This procedure allows to generate a representation of the fuel pin bundle, while a representation of the fluid domain around the pins and inside the hexcan is needed to conduct the CFD simulation. To obtain the latter, a hexagonal cross-sectional body with the internal dimension of the hexcan is first created in the CAD manager. Then, the bodies representing the fuel pins are subtracted from the hexagonal body, which extends from z^0_{CFD} to z^1_{CFD}. The extension of the spacer wires below and above the hexagonal body ensures that, after the subtraction operation, their top and bottom faces are normal to the axis of the bundle and at the same height than the upper and lower boundaries of the fluid domain, as illustrated schematically in Figure 5.11a for the upper boundary. If they had not been extended, these faces would be tilted as illustrated in Figure 5.11b, giving place to a thin wedge occupied by the fluid, which is not present in reality and produces meshing difficulties and, at the base of the bundle, a stagnation point for the fluid.

As described in Section 3.3.5, besides the small wire-cladding interpenetration ϵ_{inter} introduced to avoid the line contact between them, which leads to meshing issues, the option of smoothing out the contact lines with circular fillets has been also implemented in the CAD generation algorithm. When this option is activated, a circular fillet of radius $r_{fillet} = r^w/8$ is applied, for each fuel pin, to the two lines defined by the intersection between the spacer wire and the cladding (see Figure 3.7b), that replace the unique tangential contact line that would be defined if no interpenetration was introduced. When the filleting was employed in combination with the wire generation procedure that defines its cross section on horizontal planes, CAD generation errors where encountered in some simulations. This behaviour, discussed in Section 5.3.1.3, was not observed when the procedure using tilted planes was employed.

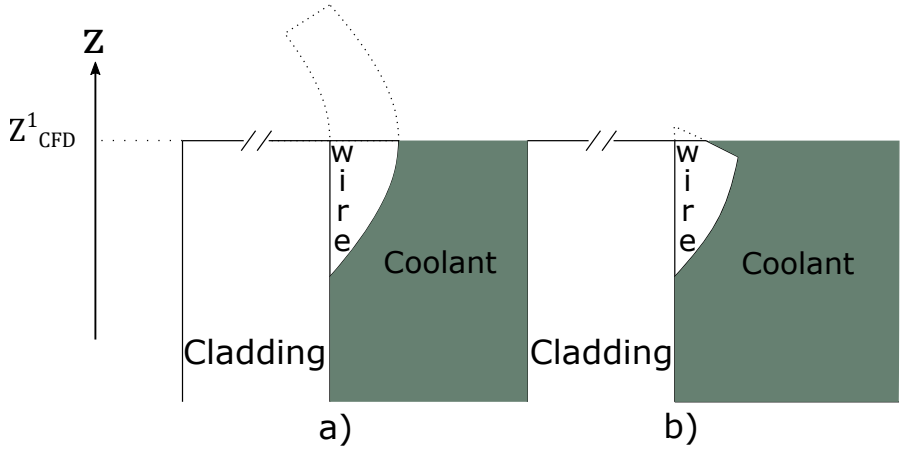

Figure 5.11.: Sketch of the upper end of the CAD representation of a wire-wrapped fuel pin. In (a), the upper face of the wire is normal to the axial direction z, and contained in the plane that defines the boundary of the fluid domain. In (b), the upper face of the wire is tilted, giving place to a thin fluid wedge.

5.3.1.2. Considering the diametral deformation and the helical flexion

When the helical flexion of the fuel pins is considered in the CAD model, they no longer present the rotational symmetry that allowed to generate the revolution bodies by rotating the axial profile of the deformed radius, as explained in the previous section. In this case, the solid bodies that represent the deformed claddings are generated using loft operations. In a loft operation, a solid body is created by fitting surfaces between a series of closed 2D sketches that define the cross section of the body, as in the example presented in Figure 5.12 where a loft body is created by joining three elliptic sketches.

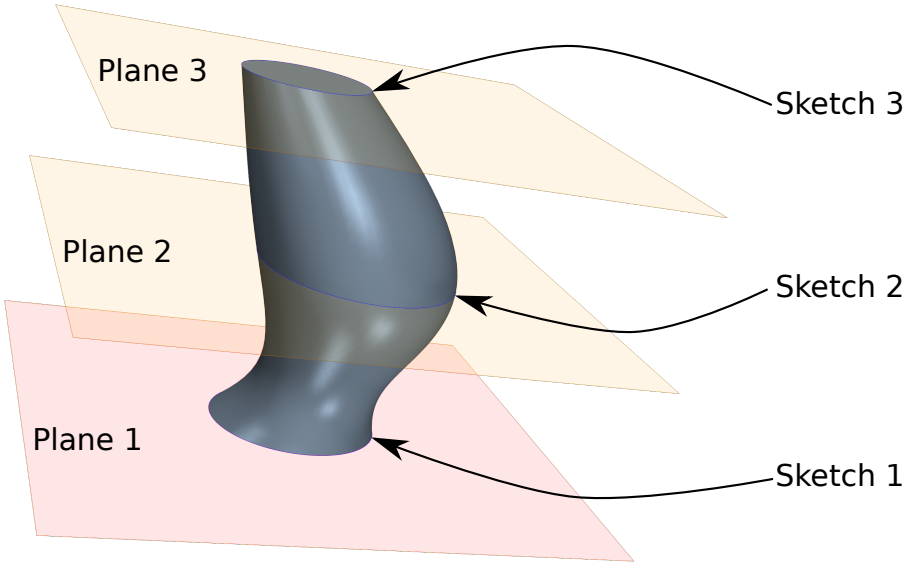

Figure 5.12.: Example of a solid body created by a loft CAD operation, joining 3 elliptic sketches. The planes on which the sketches are defined are also indicated.

To generate the body representing a given pin, the sketches used for the loft operation are the circles—since the ovalisation of the claddings is not represented—that define the cross section of the cladding at different axial positions. Since the pin is twisted, its cross section is no longer perpendicular to the vertical axis z, but to the curvilinear axis that defines its centerline. This is illustrated in Figure 5.13 for an axial position z_i. However, representing this in the CAD model would require the creation of one tilted plane per axial position, on which the circular sketch of the cladding cross section should be created. As we will see in Section 5.3.1.3, this procedure would lead to a severe slow down of the CAD generation. For this reason, to construct the flexed fuel pin, we consider that the cladding cross

section is perpendicular to the vertical axis z at every axial position computed by DOMAJEUR2[8]. This approximation is illustrated in Figure 5.13 for $z = z_j$. Evidently, this approximation improves as the angle α between the tilted and horizontal cross sections becomes smaller. In the simulations conducted in this work, the maximal value of α was $\sim 1°$, so the approximation was judged to be adequate.

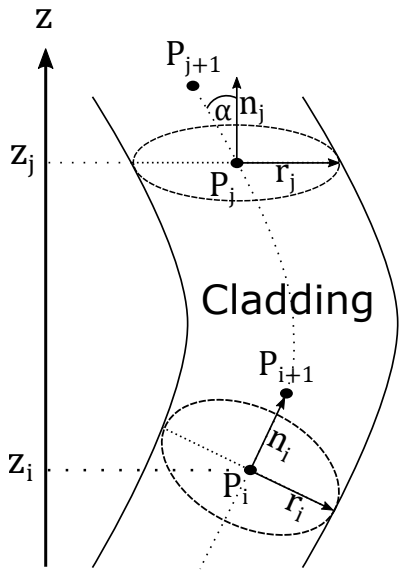

Figure 5.13.: Sketch of a twisted fuel pin, of its tilted cross section at $z = z_i$ and of the horizontal cross section, at $z = z_j$, employed—given the small value of the angle α—as an approximation to construct the CAD model of the pin.

Then, one circular sketch is defined for each axial position computed by DOMAJEUR2 between z^0_{CFD} and z^1_{CFD}, and these are used to create the loft body that represents the helically flexed fuel pin with axially varying diameter. To define the circular cross section at an axial position z_i, the deformed radius r_i computed by DOMAJEUR2 at that position is used. The center $\mathbf{P_i}$ of the circular sketch is defined by the computed lateral displacement of the cladding centerline at that axial position, Δx_i and Δy_i, such that, in Cartesian coordinates with origin at the center of the base of the non-deformed fuel pin, $\mathbf{P_i} = (\Delta x_i, \Delta y_i, z_i)$. As discussed in Section 5.4.2, the axial profiles of Δx and Δy are produced, for each fuel pin, by the automatic post-processing of the DOMAJEUR2 simulations.

The procedure to generate the body that represents the spacer wire around the pin described in the previous section is employed, and the filleting of the

[8]Considering horizontal planes allows them to be shared by all fuel pins, instead of having to define a different set of tilted planes per fuel pin.

wire-cladding contact is also an option of the algorithm in this case. This leads to a CAD representation of a deformed pin and its spacer wire like the one presented as an example in Figure 5.14.

This procedure is repeated with each fuel pin in the bundle, which is placed at its correct position in the hexagonal arrangement before performing the operation that allows to obtain the CAD representation of the fluid domain between the fuel pins and inside the hexcan, described in the previous section.

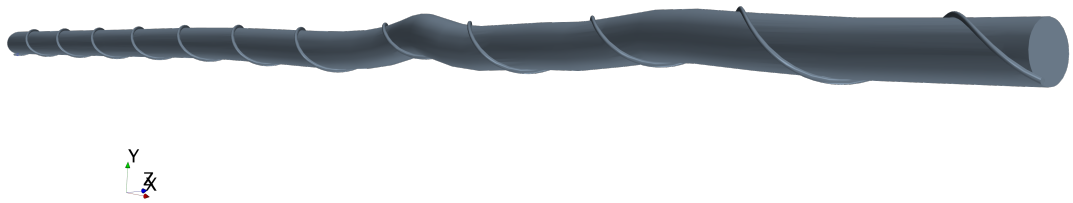

Figure 5.14.: CAD representation of a helically flexed fuel pin and its spacer wire. The lateral displacement of the pin computed by DOMAJEUR2 has been multiplied by 40 to obtain the CAD model presented in this figure.

5.3.1.3. Robustness and performance

In a coupled simulation, several CFD simulations on deformed fuel bundles are conducted, and a different CAD model is automatically generated for each of them. It is then of utmost importance that the algorithm that generates the CAD model is robust, that is, that the CAD generation is successful for any deformed bundle computed by DOMAJEUR2. Given the complex geometry and the very irregular deformation patterns computed in the thermomechanical simulations, this proved to be a challenging task, and significant efforts were made to avoid the CAD generation failure.

Consequently, several measures have been implemented in the CAD generation algorithm to avoid failure, or rather to make the necessary corrections in case of initial failure, which cannot be predicted just from its input parameters, produced by DOMAJEUR2. The general principle of these measures is that, in the case that the CAD generation produces an error, it is firstly automatically *caught* to avoid the failure of the entire coupled simulation. Then, the CAD generation procedure is restarted with the same input data, but in a—less efficient—mode in which the success of each individual CAD operation is evaluated, to determine the operation/s that produce the encountered error. Then, corrections are done and the process is

repeated until the CAD generation is successful, so that the coupled simulation can then continue.

The automatic corrections implemented include:

- The modification of the tolerance used in the CAD operations, in particular the operation in which the fuel pins are subtracted from the hexagonal prism that represents the sodium inside the hexcan;
- The modification of the radius of the fillets between the claddings and the wires, in the range $[0.9\frac{r^w}{8}, 1.1\frac{r^w}{8}]$, which was verified to have a negligible impact on the cladding temperature distribution;
- The modification of the radius of the claddings at the axial positions more susceptible of inducing a CAD error. These positions are the ones in which the distance between two CAD surfaces are close to the tolerance employed in the CAD modeller, which are automatically identified by a routine implemented that then locally changes the cladding radius by a small factor $\epsilon_{correction} < r_{ec}/1000$, which has negligible effect on the thermal-hydraulics of the bundle but allows to avoid the CAD generation error.

In every simulation where one of these corrections is automatically applied, a full report of the changes made to the geometry or the CAD modeler parameters is produced.

Out of the procedures described in the previous sections to generate the CAD model, the one that exhibited more robustness issues was the procedure that defines the cross section of the spacer wires on horizontal—instead of tilted—planes, and specially when used in combination with the filleting of the cladding-wire contact. This procedure was nevertheless kept as an option of the CAD generation algorithm because it did not lead to errors when generating non-deformed or slightly deformed fuel bundles, and because it is the fastest of the implemented procedures.

The procedure that generates the cross section of the wires on tilted planes is slightly slower, since more objects (planes, axis, points) need to be defined in the CAD modeler to generate the fuel bundle. However, the CAD generation time remains of the same order than the first algorithm, both taking about 1 hour for a 217 fuel bundle. On the other hand, the number of objects that need to be defined in the algorithm to generate twisted pins increases drastically, since one circular sketch needs to be defined per fuel pin and per axial position computed by DOMAJEUR2. This did not pose great difficulties when simulating small fuel bundles of 7 to 19 fuel pins, but the CAD generation time was found to grow more than linearly with the number of pins, which resulted in a generation time of

approximately 20 hours for a 217 pin bundle[9]. The support team of STAR-CCM+ indicated that they are currently working on solving an internal issue of the CAD modeler that produces a severe slow down of the CAD operations with growing number of total objects defined.

5.3.2. Model to estimate the coolant mass flow rate in deformed subassemblies

To be able to evaluate the impact of the geometrical deformation on the thermal-hydraulic behaviour of the fuel bundle, it is essential to consider the mass flow rate variation that it induces—caused by an increased hydraulic resistance in the deformed condition—which is used as hydraulic boundary condition at the inlet of the CFD domain. Even though only the heated length of the fuel bundle is considered in the CFD simulations here presented, the relationship between mass flow rate and deformation depends also on the geometry of the rest of the subassembly, including its inlet nozzle and upper section. Therefore, a model that represents the entire subassembly is required to estimate the coolant mass flow rate in a deformed fuel bundle.

In the model here implemented, one SFR subassembly is considered to undergo significant geometrical deformation within a non-deformed core. This situation is representative of the experimental irradiation of one subassembly, which typically remains in the core for a significantly longer period of time than the rest of the subassemblies and, as a consequence, undergoes a much higher deformation. In this case, the increased hydraulic resistance of the deformed bundle would divert some of the coolant flow towards the neighboring, less-deformed subassemblies. Then, to estimate the coolant mass flow rate in the deformed subassembly, we make the following simplifying hypotheses:

- Only the average diametral strain $\overline{\Delta D}$ of the heated length of the fuel pins is considered, and it is employed to compute a reduced hydraulic diameter D_h^*. Experimental evidence indicates that the diametral strain of the fuel pins is concentrated on their heated lengths, a result that is also obtained in the simulations conducted in this work (see Section 6.16). The other deformation mechanisms do not alter the hydraulic diameter of the fuel bundle, and their effect on the bundle pressure drop is not expected to be very significant since, after almost a decade of operation, it had not been observed

[9]Since the cladding cross section is considered to be normal to the vertical z axis, one plane per axial position z_i needs to be created, and they are shared by all fuel pins. If the tilt of the cross section was considered, one plane per pin and per axial position would be required. In this case, the slowing down of the CAD generation would be more pronounced.

in Phenix reactor (CEA 1981). This is in agreement with preliminary CFD simulations we conducted, in which the flexion of the fuel pins—as calculated by DOMAJEUR2 for a fuel bundle representative of the advanced SFR designed at the CEA—led to only 1% change in the pressure drop within the heated column;

- All the fuel assemblies present the same pressure drop between their inlet and outlet, and it is the same as the core's pressure drop ΔP_{core}. This assumption is based on the existence of lower and upper plenums that communicate, respectively, the inlets and outlets of all fuel assemblies. Current CEA experience indicates that the radial pressure gradients in these plenums are minor; indeed, for the advanced SFR designed at the CEA, the pressure difference between the outlets of different subassemblies is typically below 1% of the ΔP_{core}, which would lead approximately 0.5 % difference in mass flow if we assume a quadratic relationship between these magnitudes. In comparison, much larger mass flow rate reductions of up to 10 % have been documented in subassemblies of Phenix reactor (Pol and Bourdot 1979), and this not even for the most deformed subassemblies of that reactor;

- The variation of ΔP_{core} with the deformation of only one of its more than (typically) 200 subassemblies is neglected, since they act as parallel hydraulic resistances.

The derivation of the model here presented is based on the subassembly of the advanced SFR designed at the CEA, but we will see that it can be employed to represent subassemblies with different characteristics by modifying the value of some input parameters.

Under these conditions, the pressure drop in the subassembly can be expressed as the sum of the pressure drop within the part that undergoes deformation, ΔP_{Def}, and the part that does not, ΔP_{NonDef}, as illustrated in Figure 5.15. These magnitudes depend on the mass flow Q of the subassembly under consideration, and ΔP_{Def} depends on the level of deformation, here given by $\overline{\Delta D}$. Then, we can write:

$$\Delta P_{Def}(Q, \overline{\Delta D}) + \Delta P_{NonDef}(Q) = \Delta P_{core} \tag{5.15}$$

where, as stated before, ΔP_{core} is considered constant.

In this case, ΔP_{Def} is the pressure drop in the heated column of the bundle—the only part of the subassembly that is considered to undergo deformation—while the pressure drop in the rest of the fuel bundle, $\Delta P_{NonDefBundle}$, represents a fraction of ΔP_{NonDef}. To estimate ΔP_{Def}, we recall the definition of the Darcy-Weisbach friction factor f_D and, following Equation 2.11, we write:

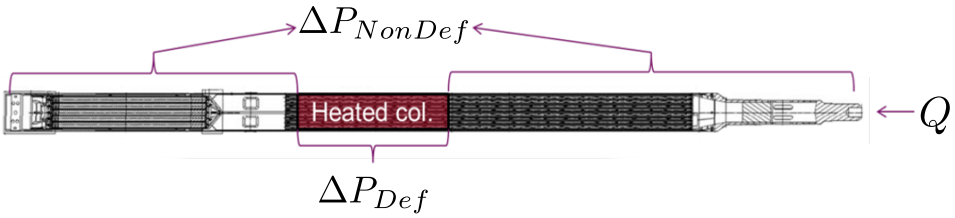

Figure 5.15.: Diagram of one subassembly. The heated column is the only part that is considered to undergo deformation, and it is highlighted in red.

$$\Delta P_{Def}(Q, \overline{\Delta D}) = \frac{f_D^* L^* Q^2}{2\rho D_h^* A^{*2}} \tag{5.16}$$

where D_h^* is the hydraulic diameter of the deformed heated column of the fuel bundle, A^* its cross sectional area, L^* its length, and ρ the fluid density. In this work, we employ the correlation developed by Rehme for wire-wrapped fuel bundles[10], given by equations 2.12 and 2.13, to compute f_D[11]. For the evaluation of this correlation, and for the evaluation of A^* and D_h^*, the average external diameter of the fuel claddings in the deformed heated column ($D_{ec}+\overline{\Delta D}$) is employed.

Similarly, for the non deformed length L of the fuel bundle we have:

$$\Delta P_{NonDefBundle}(Q) = \frac{f_D L Q^2}{2\rho D_h A^2} \tag{5.17}$$

where all the geometrical parameters and the friction factor f_D are computed using the dimensions of the non-deformed bundle.

The pressure drop in the non deformed part of the subassembly can be expressed as:

$$\Delta P_{NonDef} = \Delta P_{NonDefBundle} + \Delta P_{Nozzle} + \Delta P_{Plenum} + \Delta P_{Up} + \Delta P_{Singular} \tag{5.18}$$

where ΔP_{Nozzle} corresponds to the inlet nozzle of the subassembly, ΔP_{Plenum} to the plenum between the outlet of the bundle and the UNS (Upper Neutron

[10]It should be noted that the Detailed Cheng Todreas (CTD) correlation was found to perform slightly better than Rheme's (S. Chen, N. Todreas, and Nguyen 2014), but the first is not applicable to bundles of 7 fuel pins, which are studied in this work. Recently, and after the model presented in this section had been already implemented, the CDT correlation was updated and the new version (UCTD) is also applicable to 7-pin bundles (S. K. Chen, Y. M. Chen, and N. E. Todreas 2018).

[11]In this notation, the * superscript makes reference to the deformed bundle geometry, which implies that the starred variables depend on $\overline{\Delta D}$.

Shielding), ΔP_{Up} to the UNS and the head of the subassembly, and $\Delta P_{Singular}$ to the singular pressure drops due to, for example, drastic cross section area changes.

The pressure drops ΔP_{UP} and ΔP_{Plenum} are regrouped and written as:

$$\Delta P_{UP} + \Delta P_{Plenum} = \alpha_P Q^2 \tag{5.19}$$

where, since the flow is in the turbulent regime, we assumed a quadratic dependence with the mass flow rate (see Section 2.1.6). This regrouping is motivated by a preexisting CFD simulation of the advanced SFR designed at the CEA, which is mentioned later in this section. Similarly, the pressure drop in the subassembly inlet nozzle and due to the remaining singularities are written as:

$$\Delta P_{foot} + \Delta P_{Singular} = k_P Q^2 \tag{5.20}$$

Under these considerations, the mass flow rate Q in a deformed subassembly can be estimated by numerically solving the equation:

$$\Delta P_{Def}(Q, \overline{\Delta D}) + \Delta P_{NonDef}(Q) = \frac{Q^2}{2\rho}\{\frac{f_D^* L^*}{D_h^* A^{*2}} + \frac{f_D L}{D_h A^2}\} + (\alpha_P + k_P)Q^2 = \Delta P_{core} \tag{5.21}$$

The need for solving Equation 5.21 numerically arises from the dependence of the friction factors f_D and f_D^* on the Reynolds number and, therefore, on the coolant mass flow rate.

The procedure outlined above is employed to determine the coolant mass flow rate used as inlet boundary condition for each CFD simulation of a deformed fuel bundle, considering the average cladding diametral strain computed by DOMAJEUR2. Even though the derivation was done for the subassembly of the advanced SFR, modifying the parameters k_P, α_P and ΔP_{core}, allows to use this model to represent different subassemblies.

Typically, the parameters k_P, α_P and ΔP_{core} are part of the input data required by the algorithm that automatically sets the CFD boundary conditions. However, only α_P is known for the advanced SFR. In this case, k_P is computed by the algorithm based on a known operation point $\{Q_0, \Delta P_0\}$ in a non-deformed subassembly, as in the example below.

For the advanced SFR designed at the CEA, a preexisting CFD simulation of the plenum, the UNS, and the head of the subassembly yielded $\alpha_P = 49.5$ kg^{-1} m^{-1}. Additionally, available best estimate values of the nominal core pressure drop ΔP_0 and the subassembly mass flow rate Q_0 of this reactor can be employed to compute

k_P, which is the only unknown in the following equation:

$$\Delta P_0 = (\alpha_P + k_P) Q_0^2 + \Delta P_{NonDefBundle}(Q_0) \tag{5.22}$$

where $\Delta P_{NonDefBundle}(Q_0)$ is calculated from Equation 5.17 and the length L considered corresponds to the total length of the fuel bundle, since $\{Q_0, \Delta P_0\}$ corresponds to an operation point of the non-deformed subassembly. This gives, for $Q_0 = 27.08$ kg/s and $\Delta P_0 = 2.71$ bar, a value of $k_P = 74.5$ kg^{-1} m^{-1}. These parameters allow to evaluate the evolution of the subassembly mass flow rate as a function of the average diametral deformation of the heated column of the fuel bundle of this advanced SFR, as well as the pressure drop in the deformed and undeformed parts of the subassembly, presented in Figure 5.16.

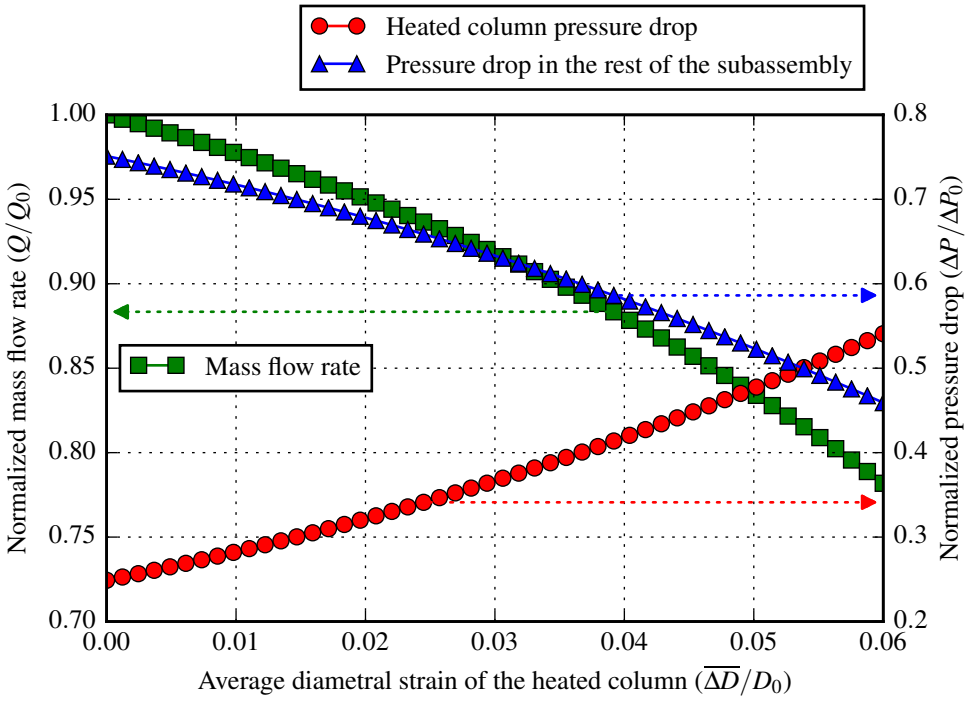

Figure 5.16.: Normalized mass flow rate and pressure drop in the heated column and in the rest of the subassembly, as a function of the average diametral strain of the heated column of the fuel bundle of the advanced SFR designed at the CEA.

The results presented in Figure 5.16 show how, as the deformation increases, so does the relative contribution of the deformed heated column to the total subassembly pressure drop. Indeed, it accounts for about 25% of ΔP_0 in the non-deformed

geometry, while it represents almost 55% when the average diametral deformation of the bundle reaches 6%. As the pressure drop in the heated column grows, the pressure drop in the rest of the subassembly is reduced due the reduction of the mass flow rate, given that the total subassembly pressure drop is fixed, as indicated by Equation 5.15. It can be noted that the mass flow rate reduction computed for 6% average diametral strain in the heated column exceeds 20%. Such a mass flow reduction would lead to an increase in the average sodium outlet temperature of more than 37°C, as computed using Equation 2.15 and considering a nominal sodium bulk heating ($\Delta\overline{T}^{0}_{Na}$) of 150°C.

In every CFD simulation for which a mass flow rate Q is set as boundary condition, the CFD computed pressure drop $\Delta P^{CFD}_{Def}(Q, \Delta D(\mathbf{r}))$ is automatically compared to $\Delta P_{Def}(Q, \overline{\Delta D})$, computed by means of Rehme's correlation. Note that in the pressure drop computed with the CFD simulation, the actual distribution $\Delta D(\mathbf{r})$ of the diametral strain of the claddings is explicitly considered. The difference between the two was found to be, in every simulation conducted in this work, below 10 %, which is within the uncertainty of the correlation. If more accuracy was required in the determination of Q, the value computed based on using the pressure drop correlation for the deformed bundle could be used as initial seed for an iterative procedure that modifies the boundary condition Q of the CFD simulation until the following condition is satisfied:

$$\Delta P^{CFD}_{Def}(Q, \Delta D(\mathbf{r})) + \Delta P_{NonDef}(Q) = \Delta P_{core} \tag{5.23}$$

For this iterative procedure to improve the predictive capabilities of the model, the mesh of the CFD simulations would need to be finer than the mesh employed in this work since, for accurately predicting the pressure drop in the bundle, the viscous sub-layer should ideally be resolved. For this reason, and with the objective of avoiding an increase in the computational cost of the coupled simulations, this procedure is not employed in this work, although its implementation— if deemed necessary—would be straightforward.

5.3.3. Heat flux in the deformed bundle

In the coupling methodology developed in this work, the effects of the deformation on the power level of the subassembly—which could potentially be caused by the neutronic feedback effects described in Section 2.3.2—are neglected, and this hypothesis is evaluated in Section 6.3. This means that the same axial profiles of linear power are used for the CFD simulations in the non-deformed and in the deformed geometries.

However, even if the linear power is not modified, the axial profile of surface heat

flux—which is the magnitude used as thermal boundary condition on the external surface of the claddings—is modified due to the increase of the heat exchange surface caused by the diametral strain of the claddings. This effect can lead to a total power increase of $\sim 5\%$, and should thus be accounted for. In order to do so, for each fuel pin, the surface heat flux $q^{''}(z_i)$ at the external surface of the cladding at an axial position z_i is given by:

$$q^{''}(z_i) = \frac{q^{'}(z_i)}{2\pi(r_{ec} + \Delta r_{ec}(z_i))} \tag{5.24}$$

where $q^{'}(z_i)$ is the linear power at z_i and $\Delta r_{ec}(z_i)$ the increment of the external radius of the cladding computed by DOMAJEUR2 for that pin at that axial position.

5.3.4. Post-processing of the CFD simulations

For a simulation with DOMAJEUR2, the cladding temperature distribution needs to be specified for different instants t_i of the irradiation, between which the code performs a linear interpolation. This is done via a text input file, in which the cladding temperature of each fuel pin and for each defined time t_i (not to be confused with the calculation times of the thermomechanical simulation, which do not need to be the same) is written in the following format:

- For each axial position z_i, out of a total n_z axial positions
  - For each radius r_i, out of a total n_r radii
    - For each azimuthal angle θ_i, out of a total n_θ angles
      - The temperature $T(z_i, r_i, \theta_i, t_i)$ is specified

In the simulations conducted in this work, considering that only one finite element is generally used in the thickness of the cladding, only the temperature at its mid-thickness ($r_i = r_{mid-thickness}$) is specified. Then, one axial temperature profile for each azimuthal angle θ_i (generally 6) and per fuel pin is defined for each time at which the temperature distribution is specified. The temperature of the finite elements composing the claddings in the DOMAJEUR2 model are then obtained by interpolating these profiles. Since the formulation of DOMAJEUR2 is Lagrangian, the temperature is specified as a function of the position in the non-deformed geometry. Two different temperature post-processing procedures were implemented to define these temperature profiles.

Method using probe lines

The first procedure is based on the use of probe lines, which are objects defined in the STAR-CCM+ environment. A probe line is a finite collection of evenly spaced

sampling points contained in a line segment in a specified direction, which have an associated sampling surface or volume. Then, by properly defining the direction and position of a probe line, and setting the cladding external surface as the sampling surface of the line, the desired cladding temperature profiles can be obtained by probing the temperature at every point composing the line. To do this, n_θ probe lines with n_z points each are created per fuel cladding, parallel to the axis of each fuel pin. The starting and ending points of the line corresponding to the angle θ_i are given by $P_0 = (r = r_{ec}, \theta = \theta_i, z = z^0_{CFD})$ and $P_1 = (r = r_{ec}, \theta = \theta_i, z = z^1_{CFD})$, where the origin of the cylindrical coordinate system is the center of the base of the considered fuel pin, r_{ec} is the nominal cladding external radius, and z^0_{CFD} and z^1_{CFD} are the axial positions of the start and end of the axial section of the fuel pin represented in the CFD simulation (typically the heated column). In the deformed claddings, we have $r > r_{ec}$, so there is no temperature computed at $r = r_{ec}$, which is then a point inside the cladding and not represented in the CFD model. However, when a point within the probe line is probed, it reports the temperature of its closest cell, which in this case corresponds to the desired cell on the surface of the deformed cladding[12].

An example of a probing line is presented in Figure 5.17, and the resulting cladding surface temperature profile in Figure 5.18. The same color coding has been employed in both figures to indicate the effect that the spacing wires have on the resulting profile. A temperature jump is observed when the probe line intersects the spacer wire wrapped around the considered cladding (red ellipses), and local temperature maxima are observed at the points where the wire of a neighboring pin comes closest to the probe line (blue ellipses). The temperature jumps observed in Figure 5.18—which become more pronounced in the deformed geometries—induce high thermal stresses that cannot be properly resolved unless the spatial discretization of the thermomechanical model is very fine. A possible solution for this would be simply increasing the number of axial temperature profiles given as input to DOMAJEUR2 per fuel pin (i.e. increasing n_θ) and relying on the temperature interpolation done by this code to *smooth out* the observed discrete jumps. However, this practice was observed to severely slow down the thermomechanical simulations, and often led to convergence problems. For these reasons, and considering that the method based on the use of straight probe lines cannot be employed for flexed fuel pins that no longer have a straight axis, a second temperature post-processing method was implemented.

[12] Technically, if the difference $\delta(\Delta r) = |\Delta r(z_i) - \Delta r(z_{i+1})|$ in the diametral deformation at two axial positions z_i and $z_{i+1} = z_i + \delta z$ was high enough, the closest cell of a probe point at z_i could be at z_{i+1}, with δz the distance between probe points. However, for this to happen, Δr should be larger than δz. For the smallest δz employed in this work, this condition gives $\Delta r/r \sim 82\%$, while in reality $max(\Delta r/r) < 10\%$.

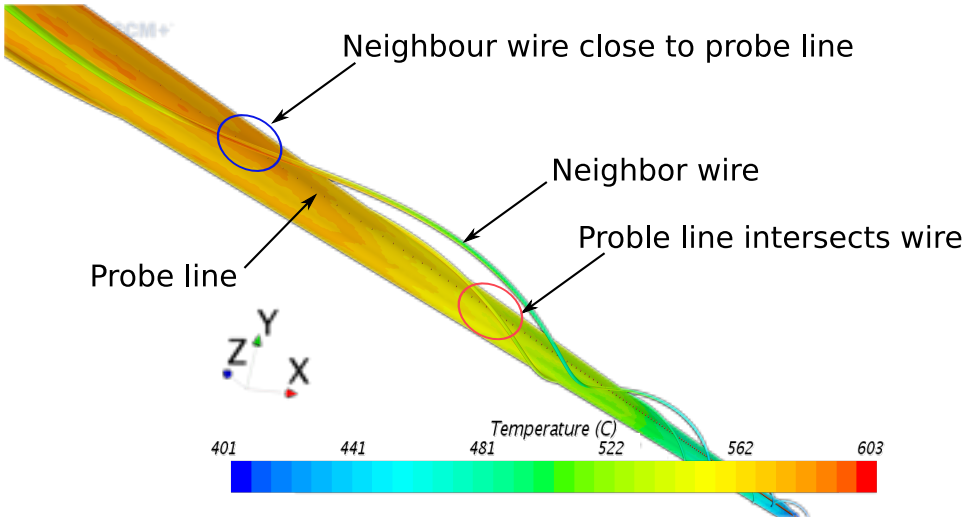

Figure 5.17.: Probe line used to sample the cladding surface temperature. Some of the points where it intersects the spacer wire or becomes close to a neighbouring wire are indicated.

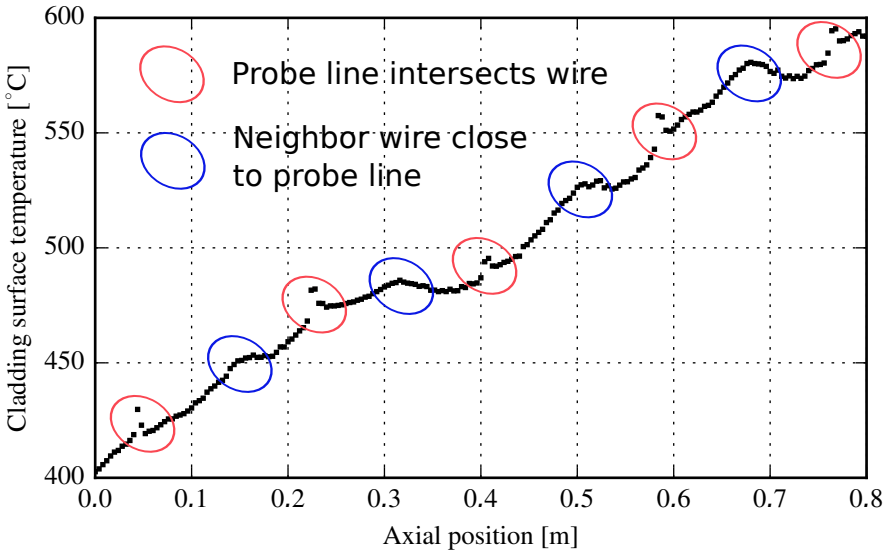

Figure 5.18.: Example of a cladding surface temperature axial profile. The temperature jumps induced by its spacer wire are encircled in red, and the local heating induced by a neighboring spacer wire are encircled in blue.

Method using probe points

The second method is based on the use of probe points, which can be employed to sample the temperature of a specified volume or surface at a given position. In this case, if n_θ axial temperature profiles are required for a given fuel cladding, $n_\theta n_{arc}$ probe points are placed, at each altitude z_i, in the circumference of the cladding, with n_{arc} the number of probe points in each of the n_θ circumference arcs in which the cladding is divided. Each of these circumference arcs is centered in one of the different θ_i. An example of the resulting probe point distribution is presented in Figure 5.19.

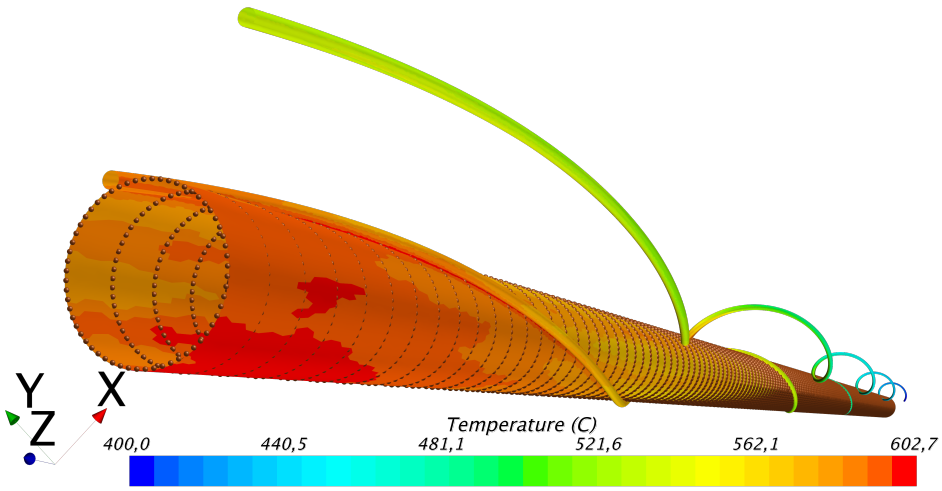

Figure 5.19.: Distribution of the probe points used to sample the cladding surface temperature.

In this method, the temperature values of the n_{arc} probe points of the circumference arc centered at θ_i are averaged to produce the value of the temperature profile associated to that azimuthal angle, at the axial position z_i. This process smooths out the temperature discontinuities associated to the probe lines intersecting the spacer wire, as can be noted in Figure 5.20, where the axial temperature profiles presented were computed for the same pin and angular position as the profile of Figure 5.18, averaging over circumference arcs of 30°and 60°.

When only the diametral deformation of the claddings is considered, their CAD representation is axisymmetric. In this case, all the probe points can be defined with the same radius $r = r_{ec}$ measured from the center of the pin, as is the case with the probe lines. However, when the helical flexion of the claddings is taken into account to construct the CAD model, as described in Section 5.3.1.2, this

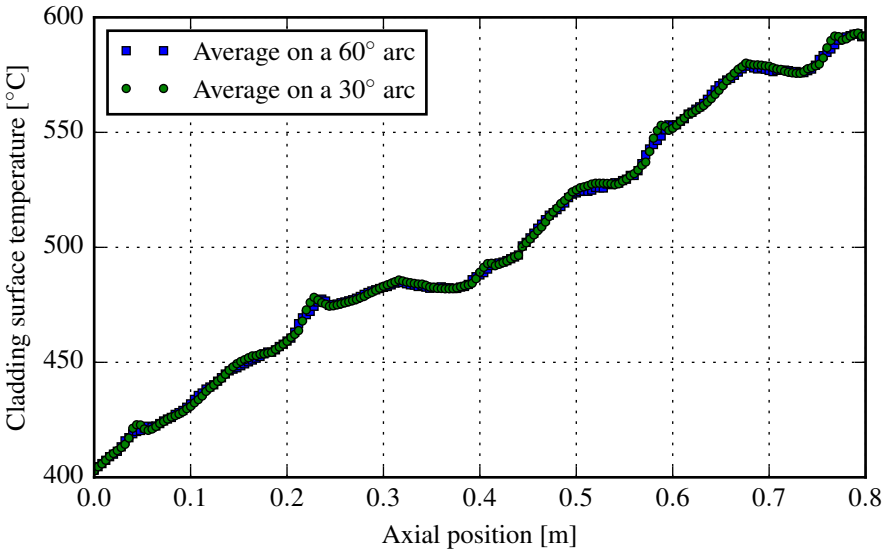

Figure 5.20.: Examples of cladding surface temperature axial profiles. Each temperature value is computed by averaging the temperatures of the probe points present, at that axial position, in a circumference arc on the surface of the cladding of either 30°or 60°.

is no longer possible. In the adopted CAD representation, the helical flexion has the effect of, at every altitude z_i, displacing the center of the cladding cross section, which remains circular, in a direction perpendicular to the vertical z axis. Therefore, in the presence of helical flexion, the same procedure can be employed by modifying the local origin of the radial coordinate of the probe points at every altitude z_i according to the horizontal displacement of the cladding cross section at that altitude. This produces, for every altitude z_i and just like in the case without flexion, a circular arrangement of probe points on the surface of the cladding, now centered in the longitudinal curvilinear axis of the flexed fuel pin.

Both this method and the one based on the use of probe lines store the required axial temperature profiles in text files, which are the base of a procedure that computes the temperature increase in the thickness of the cladding, as described next.

Temperature increase in the cladding thickness

The two procedures described above allow to compute the axial profiles of cladding surface temperature, while the temperature at the center of the cladding thickness, which is higher than the first, is specified in the DOMAJEUR2 input file. Then, the cladding surface temperature profiles are modified to take into account the

heat conduction within the cladding. Only the conduction in the radial direction is considered so the temperature at the cladding mid-thickness is computed by evaluating Equation 2.17 at $r = r_{mid-thickness} = (r_{ec} + r_{ic})/2$, which gives, for an angle θ_i:

$$T(r_{mid-thickness}, z_i, \theta_i) = T(r_{ec} + \Delta r_{ec}, z_i, \theta_i) + \frac{q'(z_i)}{2\pi\lambda_c} \ln\left(\frac{r_{ec}}{r_{mid-thickness}}\right) \quad (5.25)$$

where $q'(z_i)$ is the linear power at z_i, and λ_c the conductivity of the cladding. It should be noted that, while the CFD simulation computes the cladding surface temperature at its deformed external radius, the non-deformed dimensions are employed to compute the temperature increase in the thickness of the cladding, simplification that has negligible effects in the results[13]. In Section 6.2, the temperature profiles thus obtained are compared to the profiles computed with a CFD simulation in which the thickness of the cladding is explicitly represented to account for the heat conduction.

5.4. Thermomechanics of the fuel bundle

5.4.1. Defining the temperature history

As discussed in Section 5.2.1, the coupling methodology here developed is based on defining the time evolution of the cladding temperature distribution—here called temperature history $\tilde{T}(\mathbf{r}, t)$—used by DOMAJEUR2 for the simulation of the entire irradiation period under consideration, which is repeated iteratively. This temperature history, which is updated in every iteration, is defined by interpolating the temperature distributions computed with CFD simulations in deformed geometries obtained with DOMAJEUR2 for different calculation times. We showed, in Section 5.2.2, that if a CFD simulation is done in the deformed geometry computed at each time step of the thermomechanical simulation, this methodology is equivalent to the reference algorithm that iterates, until convergence of the temperature and deformation fields, within every time step. However, as previously discussed, both of these approaches imply an extremely high computational cost, which is why the aim of the methodology here presented is to reduce as much as possible the number of required CFD simulations. This is achieved by defining the interpolation function f, used to obtain $\tilde{T}(\mathbf{r}, t)$, as described in this section.

In the example discussed in Section 5.2.1 and used in Figure 5.4 to illustrate the methodology, a linear interpolation between the temperature distribution in

[13] This simplification avoids including the multiplicative factor $\frac{1+\varepsilon_{\theta\theta}(r_{ec})}{1+\varepsilon_{\theta\theta}(r_{mid-thickness})} \approx 1$ in the argument of the logarithm in Equation 5.25, with $\varepsilon_{\theta\theta}(r_{ec})$ and $\varepsilon_{\theta\theta}(r_{mid-thickness})$ the circumferential strains at the external and mid-thickness cladding radii, respectively.

the non-deformed and the fully deformed bundles was considered. However, as mentioned in Section 2.2.2.2 and shown in Section 6.8, the deformation rate is not constant throughout the irradiation, so the temperature is not expected to evolve at a constant rate. Indeed, during a significant fraction of the irradiation, during which the swelling incubation dose has not been yet achieved, the deformation remains very low. During this period, the temperature distribution is therefore not significantly affected by the deformation, although it will evolve according to the evolution of the subassembly power, function of its burn-up. A typical temperature evolution $T(\mathbf{r_0}, t)$ is schematically represented in Figure 5.21 for given point $\mathbf{r_0}$ within a fuel bundle—where, for simplicity, a constant power level was considered—, along with different approximate temperature histories.

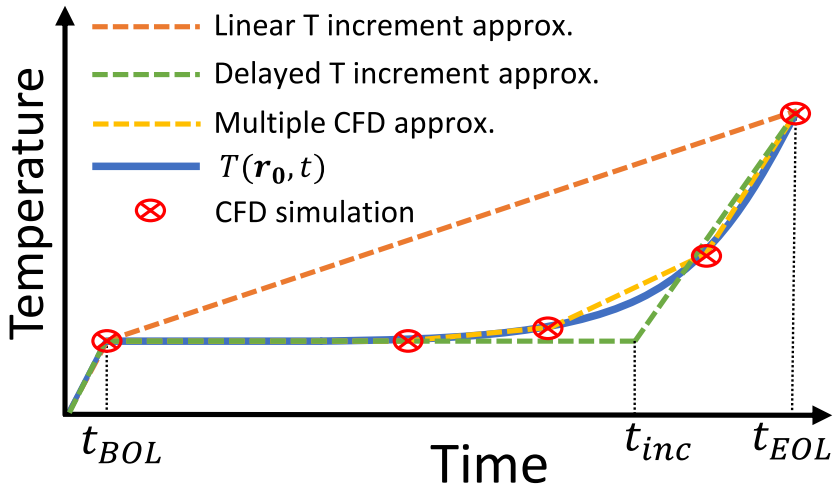

Figure 5.21.: Schematic representation of a typical temperature time evolution $T(\mathbf{r_0}, t)$, at constant subassembly power, and of different approximating functions. A point $\mathbf{r_0}$ within the fuel bundle is considered. In the "Delayed T increment" approximation, the effects of deformation on temperature are considered only after a time t_{inc}.

Out of the temperature histories illustrated in Figure 5.21, the one named "Delayed T increment", that considers the effects of deformation on temperature only after a time t_{inc}, was found to provide a far better approximation of $T(\mathbf{r}, t)$ than the "Linear T increment" approximation, without requiring additional CFD simulations[14]. With the "Delayed T increment" approximation, the temperature history computed in an iteration k, and then used as input for a thermomechanical simulation, is given by Equation 5.26 below:

[14]If the subassembly power evolves during the irradiation, one additional CFD simulation is required for the first iteration only.

$$\tilde{T}^k(\mathbf{r},t) = \begin{cases} T_{cold} + \frac{t}{t_{BOL}}(T(\mathbf{r},t_{BOL}) - T_{cold}), & \text{for } 0 \leq t \leq t_{BOL} \text{ (Startup)} \\ T(\mathbf{r},t_{BOL}) + \\ \frac{t-t_{BOL}}{t_{EOL}-t_{BOL}}(T_{Nom}(\mathbf{r},t_{EOL}) - T(\mathbf{r},t_{BOL})), & \text{for } t_{BOL} \leq t \leq t^k_{inc} \text{ (Incubation)} \\ \tilde{T}^k(\mathbf{r},t^k_{inc}) + \\ \frac{t-t^k_{inc}}{t_{EOL}-t^k_{inc}}(T^k(\mathbf{r},t_{EOL}) - \tilde{T}^k(\mathbf{r},t^k_{inc})), & \text{for } t^k_{inc} < t \leq t_{EOL} \text{ (Deformation)} \end{cases} \tag{5.26}$$

Between $t = 0$ and $t_{BOL} = 1$ FPD, a linear temperature evolution from an isothermal state T_{cold} to $T(\mathbf{r},t_{BOL})$ is considered, where $T(\mathbf{r},t_{BOL})$ is computed with a CFD simulation in the nominal (non-deformed)[15] geometry and with a power distribution corresponding to BOL. From t_{BOL} until t^k_{inc}, the temperature is assumed to evolve linearly as a consequence of the variation of the subassembly power with its burn-up. This linear evolution is computed by interpolating between $T(\mathbf{r},t_{BOL})$ and $T^{Nom}(\mathbf{r},t_{EOL})$, which is the temperature distribution obtained in the nominal geometry but with the EOL power distribution (note that it does not depend on the deformation level). Finally, between t^k_{inc} and the end of the irradiation, t_{EOL}, a linear evolution between $\tilde{T}^k(\mathbf{r},t^k_{inc})$ and $T^k(\mathbf{r},t_{EOL})$ is considered, where $T^k(\mathbf{r},t_{EOL})$ is obtained with a CFD simulation in the last computed EOL deformed geometry and with EOL boundary conditions, including the power level and the last computed mass flow rate which depends on the deformation of the fuel bundle (see Section 5.3.2). Then, to construct this temperature history, three CFD simulations are required for the first iteration if the subassembly power evolves with time—two of which, $T(\mathbf{r},t_{BOL})$ and $T^{Nom}(\mathbf{r},t_{EOL})$, are conducted in the same non-deformed geometry—, while only 2 are needed if the power is constant, like in the example presented in Figure 5.21. In both scenarios, one CFD simulation per additional iteration is required.

To define $\tilde{T}^k(\mathbf{r},t)$, the time t^k_{inc} still needs to be determined. We will see in Section 6.5 that the reduction of the coolant mass flow rate, that depends on the diametral deformation of the fuel pins, has a leading role in the global evolution of temperature. Motivated by this, to calculate t^k_{inc}, the last computed evolution of the creep and swelling induced diametral strain of each fuel pin p at the axial position of maximal EOL deformation, $\varepsilon^{k-1}_{Max,p}(t)$, is considered. By summing over all the fuel pins p we define:

[15] As discussed in Section 5.2.1, this means that the effects of thermal expansion on the temperature distribution are neglected at BOL, due to the little feedback they have on deformation.

$$\varepsilon_{Max}^{k-1}(t) = \sum_{p} \varepsilon_{Max,p}^{k-1}(t) \tag{5.27}$$

Then, we consider the following piecewise linear approximate function $\tilde{\varepsilon}_{Max}^{k-1}(t)$ that has a break at a time t_{inc}^{k}, which is its only free parameter:

$$\tilde{\varepsilon}_{Max}^{k-1}(t) = \begin{cases} 0, & \text{for } 0 \leq t < t_{inc}^{k} \\ \varepsilon_{Max}^{k-1}(t_{EOL}) \frac{t - t_{inc}^{k}}{t_{EOL} - t_{inc}^{k}} & \text{for } t_{inc}^{k} \leq t \leq t_{EOL} \end{cases} \tag{5.28}$$

Finally, the value of t_{inc}^{k} is determined, for an iteration k, by fitting $\tilde{\varepsilon}_{Max}^{k-1}(t)$ to the $\varepsilon_{Max}^{k-1}(t)$ calculated in the thermomechanical simulation of the previous iteration. The least squares method is employed for the fitting, an example of which is presented in Figure 5.22.

In Section 6.8, we compare the results obtained when the $\tilde{T}(\mathbf{r}, t)$ given by Equation 5.26 is used as input of a thermomechanical simulation, to the results obtained employing a $\tilde{T}(\mathbf{r}, t)$ computed with additional CFD simulation in partially deformed geometries, and to the one obtained with the "Linear T increment" approximation.

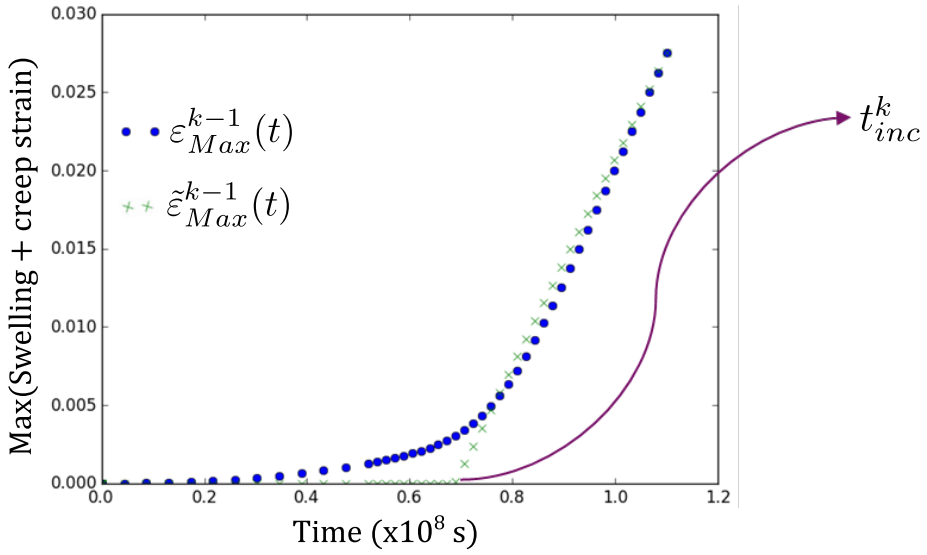

Figure 5.22.: Example of the fitting of $\varepsilon_{Max}^{k-1}(t)$ employed to determine t_{inc}^{k}.

5.4.2. Post-processing of the thermomechanical simulations

Cladding diametral strain

For the generation of the CAD model of a deformed fuel bundle, the axial profile of the deformed radius of each cladding needs to be specified. Three different methods have been implemented to compute these profiles; two for the 1D, beam based finite element model, and one for the detailed 3D model.

The first method is based on the use of an internal variable of the pipe elements that represent the claddings in the 1D model. This variable stores the diametral strain of the cladding computed, as described in Section 4.4.2, by taking into account the elastic and creep strains induced by the internal pressurization, the swelling strain, and the thermal expansion. In this case, the resulting axial profile has one value of cladding radius per pipe element.

The second method uses the diametral strain computed by the model of the modified bar element employed to represent the contacts between the claddings, and the claddings and the hexcan. In this case, the diametral strain of the cladding is computed considering the effects of internal pressure, swelling, creep, and thermal expansion, and it is corrected to take into account the effects of the pin crushing under the contact forces, as described in Section 4.4.2.

Then, when the beam based representation is employed, only the modified bar elements can account for the effects of contact on the diametral strain of the cladding. However, they are only present at the axial positions where contact is susceptible of occurring, i.e. every $1/6^{th}$ of the wire step. Therefore, the resulting diametral strain profile has lower axial resolution that the one obtained with the pipe elements, since at least 12 of them are used per wire step to represent the cladding. An additional limitation of using the modified bar elements arises from the fact that the same diametral strain is computed for the two claddings it connects, which could be exposed to different temperatures, irradiation dose and internal pressures and should, in that case, have different strains.

When the 3D finite element model is employed, the diametral deformation is computed directly from the deformed mesh, and it takes into account all the aforementioned effects. In this case, at each axial position and for each pin, the diameter increase at a calculation time t^i, $\Delta D(t^i)$, is computed by averaging the diameters within the cladding section as follows:

$$\Delta D(t^i) = \frac{1}{n}\sum_{l=1}^{n}(D_l(t^i) - D_{ec}) \tag{5.29}$$

where $D_l(t^i)$ is one of the n external diameters of the section at that calculation

time, i.e. the distance between diametrically opposed nodes on the external surface of the cladding mesh, and D_{ec} the initial external cladding diameter.

These three different methods to compute the axial distribution of the diametral strain of the claddings—namely, using the pipe elements, the modified bar elements, and the nodal displacements of the volumetric finite elements— were found to be in good agreement, specially in the prediction of the maximal strain. In the 1D modelisation, the retained method to compute the diametral strain is based on the pipe elements, and its results are compared to the results of the 3D model in Section 6.6. This choice was motivated by the higher axial discretization and by avoiding the limitation of the modified bars that consider a uniform dose, pressure and temperature in the contact areas, thus representing the average strain of two different—with potentially very different strain levels—claddings.

Cladding helical flexion

When the helical flexion of the cladding is represented in the CAD model used for the CFD simulations, additional information about the lateral displacement of the cross section of the claddings is required. The automatic post-processing of the cladding lateral displacement has been only implemented for the beam based model, which is the only one that can be employed for the simulation of fuel bundles of more than 19 pins[16]. In this model, the mesh of a given cladding coincides with its neutral axis, since it is precisely this axis that is represented with pipe finite elements. Then, displacements in the x and y directions, Δx and Δy, are computed for each node of the pipe elements, thus producing two axial profiles of lateral displacement per fuel pin, with one value per node each.

All the axial profiles mentioned above are stored in text files containing one scalar (cladding external radius or lateral displacement of the centerline of the cladding) per axial position computed by DOMAJEUR2, which are later read by the CAD generation algorithm described in Section 5.3.1.

5.5. Summary

In this chapter, we described the methodology developed in this work for the coupled thermal-hydraulic/thermomechanical simulation of SFR fuel bundles under irradiation. Firstly, we discussed the few preexisting coupled approaches and their limitations, mainly related to the use of simplified thermomechanical or thermal-hydraulic models (e.g. subchannel approach), and to not considering the effects of

[16] There is no particular technical difficulty related to the implementation of this post-processing on the 3D model, which was not done because it was not required for the simulations conducted in this work.

the bundle deformation on the mass flow rate of the coolant. Then, we introduced the methodology here developed, based on the OS coupling between STAR-CCM+, which computes the cladding temperature distribution in a deformed fuel bundle, and DOMAJEUR2, which computes the deformation of the bundle.

In this methodology, in order to limit the computational cost of a coupled simulation, the traditional OS technique, which would require updating the temperature distribution at regular time intervals during the thermomechanical simulation, is replaced by prescribing the time evolution of the cladding temperature distribution. This temperature history is given as input to DOMAJEUR2 at the beginning of the thermomechanical simulation of the irradiation of a fuel bundle, and this process is iteratively repeated until convergence. In each iteration, the cladding temperature history is updated to take into account the last computed bundle deformation. In this chapter, we discussed different methods for computing this temperature history based on the interpolation of CFD simulations of deformed bundles computed by DOMAJEUR2 at different instants during the irradiation, the choice of which renders the developed methodology very flexible.

To conduct CFD simulations in deformed fuel bundles, their CAD representation is required. In this chapter, we presented an algorithm developed to generate the CAD model of the fuel bundles based on the deformation computed by DOMAJEUR2. Additionally, the model implemented to take into account the reduction of the coolant mass flow rate caused by the deformation—based on computing the hydraulic resistance of a deformed subassembly—is also detailed.

Finally, we described the implemented automatic post-processing of the thermal-hydraulic and thermomechanical simulations—required for the information exchange between the coupled codes—, and we discussed the measures taken to render the coupled simulation methodology robust.

6. Reduced bundles study cases

In this chapter, we present a series of simulations of small SFR fuel bundles of 7 and 19 fuel pins, under conditions representative of their irradiation in a GEN IV SFR. Studying small fuel bundles, when compared to the larger bundles of 100-200 fuel pins typically employed in SFR, allows:

- To employ the detailed 3D model of DOMAJEUR2, practically applicable to small bundles only, and to compare the results with the 1D model, which is the only one that can be used for larger scale bundles;
- To conduct multiple different studies, with the goal of gaining insight on the coupling phenomena and thus guiding the development of the coupling methodology, while keeping the associated computational time reasonably low;
- To verify hypotheses adopted in the simulation methodology, while minimizing, once again, the computational cost of the simulations;
- To obtain a first evaluation of the impact of the deformation on the thermal-hydraulics of a SFR fuel bundle, and on the feedback this has on the deformation of the bundle. For a quantitative, best estimate evaluation, however, the full scale subassembly would need to be simulated.

This chapter is organized as follows. In Section 6.1, we define the studied fuel bundle and the simulation boundary conditions. Then, in sections 6.2 and 6.3 we evaluate the pertinence of two of the main modelling choices adopted in this work. These are, respectively, considering only the fluid domain in the CFD simulations, and not taking the neutronic feedbacks—consequence of the bundle deformation and of the associated temperature increase—into account. After that, in Section 6.4, we address the convergence of the coupled simulations presented in this chapter. The results of these simulations are discussed in sections 6.5, 6.6, and 6.7, where we address the impact of the deformation on the thermal-hydraulics of the bundle, and the effects of the coupling on the cladding strain and stress, respectively. Finally, in Section 6.8, we compare the different methods for generating the cladding temperature history used as input for the thermomechanical simulations, described in Section 5.4.1.

Table of Contents

6.1. Definition of the study case

Having in mind the goals outlined above, a bundle of 7 wire-wrapped fuel pins enclosed in a hexcan is here studied for different irradiation levels. The geometrical parameters and the thermal-hydraulic boundary conditions were chosen to be representative of the advanced SFR designed at the CEA, and they are presented in Table 6.1. Constant sodium properties for a temperature of 475°C (average between inlet and outlet of the bundle in nominal conditions) were employed.

Parameter	Value
Fuel pin length	2.136 m
Heated column length	0.8 m
Fuel pin pitch	10.8 mm
Fuel pin external diameter	9.7 mm
Spacer wire diameter	1.0 mm
Spacer wire helix step	180 mm
Maximum linear power	550 W/cm
Mass flow rate in nominal conditions	1.2 kg/s
Inlet sodium temperature	400°C
Hexcan plate to plate distance	30.6 mm

Table 6.1.: Geometric and thermal-hydraulic characteristics of the 7-pin fuel bundle.

Two different axial profiles of irradiation dose, with a maximum of 123 dpa and a maximum of 165 dpa respectively, were evaluated, and they are presented in Figure 6.1a together with the linear power profile used in all simulations[1]. There, and in

[1]The central region with lower power and irradiation dose observed in Figure 6.1a is characteristic of the axially heterogeneous fuel pin design of this advanced reactor, in which a central fertile

the rest of this chapter unless otherwise specified, the axial position is measured from the lower end of the heated column of the bundle. Both profiles were obtained by rescaling a reference dose profile computed for a shorter irradiation in the advanced SFR design and, even though the dose levels used in this study are superior to the ones envisaged for this reactor, they are a realistic representation of moderately to highly irradiated subassemblies. Indeed, a similarly high dose of about 160 dpa has already been reached in the BOITIX9 fuel bundle in Phenix SFR (Pelletier 2018). The internal cladding pressure was considered to evolve linearly in time during the irradiation, to reach 9 MPa at EOL, value close to the EOL internal pressurisation of Phenix fuel pins. In Figure 6.1b, the cross section of the CFD mesh of the non-deformed bundle is presented, and the pin naming system here employed is indicated. For all the CFD simulations here presented, the meshing procedure described in Section 3.3.5, and the mesh parameters defined and evaluated in Appendix A, were employed.

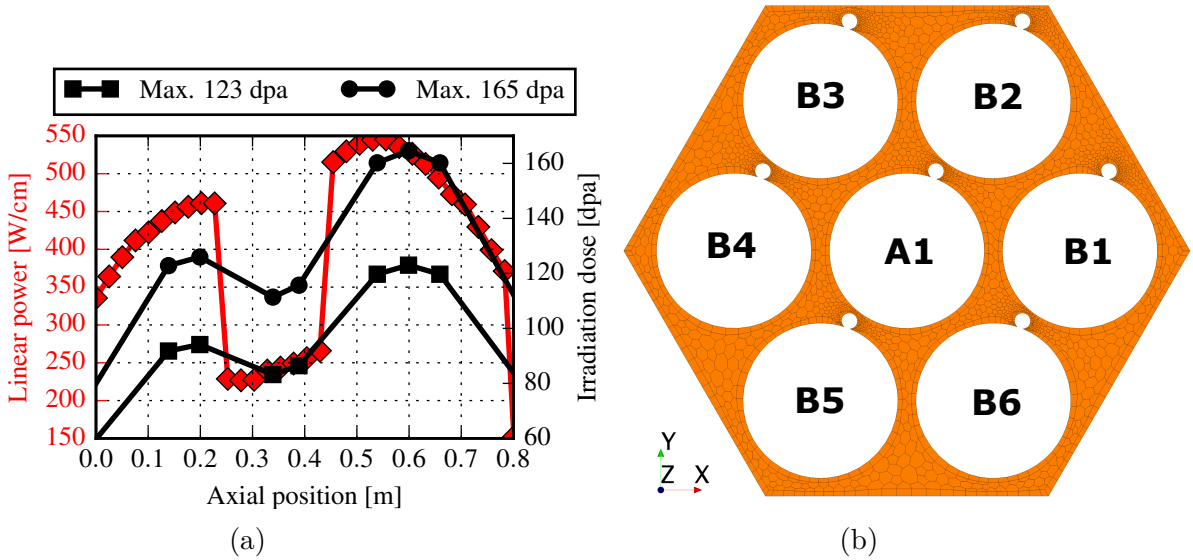

(a) (b)

Figure 6.1.: a) Axial profiles of linear power and irradiation dose employed in the numerical simulations of the 7-pin fuel bundle. b) Cross section of the CFD mesh at the outlet of the 7-pin bundle, where the pin naming system is indicated.

In the CFD simulations presented in this chapter, for the sake of simplicity and in order to limit their computational cost, the only deformation mechanism considered is the diametral strain of the claddings, while the thermomechanical simulations compute their ovalisation and flexion as well. The prioritization of the diametral strain was motivated, firstly, by its dominant impact on the coolant mass flow rate reduction (see Section 5.3.2) that, as we will show in Section 6.5, has a

column is included.

preponderant role on the thermal-hydraulics of deformed bundles. Additionally, by the fact that, unlike the fuel pin flexion that can be limited by reducing the step of the helical path of the spacer wires (Uwaba, Hiroyuki Ohshima, and M. Ito 2017), the diametral strain cannot be mitigated, at least until new, swelling resistant cladding materials are developed. The final motivation comes from considering that the mass flow redistribution that the pin flexion could cause would partially mitigate the expected coolant temperature increase due to the deformation, as discussed in Section 7.2. This would reduce the overall effects of the coupling on the central area of the bundle, where the maximal cladding temperature—a magnitude of major importance for reactor safety considerations—is located. For the studies here presented, partly aimed at evaluating the coupling effects in realistic but not necessarily optimistic conditions, this was not desired. The effects of the helical flexion of the fuel pins on thermal-hydraulics are nevertheless taken into account in the results presented in Section 7.2.

The ovalisation of the cladding, on its own, is expected to have a negligible effect on the thermal-hydraulics of the bundle, and thus on the coupling. However, in the 3rd phase of the bundle deformation (see Section 2.2.5)—not allowed in normal operation—the crushing of the cladding and the fuel pellet could lead to a significant change in the heat flux distribution in the circumference of the cladding. To take this effect into account, which is only expected to affect the cladding temperature locally, a model of the pellet and its interaction with the cladding would be required, which is out of the scope of this work but constitutes one of its future outlooks.

Additionally, in order to use similar coolant mass flow conditions to those of a subassembly undergoing significant deformation in the core of the advanced SFR designed at the CEA, the coolant mass flow rate was calculated according to the bundle deformation level, and the model and parameters described in Section 5.3.2 were employed.

Before presenting the results thus obtained—discussed in sections 6.4 to 6.8—we evaluate, in Section 6.2, the impact of considering only the fluid domain in the CFD simulations, and imposing a circumferentially uniform cladding heat flux as thermal boundary condition. Then, in Section 6.3, we evaluate the importance of the neutronic feedbacks caused by the deformation of the fuel bundle.

6.2. Conjugate heat transfer

In order to reduce the number of computational cells and to ease the convergence of the CFD simulations, only the fluid domain, defined by the coolant between

the fuel pins and the hexcan, is considered in this work. Then, since the cladding mid-thickness temperature is used as input by DOMAJEUR2, it is computed from the CFD-calculated cladding surface temperature by considering the radial heat conduction in the thickness of the cladding, as described in Section 5.3.4. Besides, an azimuthally uniform heat flux is imposed as boundary condition at the external surface of the claddings, while the spacer wires are considered adiabatic.

In reality, the heat conduction within the claddings is not only radial, since it also takes places in the tangential and axial directions. Besides, even if the heat flux at the internal surface of the claddings can be essentially considered azimuthally uniform[2], the heat flux on the external surface of the claddings is not necessarily uniform on their circumference, since it depends on the temperature distribution of the coolant. Finally, the average heat flux on the surface of the wires is expected to be significantly lower than the heat flux on the surface of the cladding, but it is not identically null. Then, in order to evaluate the adequacy of the hypotheses here employed, we conducted a CFD simulation in which the thickness of the cladding is considered.

For this simulation, the geometry and boundary conditions defined in Section 6.1 for the 7-pin fuel bundle under nominal conditions were employed. The non-deformed geometry was evaluated, and the volume of the spacer wires and of the claddings, of 0.5 mm of thickness, were included in the simulation, constituting the solid domain. The linear power profile presented in Figure 6.1a was also employed here to calculate the heat flux, in this case imposed as a boundary condition in the interior surface of the claddings. At the base and the top of the simulation domain, which corresponds to the heated column of the bundle, the surface of the claddings normal to the axis of the bundle were considered adiabatic.

Under these conditions, a Conjugate Heat Transfer (CHT) simulation was conducted with STAR-CCM+. In a CHT simulation, the heat conduction in the solid domain and the convection in the fluid domain are solved simultaneously, and they are coupled by the heat transfer between the solid and the fluid. The temperature distribution thus obtained, at the outlet of the heated column, is presented in Figure 6.2, where the mesh employed is also shown. The meshing procedure described in Section 3.3.5 and Appendix A was employed for the fluid domain, while a thetrahedral mesher was used for the solid domain. This resulted in approximately 2 million and 31 million cells in the fluid and solid domains,

[2]The temperature variation in the circumference of a non deformed cladding (up to ∼50°C), at a given altitude, is significantly smaller than the temperature difference between the centerline and the external surface of the fuel pellets—∼1500°C for MOX fuels—, which characterizes the heat flux from the pellet to the He filled pellet-cladding gap. Then, neglecting the circumferential heat transport in this thin gap, the cladding temperature variations should not significantly disrupt the azimuthal symmetry of the heat flux at its inner surface.

respectively. The resulting fluid and solid meshes are non-conformal (i.e. the faces of the cells adjacent to the interface do not match exactly), so an indirect mapped interface was employed between the two domains. In this approach, a proximity based mapping algorithm is used to transfer information—thermal energy in our case—from one side of the interface to the other.

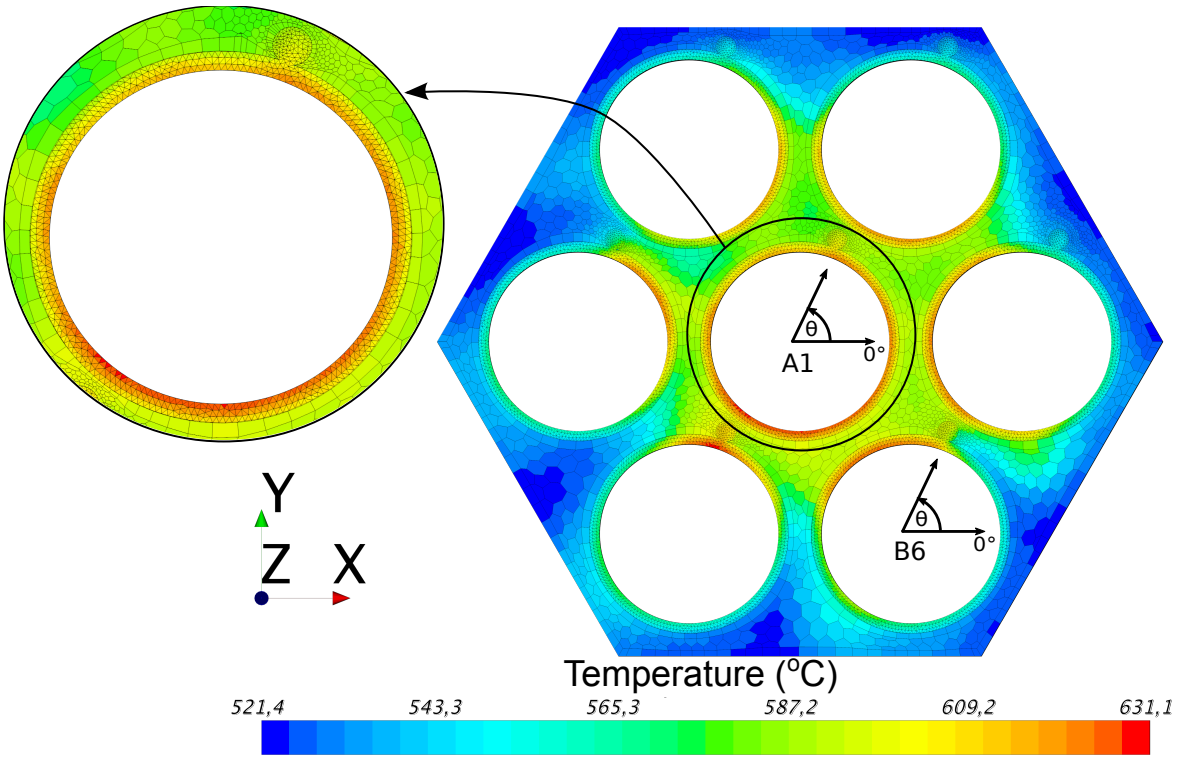

Figure 6.2.: Temperature distribution at the outlet of the heated column, computed by the CHT simulation.

In Figure 6.3, the cladding surface temperature obtained for the central pin A1 with the CHT simulation is compared to the one obtained with a CFD simulation in which only the fluid domain is considered. Two axial temperature profiles are presented in this Figure for each simulation, corresponding to azimuthal angles (θ) of 0° and 120°. In Figure 6.4, the same comparison is presented for the peripheral pin B6. In both figures, a very good agreement is observed between the CHT and the fluid only simulation, as expected from the sodium conductivity being ~ 3 times larger than the conductivity of the cladding.

In Figure 6.5, the difference between the temperature profiles computed by the CHT and the fluid only CFD simulations is presented as a function of the axial position. The results there presented correspond to the peripheral pin B6, that

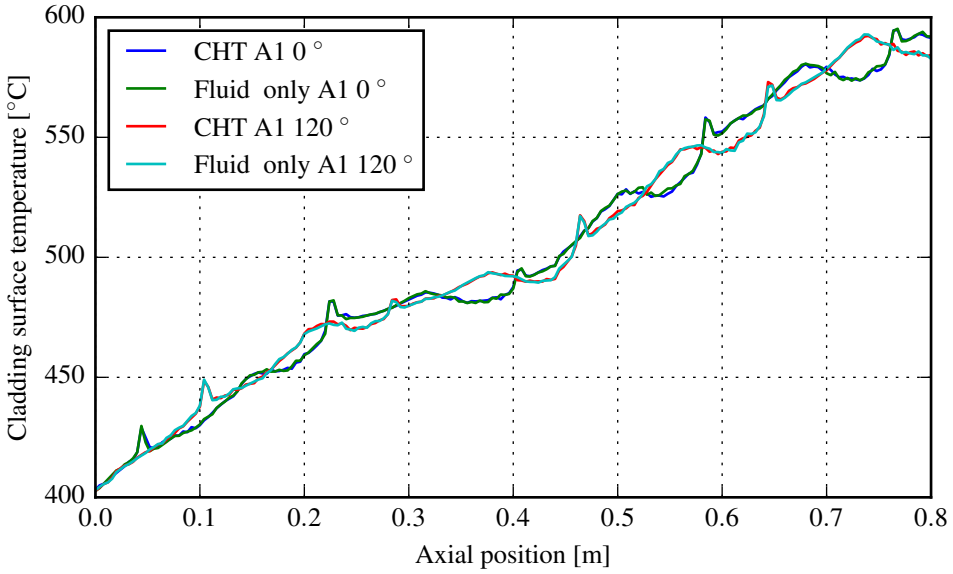

Figure 6.3.: Axial profile of cladding temperature at its external surface, computed by the CHT and by the fluid only CFD simulations, for the central pin A1. The profiles correspond to azimuthal angles of 0° and 120°.

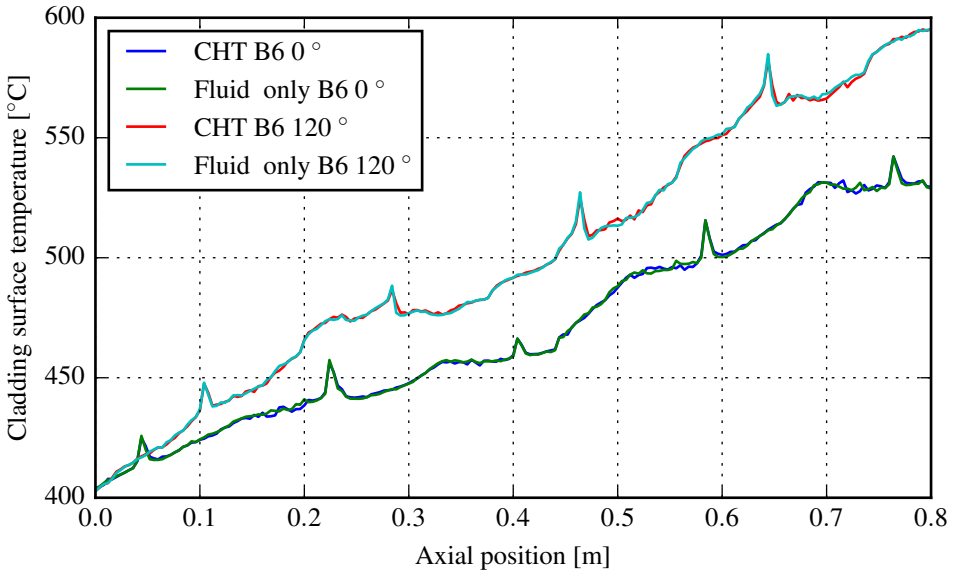

Figure 6.4.: Axial profile of cladding temperature at its external surface, computed by the CHF and by the fluid only CFD simulations, for the peripheral pin B6. The profiles correspond to azimuthal angles of 0° and 120°.

showed a difference between the two simulations slightly superior to that of the central pin. It can be observed that, for most of the length of the bundle, the CHT simulations leads to temperature values that differ in less than 2°C from the results obtained by considering only the fluid domain. However, local differences of up to 4.5°C can be observed at some axial positions, which correspond to the intersections of the sampling line with the spacer wire, and to the points at which a neighboring wire becomes closest to the sampling line.

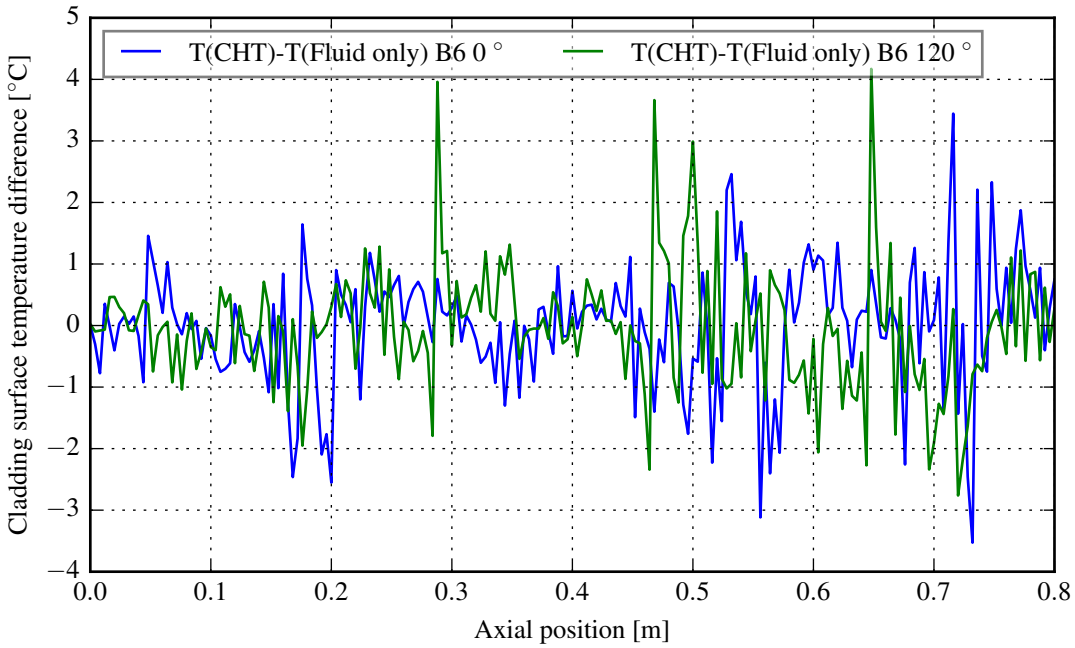

Figure 6.5.: Axial distribution of the difference in the cladding surface temperature computed by the CHT and by the fluid only CFD simulations, for the peripheral pin B6, at azimuthal angles of 0°and 120°

In Figure 6.6, the cladding temperature distributions at its external and internal surfaces, computed for the peripheral pin B6 at an angle of 120° by the CHT and the fluid only CFD simulations, are presented. In the CHT, both the internal and external cladding temperatures are computed by the CFD simulation. In the CFD simulation in which only the fluid is represented, only the cladding temperature at its external surface is computed. In this case, the temperature at the internal surface of the cladding is calculated from the external temperature and the local linear power, by considering the radial heat conduction in the thickness of the cladding (see Equation 2.17). It can be observed in this figure that both approaches lead to very similar results, which, for the internal cladding surface, differ in less than 1.5°C in average. However, a maximal difference of 11°C was obtained at

the limits of the fertile blanket, where the linear power changes abruptly. This relatively high difference is very localized, and it should be lower if the comparison was conducted at the mid-thickness point of the cladding[3], which is the temperature actually exported to be later used as input for the thermomechanical simulations.

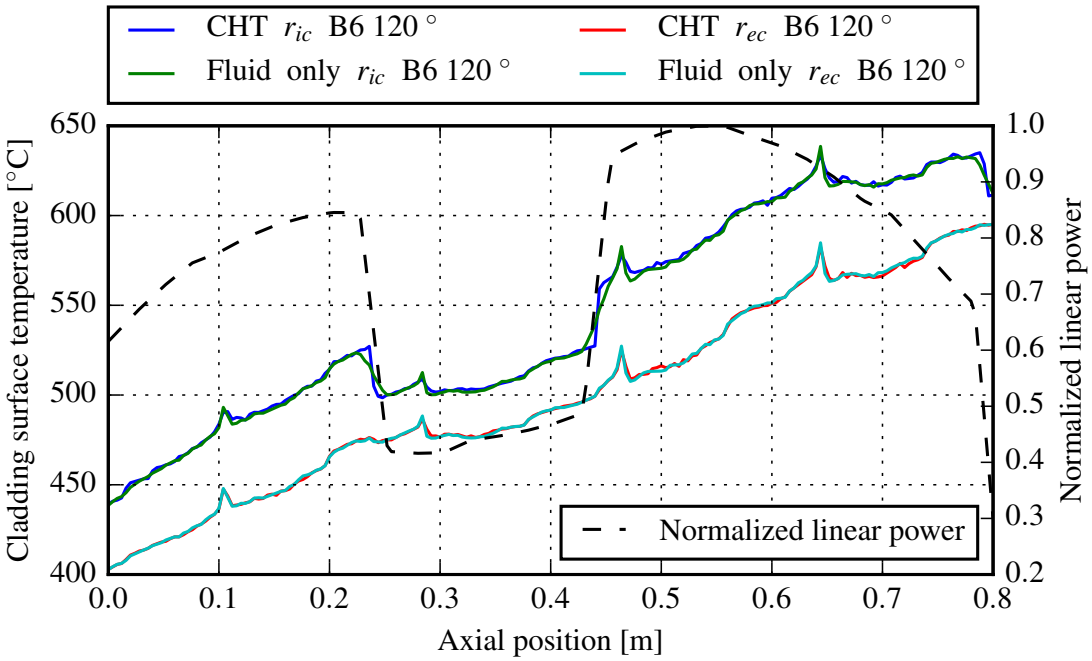

Figure 6.6.: Comparison of the cladding temperature at its internal surface (at a radius $r = r_{ic}$) and at its external surface ($r = r_{ec}$), as computed by the CHT and the fluid only CFD simulations. The profiles presented correspond to the peripheral pin B6 at an azimuthal angle of 120°. The normalized profile of linear power is also presented.

The heat flux on the circumference of the cladding of the central pin A1, at its external wall, is presented in Figure 6.7a as a function of the azimuthal angle, at the axial position of the compact plane closest to the maximal heat flux ($z = 0.555$ m). In the compact planes, the wire of a given pin becomes closest to the cladding of a neighboring pin, thus inducing a local perturbation in its temperature distribution, which is why this axial position was chosen for the present analysis. The results obtained for the peripheral pin B1 are presented in Figure 6.7b. It can be noted

[3]This was not done because at the cladding mid-thickness there are not always cell centroids present. Then, if the temperature was probed at his point, the temperature of the nearest cell would be reported. On the other hand, the temperature at the internal and external surfaces of the cladding is always computed.

in these figures that the amplitude of the variation of the heat flux is, for most of the cladding circumference, inferior to 15% of its average value. However, large perturbations are induced by the spacer wire of the considered pin, at an angle of -60°, and by a neighboring wire that approaches the considered pin, at an angle of 120°. At these points, the heat flux departure from its average in the circumference exceeds 50% of this average, but this is only for a few computational cells (i.e. for a very small surface). It should be noted that, besides, the computational cells affected are significantly smaller than the average cell on the surface of the cladding, since the mesh is refined at the intersection of the spacer wire and the cladding, and close to the point where a wire comes closest to a neighboring cladding. Therefore, the heat exchanged in these cells, product of the heat flux and the cell surface in contact with the wall, remains limited.

In this simulation, the average heat flux of the spacer wires was 10 times smaller than the average on the surface of the claddings so that, for our application, considering adiabatic wires is judged to be adequate. If deemed necessary for a best estimate simulation, this information—or a similar analysis conducted under conditions representative of the case of interest—could be used to introduce a multiplicative factor, inferior to unity, to calculate the heat flux profile to be employed for the spacer wires from the one used for the claddings, instead of considering the wires adiabatic. However, note that this procedure would lead to higher temperatures than the CHT simulation near the contact between a cladding and a spacer wire, since in these areas the heat was observed to flow from the sodium into the wire, and not the other way around. Nevertheless, this local temperature overestimation would not affect the prediction of the macroscopic evolution of the geometry of the bundle under irradiation.

In view of the results presented in this section, the simplifications made considering the heat flux distribution and the heat conduction within the claddings are considered adequate for the purposes of this work. It should be noted that the ovalisation of the cladding was not considered in this analysis, although it might disrupt the azimuthal symmetry of the heat flux. This effect—also expected to have only a local impact on temperature—could be potentially larger, since it would change the thermal resistance from the centerline of the fuel pellet. Studying the impact of the cladding and fuel pellet ovalisation on the heat exchange characteristics of the fuel bundle is therefore one of the future outlooks of this work.

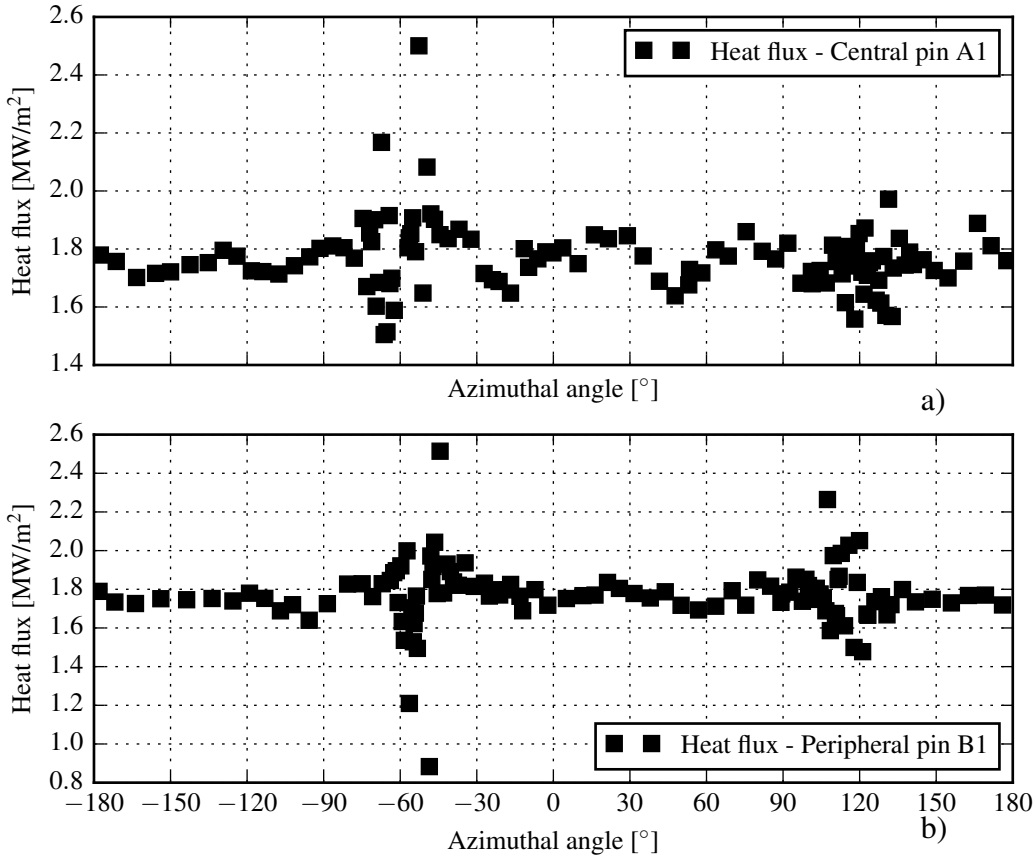

Figure 6.7.: Heat flux as a function of the azimuthal angle, for the central pin A1 (a) and the peripheral pin B1 (b), at the axial position $z = 0.555$ m.

a

6.3. Neutronic feedbacks

In this section, we evaluate the effects of the cladding diametral strain of highly deformed subassemblies on the reactivity of an SFR core and on its power distribution. These effects, caused by the neutronic feedbacks discussed in Section 2.3.2, arise mainly from:

- The sodium being *displaced* by the diametral strain of the claddings, which leads to less sodium being present in the deformed cross section of the subassembly. The resulting effects are not the same in the central region of the core of the reactor, where the neutron energy spectrum hardening and the neutron absorption reduction dominate, than in its peripheral region, where the effect on neutron leakage becomes more relevant;

- The change in sodium density, caused by the sodium temperature increase observed in the deformed bundle, the effects of which have the same spatial dependence than the sodium displacement;
- The Doppler effect, associated to the fuel temperature increase caused by the sodium temperature increase.

Cases evaluated

In particular, we consider an enveloping value of 6% diametral strain of the claddings in the entire fissile column of some subassemblies of the advanced SFR designed at the CEA. The cases here evaluated are:

- Case I: 6 deformed central subassemblies;
- Case II: 6 deformed peripheral subassemblies;
- Case III: 45 deformed central subassemblies (one fourth of the total number of subassemblies).

Reactivity feedbacks considered

The outlet sodium temperature increase of a subassembly with 6% diametral strain in its entire fissile column is $\sim 35°C$[4], which induces a 0.6% reduction in the average sodium density within the bundle. This reduction is more than 50 times smaller than sodium density reduction equivalent to the sodium displacement caused by the 6% diametral strain, which, additionally, affects the entire fissile length. For this reason, this temperature-induced sodium density change is not considered in what follows. This means that the same sodium temperature is considered for the deformed and non-deformed subassemblies.

Additionally, as discussed in Section 2.3.2, the Doppler reactivity feedback associated to a 50°C fuel temperature increase in the entire core of the advanced SFR designed at the CEA is only of about 20 pcm. Even in the very conservative Case III, the average sodium temperature increase induced by the deformation evaluated in this section—within the entire active length of the core— is lower than 5°C[5]. Then, in what follows, this effect is not considered, which means that the same fuel pellet temperature is considered for the deformed and non-deformed subassemblies.

The remaining reactivity feedback is caused by the sodium displaced by the diametral deformation of the fuel claddings, and it is evaluated in this section.

[4] As estimated using the coolant mass flow rate model presented in Section 5.3.2 (see Figure 5.16) and Equation 2.15.

[5] Considering a 35°C outlet temperature increase in each deformed subassembly.

Neutronic simulation model

To evaluate this effect, we employed the CEA neutronic calculation code system ERANOS, based on the simulation codes ECCO and TGV/VARIANT (Ruggieri, Tommasi, Lebrat, et al. 2006). The neutronic simulation scheme is divided into two main stages to compute the distribution of the neutron population in the core—and its derived variables—, namely the cell and core calculations. This division is motivated by the existence of geometric parameters at the subassembly scale that are very small when compared to the size of the core of the reactor.

In each cell calculation, performed with ECCO, the cross section of the geometry of one subassembly is represented in detail, and it is finely meshed. Typically, the subassembly is considered to be infinite in the direction perpendicular to its cross section, so the simulation is 2D. This stage allows to compute the energy dependent neutron cross sections of each material in the cell. These cross sections are then averaged in space (homogenized) and discretized in energy groups (condensed), to be later used as input for the core calculations. With ECCO, the neutron transport equation, that rules their space, time and energy distribution, is solved in the cell employing the Collision Probability method (Stamm'ler and Abbate 1983). In practice, a different cell calculation is conducted for each different type of subassembly, and for each axial position with a different composition or geometry. For example, different cell calculations are required for the fertile and fissile columns of the fuel subassemblies.

In the core calculations, performed with TGV/VARIANT, a coarser energy discretization and geometric description of the entire core is used, and, in general, a more approximate method is employed to solve the neutron transport equation than the one used at the cell level. In the simulations here conducted with TGV/VARIANT, the SP_N method was employed (McClarren 2010). The details in the geometry of each subassembly (fuel pin bundle, spacer wires, fuel pellets, etc) are not explicitly represented. Instead, each of the volume meshes in which the core is divided is assigned the homogeneous neutron cross sections previously computed by a cell calculation representative of that sector.

In Figure 6.8a, a cross sectional view of an angular sector of the core of the advanced SFR is presented. The positions of the fuel subassemblies of the internal and external core, that have different characteristics, are indicated. Each hexagon observed in the presented cross sectional view corresponds to a different subassembly, within which an homogeneous—in the cross section—material is specified for the core calculation. Each subassembly is divided axially in about a dozen different sectors, to which different neutron cross sections are assigned. In Figure 6.8b, the cell model of one fuel subassembly is presented, and a zoom on one fuel pin is shown in Figure 6.8c, where the different components that constitute the cell are identified.

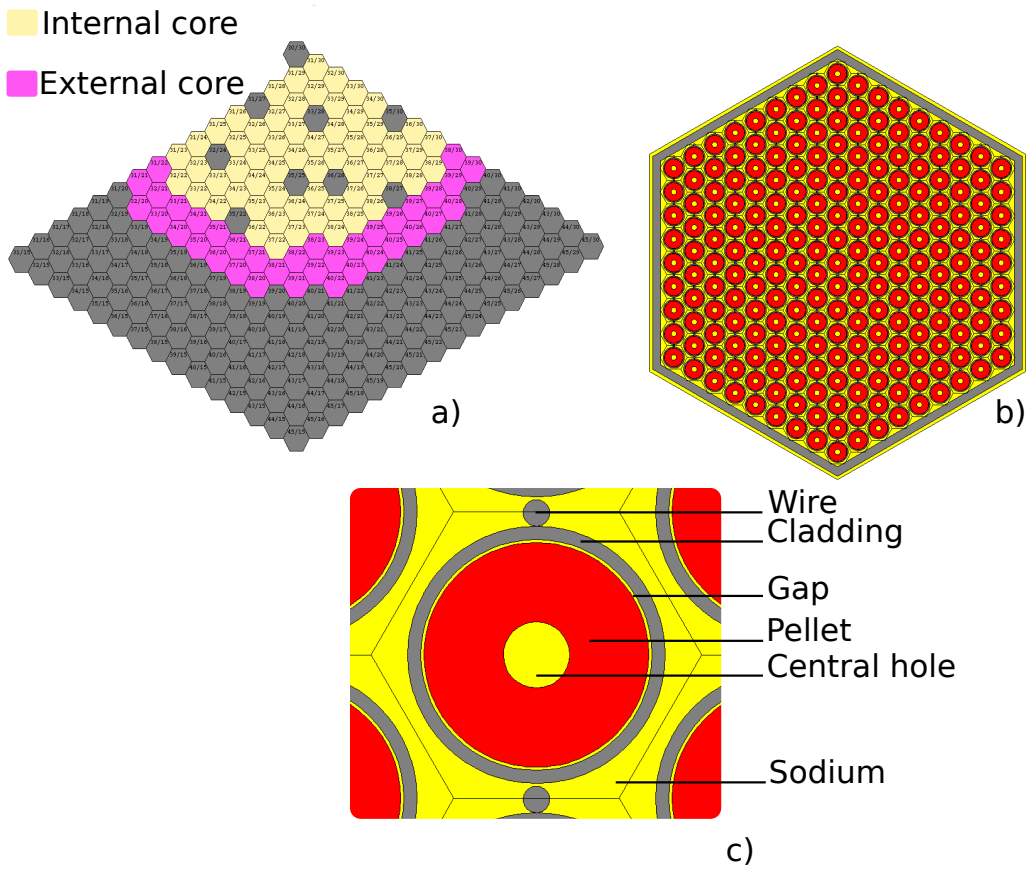

Figure 6.8.: a) Angular sector of the cross section of the core, where the internal and internal subassemblies are indicated. b) Cell representation of one fuel subassembly. c) Zoom on one fuel pin in the cell representation of a fuel subassembly, in which different components of the cell are indicated.

For the simulations conducted here, we employed a preexisting core model of the advanced SFR designed at the CEA, and preexisting cell models of all the subassemblies defined in that core model. Then, to evaluate the effects of the subassembly deformation on neutronics, a new cell model for the fissile column of a deformed fuel bundle was firstly defined. The geometric parameters that characterize the cell are presented in Table 6.2, where they are compared to those of the cell model of the non-deformed fissile column. In the deformed cell, the external radius of the cladding was increased by 6%, and its thickness and the thickness of the gap between the fuel pellet and the cladding were defined as to conserve the cladding mass in the cell. Since the dimensions of the fuel pellet are not modified, its mass is also conserved. The main consequence of the change in geometry is a 31% reduction in the total sodium in the cell, the effect of which we

Parameter	Nominal geometry	Deformed geometry
Central hole diameter [mm]	2.49	2.49
Pellet diameter [mm]	8.47	8.47
Fuel/Clad Gap [mm]	0.115	0.4372
Cladding thickness [mm]	0.5	0.4688
Spacer wire diameter [mm]	1	1
Axial wire step [mm]	180	180

Table 6.2.: Geometric characteristics of the cell model of the nominal and of the deformed fissile column.

want to quantify. For simplicity, the densities of the materials in the deformed cell were not modified, which, considering the increase in the thickness of the gap, led to an increase in the mass of Helium, the gas employed in the model to fill this gap. Since Helium is in gaseous form and it is not a strong neutron observer, its macroscopic neutron cross section is very low. Then, it barely interacts with the neutrons, so increasing its mass in the gap does not have a significant impact on the results.

The new cell model was used to obtain the homogenized and condensed neutron cross sections employed to represent the deformed subassemblies in three new core models, one for each of the study cases I,II, and III, defined above. In each case, only the fissile column of the deformed subassemblies was modified. Then, core calculations were conducted with each model to obtain the neutron flux distribution— and thus the power distribution—and the reactivity of each case, keeping the total reactor power constant.

Results

In Table 6.3, the maximal power change in the deformed subassemblies and in the reactivity, with respect to the reference core, are presented for each case. As an example, the position of the deformed subassemblies in Case I is indicated in Figure 6.9a, and the resulting distribution of subassembly power change in an angular sector of the core is presented in Figure 6.9b.

It can be noted that the deformation of 6 central or peripheral subassemblies has a negligible impact on reactivity, and a very small effect on the subassembly power. As can be observed in Figure 6.9, the subassemblies adjacent to the deformed ones are more affected than the deformed subassemblies themselves, consequence of the large neutron mean free path. Even if Case III is well beyond the scope of this work—in which we focus on the simulation of one, or a few, highly deformed subassemblies in a non-deformed core—, the computed reactivity change in this

Case N° (N° of deformed subassemblies)	Position	Reactivity change [pcm]	Maximum change in subassembly power [%]
I (6)	central	+9	+0.3
II (6)	peripheral	+9	+0.2
III (45)	central	+50	+1.65

Table 6.3.: Reactivity change and maximum change in subassembly power obtained with the three different cases here evaluated, with respect to the nominal, non-deformed core.

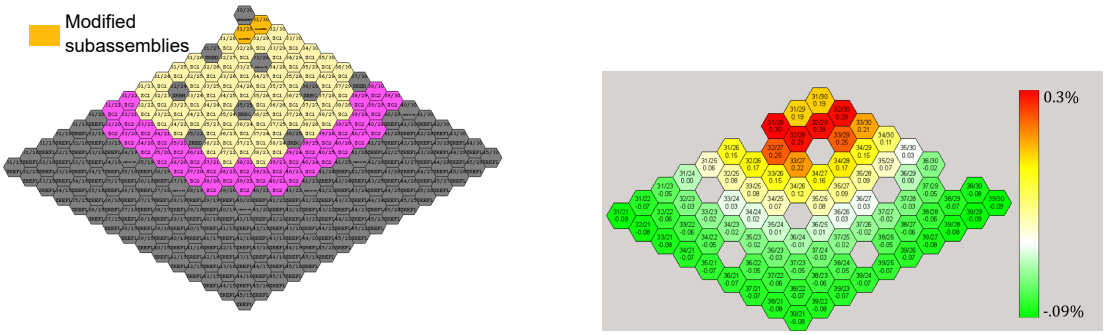

(a) (b)

Figure 6.9.: a) Angular sector of the core of Case I, where the modified subassemblies are indicated in yellow. The core presents a 120°symmetry. b) Distribution of the subassembly power change computed in Case I with respect to the nominal, non-deformed core.

case remains small, and so is the maximal change in subassembly power.

These results confirm that the neutronic effects linked to the sodium displacement caused by the bundle deformation—as the neutronic effects associated to the deformation induced temperature increase—are of second order, and they are therefore not considered in the coupled simulations presented in this work.

6.4. Convergence of the coupled simulations

In this chapter, the maximum number of iterations was prescribed at the beginning of each coupled simulation, and the convergence was monitored by evaluating the difference, between successive iterations, in the computed axial profiles of diametral deformation of the claddings and in the axial profiles of cladding surface temperature. In every simulation here evaluated, less than 5 global iterations were required

to reach convergence. In this section, we present an example of the convergence of a coupled simulation—corresponding to the case with a maximal dose of 165 dpa described in Section 6.1—, the results of which are described in detail in sections 6.5 and 6.6.

The computed diametral strain profiles of the central pin of the bundle are presented in Figure 6.10a, as computed by DOMAJEUR2 in each iteration. In Figure 6.10b, axial temperature profiles on the surface of the same pin are presented, as obtained with the successive CFD computations of the coupled simulation. It can be noted that the strain and temperature profiles are in very good agreement between all the simulations after the 3^{rd} iteration. The absolute value of the maximal difference, between successive iterations, of the computed diametral strain and cladding temperature are presented in Table 6.4. It can be there noted that the maximal strain and temperature differences between the last two DOMAJEUR2 and CFD simulations are 0.02% and 1.1°C, respectively, so we can consider that the coupled simulation has converged.

Simulations considered	Maximal strain difference [%] (absolute value)	Maximal temperature difference [°C](absolute value)
0-1	1.9	50.8
1-2	0.4	14.3
2-3	0.1	3.5
3-4	0.02	1.4
4-5	-	1.1

Table 6.4.: Absolute maximal difference in the strain of the central pin, averaged on its circumference, and in the cladding surface temperature of the same pin at $\theta = 0°$, between successive simulations.

In Section 5.2.1, we showed that the iterative process resulting from an OS coupling could be understood as performing fixed point iterations of an operator Φ. In that section, we saw that Φ being a contractor (see Equation 5.2) in a domain including both the first iterand and the fixed point solution is sufficient to guarantee the convergence of the iterative process. In our application, the contracting character implies that the difference (in temperature or deformation) between two successive iterations n and $n+1$ is monotonically reduced with growing n. Given the complexity of our problem, proving this condition is met is extremely challenging. However, the results presented in this section allow to qualitatively show the contracting character of the operator involved in the iterative process, which leads to its convergence.

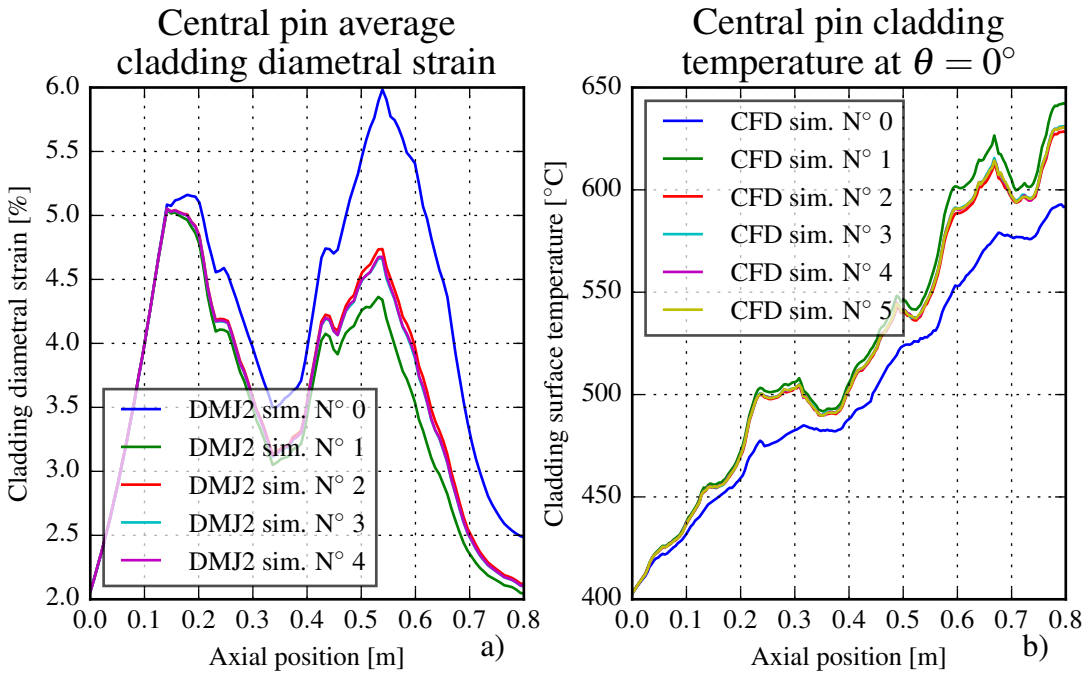

Figure 6.10.: a) Axial profiles of the average diametral strain of the central pin, computed by the successive DOMAJEUR2 calculations in one coupled simulation. The N°0 simulation uses the nominal temperature distribution as input. b) Axial profiles of cladding surface temperature of the central pin, at an angle $\theta = 0°$, computed with the successive CFD calculations in one coupled simulation. The N°0 simulation is conducted in the non-deformed geometry, and it provides the nominal temperature distribution.

6.5. Impact of deformation on thermal-hydraulics

To study the impact that the deformation has on the thermal-hydraulic behavior of the fuel bundle, we conducted CFD calculations in the non-deformed bundle and in two different deformed bundles, computed with DOMAJEUR2 under the conditions described in Section 6.1. For these simulations, unless otherwise specified, the coolant mass flow rate was adjusted in order to consider the effects of the deformation of the bundle.

The first bundle presents an average diametral deformation of 2.0 %, corresponding to an EOL maximum irradiation dose of 123 dpa, while the average diametral strain of the second one is 4.9 %, associated to a maximum dose of 165 dpa. It is worth noting that, even though the same irradiation dose profile was employed for all fuel pins, they present different deformation levels due to the non-uniform temperature distribution within the bundle. Using the mass flow rate model de-

scribed in Section 5.3.2 resulted in a reduction—with respect to the nominal mass flow rate of the non-deformed bundle—of 6% for the less deformed bundle (123 dpa, 2.0% average diametral strain), while a 17% reduction was obtained for the most deformed one (165 dpa, 4.9% average diametral strain).

Axial temperature profile and maximal temperature

The axial profiles of cladding surface temperature of the central pin of the bundle are presented, for the three deformation levels studied, in Figure 6.11a, while the axial profiles of sodium bulk temperature are presented in Figure 6.11b. The cladding surface temperature profiles presented were obtained by averaging, for each axial position, the temperature over one sixth of the cladding circumference, and they correspond to the cladding arc centered on the point closest to pin B1, indicated in Figure 6.11a by a red star. Increases of average sodium temperature of 9°C and 30°C are observed at the outlet of the heated column of the least and most deformed geometries, respectively, with respect to the non-deformed bundle. It can also be observed that the local perturbations due to the spacer wires are augmented as the deformation increases.

In addition, the maximum cladding surface temperature, obtained by averaging over on sixth of the claddings circumferences, increases from 600°C in the nominal geometry to 657°C in the most deformed bundle, and the dispersion in the maximum temperature of the different fuel pins is also augmented with the deformation. Its standard deviation increases from 4.7°C in the nominal geometry to 8.1°C in the most deformed one.

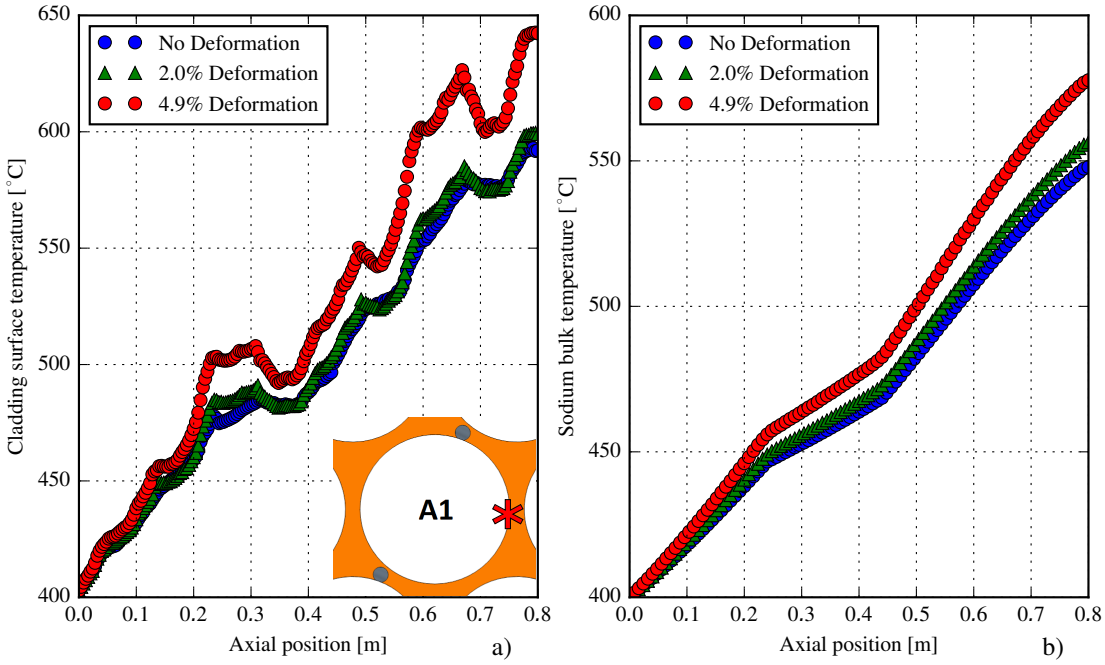

Figure 6.11.: Cladding surface temperature along the heated length of the central pin, obtained by averaging for each altitude, over one sixth of the cladding circumference centered in the red cross indicated in the diagram (a) and axial profiles of sodium bulk temperature (b) for the deformed and non-deformed bundles.

Mass flow rate reduction

It should be noted that the results presented above are a consequence of the deformation itself, but also of the coolant mass flow rate reduction associated with it, which has a preponderant role. To illustrate this, the temperature distribution obtained in the non-deformed bundle was compared to the ones obtained in the most deformed bundle (4.9% average diametral strain) considering the reduction of the coolant mass flow Q and keeping its nominal value. The resulting temperature distributions are presented, over two diagonals at the outlet of the heated column of the bundle, in figures6.12a and 6.12b. These diagonals are indicated in Figure 6.12c, where the nominal outlet sodium temperature distribution is shown.

It can be noted in Figure 6.12 that the reduction of the coolant mass flow rate induces temperature changes, with respect to the nominal temperature distribution, significantly larger than those caused by the change in geometry alone. Additionally, it can be observed that the temperature asymmetry induced by the spacer wires is increased by the deformation, since their influence is increased as they become closer

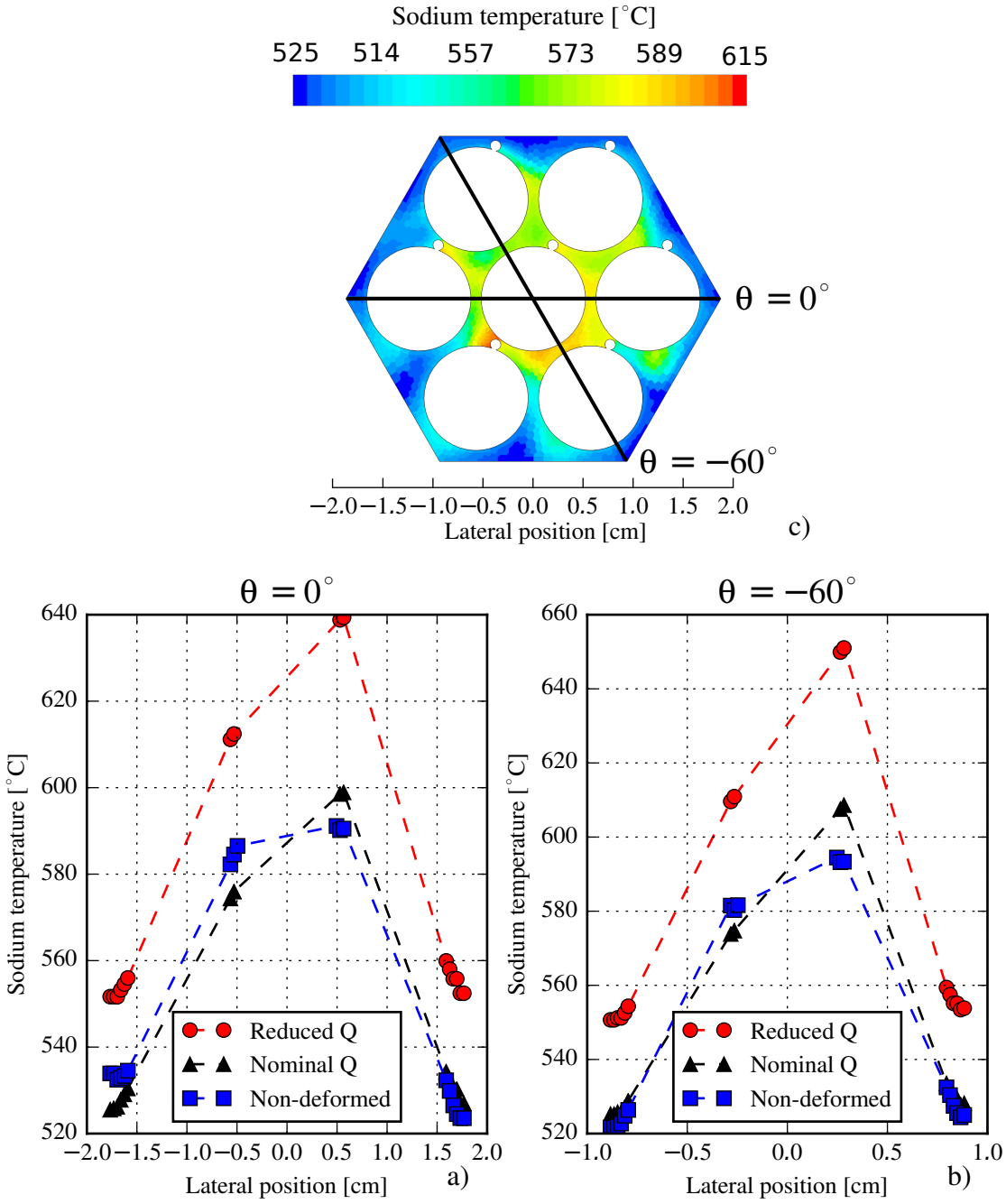

Figure 6.12.: Sodium temperature at the outlet of the heated column computed in the non-deformed geometry, and in the most deformed geometry—with an average diametral strain of 4.9%—with and without reducing the coolant mass flow rate. The temperatures sampled over a diagonal at $\theta = 0°$ are presented in (a), the ones sampled over a diagonal at at $\theta = -60°$ in (b), and these two diagonal sampling lines are indicated in (c), where the outlet sodium temperature distribution in the nominal geometry is presented.

to the neighboring pins with the diametral strain of the claddings. This increased asymmetry leads to sodium temperature increments in some regions—with respect to the nominal temperature distribution—and temperature reductions in other areas. When the mass flow rate reduction is considered, the superposition of the increased asymmetry and the increase of bulk temperature lead to higher sodium temperature at all the evaluated points. In the results presented in what follows, the mass flow rate reduction associated to the evaluated deformation levels are taken into account.

Circumferential temperature gradients

The deformation of the bundle also leads to a significant increase in the azimuthal temperature gradients around the fuel pins. To illustrate this, the peripheral pin B6 (see Figure 6.1b) was selected. The sodium temperature on its surface was sampled every 60 degrees, at the outlet of the heated column of the bundle, and its distribution around the circumference of the pin is presented in Figure 6.13 for the 3 deformation levels evaluated. The increase of the azimuthal temperature gradients with deformation is evidenced by the departure from the regular hexagon shape that would be obtained in a zero gradient case. The maximum temperature difference between diametrically opposed points on the surface of the cladding increases with the deformation. In particular, the difference between the maximum and minimum temperature computed at those 6 points increases from 62°C in the nominal geometry to 66°C in the 2.0% deformed geometry, and to 96°C in the 4.9% deformed geometry.

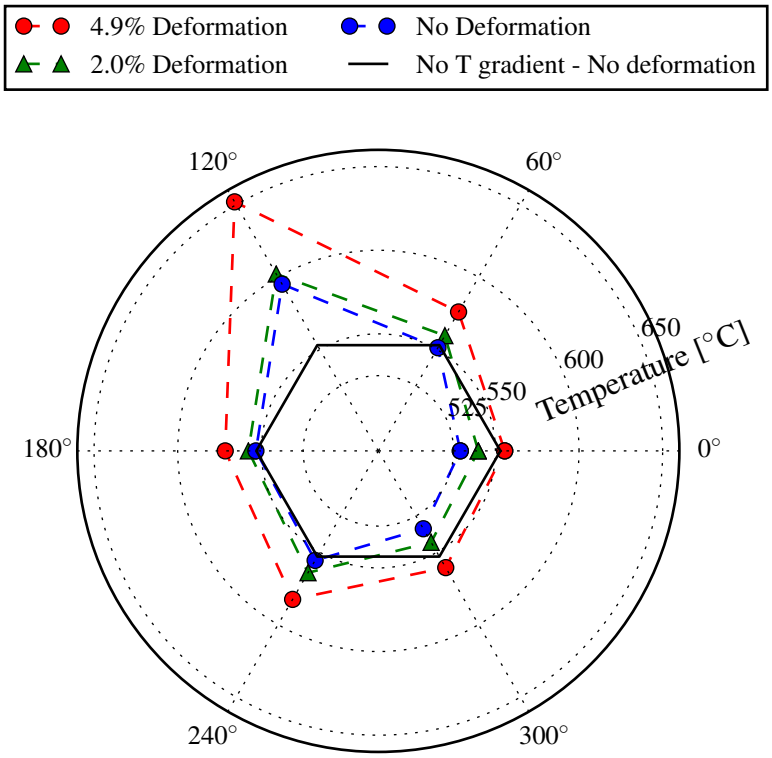

Figure 6.13.: Temperature distribution around the peripheral pin B6, at the outlet of the heated column, in the deformed and non-deformed geometries.

Local flow disruptions

Additionally, the deformation of the bundle leads to the contact between spacer wires and neighboring fuel pins, which, besides giving place to hot spots in the cladding in the contact area, induces local sodium flow disruptions. As an example, Figure 6.14 illustrates how the contact between spacer wires and neighboring pins, at the outlet of the heated column, completely blocks the sodium flowing from the colder periphery to the hotter central region, and vice versa, in the regions where contact occurs. In this figure, the temperature scales have been adjusted as to highlight the sodium cold and hot jets flowing into and from the central region, respectively, which are absent in the deformed bundle.

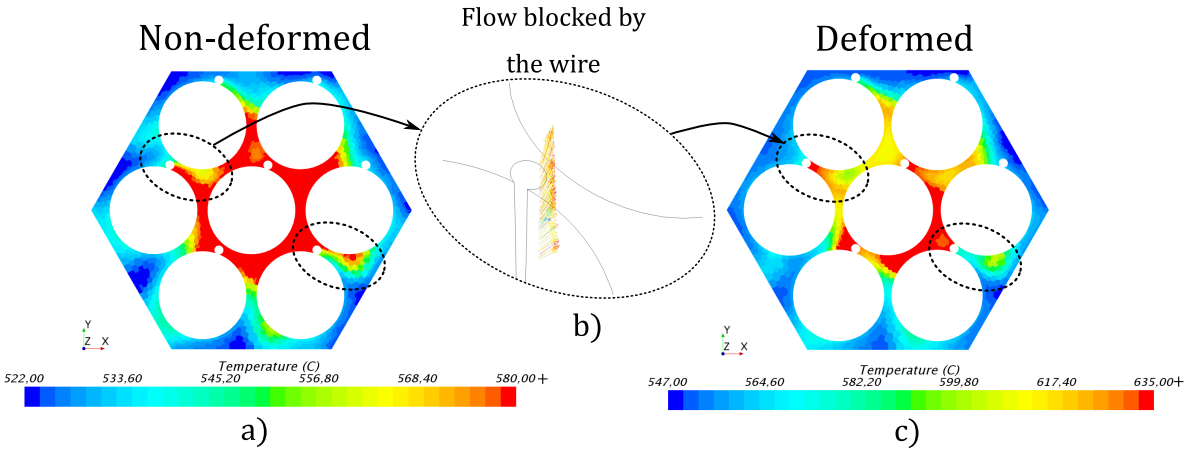

Figure 6.14.: Sodium temperature at the outlet of the heated column of the non-deformed (a) and deformed (c) bundle. The sodium velocity vectors in one of the gaps closed by the deformation is also presented (b).

Section summary

The results presented in this section show that the diametral deformation of the fuel pins induces a significant increase in the sodium temperature, which grows with the axial position within the bundle and is mainly caused by the deformation-induced sodium mass flow rate reduction. Additionally, the deformation leads to a large increase in the circumferential temperature gradient on the surface of the claddings, and to the closing of the gaps between pins that—besides leading to hot spots in the cladding—significantly affects the sodium cross flow. To determine these two effects, a detailed thermal-hydraulic model, in which the wires are explicitly represented, is required. Finally, all these effects become relevant only for high irradiation dose levels, and were not observed for an irradiation dose lower than 125 dpa.

The temperature perturbation described above, induced by the deformation, has a feedback on thermomechanics. To assess this effect, coupled thermomechanical/thermal-hydraulic simulations of the irradiation of the 7-pin fuel bundle were conducted, and the results are presented hereafter.

6.6. Effects of the coupling on the bundle deformation

The irradiation of the 7-pin bundle was simulated employing the coupling methodology described in Section 5.2 for the two different dose levels presented in Figure 6.1a

and evaluated in the previous section. The detailed 3D model of DOMAJEUR2, described in Section 4.4.1 was employed.

To construct the cladding temperature histories used as input for the thermomechanical simulations, the Linear Temperature Increment method (see Section 5.21), was employed. In this method, the temperature is considered to evolve linearly between the distribution computed with a CFD simulation in the non-deformed geometry at BOL, and the distribution computed with a CFD simulation in the EOL deformed geometry. In Section 6.8, this temperature interpolation method is compared to the other options discussed in Section 5.21.

Effects of the coupling on the diametral strain

For the lowest dose profile with a maximum of 123 dpa, the temperature increase evidenced in Section 6.5 (see Figure 6.11) is not high enough to provide a significant feedback on the deformation of the bundle. Therefore, in this case, the deformed geometry obtained with the coupled simulation does not significantly differ from the one obtained in the non-coupled calculation using the nominal temperature distribution, as can be observed in Figure 6.15, where the average diametral strain profiles of the central and one peripheral pin obtained with and without coupling between thermal-hydraulics and thermomechanics are presented.

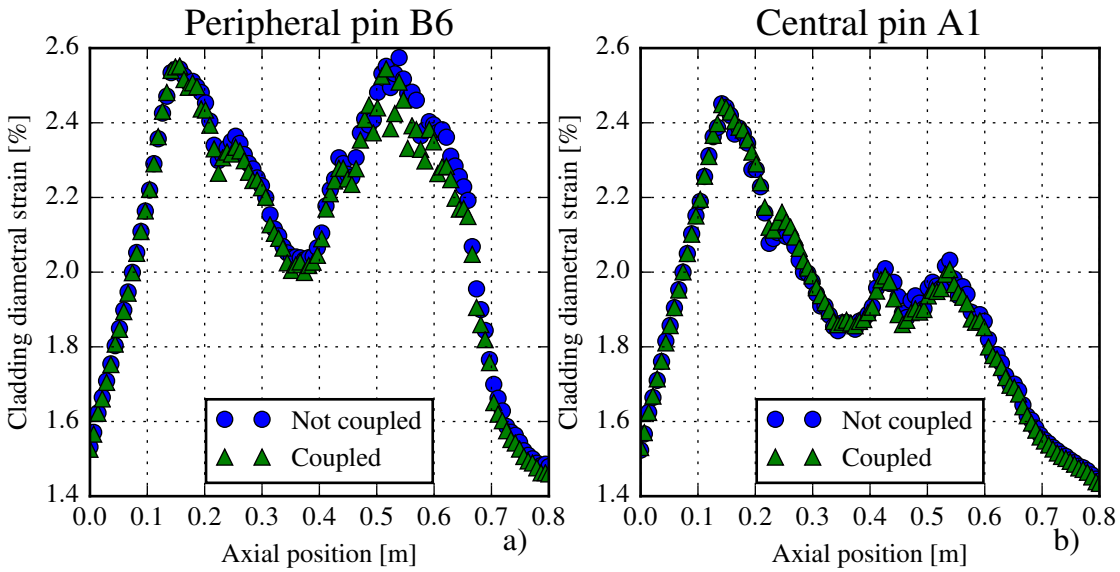

Figure 6.15.: Diametral strain of the cladding of the peripheral pin B6 (a) and of the central pin A1 (b) along the heated column, obtained with and without coupling, for a maximal irradiation dose of 123 dpa.

For the higher dose profile with a maximum of 165 dpa, on the other hand, the deformation level is higher and it induces a greater temperature increase. In this case, the EOL deformation of the bundle obtained with the coupling is significantly different from the one obtained using only the nominal temperature distribution as input for the thermomechanical calculations. This can be observed in Figure 6.16, where, again, the average diametral strain profiles of the central and one peripheral pin obtained with and without coupling are presented. It can be there observed that, in the upper half of the heated column, the coupling leads to a diametral strain up to 30% lower than the non-coupled simulation.

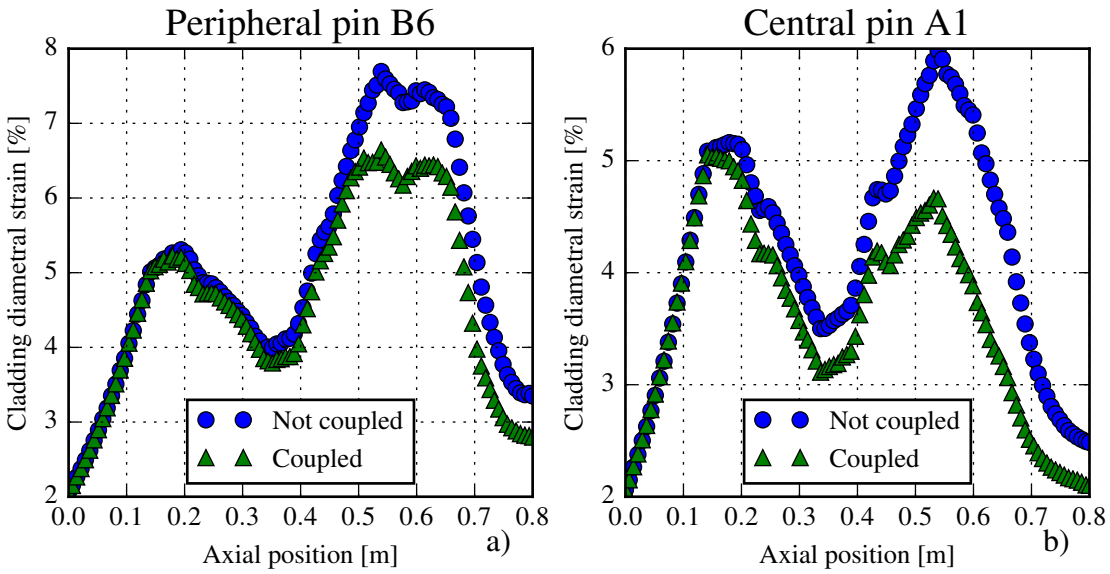

Figure 6.16.: Diametral strain of the cladding of the peripheral pin B6 (a) and of the central pin A1 (b) along the heated column, obtained with and without coupling, for a maximal irradiation dose of 165 dpa.

The observed effect can be explained by the temperature dependence of the physical phenomena that cause the deformation, mainly swelling and irradiation creep. As discussed in Chapter 4, the cladding swelling is computed by DOMAJEUR2 using equations 2.24 to 2.28, which allow to take into account its temperature dependence, depicted in Figure 6.17 for two different irradiation doses, corresponding to the maxima of the dose profiles evaluated in this work. It can be noted that there is one temperature for which swelling is maximized, which increases with the irradiation dose. The irradiation creep, computed using equations 2.32 and 2.33, presents a similar temperature dependence (see Figure 2.14). Therefore, the observed reduction in deformation is explained by the fact that, in the upper part of the heated column, the temperature of both the central and the peripheral pin is superior to that that maximizes swelling and irradiation creep, thus the deformation

induced temperature increase has a negative feedback on deformation. This can be observed in Figure 6.18, where the temperature ranges that maximize swelling and irradiation creep are plotted—for a dose range of [100,165] dpa[6]—together with the temperature profiles of the two pins considered in the non-deformed geometry.

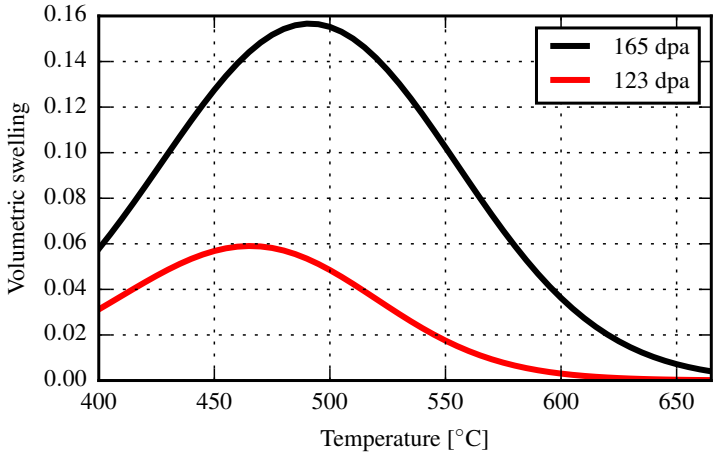

Figure 6.17.: Cladding swelling as a function of temperature, for two different irradiation dose levels, as calculated with the empirical law employed in DOMAJEUR2.

Note that the impact of the coupling on the deformation is higher in the upper half of the heated column. This is firstly due the higher temperature perturbation in this region with respect to the nominal temperature distribution, as can be noted in Figure 6.11. Additionally, as can be observed in Figure 6.18, the cladding temperature in the non-deformed geometry is, in the lower part of the heated column, closer to the temperature level that maximizes swelling and irradiation creep, around which their partial derivatives with respect to temperature ($\partial\epsilon/\partial T$) have a smaller absolute value (see Figure 6.17). For similar reasons, the diametral deformation reduction caused by the coupling is expected to be less significant in an axially homogeneous pin design, which typically present a deformation maximum near the core mid-plane, where the deformation induced temperature increase is relatively low. In this case, the temperature increase would mostly affect a part of the bundle that already exhibits a low deformation level, thus inducing low feedback in absolute terms.

[6]The temperature that maximizes the irradiation creep is also dependent on the cladding equivalent stress, here set to 100 MPa, since the term of Equation 2.32 proportional to σ_{eq}^2 gains relative importance with growing σ_{eq}. However, since the creep term proportional to the swelling rate dominates, this dependence is very low.

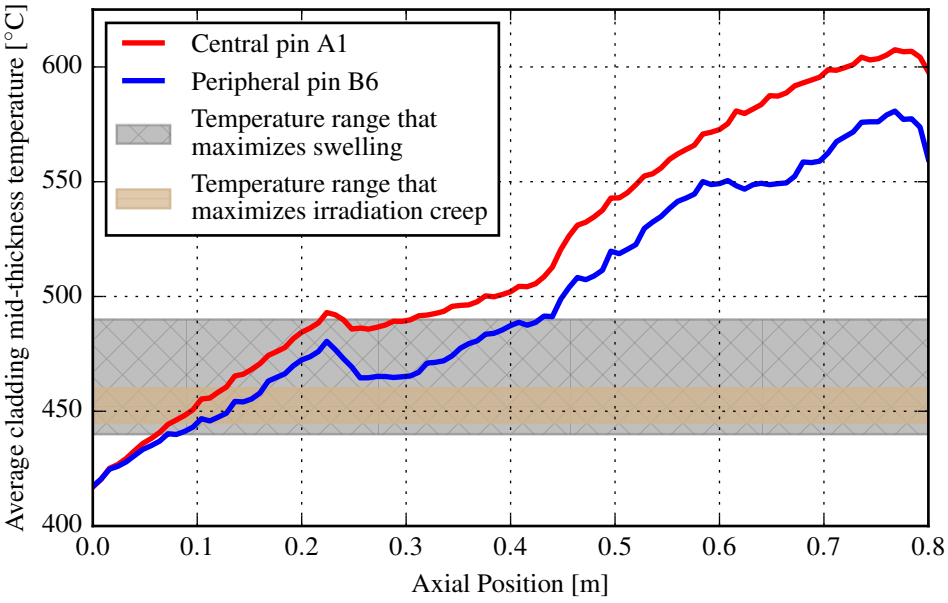

Figure 6.18.: Average cladding temperature along the heated column of the central and one peripheral pin of the non-deformed bundle. The temperature ranges that maximize swelling and irradiation creep—for a dose range of [100,165] dpa—are indicated.

Impact of temperature gradients on the diametral strain

The temperature gradients around the circumference of the claddings were shown to be very significant (see Figure 6.13), representing up to 64% of the nominal bulk sodium heating within the bundle. In order to quantify their impact on the EOL diametral strain of the claddings, two DOMAJEUR2 simulations using different cladding temperature distributions were compared, for both dose levels here studied. In the first simulation, the temperature of each cladding was defined using 6 axial profiles around its circumference, one every 60 degrees. In the second, only one averaged temperature profile per pin was employed. For both simulations, the detailed 3D model of DOMAJEUR2 was used.

DOMAJEUR2 maps the user-inputted temperature profiles onto the mesh of the model; this procedure led, in the two simulations here compared, to the temperature distributions presented in Figure 6.19 for the upmost part of the fuel bundle. From this figure, it would seem that employing only one temperature profile is a poorer approximation for the peripheral pins, which are subject to significantly higher temperature gradients on the circumference of the claddings than the central one. However, even in this case, the impact of these gradients on the diametral strain is very limited. This can be observed in Figure 6.20, where the diametral strain profiles of a peripheral pin of both simulations—i.e. using 1 and 6 temperature

values in the circumference of each cladding—are presented, for the two dose levels analyzed. For the lower dose essayed, using 6 profiles leads to a diametral strain 1.2 % higher than using only one, and the maximum local relative difference is 5%. For the higher dose, no significant differences are observed. For both dose levels, the calculations with only one temperature profile per pin demanded significantly less computation time.

It should be noted that the circumferential temperature gradients here presented lead to uneven distributions of the thermal expansion and of the swelling strain—addressed later in this section—which give place to secondary stresses.

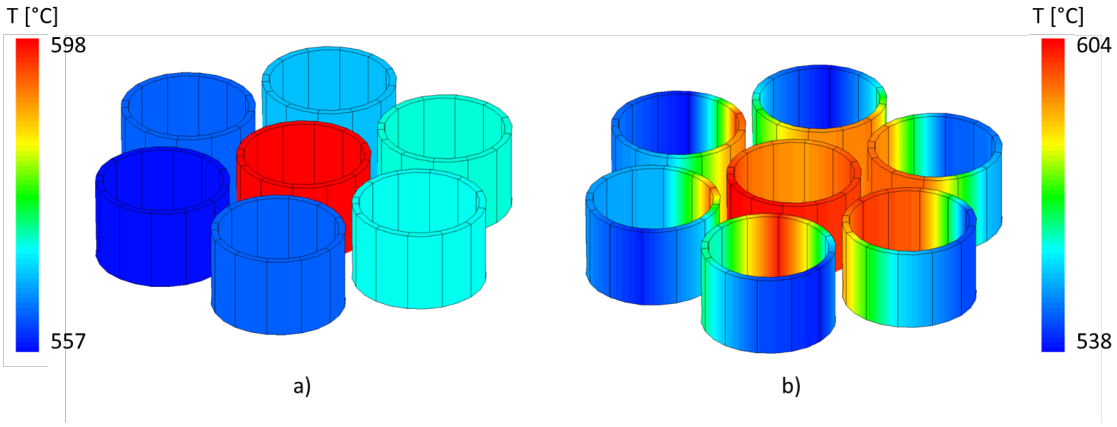

Figure 6.19.: Detail, at the upmost section of the fuel bundle, of the temperature distribution used as input for the DOMAJEUR2 simulations when 1 averaged temperature profile per pin is employed (a) and when 6 different profiles per pin are used (b).

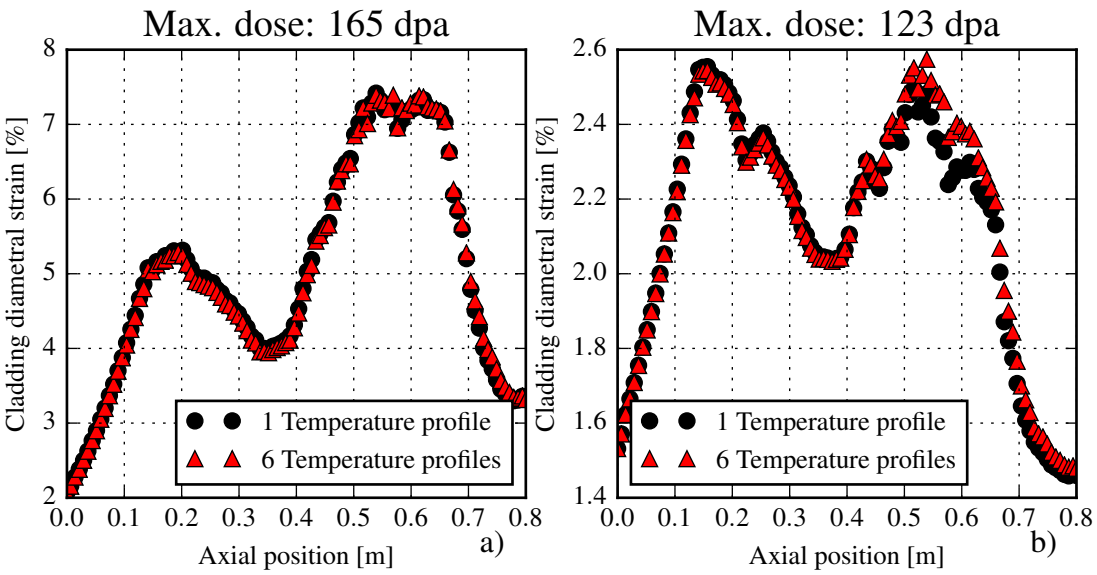

Figure 6.20.: Diametral strain profile of the peripheral pin B6 obtained with DOMAJEUR2 using one and six axial temperature profiles per pin, for a maximum dose of 165 dpa (a) and 123 dpa (b).

Effects of the coupling on the cladding strain: 3D vs 1D finite element models

The low impact that the circumferential temperature gradients of the claddings have on their diametral strain, on which the coupling here evaluated is based, suggests that the beam-based 1D model of DOMAJEUR2, which only allows using one temperature profile per fuel pin, might be a reasonable option for the coupling methodology. For this reason, the irradiation of the 7-pin bundle was simulated using the 1D model of DOMAJEUR2, for the two irradiation dose levels, and the results thus obtained are here compared to the results obtained with the 3D model, which considers the circumferential temperature gradients.

The axial profiles of cladding diametral strain obtained with each model are presented in Figure 6.21 for the central pin, which evidenced the highest differences between models, for the two dose levels evaluated. For 123 dpa, the 3D model led to an average diametral strain 1% lower than the 1D model, while it yielded an average deformation 7% higher for 165 dpa. The circumferential temperature gradients on the claddings, not considered in the 1D modelisation, were shown to have very low impact on the diametral strain of the fuel pins (see Figure 6.20), so they cannot explain the difference found between the two models, which is larger for the most irradiated bundle and towards the upper end of the heated column. In addition, as we will show later in this section, the cladding viscoplastic strains

obtained with both models are in very good agreement, and both compute the same thermal expansion. Then, the difference lies in the calculation procedure of the elastic strain between the two models.

In the 1D modelisation, each cladding is represented by a series of pipe elements. The diametral strain of each of these elements is calculated from the internal pressure and the thermal and irradiation loads it is subject to, and it is completely independent from the diametral strain at other axial positions. For this reason, the diametral strain obtained with this model decreases abruptly towards the end of the heated column, where the irradiation dose and temperature levels induce a sudden reduction in the swelling and creep strains. On the other hand, each of the multiple elements used to represent an axial section of the cladding in the 3D model shares nodes with elements above it and below it. Therefore, in this case, the diametral strain of any given section of the cladding depends on sections below and above it. In particular, and as shown for a dose of 165 dpa in Figure 6.21a, a residual diametral strain is obtained in the upmost region of the heated column of the cladding. In this case, the strain reduction towards the end of the bundle is smoothed out due to the forces that the elements of a highly deformed section of the cladding exert on the elements of the section above it, which tend to increase its diameter.

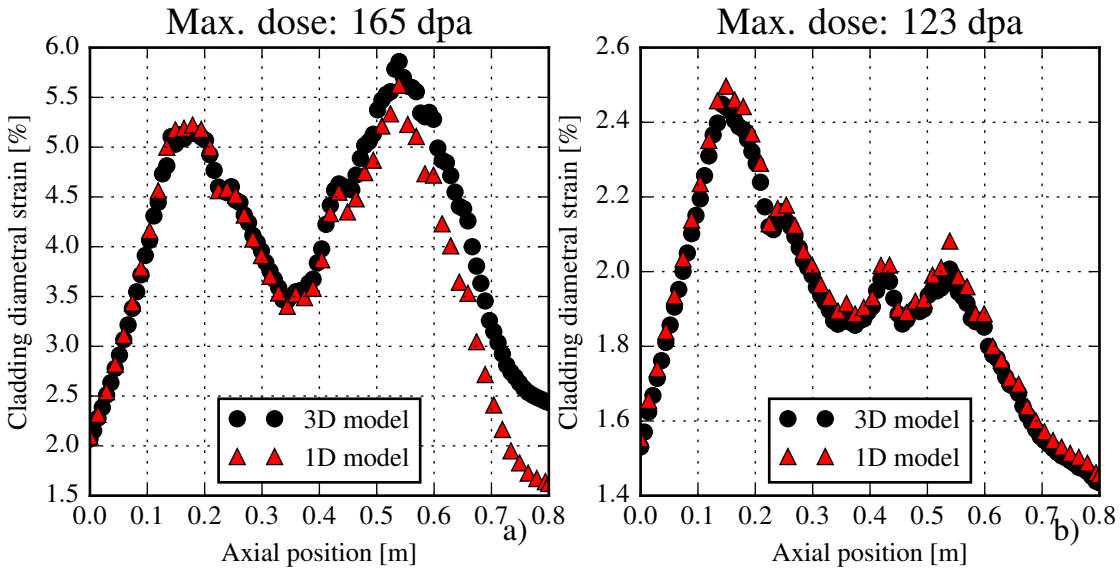

Figure 6.21.: Diametral strain profile of the central pin obtained with the 3D and 1D models of DOMAJEUR2, for a maximum dose of 165 dpa (a) and 123 dpa (b).

However, the maximal diametral strains obtained with the two models are in very

good agreement and, as explained before, the difference in the diametral strain is concentrated in the upmost part of the heated column. Since both the deformation level and the linear power are relatively low in this region, the higher strain obtained with the 3D model only leads to a 10°C increase in the maximum cladding surface temperature—calculated by averaging over one sixth of the circumference of the cladding—, over which operational limits are imposed in SFR for safety reasons. Half of this increase is caused by the difference in the coolant mass flow rates computed in the two deformed geometries. The impact of the strain difference on the average cladding temperature at a given axial position is even smaller, averaging less than 5°C in the upper half of the central pin, where the effect was most noticeable.

As mentioned above, both models compute similar swelling and creep induced strains. This can be observed in Figure 6.22 where the EOL swelling strain axial profiles, averaged over the cross section of the cladding, are presented for the central pin A1 (a) and for the peripheral pin B2 (b), as computed with the 1D and 3D models of DOMAJEUR2 in coupled and non-coupled simulations. Similarly, the irradiation creep strain profiles are presented in Figure 6.23a for the central pin, and in Figure 6.23b for the peripheral pin B2. In these figures, the bundle irradiated up to 165 dpa is considered.

It can be noted that the axially heterogeneous fuel pin concept leads to swelling and irradiation creep profiles with two distinct maxima each, one in each fissile blanket. In the lower part of the heated column, the irradiation creep strain is slightly dominant, since it is maximal for slightly lower temperatures than swelling, specially for doses close to the maximum of 165 dpa evaluated here (see Figure 6.18). In the upper part, on the other hand, the swelling strain dominates. Additionally, the deformation of the peripheral fuel pin is superior to that of the central pin due to its lower temperature that, in the upper half of the heated column, favours both swelling and irradiation creep.

Concerning the effects of the coupling, it can be noted that it affects the swelling more than the creep strain, and that its impact is maximal for the central pin (figure 6.22a), where the swelling strain reduction reaches 30%. As mentioned before, the strain reduction due to the coupling is higher in the upper part of the heated column, where the temperature increase induced by the deformation and $|\partial\epsilon/\partial T|$ are both higher. The maximal swelling strain—of particular importance in view of the design limits imposed on it—is in excellent agreement between the two models, both in the coupled and not coupled simulations. However, it should be noted that these values are averaged in the circumference of the cladding.

These results confirm the capability of the beam-based, 1D model of DOMAJEUR2 to predict an axial distribution of cladding diametral strain that agrees well

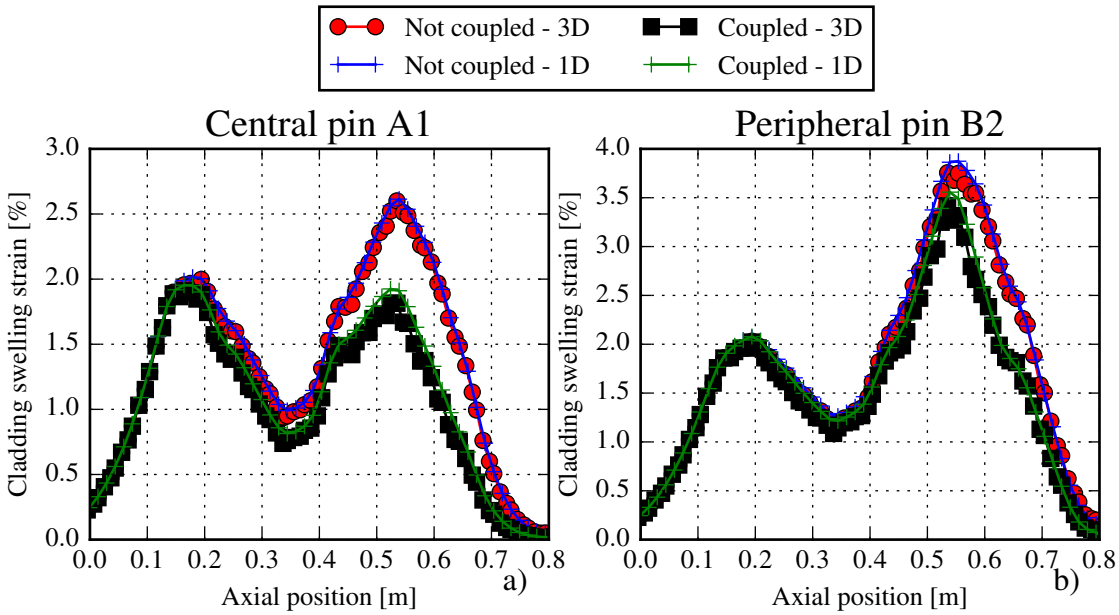

Figure 6.22.: Axial profiles of swelling strain computed with the 1D and the 3D models of DOMAJEUR2, in coupled and non-coupled simulations. The results obtained for the central pin A1 (a) and the peripheral pin B2 (b) are presented.

with the reference distribution computed with the 3D model, especially concerning the maximal strain. Besides the implications that this has on the prediction of the temperature distribution in the bundle, this is particularly important since the diametral strain of the claddings is the main cause of interaction between the fuel pins and between the pins and the hexcan, which leads to contact stresses evaluated in Section 6.7. For these reasons, the 1D model is a suitable option for conducting coupled simulations aiming to predict the macroscopic evolution of the geometry of the bundle, and its effects on thermal-hydraulics. However, only the 3D models allows to evaluate the effects of the high temperature gradients, as discussed next.

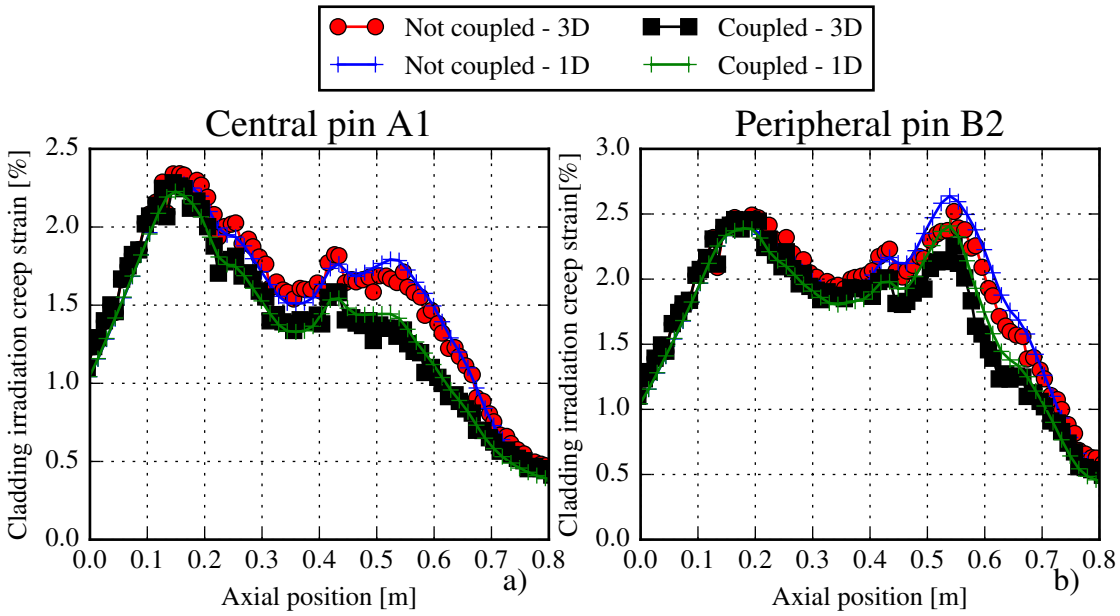

Figure 6.23.: Axial profiles of irradiation creep hoop strain computed with the 1D and the 3D models of DOMAJEUR2, in coupled and non-coupled simulations. The results obtained for the central pin A1 (a) and the peripheral pin B2 (b) are presented.

Swelling strain gradients

Void swelling is strongly temperature dependent and, therefore, under the temperature gradients evidenced by figures 6.13 and 6.19b, high swelling gradients are established within the fuel claddings, and only the 3D model is able to represent them[7]. To illustrate this, the swelling strain profile along the circumference of a peripheral fuel pin is presented in Figure 6.24a for an axial position of 0.545 m, where both the swelling strain and its circumferential gradient are maximal. Both the results obtained with the non-coupled and the coupled simulations conducted with the 3D model of DOMAJEUR2 are presented. Additionally, in Figure 6.24b, the swelling strain distribution within a 1.5 cm long axial section of the cladding, at the same axial position, is presented for the non-coupled and coupled simulations.

As can be observed in Figure 6.24a, the swelling strain is highly inhomogeneous within the circumference of the cladding. The difference between the maximal and minimal strain represents, in the non-coupled simulation, 40% of its average. As explained before, the temperature gradients are increased in the deformed geometry. Thus, in the coupled simulation, the difference between the maximal and minimal

[7]Similarly, thermal strain gradients are also established. However, these are significantly lower than the swelling induced strains.

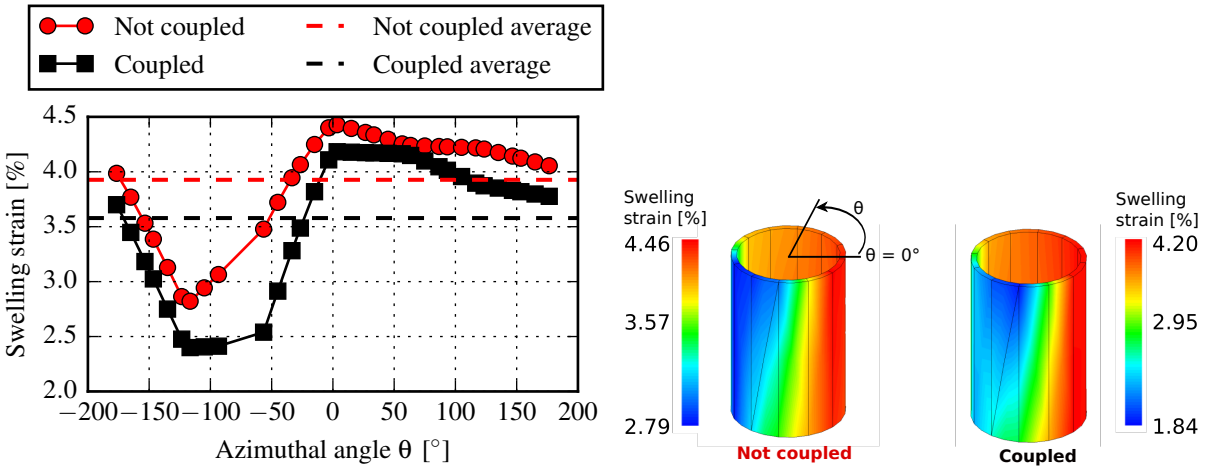

Figure 6.24.: a) Swelling strain in the circumference of the cladding of a peripheral fuel pin, at an altitude z = 0.545 m, computed with the 3D model of DOMAJEUR2 in a coupled and a non-coupled simulation. b) Swelling strain distribution within a 1.5 cm tall section of the cladding, centered at z = 0.545 m, computed with the 3D model of DOMAJEUR2 in a coupled and a non-coupled simulation.

swelling strain within the cladding circumference is larger and represents a 50% of its average, which is lower than without coupling. At this axial position, the ratios of maximal to average swelling strain are 1.13 and 1.17 in the non-coupled and in the coupled simulations, respectively.

In Figure 6.24b, a qualitatively similar swelling distribution can be observed within the axial cladding section in the coupled and in the non-coupled case. However, the coupling increases the swelling strain amplitude by 44%. This amplitude is higher than the one computed over a circumferential line (figure 6.24a) since the axial temperature gradients induce axial swelling gradients too. It is worth noting that these axial gradients can only be correctly reproduced if the azimuthal gradients are considered, since the first are strongly *smoothed* out if the cladding temperature is considered homogeneous within its cross section.

Being able to correctly predict the swelling strain distribution is of particular importance, firstly, because, as discussed in Section 2.2.2.2, it has been shown to produce excessive embrittlement of the austenitic steel of the cladding above approximately 2%, which is why all SFR programs have a design criteria limiting the maximal swelling strain. Here, its calculation was made possible by the detailed temperature field provided by the CFD simulation, and by the use of the 3D model of DOMAJEUR2. In cases where the size of the bundle makes it

unpractical to employ the 3D model of DOMAJEUR2, a simulation of a smaller representative bundle, like the 7-pin bundle studied here, could be conducted to identify a factor—or different factors representative of peripheral and central pins, or different axial positions—relating the average and maximal swelling strain within the circumference of the cladding (1.17 in the example presented in Figure 6.24a). Then, to approximate the maximal swelling that would be computed by the 3D model from the value obtained with the 1D model, the latter could by multiplied by the factor identified in the representative 3D simulation, since, as discussed before, the maximal swelling, averaged on the circumference of the cladding, is in excellent agreement between both models.

Additionally, the swelling gradients—like is the case with the differential thermal expansion—give place to secondary stresses that, despite normally being relaxed by the irradiation creep (Uwaba and Ukai 2002), could activate the damaging thermal creep if they were sufficiently high[8]. To be able to precisely quantify these stresses, a very fine spatial discretization would be required. Due to time requirements and limitations in the available computational resources, this evaluation was not conducted in this work. However, the developed simulation methodology could be employed to this end, which constitutes a future outlook of this work.

Section summary

In this section we showed that, under conditions representative of advanced SFR, the coupling between thermal-hydraulics and thermomechanics leads to a significant reduction of the cladding diametral strain, explained by the temperature dependence of swelling and irradiation creep, and by the deformation induced cladding temperature increase. In the axially heterogeneous bundle here evaluated, which presents two deformation maxima along the length of its heated column, the coupling-induced deformation reduction affects mostly the maximum located in the upper part of this column. In addition, the important temperature gradients in the circumference of the cladding were shown to have very little effect on its diametral strain, averaged in the circumference. The 1D model of DOMAJEUR2 was found to predict a cladding diametral strain profile along its length that is in good agreement with the one predicted by the 3D model, particularly concerning the maximal diametral strain. This makes the 1D model, which is significantly less

[8] It should be noted that, although not evaluated in this work, important swelling gradients also exist in the thickness of the cladding, consequence of the high temperature gradient it exhibits. However, the estimation of this swelling gradient is more straightforward than the evaluation of the gradients in the circumference, since the temperature difference between the inner and outer surfaces of the cladding depends only on its dimensions and on the local linear power. Additionally, these gradients are already the subject of studies conducted at the CEA with the fuel performance code GERMINAL, which, on the other hand, cannot predict the gradients in the circumference of the cladding because it is based on an axisymmetric assumption.

computationally expensive, a suitable option for conducting coupled simulations. However, the temperature gradients induce important swelling gradients in the circumference of the claddings, which only the 3D model can predict and which induce secondary stresses. The quantification of these stresses is one of the outlooks of this work.

The effects of the coupling on the deformation of the bundle have consequences on its stress distribution, which are discussed next.

6.7. Effects of the coupling on the cladding stresses

We showed how considering the temperature perturbations induced by the deformation leads to a reduction of the swelling and the irradiation creep of the claddings, thus to a reduction of their diametral strain. Since the latter is the driving force for the mechanical interactions between fuel pins and between the pins and the hexcan, the predicted mechanical loads of these contacts are also reduced in the coupled simulations with respect to the simulations using the non-coupled approach. In what follows, we evaluate only the bundle irradiated until reaching a maximal irradiation dose of 165 dpa, for which the coupling effects were observed to be significant.

Using the 1D model of DOMAJEUR2

To illustrate the effects of the coupling on the cladding stress, the equivalent von Mises stress calculated by the modified bar contact elements of the 1D model of DOMAJEUR2 (see Section 4.4.2), with and without coupling, are presented in Figure 6.25a for the central pin, and in Figure 6.25b for the peripheral pin B2. In the not coupled simulation, the maximal equivalent stresses of 134 MPa[9] for pin A1 and 123 MPa for pin B2 are located, for both pins, at an axial position z = 0.545 m. Considering the coupling leads to a lower diametral strain and thus relaxes the mechanical contacts, leading to a very significant reduction (27% for both pins) of the equivalent stress at that point.

To better understand the evolution of the cladding stress at the points where contact is susceptible of occurring, it is helpful to observe the evolution of the Total Available Gap (TAG), systematically computed by DOMAJEUR2. The TAG is defined, for each diagonal of the hexagonal subassembly, as the difference between the available space within the hexcan, TAH, and the space occupied by the deformed fuel pins in the diagonal, TAP, computed from the average external

[9] This values are not to be compared directly with the limit of ∼200 MPa given in Section 2.2.1.2—conservative value for the advanced SFR designed at the CEA—since this limit applies to the total equivalent stress, including the secondary stresses not considered here.

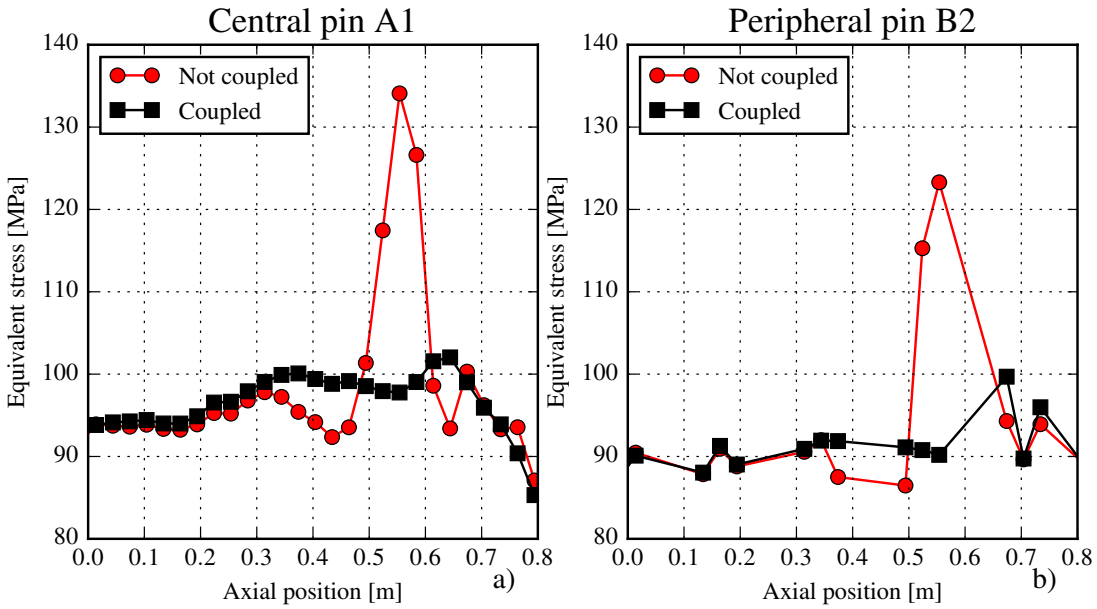

Figure 6.25.: Axial profile of the equivalent stress predicted by the 1D DOMAJEUR2 model, for the central pin A1 (a), and for the peripheral pin B2 (b).

diameter of their claddings and spacer wires. The TAH is the sum of the length of the red and blue segments presented in Figure 6.26. In this figure, the spacer wires of the pins A and B susceptible of becoming in contact with the hexcan are represented by dotted circles, and they are located 1/12th of the wire step below or above the diagonal being considered. The TAP is computed by adding the deformed diameters of the claddings and spacer wires within the diagonal, plus the diameter of one of the spacer wires susceptible of contacting the hexcan (one of the two dotted circles). With this definition, $TAG = TAH - TAP = 0$ marks the start of the second phase of the bundle deformation, when all the pins in the diagonal become in contact with each other and with the hexcan through the spacer wires[10]. At this point, there is still available space to accommodate the bundle deformation towards the hexcan wall opposed to the wall in contact with the spacer wires at the considered altitude, which is mainly done by the helical flexion of the fuel pins. When $TAG = -\overline{D_w}$, with $\overline{D_w}$ the average diameter of the spacer wires of the pins in the diagonal, the third phase of bundle deformation begins; at this moment, a cladding makes direct contact with the hexcan and there is no more available space to accommodate the diametral strain of the pins.

[10]This is true if all the pins present the same diametral deformation. In practice, the peripheral pins, which are exposed to lower temperatures, present a higher deformation level. For this reason, the contacts typically occur first in the periphery of the bundle.

Then, in Figure 6.27 and Figure 6.28, the evolution of the von Mises stress at the position of maximal EOL stress is presented, together with the evolution of the TAG, for the central pin A1 and the peripheral pin B2, respectively. The TAG limits that define the start of the second and third bundle deformation phases are also indicated[11].

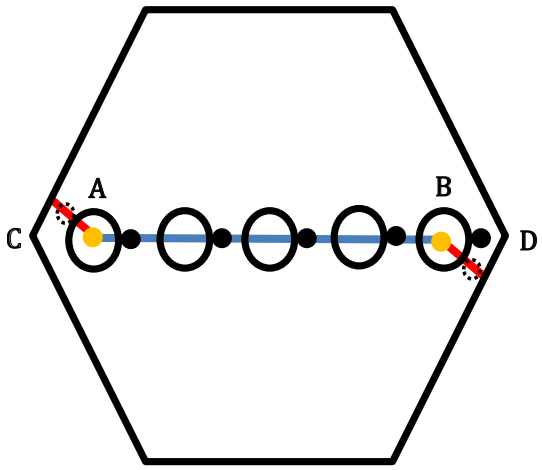

Figure 6.26.: Scheme of the fuel pins within a diagonal of the hexcan. The segments employed to compute the available space, within the hexcan, to accommodate the diametral strain of the pins (TAH) are indicated in red and blue.

By analysing figures 6.27 and 6.28, the lower EOL stress predicted by the coupled calculations (see Figure 6.25) can be explained by a delay of the third phase of bundle interaction, in which only the ovalisation of the claddings, a more rigid deformation mechanism than their flexion, can accommodate their increasing diametral strain. The start of this phase is therefore characterized by a rapid increase in the equivalent stress, observed at approximately 1540 days of irradiation in the non-coupled simulation. In the coupled simulation, this phase—which is not allowed during nominal operation—is not yet reached within the irradiation period considered. Additionally, the first contact-induced stress increase, observed between 1100 and 1200 FPD for pin B2 and between 1200 and 1300 FPD for pin A1, is also retarded by the coupling. It should be noted that this stress increase appears, for the central pin, later than the start of the second phase ($TAG = 0$). This is because, in this case, the second phase starts with the contact between the hexcan and the peripheral pin, which interacts with the central pin later on.

[11]The difference in the 3^{rd} phase limit computed with the different simulations is due to the difference in the computed thermal expansion of the wires.

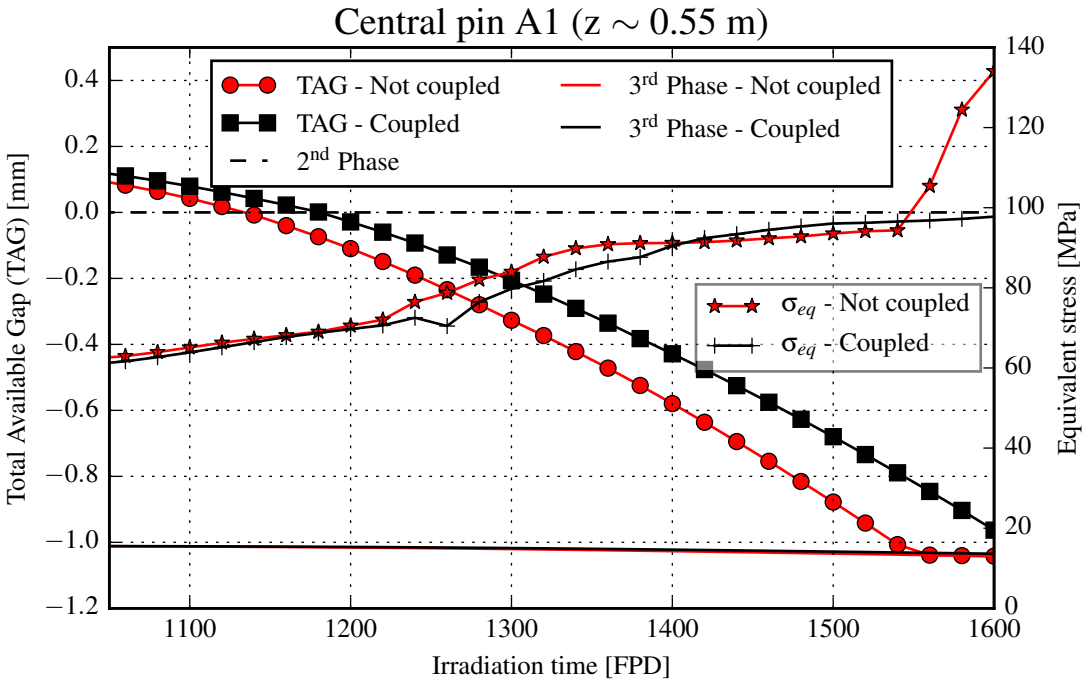

Figure 6.27.: Evolution of the TAG and of the equivalent cladding stress (σ_{eq}) at the axial position of maximal EOL stress, for the central pin A1. The results obtained with coupled and not coupled simulations are presented, and the TAG limits marking the start of the 2^{nd} and 3^{rd} bundle deformation phases are shown.

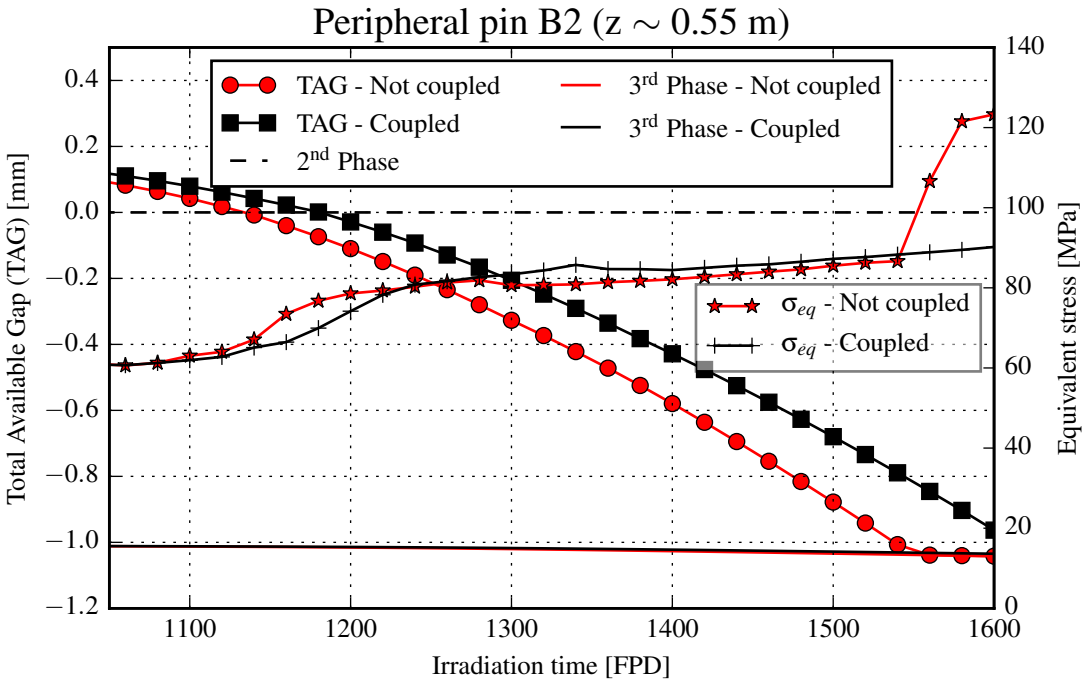

Figure 6.28.: Evolution of the TAG and of the equivalent cladding stress (σ_{eq}) at the axial position of maximal EOL stress, for the peripheral pin B2. The results obtained with coupled and not coupled simulations are presented, and the TAG limits marking the start of the 2^{nd} and 3^{rd} bundle deformation phases are shown.

Using the 3D model of DOMAJEUR2

Unlike the case of the modified bar contact elements employed in the 1D model of DOMAJEUR2, the maximal von Mises stress due to the contact between pins is not an internal variable of the link elements employed in the 3D model. Instead, the stress is computed at the integration points of the volumetric finite elements that constitute the claddings. In the simulations with the 3D model so far presented, and as discussed in Section 4.4.1, 13 finite elements were employed along the cladding circumference, each with a length of 1/12th of the wire step. This spatial discretization is not sufficient to accurately predict the maximal stress under the contact points and in presence of high temperature gradients. Therefore, in order to improve the accuracy in the determination of the maximal stress, a simulation with twice as many elements in the length and in the circumference of the claddings was conducted to this end[12].

The resulting evolutions of the maximal cladding stress in the coupled and not coupled simulations are presented in Figure 6.29 for the central pin A1, where they are compared to the evolutions obtained with the modified bar elements of the 1D model. The values reported for the 3D model correspond to the average in a 1 cm long cladding section[13], and at the azimuthal angle where contact occurs. It can be noted that both models predict a very similar reduction of the EOL maximal cladding stress due to the coupling. However, the local stress maxima computed by the 3D model, consequence of the succession—in time—of the contacts between the pins in the considered plane, are not predicted by the 1D beam model. This could be explained by an underprediction of the 1D model of the flexion stiffness of a series of pins in contact with each other. Additionally, the maximal stress computed by the 3D model is located ∼7 cm higher than the one obtained with the 1D model. It should be noted that the central pin of this 7-pin bundle is more representative—in terms of contact condition and on temperature gradients—of the majority of the pins of a larger fuel bundle (217 pins for example) than the peripheral pins.

For the peripheral pin B2, however, the agreement between the 1D and the 3D models is less satisfactory. This can be observed in Figure 6.30, where the evolution of the maximal cladding equivalent stress of the peripheral pin B2 is presented, as computed by the 1D and 3D models. It should be firstly noted that, since B2 is a peripheral pin, it is exposed to much higher temperature gradients, as illustrated in Figure 6.31 for the non-deformed geometry. These gradients are not considered in the 1D model, so the comparison between the two is less straightforward than for

[12] Increasing the number of elements in the thickness of the cladding was not possible with the available computational resources, since the convergence of the simulation was significantly slowed down in this case.

[13] Out of the three integration points in the thickness of the cladding, only the ones closest to its inner surface were considered, since the maximal stress is located at this surface.

the central pin A1. Besides, as discussed in Section 6.5, the temperature gradients are increased with the coupling, thus inducing higher secondary stresses due to differential thermal expansion and swelling gradients. A higher discretization might be needed in this case to fully resolve these secondary stresses, but this was not possible due to limitations on the available computational resources and due to time constraints.

In spite of these limitations, the results concerning pin B2 are presented because two qualitative observations can nevertheless be made. Firstly, the succession of steep increases of the stress observed for the central pin are also reproduced here in the 3D simulations. Like for the central pin, the 1D model fails to capture this behaviour, even though it predicts, as the 3D model does, the contact between pins. Secondly, as observed for the central pin with both models, the coupling leads to a delay in the stress increases induced by the contacts. However, the 3D models predicts an earlier increase in the cladding stress, which is why the coupled simulation does not lead to a significant reduction of the EOL maximal stress, since the third phase of bundle deformation is also reached in this simulation.

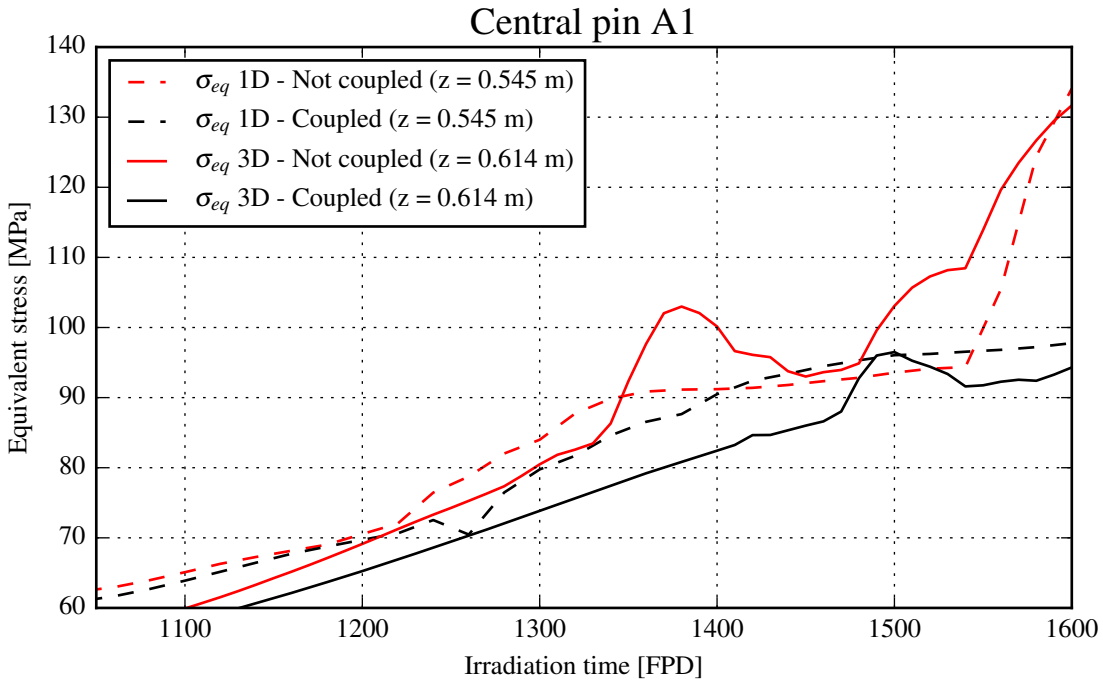

Figure 6.29.: Evolution of the equivalent cladding stress at the axial position of maximal EOL stress, for the central pin A1. The results obtained with the 1D and the 3D models in coupled and not coupled simulations are presented, and the axial position evaluated in each model is indicated.

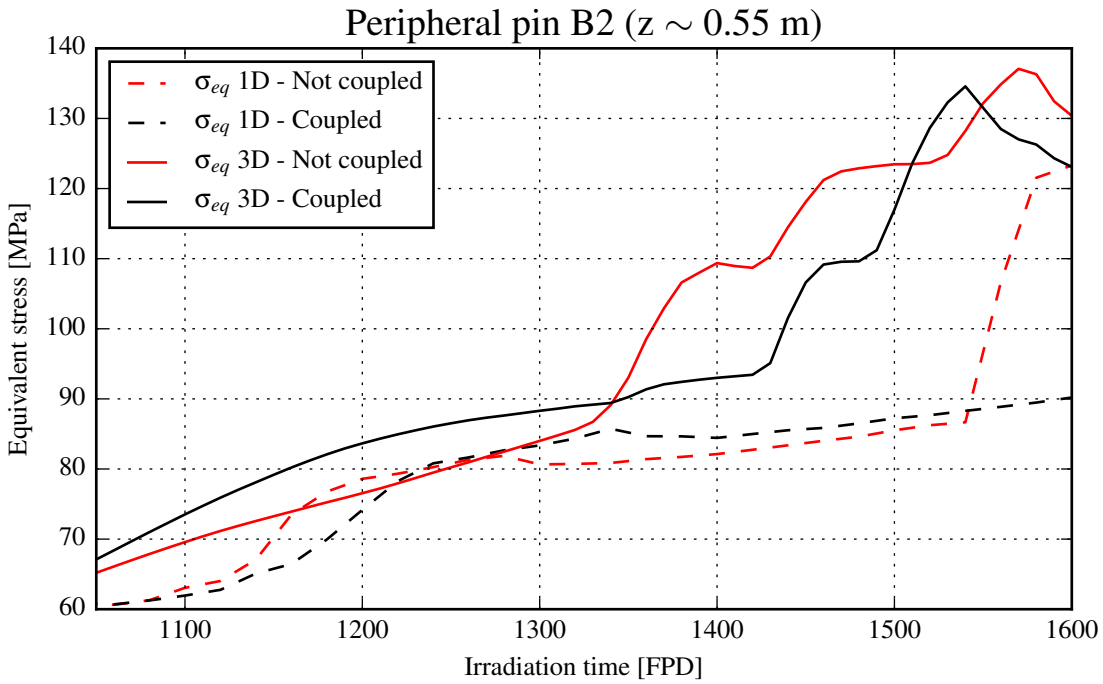

Figure 6.30.: Evolution of the equivalent cladding stress at the axial position of maximal EOL stress, for the central pin A1. The results obtained with the 1D and the 3D models in coupled and not coupled simulations are presented.

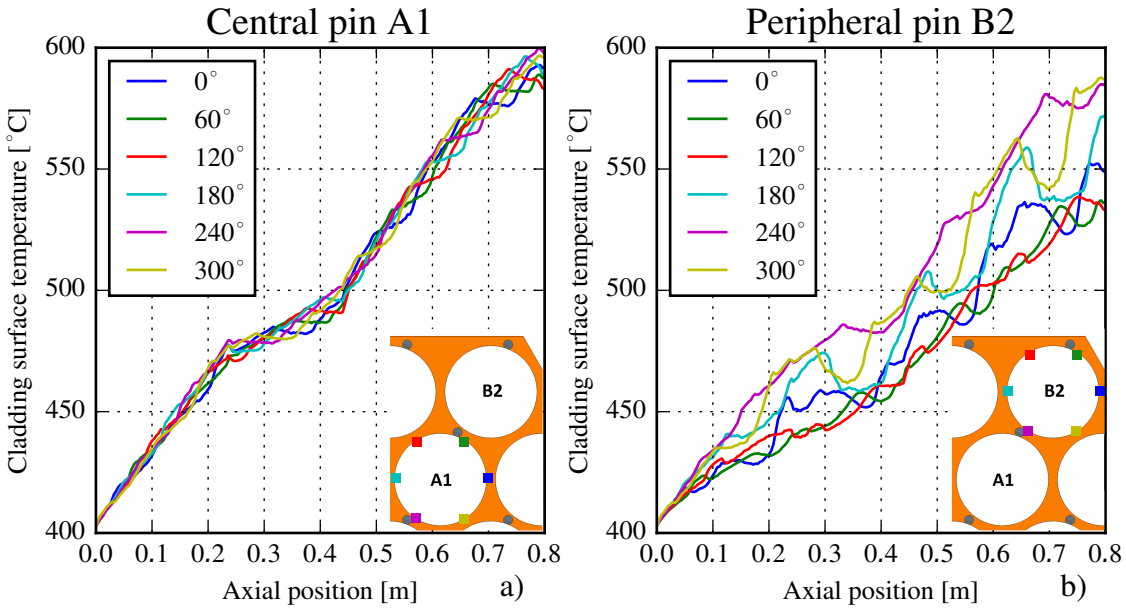

Figure 6.31.: Cladding surface temperature axial distribution of the central pin A1 (a) and the peripheral pin B2 (b), in the non-deformed geometry. Each profile corresponds to a different azimuthal angle.

Section summary

The results presented in this section show how the reduction of the diametral deformation, caused by the coupling, leads to a delay in the third phase of the bundle deformation. This phase is characterized by a high cladding ovalisation caused by the contact between fuel pins, which induces high mechanical stresses within the cladding. For the central pin, the 3D and the 1D models of DOMAJEUR2 were shown to predict a similar reduction in the maximal EOL cladding stress. For a peripheral pin, on the other hand, the agreement between both models resulted to be less satisfactory, since—unlike the 1D model—the 3D model predicts the attainment of the third phase of deformation for both the coupled and not-coupled simulations. This comparison is, however, of qualitative character, since the secondary stresses are considered in the 3D model but not in the 1D model. A precise evaluation of these stresses constitutes an outlook of this work.

6.8. Comparison between different temperature interpolation methods

In this section, we firstly compare the results of coupled simulations using the two different temperature interpolation techniques presented in Section 5.4.1, namely the *Linear Temperature Increment* and the *Delayed Temperature Increment*. Both these methods require doing only one CFD simulation in a deformed geometry per global iteration (i.e. per thermomechanical simulation of the irradiation period under consideration). At the end of this section, the results obtained with these methods are compared to the results obtained by considering multiple CFD simulations, in partially deformed geometries, for the temperature interpolation.

Linear vs. Delayed Temperature Increase

In these two methods, the cladding temperature history used for each thermomechanical simulation is defined as described below.

- **Linear Temperature Increment method**: The BOL and EOL temperature distributions are computed with CFD simulations in the nominal and EOL deformed geometries, respectively, using the boundary conditions (power, mass flow) associated to those instants. After a 1 FPD long period of heating up from a *cold* reactor state, the temperature distribution is interpolated linearly between a time $t = 1$ FPD (BOL) and a time $t = t_{EOL}$ (EOL). Between BOL and EOL, both the temperature changes (in time and space) induced by the fuel burn-up and by the bundle deformation are considered.
- **Delayed Temperature Increment method**: This method is motivated by the existence of an incubation period, extending up to a time t_{inc}, during

which the deformation is very low. As in the previous method, a 1 FPD long initial period of heating up is considered. Then, between $t = 1$ FPD and $t = t_{inc}$, the temperature is considered to change only under the effects of the changes in power, and not due to the deformation of the bundle. The time t_{inc} is determined, at each global iteration of the coupled simulation, based on the last computed evolution of the bundle deformation, as described in Section 5.4.1. The temperature distribution at t_{inc} is computed by interpolating two CFD simulations in the non-deformed geometry; one with BOL and one with EOL boundary conditions. Finally, between $t = t_{inc}$ and $t = t_{EOL}$, both the effects of the changing power and of the deformation are taken into account, and the temperature distribution is considered to evolve linearly until reaching the distribution computed by a CFD simulation in the EOL deformed geometry.

Since the 1D model of DOMAJEUR2 was shown, in Section 6.6, to yield a cladding diametral strain distribution in very good agreement with the prediction of the 3D model, the first was employed for the studies presented in this section, which allowed to increase, with respect to the simulations presented so far, the number of fuel pins to 19[14]. All other geometric parameters of the 7-pin bundle presented in Section 6.1 were conserved, except for the hexcan plate to plate distance that was set to 49.31 mm to accommodate the 19 fuel pins. A 19-pin bundle was selected because its simulation requires significantly less CFD computational time than larger bundles—which are the object of Chapter 7—, but it allows to evaluate whether the coupling induces the same qualitative effects than the ones obtained for the 7-pin bundle or not.

The inlet sodium mass flow rate was set to 2.34 kg/s, as to obtain, like with the 7-pin bundle, an outlet bulk sodium temperature of about 550°C in nominal conditions, considering an inlet temperature of 400°C. The EOL irradiation dose profile presented in Figure 6.1a, with a maximum of 165 dpa, was used. Different BOL and EOL linear power profiles were employed—the same for all fuel pins—to account for the fuel burn-up. These profiles are presented in Figure 6.32a. The meshing procedure described in Section 3.3.5 and the meshing parameters defined in Appendix A were also employed for the simulations presented in this section, resulting in a total cell count of about 6 million. As an example, the mesh obtained for the non-deformed geometry at the outlet of the bundle is presented in Figure 6.32b, where the fuel pin naming system is indicated.

Under these conditions, coupled simulations of the irradiation of the 19-pin bundle were conducted using both methods for interpolating the temperature distributions to produce the required temperature history for the thermomechanical

[14] As discussed in Section 4.4.1, the use of the 3D model of DOMAJEUR2 is very challenging for bundles of more than 7 fuel pins.

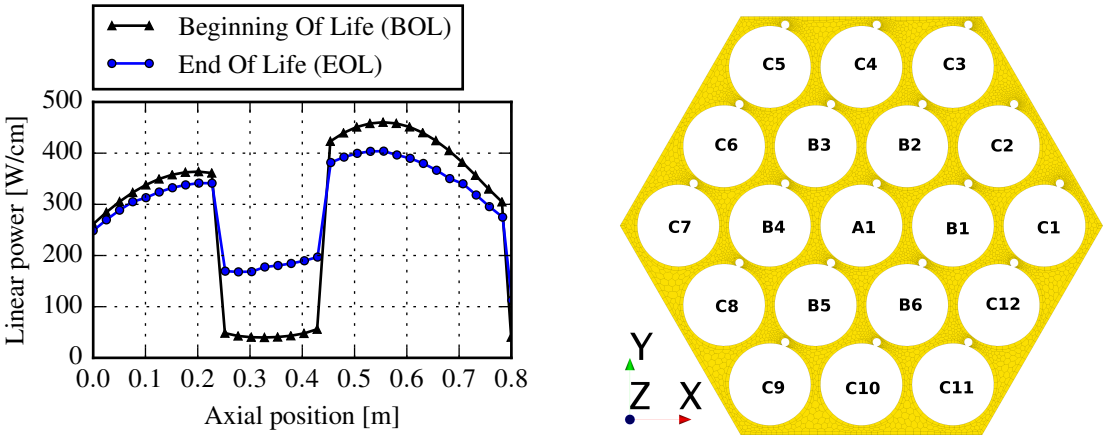

(a) (b)

Figure 6.32.: a) BOL and EOL linear power axial profiles used for all the fuel pins of the 19-pin bundle. b) Cross section of the CFD mesh at the outlet of the fuel bundle, where the pin naming system is indicated.

simulations. The resulting cladding surface temperature evolutions are presented in Figure 6.33a for 3 different fuel pins, at an altitude z = 0.54 m—where the EOL diametral strain is maximal—, where the evolution in the non-coupled simulation, in which only the evolution of the power is considered, is also presented. With the Delayed Temperature Increment approach, $t_{inc} = 976$ FPD was computed. It can be noted that, due to the increase in power of the central fertile blanket (see Figure 6.32a), the temperature increases during the irradiation, independently of the effects of deformation. For each pin and each simulation, the resulting EOL deformation is presented in Figure 6.33b.

It can be noted in Figure 6.33 that significantly different temperature time evolutions lead to relatively similar EOL diametral deformation profiles, although the effect of taking into account the *delay* in the temperature increase caused by the deformation can be observed. In addition, both coupled approaches lead to very similar maximum cladding temperatures, as can be noted in Figure 6.34 where the maximum cladding surface temperature of all pins (averaged over $1/6^{th}$ of the cladding circumference) is presented as computed with the 3 different approaches. Both coupled simulations lead to maximal temperatures highly superior ($\sim +40$°C) to those obtained with the non-coupled approach. The observed effects of the coupling on the cladding temperature evolution and on the cladding EOL diametral strain confirm the trends obtained for the 7-pin fuel bundle.

Figure 6.35a compares the evolution of the average viscoplastic diametral strain (swelling and irradiation creep) of the fuel pins of the bundle, obtained with the three approaches. It is observed that, up to approximately 1000 FPD, the plastic

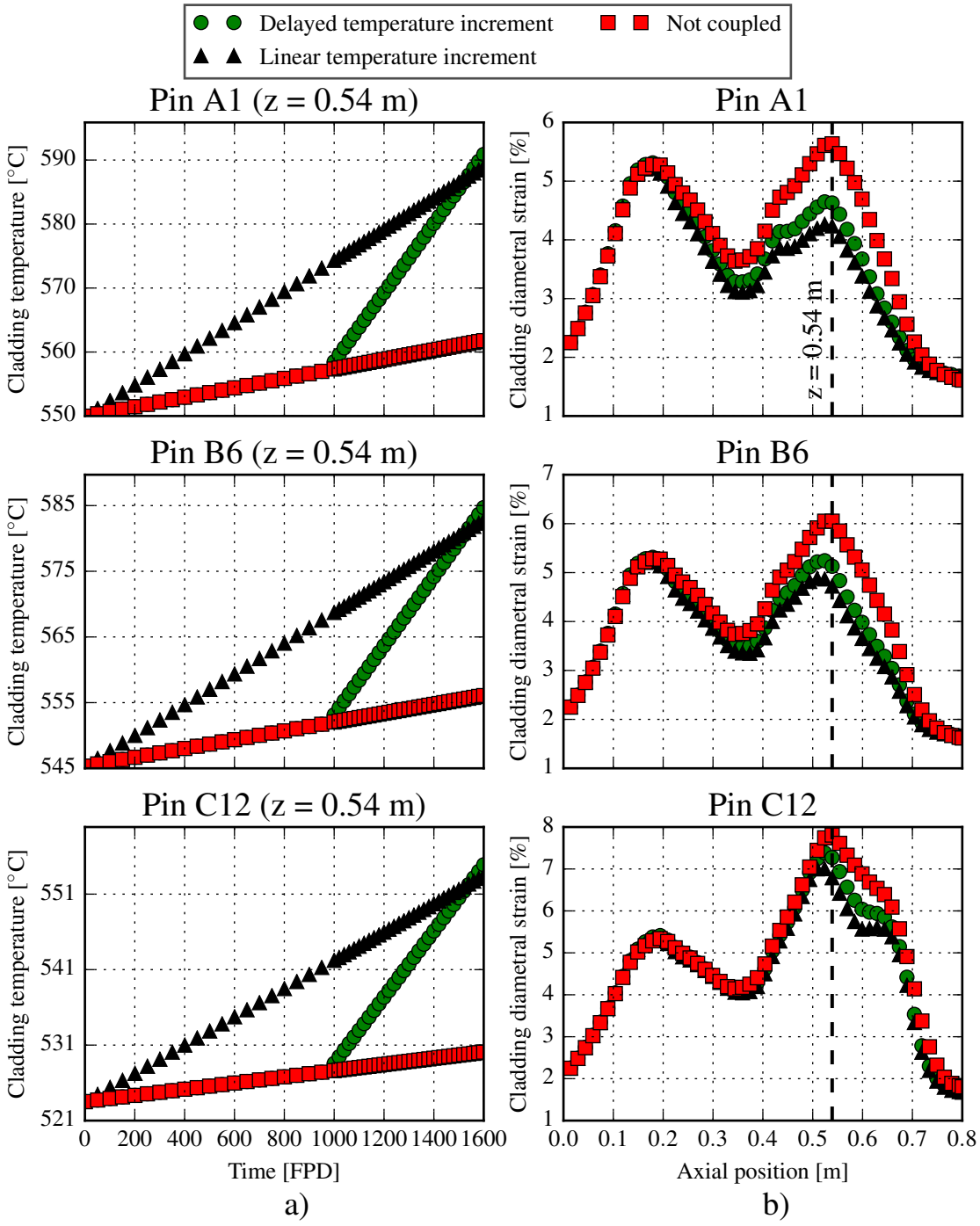

Figure 6.33.: a) Cladding temperature evolution at $z = 0.54$ m obtained with the coupled simulations—with two different temperature interpolation methods—and without coupling, for three different fuel pins. b) EOL diametral strain profiles computed in each simulation and for each pin.

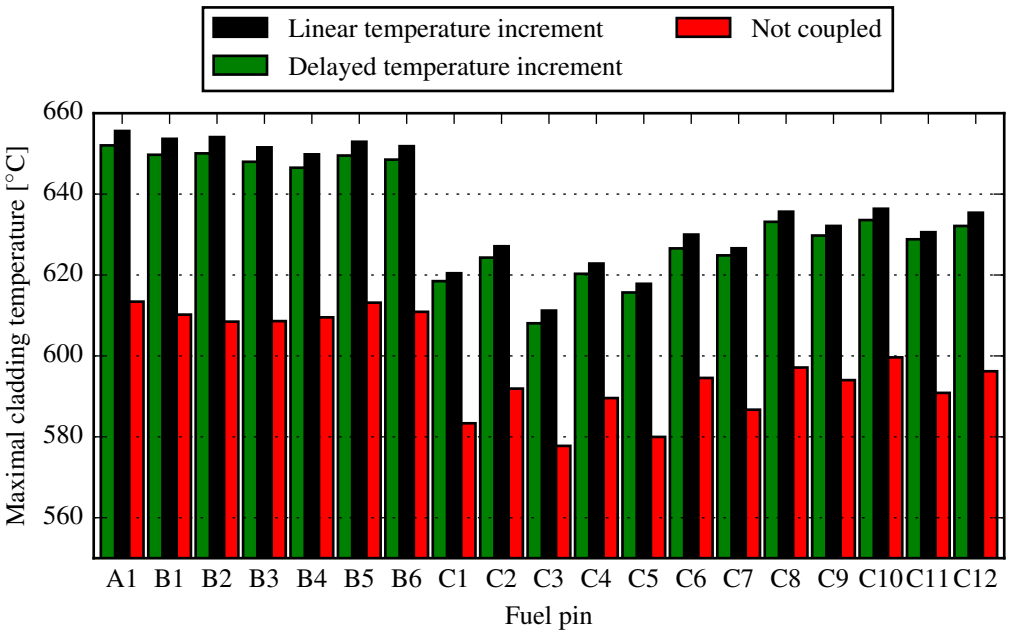

Figure 6.34.: Maximal cladding surface temperatures of all fuel pins computed with the coupled simulations using different temperature interpolation methods, compared to the ones obtained without coupling.

deformation is lower than 20 % of the EOL plastic strain, which was employed for the normalization of the strain profiles there presented. It can be noted that the three cases lead to similar evolutions of the average viscoplastic diametral strain. In Figure 6.35b, the normalized viscoplastic strain difference between both coupled approaches is presented. It can be observed that at 800 FPD—half of the total irradiation time—the difference between both approaches is only about 10% of the maximal difference, even though the temperature distributions employed in both cases differ significantly during this first half, as evidenced by Figure 6.33a for $z = 0.54$ m. However, as the irradiation proceeds and the deformation becomes more significant, the temperature difference between both methodologies decreases as well, thus its impact on the EOL deformation is reduced. In other words, the impact of the temperature difference obtained with both coupled methodologies on the EOL diametral deformation of the fuel pins is limited because this difference is reduced towards the end of the irradiation period ($t > 1000$ FPD), when most of the cumulated strain is produced. In addition, the observed temperature differences have a low effect on the swelling incubation dose, as shown in Table 6.5, where the results of a simulation with additional CFD computations—discussed next—are also included.

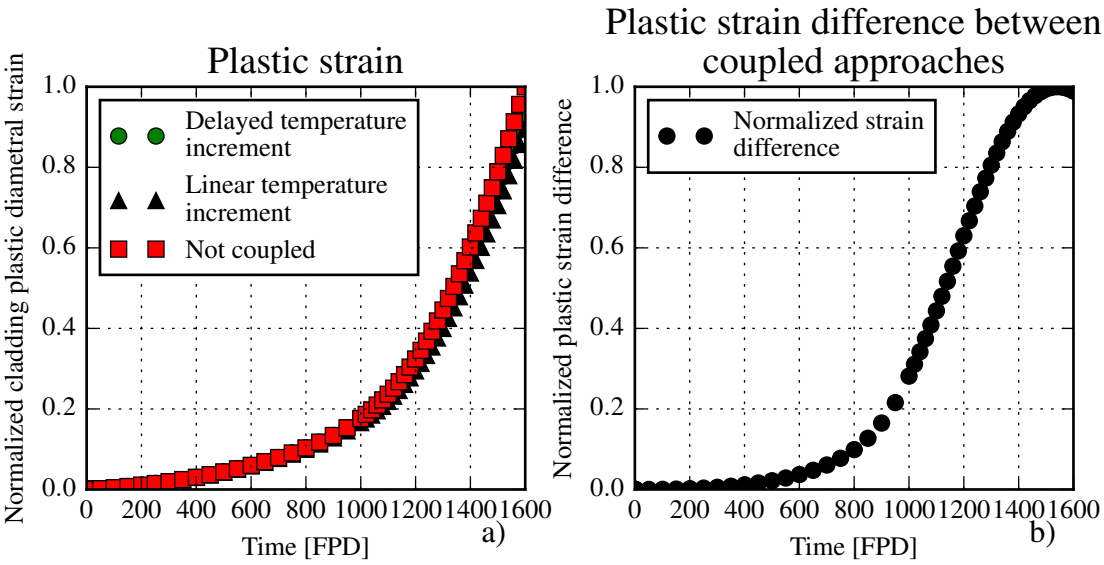

Figure 6.35.: a) Evolution of the average viscoplastic diametral strain of the fuel pins of the bundle, computed with coupled simulations with two different temperature interpolation methods, and without coupling. The maximal average strain computed amongst all simulations was used for the normalization. b) Evolution of the difference in the average viscoplastic diametral strain computed with the two coupled simulations, normalized with the maximal difference.

Case	Average T in [1,1000] FPD (A1, $z = 0.54$ m) [°C]	Incubation dose at that T [dpa]
Delayed temperature increment	554	125.5
Linear temperature increment	562	128.0
Two intermediate CFD simulations	557	126.3

Table 6.5.: Average cladding temperature of the central pin A1 at z = 0.54 m in the period from $t = 1$ FPD up to $t = 1000$ FPD, and swelling incubation dose computed for that temperature. The results obtained with the two temperature interpolation methods are compared to the results obtained when additional CFD simulations are considered in the temperature evolution.

Using additional CFD simulations

In the Delayed Temperature Increment approach, the temperature distribution is considered to be linear between BOL and t_{inc}, and between t_{inc} and EOL, and it is constructed by interpolating the results of CFD simulations. However, the increment of temperature is not a linear function of the deformation level, and it depends both on the geometry change and on the reduction of the mass flow rate that comes with it, which in this case reached approximately 14% at EOL. For this reason, CFD simulations on partially deformed geometries were conducted, and the temperature distributions thus obtained were employed to construct a new temperature history that supposes a linear evolution between the following states:

- State I: Isothermal *cold* state;
- State II: BOL, obtained with a CFD simulation in the non-deformed geometry and with BOL boundary conditions;
- State III: Intermediate state at $t_{inc} = 976$ FPD[15], obtained with a CFD simulation in the intermediately deformed geometry and with boundary conditions corresponding to 976 FPD. This geometry was computed by DOMAJEUR2 at 976 FPD, and the coolant mass flow rate reduction associated to that deformation level was taken into account;
- State IV: Intermediate state at $t = (t_{inc} + t_{EOL})/2 = 1287$ FPD, obtained like State III but for the deformation and boundary conditions computed for $t = 1287$ FPD;
- State V: EOL, obtained with a CFD simulation in the EOL deformed geometry and with EOL boundary conditions.

This temperature history was employed to conduct a new thermomechanical simulation with DOMAJEUR2. The evolution of the cladding temperature at an altitude of z = 0.54 m is presented, for three different pins, in Figure 6.36a, as computed using the 4 different temperature histories evaluated in this section, while the associated EOL diametral deformation profiles are presented in Figure 6.36b.

It can be observed in Figure 6.36a that, at z = 0.54 m and $t = t_{inc} = 976$ FPD, the CFD simulation yields a cladding temperature only ∼5°C higher than the Delayed Temperature Increment interpolation. Additionally, this difference is significantly reduced for $t = 1287$ FPD, which—as discussed earlier in this section—is more relevant since the strain rate is higher at this later time. As a consequence, as can be noted in Figure 6.36b, using two additional CFD calculations in partially

[15]Note that this is the same value of t_{inc} computed by the Delayed Temperature Increment method, and represents the time up to which the deformation is assumed to have a negligible impact on temperature in that approach. Conducting a CFD simulation in the geometry obtained precisely at his time allows to evaluate the adequacy of this hypothesis.

deformed geometries to construct the temperature history, employed as input for the thermomechanical simulation, does not have a noticeable impact on the EOL diametral strain of the fuel pins.

In view of these results, the Delayed Temperature Increment approach for the computation of the temperature history of the fuel claddings is retained in this work, and it is used for application cases presented in Chapter 7. This approach allows reducing the number of computationally expensive CFD simulations needed for a coupled calculation, by replacing them with appropriate interpolations—based on the computed evolution of the geometry—, without compromising the most relevant results: the EOL deformation of the fuel pins and their EOL temperature distribution. Firstly, the EOL deformation of the bundle is not, as evidenced by Figure 6.36b, significantly impacted by considering additional CFD simulations. Then, given that the EOL geometry is not impacted, the EOL temperature distribution, which is in all cases obtained with a CFD simulation in that deformed geometry, is also unaffected.

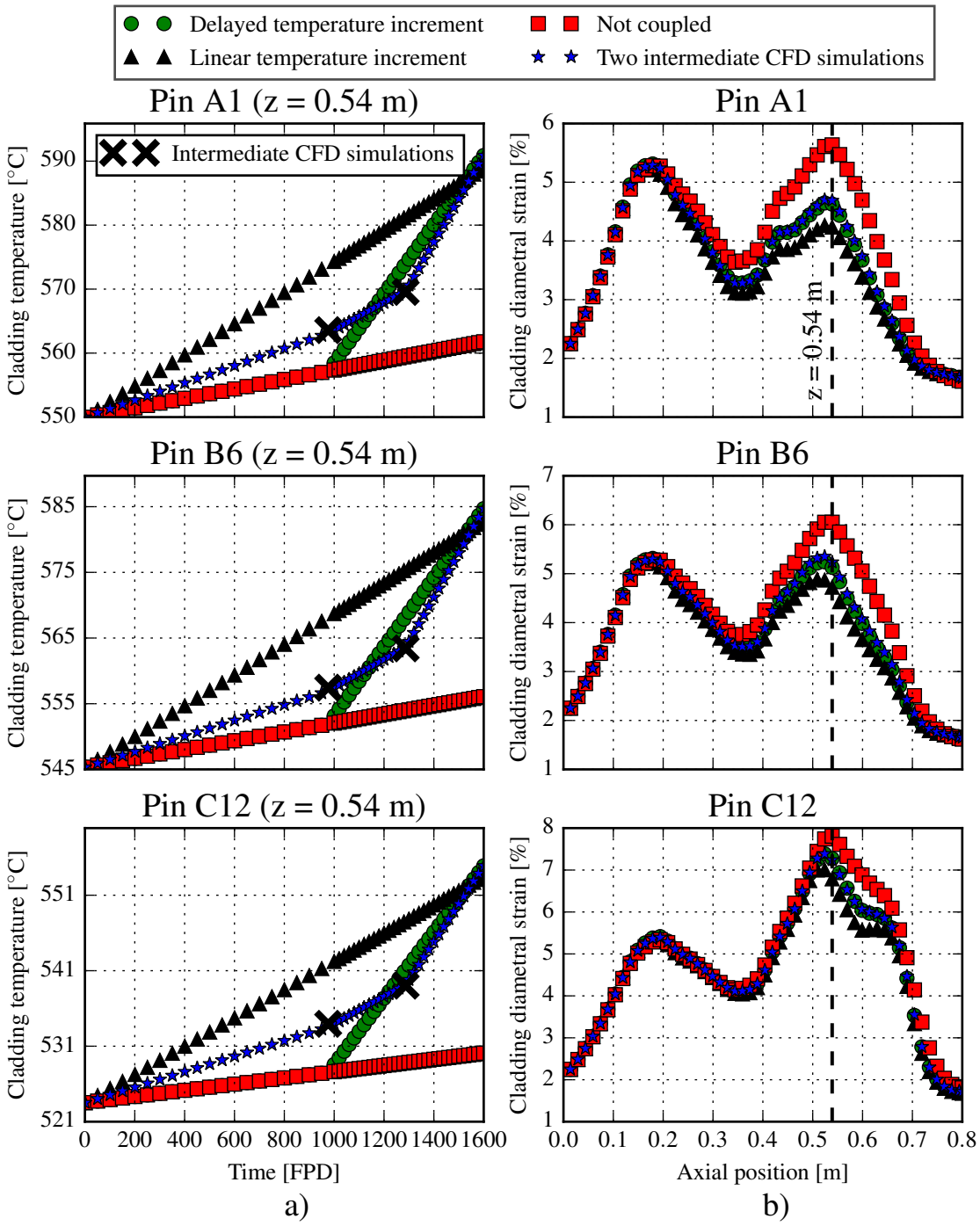

Figure 6.36.: a) Cladding temperature evolution at $z = 0.54$ m obtained with the coupled simulations—with two different temperature interpolation methods—, compared to the evolution computed by including two intermediate CFD simulations, and to the results obtained without coupling, for three different fuel pins. b) EOL diametral strain profiles computed in each simulation and for each pin.

6.9. Summary

In this chapter, we presented a series of numerical simulations of the irradiation of reduced fuel bundles (7 and 19 pins), with characteristics representative of advanced SFR designs. We firstly showed that, for our application, including only the fluid domain in the CFD simulations, considering only the radial heat conduction in the thickness of the cladding, and assuming the spacer wires are adiabatic, are adequate approximations. The impact of the cladding ovalisation on the thermal-hydraulics of the bundle was not considered, and its evaluation constitutes a future outlook of this work. Similarly, we showed that the neutronic feedbacks are of second order, and therefore they do not need to be taken into account in the coupling simulation methodology developed in this work.

Then, we showed that the diametral deformation of the fuel pins leads to a significant temperature increase of the coolant and of the fuel claddings, dominated by the reduction of the coolant mass flow rate induced by the deformation. We also showed that, for high irradiation doses that lead to a large deformation and thus to a large temperature increase, this increase has a negative feedback on the cladding deformation, determined by the temperature dependence of swelling and irradiation creep. For this reason, the coupled simulations yield a lower EOL deformation than the non-coupled simulations. Concerning the deformation of the claddings, similar results were obtained with the 1D model of DOMAJEUR2 and with the 3D model, partially justified by the very low impact of the circumferential cladding temperature gradients (not considered in the 1D model) on the cladding diametral strain. However, important swelling gradients were computed with the 3D model; a quantification of the associated secondary stresses is one of the future outlooks of this work.

Additionally, we showed that the deformation reduction induced by the coupling delays the third phase of the bundle interaction, and thus the apparition of very high stresses associated to a high cladding ovalisation.

Finally, we showed that, for the computation of the cladding temperature history used as input for DOMAJEUR2 at each global iteration of a coupled simulation, using only one CFD simulation in a deformed geometry is sufficient for the purposes of this work.

7. Application cases

In this chapter, we present two application cases of the coupled simulation methodology developed in this work. Firstly, in Section 7.1, we present the simulation of a subassembly irradiated in Phenix SFR, and the computed cladding deformation is compared to the available experimental data. Then, in Section 7.2, we present a numerical benchmark in which the simulation of a Joyo SFR (Soga, C. Ito, Aoyama, et al. 2009) subassembly is conducted with the methodology here developed, and the results thus obtained are compared to the results computed with a preexisting coupled simulation approach for SFR subassemblies.

Table of Contents

7.1. Simulation of an irradiation experience: Phenix subassembly

In this section, we present the simulation of the irradiation of a Phenix subassembly. Ideally, such a simulation would be used to quantitatively evaluate the predictive capabilities of the developed methodology. However, in order to do this, precise measurements of both the bundle temperature and deformation distributions are required. Many Phenix subassemblies have undergone post irradiation examinations that provide information about the EOL deformation of their fuel claddings, but the temperature distribution within the subassembly was never measured[1]; the only temperature measurements were done at the inlet of reactor core and 12 cm above the outlet of each subassembly, which is not sufficient for a quantitative validation of the coupling methodology.

In addition, in this case, one cannot differentiate the errors introduced by the multiple uncertain input parameters from the ones potentially introduced by the coupling methodology itself. Noteworthy examples of highly uncertain parameters are the distribution of the irradiation dose of the claddings, and the coefficients of the swelling material laws, which, as we discussed in Section 2.2.2.2 and as we will later see in this section, are highly sensitive to the composition, and to the fabrication and the irradiation conditions of the cladding steel. Furthermore, these parameters have a leading role in the evolution of the geometry of the fuel bundle. In view of the large discrepancies found between the predicted and measured deformation of several experimental irradiations, both the dose distribution and the swelling law coefficients are currently being recalculated, at the CEA, for a selection of experimental subassemblies.

In spite of the aforementioned limitations associated to the available experimental data and simulation input parameters, simulating the irradiation of a Phenix subassembly is valuable for two main reasons:

- It allows to demonstrate that the implementation of the coupled simulation methodology developed in this work can handle large scale fuel bundles. In this case, 217 fuel pins as opposed to the 7 and 19 fuel pin bundles evaluated in Chapter 6, which represents a scale up that significantly increases the complexity of the problem;
- It allows to demonstrate that the simulation methodology produces results that are qualitatively consistent with the experimental deformation measurements.

[1] There exists an irradiation experience conducted in Rapsodie reactor in which thermocouples were used to measure the temperature distribution at the outlet of a fuel bundle. However, the lack of neutronic data and the complexity of the irradiation (e.g. rearrangement of the fuel pin distribution in the bundle between two irradiation cycles) do not allow to use this experience for validation purposes.

To select the subassembly to be simulated, the following criteria were considered:

- Availability of extensive post irradiation examination of the fuel pins;
- Sufficiently high EOL deformation;
- Availability of the required input data, including the distribution of the irradiation dose at different instants of the irradiation, and the evolution of the internal pressure of the claddings, which are calculated, respectively, by neutronic and fuel performance codes;
- *Smooth* irradiation history, which implies little or no modification of the subassembly position and orientation in the core during its irradiation, and limited variations in the core power level. This criteria aims to reduce the uncertainty associated to the neutronic data (power, irradiation dose distribution, etc.).

7.1.1. Case description

Following the criteria defined above, the irradiation of the MYOSOTIS subassembly was selected. The main geometric and thermal-hydraulic characteristics of MYOSOTIS are summarized in Table 7.1, where some relevant irradiation conditions are also included. MYOSOTIS is a standard Phenix subassembly[2] irradiated up to a maximal dose of approximately 120 dpa, leading to a maximal cladding diametral deformation of about 5%. It was irradiated in an experience aimed to evaluate the behaviour of Phenix subassemblies during long residence time in the reactor in a low dose rate condition. For this reason, it was placed in a peripheral position within the core, which is why it presents a very large radial dose gradient, as illustrated in Figure 7.1. MYOSOTIS was irradiated during 1273 FPD in the same position in the core of the reactor and, unlike other subassemblies within the core, it was never rotated around its vertical axis.

The normalized evolution of the maximal linear power amongst the fuel pins of MYOSOTIS—obtained from the reports of the irradiation cycles of Phenix—is illustrated in Figure 7.2a. An overall reduction with time is observed, consequence of the burn-up of the fuel, and local variations are due to the modification of the reactor operation regime. For the simulation here conducted, a linear interpolation between the power levels at the states S1 and S2, indicated in Figure 7.2a, was considered. These are, respectively, the first and last computed values with the reactor operating at full power. As can be inferred from Figure 7.2, interpolating between these values is more representative of the overall power evolution than interpolating between the very first and last available power values, which were

[2]The subassembly inlet nozzle was slightly modified from the standard subassembly, in order to obtain the desired mass flow rate during the irradiation.

Parameter	Value
Fuel pin length	1.793 m
Heated column length	0.85 m
Fuel pin pitch	7.79 mm
Fuel pin external diameter	6.55 mm
Spacer wire diameter	1.15 mm
Spacer wire helix step	150 mm
BOL sodium mass flow rate	17.1 kg/s
EOL sodium mass flow rate	14.4 kg/s
Inlet BOL sodium temperature	395°C
Inlet EOL sodium temperature	389°C
Hexcan plate to plate distance	116.9 mm

Table 7.1.: Main geometric and thermal-hydraulic characteristics of MYOSOTIS.

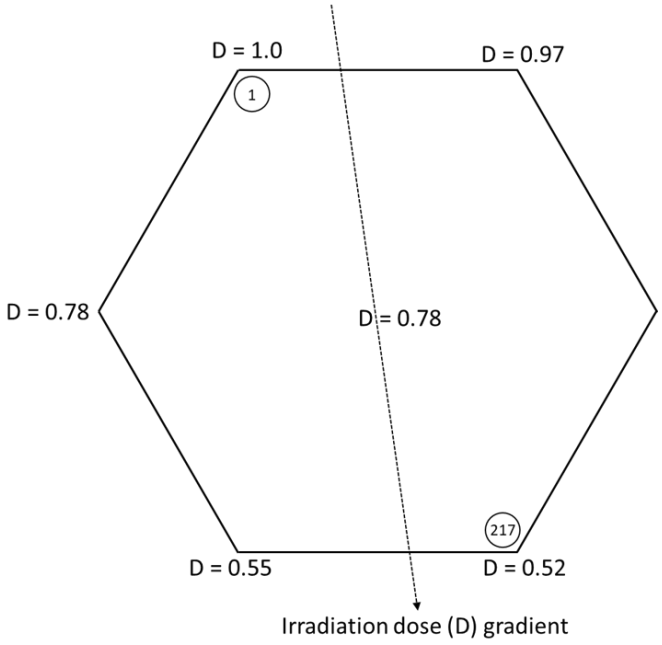

Figure 7.1.: Distribution of the normalized maximal EOL irradiation dose calculated within the fuel bundle of MYOSOTIS, which presents a high radial gradient due to its peripheral position within the core. The positions of the most and least irradiated fuel pins (pin N°1 and N°217, respectively) are indicated.

obtained with the reactor operating at a partial power regime. Then, in the simulation, the power distribution corresponding to S1 was assigned to t = 1 FPD (BOL), and that corresponding to S2 was assigned to $t = t_{EOL}$ (EOL), and the power was linearly interpolated for intermediate times. The spatial power distributions at these instants were obtained from preexisting neutronic simulations of MYOSOTIS. As an example, the axial profiles of normalized linear power of the most powerful fuel pin (the corner pin N°1, see Figure 7.1) thus obtained are presented in Figure 7.2b, for BOL and EOL. In this figure, and in the rest of this section, the axial position is measured from the base of the fuel pins, so that the heated column starts at an axial position $z = 0.818$ m.

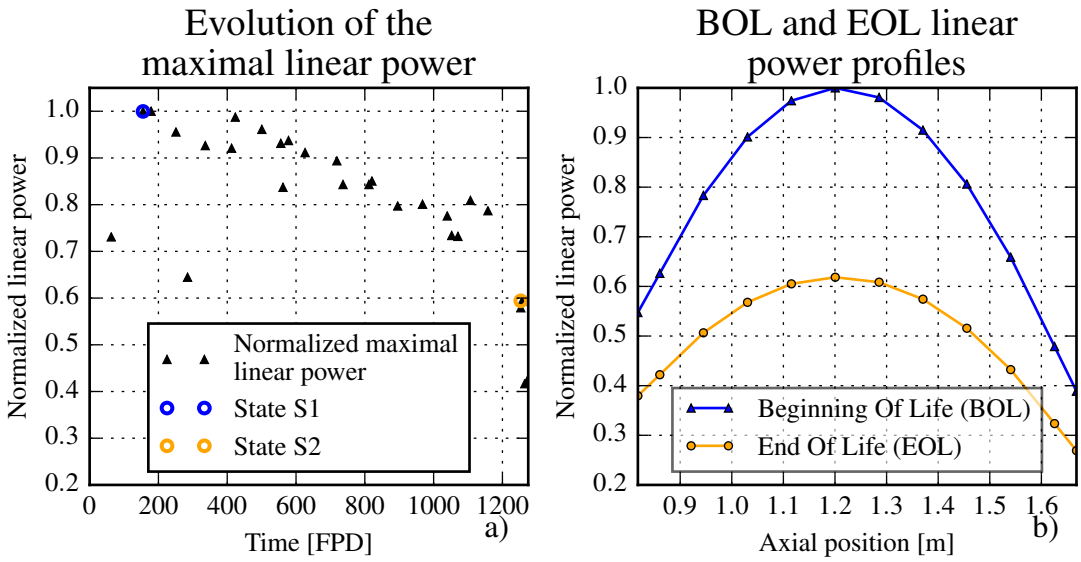

Figure 7.2.: a) Evolution of the normalized maximal linear power of MYOSOTIS. The encircled S1 and S2 states correspond to the first and last, respectively, in which Phenix reactor was operating at full power. Each reported value corresponds to the state at the end of an irradiation cycle. b) Normalized BOL and EOL axial profiles of linear power employed in the simulations for the corner pin N°1, which correspond to the states S1 and S2, respectively.

The inlet sodium temperature and the coolant mass flow rate, reported in Table 7.1 and employed for the simulation, were obtained, both for BOL and EOL, from the available data in the report of the corresponding irradiation cycles of Phenix. In particular, the measured sodium temperature difference between the inlet and the outlet of the subassembly, $\overline{\Delta T}_{Na}$, and the computed total subassembly power,

P_{SA}, were employed to compute the mass flow rate Q according to:

$$Q = \frac{P_{SA}}{C_p \overline{\Delta T}_{Na}} \tag{7.1}$$

where C_p is the specific heat of sodium and was evaluated at the average between the inlet and outlet sodium temperature. To compute the BOL and EOL mass flow rates, as was done with the linear power distribution, the first and last reported states [P_{SA}, $\overline{\Delta T}_{Na}$] with the reactor operating at full power were considered.

The procedure defined in Section 5.2 and employed to conduct the coupled simulations of the 7-pin and the 19-pin bundles, presented in Chapter 6, was employed to conduct the simulation of MYOSOTIS. The "Delayed Temperature Increment" method (see Section 5.4.1) for interpolating the evolution of the temperature distribution in the subassembly between the BOL and EOL distributions—computed with CFD simulations—was selected.

As mentioned above, for the simulation of MYOSOTIS, the EOL mass flow rate was obtained from the reactor cycle report, as opposed to being computed from the core pressure drop and the bundle deformation like in the simulations presented so far. The reason for this is that the core pressure drop, required by the model to compute the mass flow rate in deformed bundles (see Section 5.3.2), was not measured during the operation of Phenix. An estimated value is indicated in the cycle reports but, as discussed in (Guidez and Martin 1987), it should rather be considered as a hydraulic parameter than as a good estimation of the absolute magnitude of the pressure drop.

As a consequence of prescribing the coolant mass flow rate, a comparison between non-coupled and coupled simulations cannot be done. Indeed, as discussed in Section 6.5, the effects of the deformation on the temperature distribution are due to the modification of the geometry itself, but also due to the associated mass flow rate reduction, which has a preponderant role. In this case, the latter is implicitly taken into account in the mass flow rate used for EOL, which is derived from the measured $\overline{\Delta T}_{Na}$.

7.1.2. Simulation results

Since, as discussed above, the CFD simulations conducted in the nominal and in the deformed geometries use the same boundary conditions, they lead to similar temperature distributions. This can be observed in Figure 7.3, where the axial distribution of the average cladding surface temperature of the central pin N°109 and the corner pin N°1, which presents the highest power level, are presented. The coolant temperature distribution at the outlet of the non-deformed fuel bundle

geometry is also presented in this figure. It can be observed that the axial temperature distribution of the cladding temperature of the central pin is not noticeably affected by the deformation, while a slight temperature increase of up to 6°C on the cladding surface temperature—averaged on its circumference—can be noted for the corner pin N°1. Such a small temperature perturbation has a negligible feedback on the deformation of the bundle, which is why the simulation converged after only one iteration.

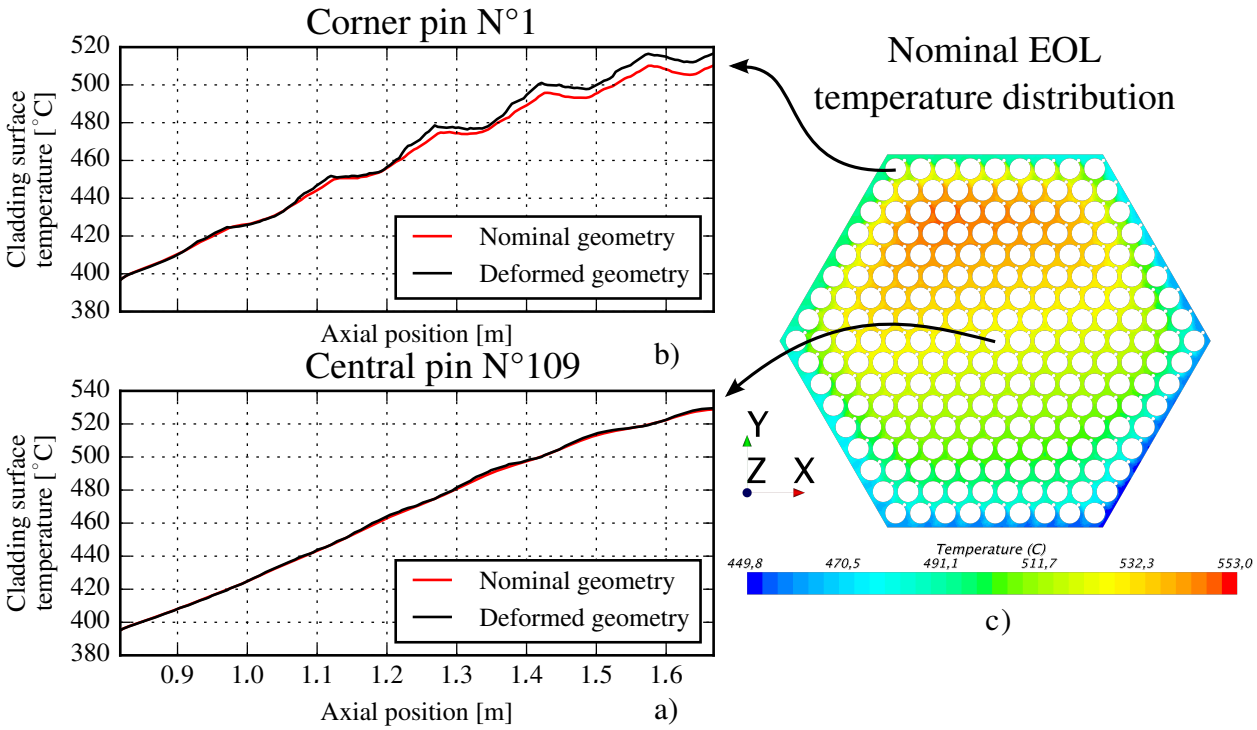

Figure 7.3.: Axial profiles of average cladding surface temperature for the central pin N°109 (a) and the corner pin N°1 (b), computed with CFD simulations in nominal and deformed geometries with the same EOL sodium mass flow rate and power. The outlet sodium temperature distribution in the nominal geometry is presented in (c), computed with the same EOL boundary conditions.

The computed axial profiles of normalized diametral viscoplastic strain (i.e. swelling and creep strains) are presented, for three different fuel pins, in Figure 7.4, where they are compared to the normalized strain profiles obtained from the post irradiation measurements. In all cases, the maximal computed strain was employed for the normalization. It can be observed that the position and magnitude of the maximal deformation of the corner pin N°1, the most deformed

pin, is correctly predicted. Additionally, the deformation computed for less irradiated pins is consistently lower. However, the prediction of the strain maximum becomes poorer towards the less irradiated corner of the bundle, where the absolute value of the deformation is also lower. Concerning the observed differences in the shape of the strain profiles, it should be noted that the sudden strain increase and drop observed at the start and end of the heated column, z = 0.818 m and z = 1.668 m respectively, are a consequence of considering a null linear power outside this region. Due to this, there are temperature discontinuities at these points—whose magnitude is determined by the temperature difference between the surface and the mid-thickness of the cladding at the extremes of the heated column—without which the transition towards a null diametral strain would be smoother, as observed experimentally. This simplification, however, does not affect the strain profile within the heated column, which is the region of interest in our case.

In Figure 7.5, the maximal calculated diametral strain is presented for each fuel pin together with the measured value—both normalized with the maximal computed strain of the pin N°1—in a histogram ordered according the maximal irradiation dose of each pin. It can be noted that the best agreement between simulation and experimental data is found for the most irradiated pins, and that the simulation systematically overpredicts the maximal diametral deformation.

A similar trend can be observed for the relative error in the maximal diametral strain, defined as:

$$E_{rel} = \frac{\epsilon^{max}_{simulation} - \epsilon^{max}_{experimental}}{\epsilon^{max}_{experimental}} \tag{7.2}$$

where $\epsilon^{max}_{simulation}$ and $\epsilon^{max}_{experimental}$ are the computed and measured maximal viscoplastic diametral strains, respectively. This error is presented, for all measured pins, in Figure 7.6, where a clear decrease with increasing maximal irradiation dose and increasing maximal deformation can be noted. This means that the relative error is greatest for the less irradiated, and less deformed—and thus less relevant from a thermomechanical and thermal-hydraulic point of view—fuel pins. It is to be noted that here, as in all the reported deformation values in this section, only the contribution of swelling and creep to the diametral strain of the claddings is reported. This means that the contribution of thermal expansion is not reported, which is done for the sake of comparison with the experimental data, obtained at room temperature. Thermal expansion induces an additional diametral strain of up to 1%, the consideration of which would significantly reduce the relative error presented in Figure 7.6.

In order to understand the discrepancies between the simulation and the experimental data, it is important to note, firstly, that the coefficients of the swelling law used for the simulation were originally determined—from the experimental irradiation of fuel pins of numerous subassemblies—by associating a measured swelling strain with calculated dose and temperature values. Secondly, that the

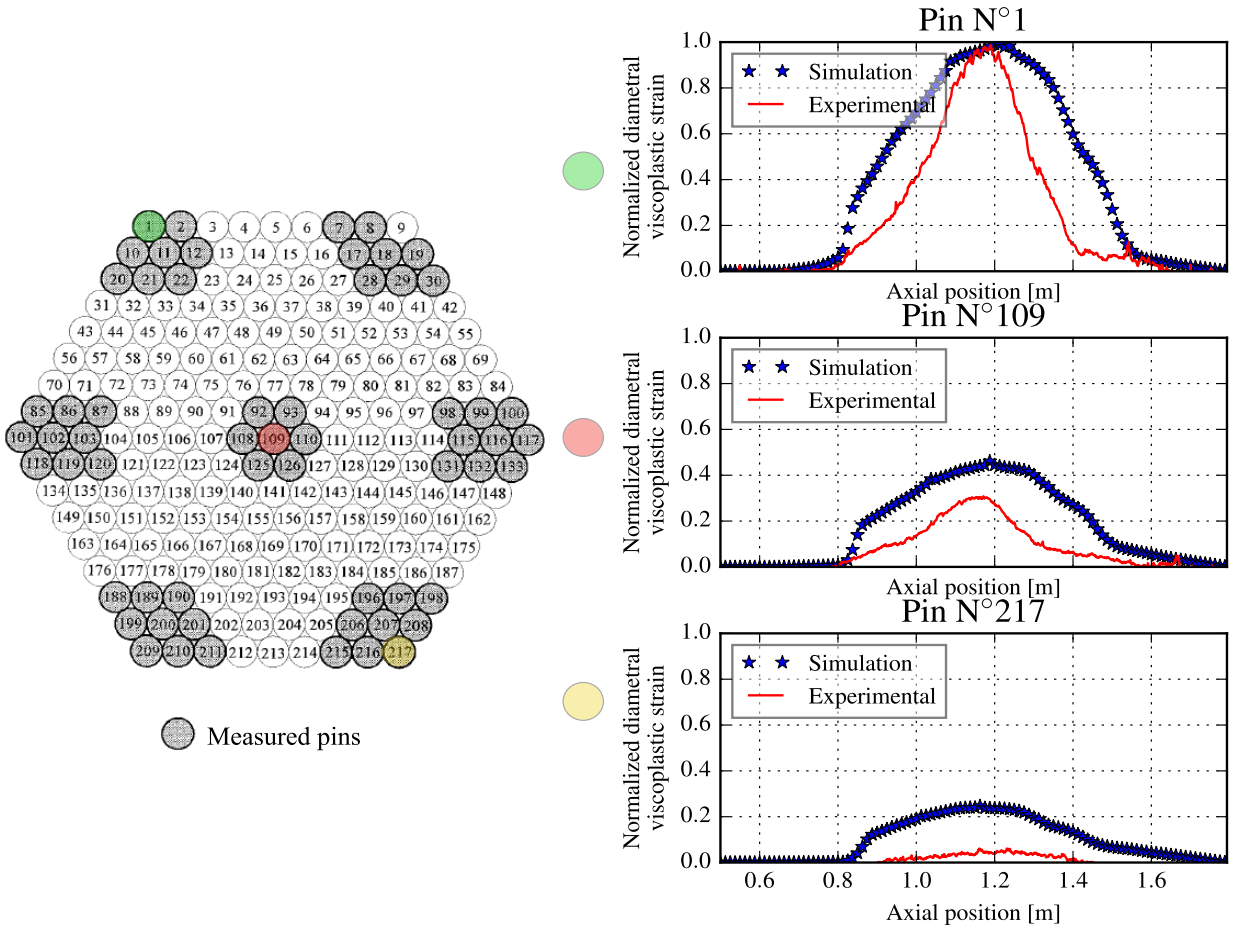

Figure 7.4.: Axial profile of normalized diametral viscoplastic strain computed by the coupled simulation and experimentally measured, for three selected fuel pins. The position of these pins within the bundle is indicated by the coloured circles, and the pins that were examined after the irradiation are shaded.

irradiation positions close to the center of the reactor core, and axial sections of the claddings with relatively high deformation levels, were privileged in the experimental post irradiation examination of the fuel pins. As discussed in Section 2.2.2.2, swelling depends on multiple parameters, but only the irradiation dose and temperature are taken into account in the swelling laws of the French SFR program. Then, by determining these laws based experimental data that is more representative of highly deformed claddings irradiated at a high dose rate, a bias is likely introduced. It is then not surprising to find that the predictive capabilities of the swelling law used here are greatest concerning the maximal diametral strain of the most irradiated fuel pins.

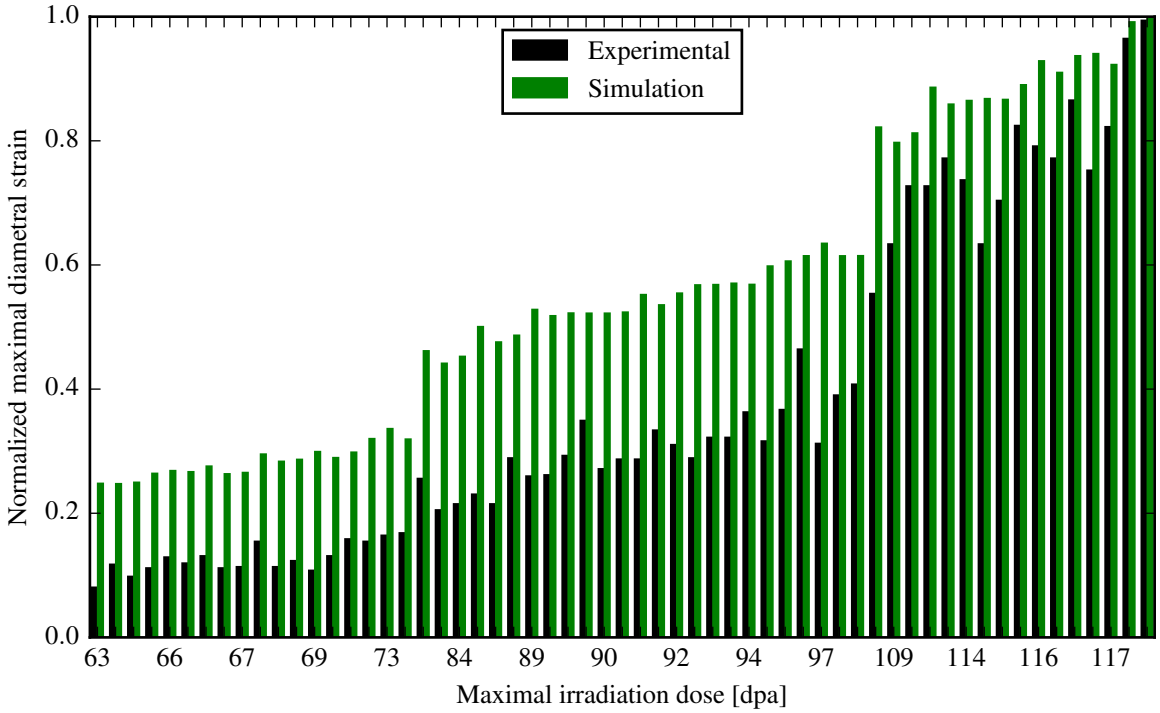

Figure 7.5.: Normalized measured and calculated maximal diametral strain of the fuel pins as a function of their maximal computed irradiation dose.

Another factor that compromises the capability of the simulations here presented of accurately predicting the deformation distribution, is the high dispersion in the swelling resistance of different batches of the same fabrication lot of the cladding steel. An example of this is presented in Figure 7.7, where the maximal measured cladding diametral strains of different pins of the same Phenix subassembly are presented as a function of of their maximal irradiation dose, for different batches of the CF lot of the 15-15Ti steel used to fabricate them. The reported values have been normalized with the overall strain maximum. It can be noted in Figure 7.7 that a relative difference in maximal diametral deformation of up to $\sim 100\%$ is obtained, with different batches of this lot, for maximal doses differing in less than 3 dpa. The claddings of MYOSOTIS were fabricated with the batch 7 of the CF lot; however, the only swelling law parameters available to us were derived from considering all the CF batches, which therefore introduces another bias.

These limitations are part of the reasons why the simulation presented in this section was conducted with the goal of demonstrating the capability of the coupling methodology of simulating full scale fuel bundles and obtaining physically

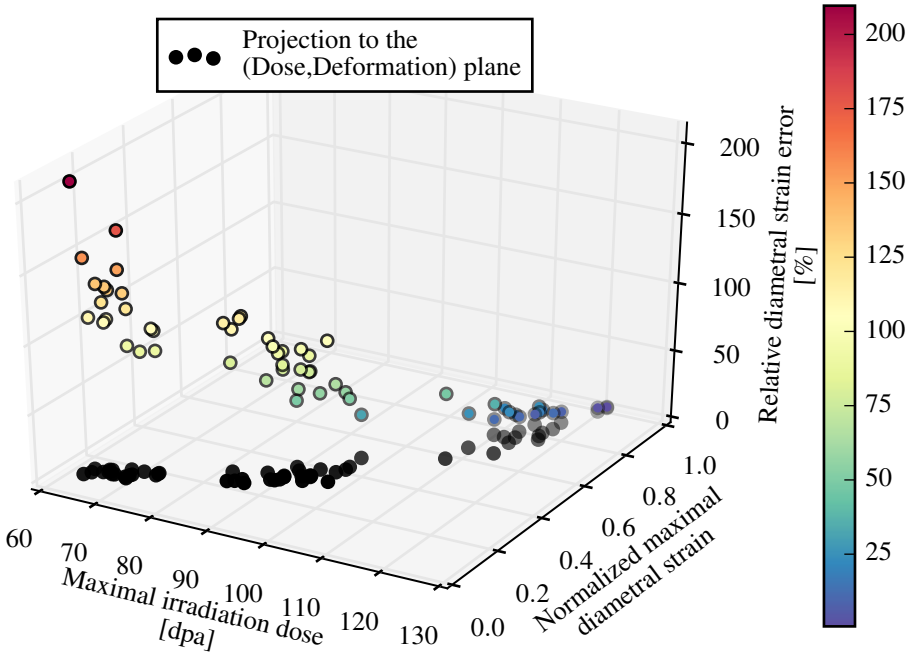

Figure 7.6.: Relative error in the maximal diametral deformation of the pins, as a function of the maximal irradiation dose and of the maximal deformation.

consistent results, and not as a quantitative validation. The simulation was indeed conducted satisfactorily and, in view of the good prediction of the position and magnitude of the maximal cladding diametral deformation within the bundle, and of the direction of the deformation gradient, we consider this goal to be fulfilled.

An outlook of this work is to employ the developed methodology to contribute to the redefinition of the swelling laws, thus taking the coupling effects into account and profiting from the superior detail in the temperature distribution, with respect to the lumped parameters codes originally employed for defining these laws, provided by the CFD simulations.

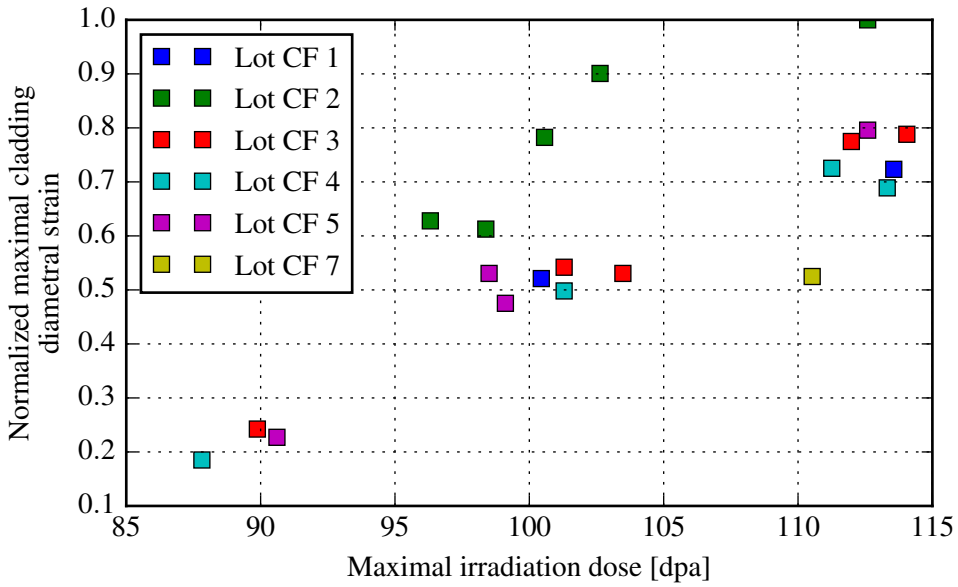

Figure 7.7.: Maximal measured cladding diametral strain as a function of the maximal computed irradiation dose, for different fuel pins—irradiated in the same Phenix subassembly—fabricated with different batches of the lot CF of the 15-15Ti steel. The reported values have been normalized with the maximal strain amongst all measurements. The claddings of MYOSOTIS were fabricated with Lot CF7.

7.2. Numerical benchmark: Joyo subassembly

In this section, we present a numerical benchmark based on the simulation of the irradiation of the PFD512 subassembly in the Mk-II core of the experimental SFR Joyo, originally presented in (Uwaba, Hiroyuki Ohshima, and M. Ito 2017). In that work, the coupling between the subchannel code ASFRE and the bundle thermomechanical code BAMBOO was employed to simulate the irradiation of PFD512, considering the actual PFD512 irradiation period of 327 FPD, as well as a longer 846 FPD irradiation as to evaluate the effects of a high deformation level. Here, we replicate the simulation of the 846 FPD irradiation of PFD512 by using the developed coupling between DOMAJEUR2 and STAR-CCM+. The goal of this benchmark exercise is to compare the bundle deformation and temperature distribution computed with the STAR-CCM+/DOMAJEUR2 coupling with the results obtained with ASFRE/BAMBOO.

7.2.1. Benchmark definition

The main design parameters of the PFD512 subassembly are presented in Table 7.2, where they are compared to the parameters of the advanced SFR designed at the CEA and to those of MYOSOTIS. The definition of the simulation conditions is based on the data reported in (Uwaba, Hiroyuki Ohshima, and M. Ito 2017), and it is described in what follows.

Parameter	PFD512	Advanced CEA SFR	MYOSOTIS
Number of fuel pins	127	217	217
Fuel pin length [m]	1.533	2.136	1.793
Heated column length [m]	0.55	0.8	0.85
Fuel pin pitch [mm]	6.47	10.8	7.79
Fuel pin external diameter [mm]	5.5	9.7	6.55
Cladding thickness [mm]	0.35	0.5	0.45
Spacer wire diameter [mm]	0.9	1	1.15
Spacer wire helix step [mm]	209	180	150
Hexcan plate to plate distance [mm]	74.7	161.5	116.9
Maximum BOL linear power [W/cm]	333	460	~ 300
BOL sodium mass flow rate [Kg/s]	8.85	27	17.1
Inlet sodium temperature [°C]	370	400	395
Bulk sodium heating rate [°C/m]	327	188	175

Table 7.2.: Main geometric and thermal-hydraulic characteristics of PFD512, compared to those of the advanced SFR designed at the CEA and of MYOSOTIS.

In (Uwaba, Hiroyuki Ohshima, and M. Ito 2017), the linear power profile of the highest power fuel pin—the central pin in this case—is given, and the power and neutron flux radial gradients within the subassembly are reported to be lower than 2%. These gradients are here neglected, since we use the same linear power profile for all pins, computed by normalizing the profile of the central pin as to obtain the reported total subassembly power of 1.94 MW. The reported profile is presented in Figure 7.8, where the normalized profile used here for all pins is also presented. In this figure, and in the rest of this section, the axial position z is measured from the base of the heated column of the fuel bundle, and it is nondimentionalized with the heated column length L. The reported sodium inlet temperature and sodium mass flow rate of 370°C and 8.85 kg/s, respectively, are employed and they are, following the hypothesis adopted in (Uwaba, Hiroyuki Ohshima, and M. Ito 2017), kept constant during the irradiation. This means that the reduction of the coolant mass flow rate caused by the deformation is not considered, hypothesis that is evaluated at the end of this section.

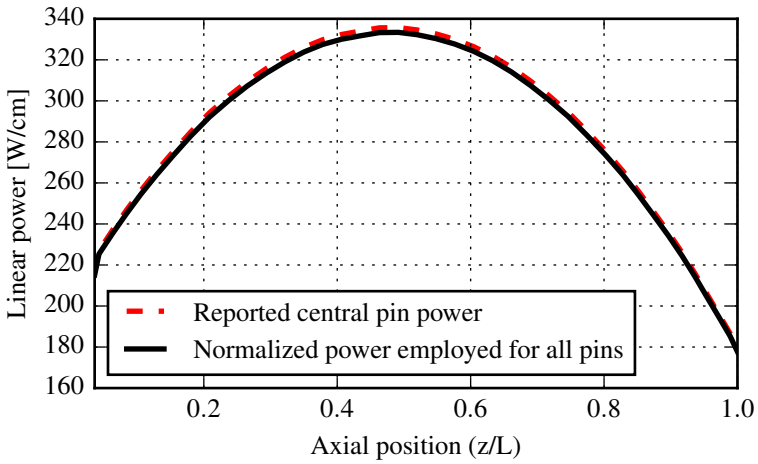

Figure 7.8.: Axial profile of linear power of the highest power fuel pin of PFD512, reported in (Uwaba, Hiroyuki Ohshima, and M. Ito 2017), and normalized profile employed for all fuel pins in the simulations here presented. The axial position z is measured from the base of the heated column, and it is nondimentionalized with the heated column length L.

The reported swelling empirical law is given by Equation 7.3 below:

$$g = \begin{cases} 0 & \text{for } \phi_t \leq \tau_{inc} \\ R(\phi_t - \tau_{inc})^{1.6} & \text{for } \phi_t > \tau_{inc} \end{cases} \tag{7.3}$$

where g is the volume void swelling (Vol%), ϕ_t the fast neutron fluence (x10^{26}/m^2), τ_{inc} the swelling incubation fluence (x10^{26}/m^2) and R the swelling rate parameter. R and τ_{inc} are functions of temperature and they are written as follows:

$$R = \frac{0.47}{e^{(\frac{T-480}{35})^2}} \tag{7.4}$$

$$\tau_{inc} = \frac{16.6}{e^{(\frac{T-469}{105.5})^2}} - 2 \tag{7.5}$$

where T is the temperature in °C.

The reported irradiation creep law is[3]:

$$\frac{\dot{\epsilon_{eq}}}{\sigma_{eq}} = B_0 + C\dot{g}_{linear} \tag{7.6}$$

where $\dot{\epsilon_{eq}}$ is the equivalent irradiation creep strain rate per fast neutron fluence ($(\text{x}10^{26}/\text{m}^2)^{-1}$), σ_{eq} the equivalent stress (MPa) and $\dot{g}_{linear}$ the linear swelling rate per fast neutron fluence ($(\text{x}10^{26}/\text{m}^2)^{-1}$). B_0 is the creep compliance parameter, and C is the irradiation creep-void swelling coupling coefficient. The reported values of these coefficients are $B_0 = 4.0\text{x}10^{-6}$ $(\text{x}10^{26}/\text{m}^2)^{-1}\text{MPa}^{-1}$ and $C = 5.5\text{x}10^{-3}$ MPa^{-1}.

It can be noticed that, unlike the material laws employed in the French SFR program, these laws are expressed in terms of neutron fluence instead of irradiation dose. Besides, the swelling law has a different functional form, even though it reflects the same general behaviour (see Equation 2.24). Namely, an incubation period with very low swelling (null in this case), followed by a period during which the swelling rate grows with increasing neutron fluence. The swelling temperature dependence is similar to that of the laws used until now in this work, while, unlike in the French SFR program, the creep compliance parameter is not considered to depend on temperature. The dependence of creep on temperature is nevertheless taken into account in the term of Equation 7.6 proportional to the linear swelling rate.

The laws given by equations 7.3 to 7.6 were implemented in DOMAJEUR2 and used, in the simulations, for the cladding and the spacer wires. A maximal fast neutron fluence of $23\text{x}10^{26}\text{n/m}^2\text{/s}$ is reported in (Uwaba, Hiroyuki Ohshima, and M. Ito 2017) for the 846 FPD irradiation, at the position of maximal linear power. Here, we considered this same maximal fluence for all the fuel pins at EOL (846 FPD), and we assumed the same normalized axial distribution than that of the linear power (see Figure 7.8), and a linear time evolution between BOL and EOL. No information concerning the neutron fluence of the hexcan is provided, but a maximal plate to plate strain of only 0.4% is reported, while the maximal cladding strain is close to 5%. Considering this, the swelling and creep of the hexcan were not considered in our simulations, and only the deformations due to thermal expansion were taken into account. The hexcan temperature was considered to grow linearly from 370°C at its bottom up to 500°C at he outlet of the heated column of the bundle, which is similar to the axial temperature distribution of a peripheral pin.

Finally, the internal cladding pressure was considered to evolve linearly from 0.1 MPa at BOL, to reach 2.5 MPa at 327 FPD, both values reported in (Uwaba,

[3]In (Uwaba, Hiroyuki Ohshima, and M. Ito 2017), a slightly different law is reported, in which the linear swelling $\dot{g}_{linear}$ was mistakenly replaced with the volume swelling rate $\dot{g}$. This misprint, confirmed by the authors of that work, has been corrected here.

Hiroyuki Ohshima, and M. Ito 2017). In order to facilitate the direct comparison of the results, we followed the approximation adopted in (Uwaba, Hiroyuki Ohshima, and M. Ito 2017), which neglects any pressure increase after 327 FPD.

Considering the initial and boundary conditions defined above, the simulation of the irradiation of PFD512 was conducted using the coupling between DOMAJEUR2 and STAR-CCM+. For the CFD simulations of PFD512, and unlike all the simulations presented so far, using a flat velocity profile as inlet boundary condition was found to affect the sodium temperature distribution all the way up to the outlet of the domain. As presented in Table 7.2, the heated column of PFD512 is significantly shorter than the heated column of the advanced SFR and than that of MYOSOTIS, which means that a more significant fraction of the total sodium bulk heating takes place in a region where the velocity profile is still developing. Besides, the bulk sodium heating in the developing region is also larger in absolute terms, since the average sodium temperature increase within the heated column is larger as well ($\sim$ 180 °C vs 150 °C). Due to this, for the CFD simulations of PFD512, the inlet sodium velocity profile was extracted from a cross section located 41.8 cm (twice the step of the spacer wire helix) downstream of the inlet, once the hydraulic field had been converged. The velocity distribution imposed at the inlet was normalized to ensure the mass conservation.[4]

7.2.2. Results comparison

In what follows, the comparison between the results obtained with STAR-CMM+/DOMAJEUR2 and those computed by ASFRE/BAMBOO is presented in the following order:

1. **Result I**: Comparison of the temperature distribution computed in the non-deformed geometry;

2. **Result II**: Comparison of the EOL deformation computed with the coupled simulations. As in the previous coupled simulations presented in this work, only the diametral strain of the claddings is considered in the CFD simulations conducted with STAR-CMM+, even though DOMAJEUR2 also computes the flexion of the pins. However, the effects of the helical flexion of the fuel pins are considered in ASFRE;

3. **Result III**: Comparison of the temperature distribution in the EOL deformed geometry, without representing the helical flexion of the fuel pins in the CFD simulations;

[4] In this case, the inlet plane and the plane 2 wire steps downstream do not have a conformal mesh. Therefore, the small errors of the velocity interpolation at the inlet lead to a modification of the total mass flow rate, which is why the normalization was required.

4. **Result IV**: Comparison of the temperature distribution in the EOL deformed geometry. In this case, the helical flexion of the fuel pins is represented in the CFD simulation employed to compute the EOL temperature distribution, since, as discussed later in this section, it was found to have a significant impact on the temperature distribution at the outlet of the PFD512 subassembly;

5. **Result V**: Evaluation of the impact of considering the coolant mass flow rate reduction caused by the deformation, neglected in the benchmark up to this point for the sake of comparison with ASFRE/BAMBOO, which does not consider this effect.

Result I: Temperature in the non-deformed bundle

To compare the results, we consider the subchannels in one of the diagonals of the hexagonal subassembly cross section, as indicated in Figure 7.9. The average sodium temperatures computed, with a CFD simulation, for each subchannel at the outlet and the midplane ($z/L = 0.5$) of the heated column, are presented in Figure 7.10. These results correspond to the non-deformed geometry, and they are there compared with the results presented in (Uwaba, Hiroyuki Ohshima, and M. Ito 2017), computed with the subchannel code ASFRE. The results obtained with the two methods are in general good agreement, although ASFRE predicts an outlet temperature for the central subchannels of about 7°C higher, and outlet temperatures up to 14°C higher in the corner subchannels. A larger temperature difference in the peripheral subchannels, with respect to the CFD results, is in line with the results discussed in Section 3.1.1.

The axial profiles of average cladding mid-wall temperature for the central and and the right corner pin are presented in Figure 7.11, as calculated with ASFRE and with the CFD simulation in the non-deformed geometry. Once again, it can be observed that ASFRE yields a temperature slightly higher (up to 10°C difference) than the CFD simulation for the central pin. Besides, the CFD-calculated profile for the corner pin shows temperature oscillations, induced by the spacer wires and discussed in Section 2.1.5, which are not captured by the subchannel simulation in which the wires are not explicitly represented.

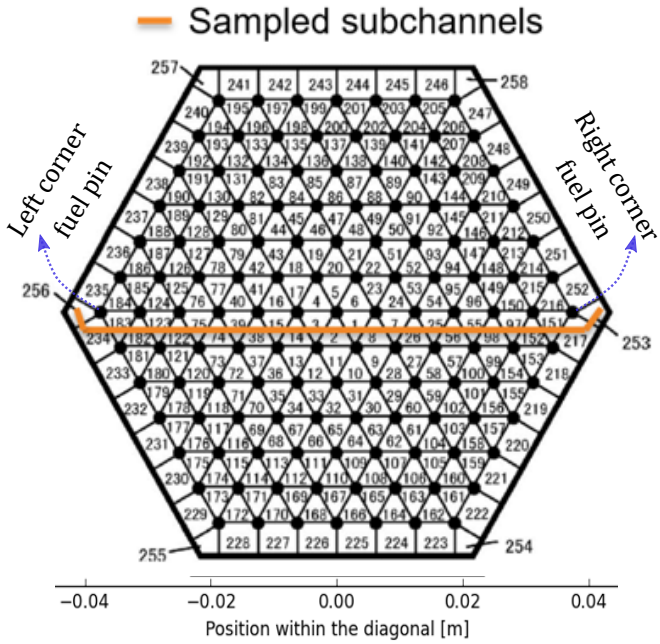

Figure 7.9.: Cross section of PFD512 indicating the subchannels sampled in the CFD simulations. Adapted from (Uwaba, Hiroyuki Ohshima, and M. Ito 2017).

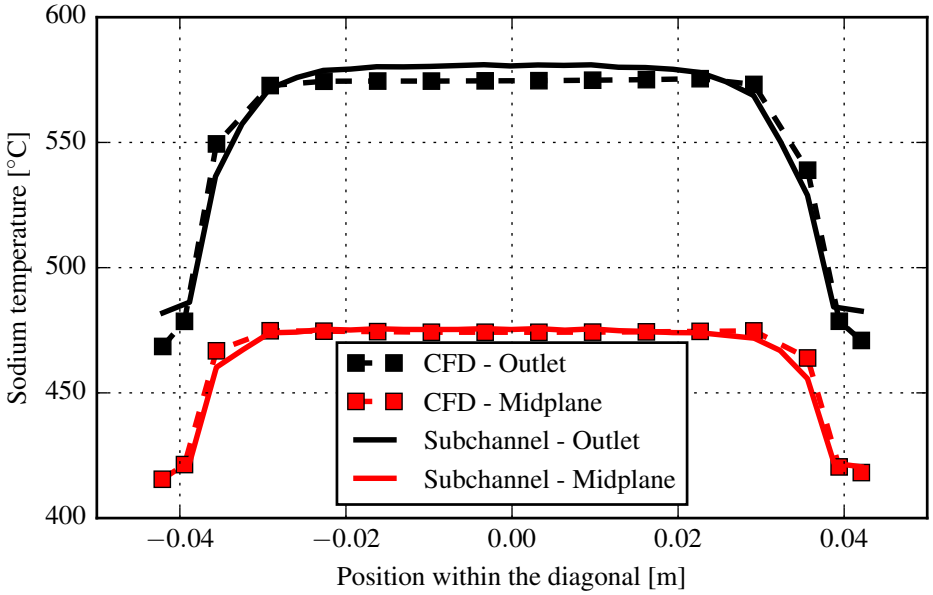

Figure 7.10.: Sodium temperature distribution at the outlet and midplane of the fuel bundle, computed with the subchannel and the CFD simulations in the non-deformed geometry. The reported temperature values are averaged in the subchannels following a diagonal of the hexagonal subassembly cross section.

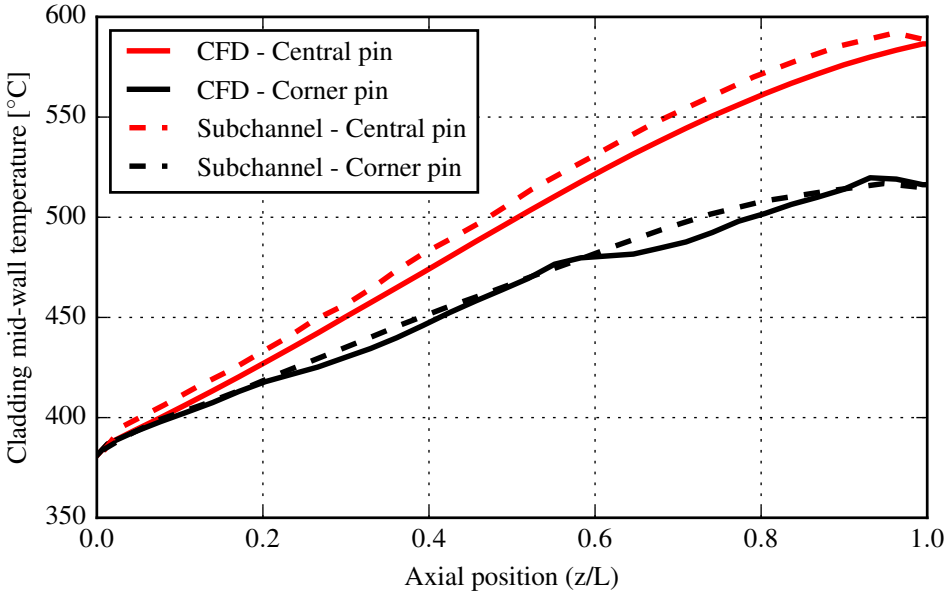

Figure 7.11.: Axial profiles of average cladding mid-wall temperature for the central and the right corner pin, as computed by the CFD and the subchannel simulations in the non-deformed geometry.

Result II: Deformation

The axial profiles of swelling induced and total EOL viscoplastic (swelling and creep) diametral strain of the central pin of PFD512 computed with the STAR-CCM+/DOMAJEUR2 coupling are presented in Figure 7.12, where they are compared to the profiles computed by ASFRE/BAMBOO. A very good agreement can be observed between the two simulations, although DOMAJEUR2 computes a slightly higher maximal swelling— and thus total—strain.

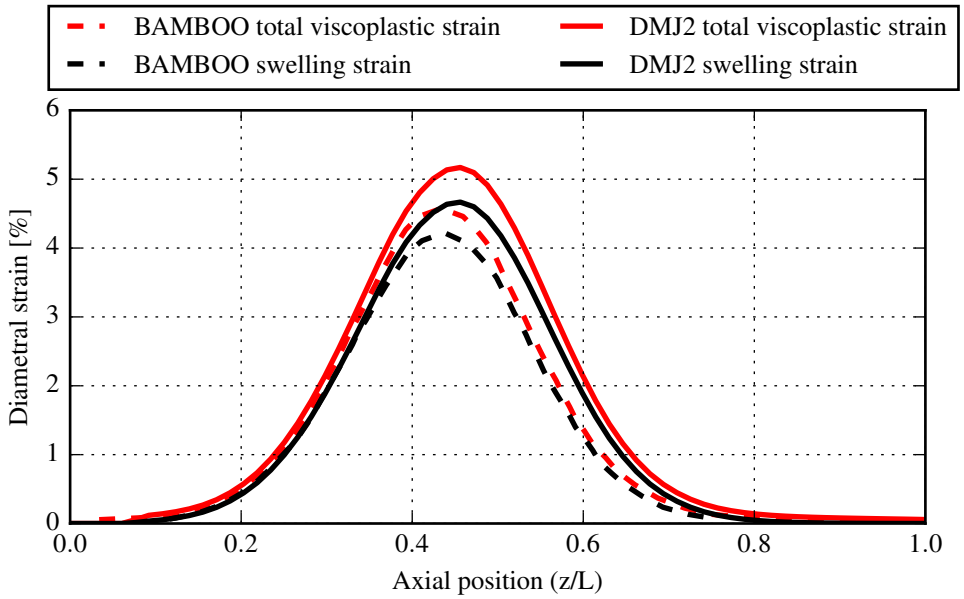

Figure 7.12.: Axial profiles of swelling strain and total viscoplastic diametral strain of the central pin of PFD512, as computed by DOMAJEUR2 and by BAMBOO at EOL.

The EOL axial profile of lateral displacement of the fuel pin presenting the highest helical flexion—the left corner fuel pin that occupies the subchannel N°256 as indicated in Figure 7.9—computed by DOMAJEUR2 and BAMBOO is presented in Figure 7.13. It can be there observed that both codes yield a similar pin displacement profile, and, in particular, that they are in good agreement concerning the position of the maximal deflection and its magnitude. We will see later in this section that the magnitude of the computed lateral displacement is very large compared to typical SFR values, and that it has consequences on the temperature distribution in the bundle.

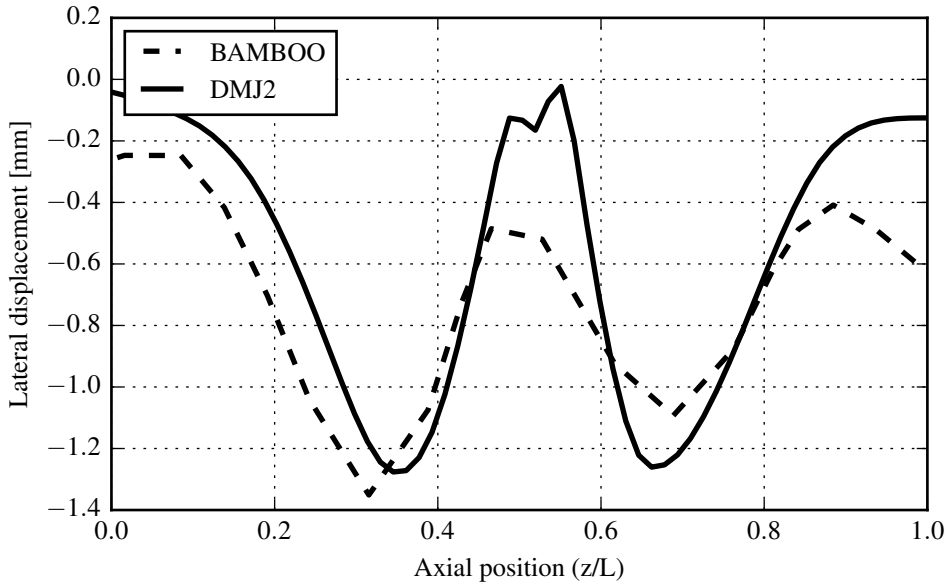

Figure 7.13.: Axial profile of lateral displacement of the left corner pin, computed by BAMBOO and by DOMAJEUR2 at EOL. The displacement is measured over the diagonal indicated in Figure 7.9, and it is negative towards the left, i.e. towards the hexcan corner in subchannel N°256.

Result III: EOL temperature distribution. Pin flexion not considered in STAR-CCM+

The computed sodium temperature distribution in the EOL deformed geometry is presented in Figure 7.14, where the reported temperature values are averaged in each subchannel within the sampling path indicated in Figure 7.9. The results obtained with STAR-CCM+ and with ASFRE are presented, and they are compared to the temperature distributions obtained at 0 FPD in the non-deformed geometry. It can be noted the two codes predict opposite effects of deformation on temperature. STAR-CCM+ predicts a slight temperature increase in the central region of the bundle, while ASFRE yields a marked temperature decrease in that region, which is accompanied by an increase of up to about 40°C in the corner subchannels. This effect, caused by the helical flexion of the pins, is not observed in the CFD simulation, which takes into account only the diametral deformation of the claddings.

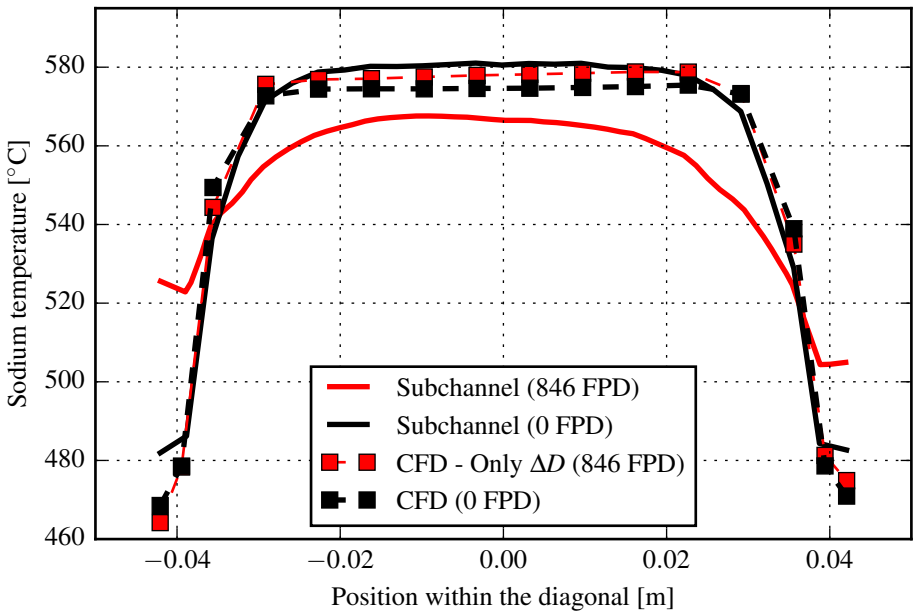

Figure 7.14.: Sodium temperature distribution at the outlet of the fuel bundle, computed with the subchannel and the CFD simulations in the nominal (0 FPD) and deformed (846 FPD) bundles. The reported temperature values are averaged in the subchannels following a diagonal of the hexagonal subassembly cross section. Only the diametral strain of the pins is considered in the CFD simulation in the deformed bundle.

Result IV: EOL temperature distribution. Pin flexion considered in STAR-CCM+ and in ASFRE

As shown in Figure 7.13, the maximal lateral displacement of the pin occupying the left corner subchannel, where ASFRE predicts the greatest temperature increase with respect to the non-deformed bundle (see Figure 7.14), is larger than 1.2 mm, both in the DOMAJEUR2 and the BAMBOO simulations. This maximal deflection is six times larger than the one obtained in a best estimate simulation of the irradiation of the advanced SFR designed at the CEA (Masoni 2016), and more than two times larger than the maximal displacement measured in the most irradiated Phenix subassembly, BOITIX9[5]. One of the reasons for the high lateral pin displacement is the geometry of the PFD512 fuel bundle. Indeed, as can be noted in Table 7.2, PFD512 has a large wire step, which increases the vertical distance between contacts and thus the length of the flexed cladding segment, reducing its bending stiffness. Additionally, it has small cladding external diameter

[5]The geometric characteristics of BOITIX9 are identical to the ones presented for MYOSOTIS in Table 7.2.

and thickness, which also reduces its resistance to bending, while its wire diameter, which determines the maximal available displacement before direct cladding-hexcan contact is reached, is not significantly smaller than the ones employed in other SFR.

Not only the geometry of PFD512 leads to a large pin helical flexion, but also the higher bulk sodium heating rate, with respect to MYOSOTIS and to the advanced SFR designed at the CEA (see Table 7.2), maximizes its impact on thermal-hydraulics. To evaluate this impact, a CFD simulation was conducted on the deformed bundle computed by DOMAJEUR2 in the coupled simulation, this time considering both the diametral strain and the helical flexion of the fuel pins, as described in Section 5.3.1.2.

The sweeping of the spacer wire, the helical flexion of the fuel pins, and their diametral strain, lead to a modulation of the cross section of the peripheral subchannels, as can be observed for the left and right corner subchannels in figures 7.15 and 7.16, respectively. In these figures, the cross sectional area of each subchannel is presented as a function of the axial position in the bundle, as computed from the deformation obtained with DOMAJEUR2 and with BAMBOO. A good general agreement between the two codes can be there observed, in particular concerning the magnitude and position of maximal subchannel cross section reduction.

The outlet sodium temperature computed with the CFD simulation in this new deformed geometry[6] is presented in Figure 7.17, together with the results obtained in the non-deformed geometry, where they are compared with the results obtained with ASFRE. It can be observed that, when the helical flexion is considered in the CFD simulations, the temperature distribution is in good general agreement with that obtained with the subchannel code ASFRE, although the temperature transition from the center towards the periphery of the bundle shows some differences. In this case, the deformation also leads to a decrease in the sodium temperature in the center of the bundle, and to a very large temperature increase of about 50°C in the left corner subchannel. On the right side of diagonal, the CFD simulation predicts a more abrupt transition from a high temperature central zone towards a low temperature peripheral zone than the subchannel simulation. Both simulations predict a marked asymmetry in the sodium temperature distribution in the deformed bundle, with the left corner being more than 20°C hotter than the right one. To understand this asymmetry, it is useful to evaluate the coolant velocity distribution.

As in the temperature distribution, a pronounced asymmetry is also observed

[6] In this geometry, a 0.4% uniform increase in the plate to plate distance of the hexcan was also considered. As discussed in Section 2.4, this avoids an unrealistic pin-hexcan interpenetration that, besides, lead to sodium stagnation areas that make the convergence of the simulations more difficult.

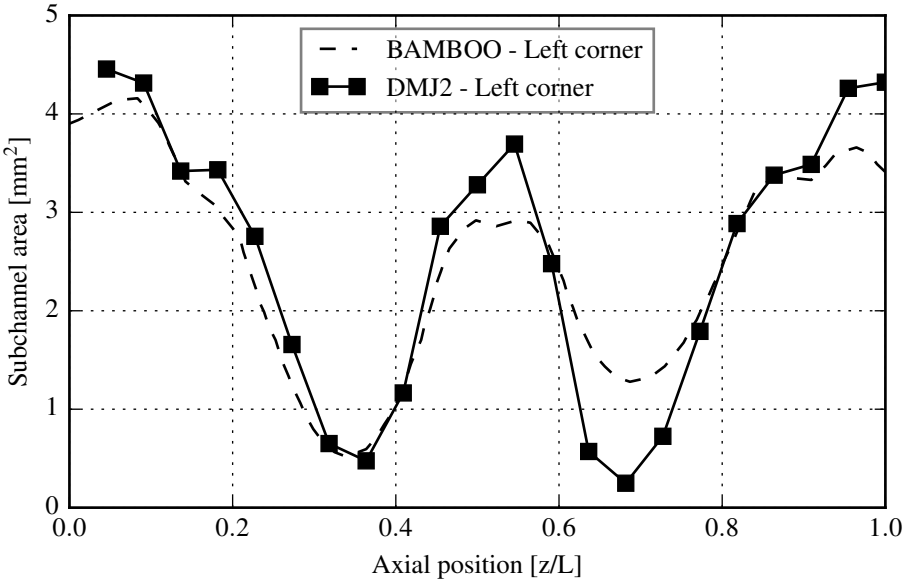

Figure 7.15.: Cross sectional area of the left corner subchannel, as computed by BAMBOO and DOMAJEUR2 as a function of the axial position within the bundle.

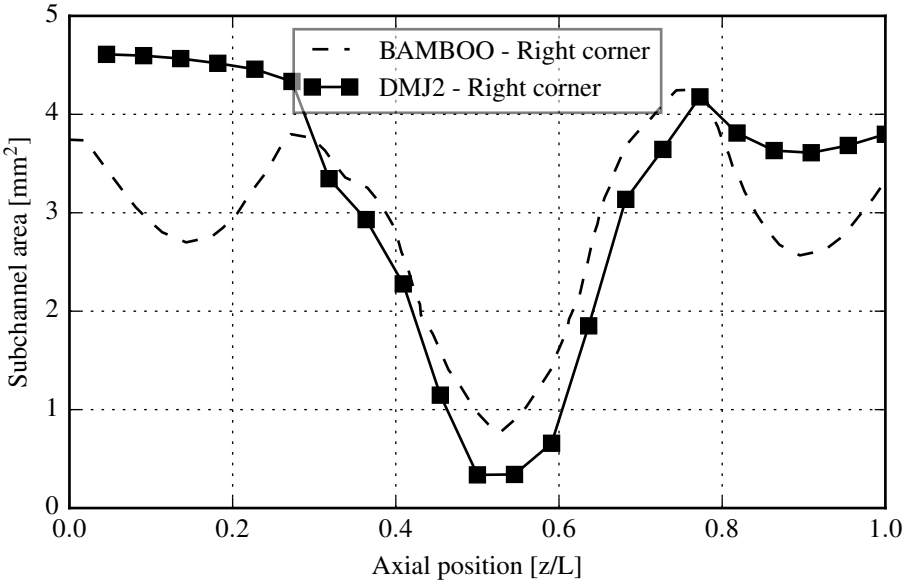

Figure 7.16.: Cross sectional area of the right corner subchannel, as computed by BAMBOO and DOMAJEUR2 as a function of the axial position within the bundle.

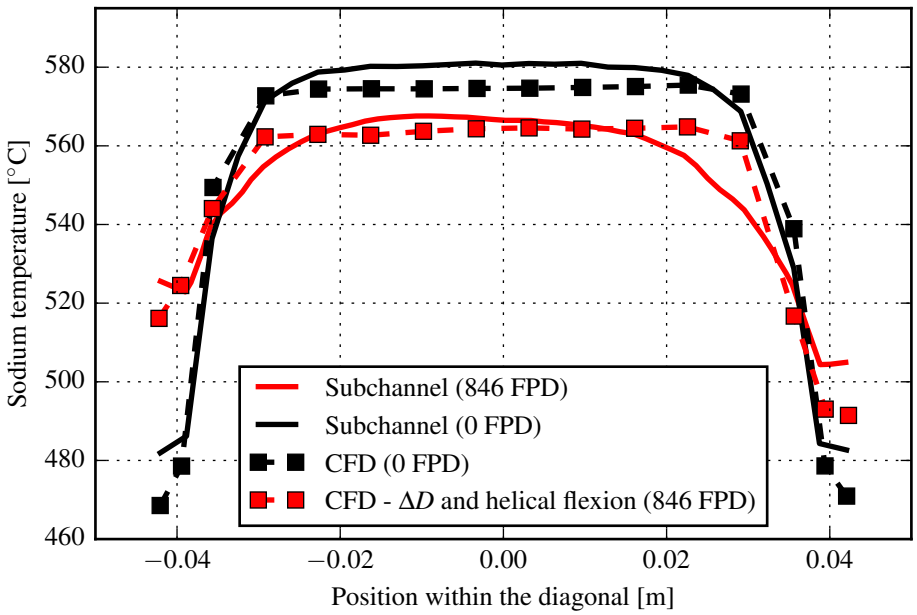

Figure 7.17.: Sodium temperature distribution at the outlet of the fuel bundle, computed with the subchannel and the CFD simulations in the nominal (0 FPD) and EOL (846 FPD) bundles. The reported temperature values are averaged in the subchannels following a diagonal of the hexagonal subassembly cross section.

in the distribution of the average axial velocity within the subchannels, presented in Figure 7.18a as computed by the CFD simulations[7]. The results obtained in the nominal geometry, in the deformed geometry considering only the cladding diametral strain, and in the deformed geometry considering both the diametral strain and the helical flexion of the pins are presented in this figure. In each case, the distribution was normalized using the average axial velocity amongst the considered subchannels. It can be noted that the diametral strain of the claddings leads only to a minor variation in the axial velocity distribution, while a steep reduction in the axial velocity in the left corner subchannel is caused by the helical flexion.

In Figure 7.18b, the axial velocity distribution in the non-deformed geometry is presented. The spacer wires of the corner pins are shown, since their orientation explains the asymmetry in the non-deformed velocity profile, as well as the larger velocity reduction induced by the flexion of the left corner pin. Indeed, the left corner subchannel is occupied by a spacer wire closer to the outlet than the right corner subchannel is. This leads to a higher tangential flow and lower

[7]No data concerning the coolant velocity distribution computed by the ASFRE/BAMBOO coupling was made available.

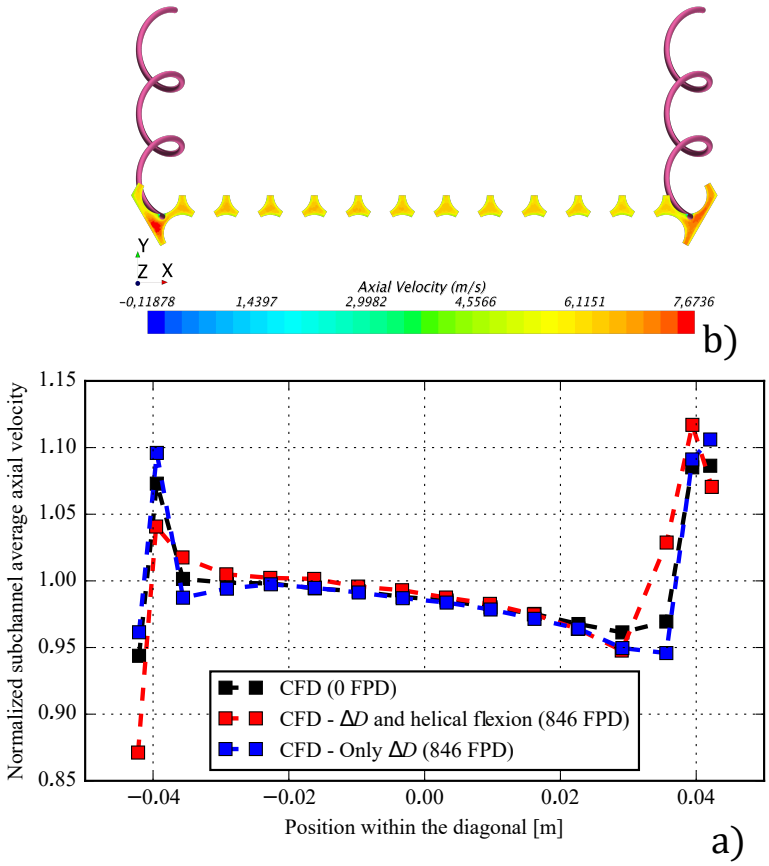

Figure 7.18.: **a)** Normalized sodium axial velocity distribution at the outlet of the fuel bundle, for the non-deformed geometry, the deformed geometry considering only the diametral strain of the pins, and the deformed geometry considering their diametral strain and helical flexion. For each geometry, each reported value corresponds to the average in a subchannel within a diagonal of the subassembly, normalized with the average axial velocity amongst the considered subchannels in that geometry. **b)** Distribution of the outlet sodium axial velocity in the subchannels considered in a), in the non-deformed geometry. The spacer wires of the corner pins are represented.

axial flow in the left corner at the outlet of the bundle. Additionally, the wire position also determines the points at which contact between the corner pins and the hexcan is established through the wires, thus changing the pin flexion profile. As a consequence, as can be noted by comparing figures 7.15 and 7.16, the left subchannel exhibits a larger average cross section reduction, and its cross section reaches its minimum closer to the outlet of the bundle than the right corner subchannel. This also contributes to the asymmetry in the axial velocity observed in Figure 7.18b, which explains the temperature asymmetry observed in Figure 7.17.

It should be noted that the temperature distribution obtained in the geometry which considered the helical flexion of the pins is not the result of a coupled simulation, but rather of a CFD simulation in the deformed geometry—which is in good agreement with the one computed by BAMBOO/ASFRE—obtained in a coupled simulation that considered the effects of the diametral strains of the claddings only. In other words, the coupled simulation conducted with DOMAJEUR2/STAR-CCM+ led to very similar EOL bundle deformation, but to a significantly different EOL temperature distribution than BAMBOO/ASFRE. One additional CFD simulation was therefore conducted taking into account the helical flexion of the pins, which had been neglected in the CFD calculations of the coupled simulation. Then, further iterations should be conducted to fully converge the temperature and deformation distributions, which was not done due to convergence issues caused by the generalized contact of the claddings and the hexcan.

However, even if further iterations should be conducted to achieve a fully converged solution, the results presented here are not expected to be greatly modified by doing so. Firstly, we have seen that the effects of the helical flexion of the pins dominates the impact of the deformation on thermal-hydraulics. Simulations we conducted in 7-pin and 19-pin bundles showed that the helical flexion is not greatly dependent on the cladding temperature distribution, since it is dominated by the contact forces between pins. Additionally, for most of the fuel bundle, the temperature difference between the CFD simulation with and without helical flexion is not high enough to induce a significant change in the diametral strain of the fuel pins[8].

[8]It should be noted that the temperature differences presented in Figure 7.17 correspond to the outlet of the bundle, where the diametral strain of the pins is very low. Unlike the case with an axial heterogeneous heated column, the maximal strain of the PFD512 fuel pins is located at the core mid-plane, where the temperature difference between the CFD simulations with and without considering the helical flexion is significantly lower.

Result V: Impact of the deformation-induced coolant mass flow reduction

Up to now, the simulations of PFD512 were conducted considering a constant subassembly mass flow rate, neglecting the effects that the deformation has on it. This was done to allow a direct comparison with the results presented in (Uwaba, Hiroyuki Ohshima, and M. Ito 2017), where this hypothesis is employed even though the authors acknowledge that the mass flow should be different in the deformed bundle. To evaluate these effects, a CFD simulation was conducted in the deformed bundle (considering the helical flexion and the diametral strain of the pins), using a lower mass flow rate. To do so, the model presented in Section 5.3.2 was employed, which implies that the same relative mass flow reduction than that estimated for the advanced SFR, for the same average diametral deformation, was considered. The outlet sodium distribution thus obtained is presented in Figure 7.19, where the distribution obtained in the same geometry without reducing the coolant mass flow rate is included for comparison.

It can be observed in Figure 7.19 that considering the mass flow rate reduction leads to a significant sodium temperature increase in the central region of the bundle, of about 20°C. It also induces a smaller temperature increase in the peripheral subchannels. Then, in this case, the helical flexion has a preponderant role in the periphery of the bundle, while the effect of the mass flow reduction in the central region of the bundle is greater than the effects, in this region, of the mass flow redistribution caused by the helical flexion of the pins.

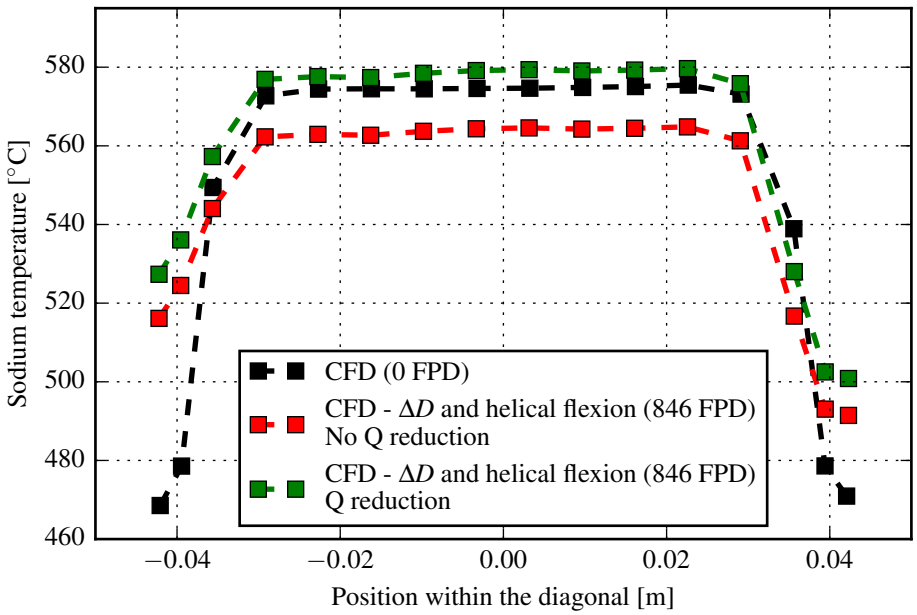

Figure 7.19.: Sodium temperature distribution at the outlet of the fuel bundle, computed with the CFD simulations in the nominal (0 FPD) and EOL (846 FPD) deformed bundles. The reported temperature values are averaged in the subchannels following a diagonal of the hexagonal subassembly cross section. The distribution computed with a CFD simulation with reduced sodium mass flow rate is also presented.

Results summary

The results presented in this section show that the diametral strain and the helical flexion of the fuel pins computed by the DOMAJEUR/STAR-CCM+ coupling are in good agreement with the results obtained with BAMBOO/ASFRE. Also, if the helical flexion of the pins is considered in the CFD simulations, the effects of the deformation on the temperature distribution within the deformed bundle are also in good agreement. The helical flexion was observed to lead to a coolant flow redistribution that flattens its temperature distribution (i.e. it increases temperature in the periphery and it lowers it in the central region of the bundle). However, local temperature differences were observed between the results of these two code systems, in particular in the peripheral subchannels, were the wires induce a larger cross flow, and in the transition from the periphery to the central region of the bundle. These differences could be explained by the lack of an explicit representation of the spacer wires in the subchannel code, which makes the prediction of their effect on the sodium flow very challenging, particularly for deformed bundles. In addition, considering the coolant mass flow rate reduction

caused by the deformation was found to lead, in the central region of the bundle, to a higher temperature perturbation than the one induced by the change in geometry alone, while the effects of the helical flexion were shown to dominate in the periphery.

7.3. Summary

In this chapter, we presented two application cases of the coupled simulation methodology developed in this work. The first case is based on the simulation of MYOSOTIS, a subassembly irradiated in Phenix reactor. This application case allowed to verify that the methodology can be successfully employed to simulate full scale (217 pins) fuel bundles, obtaining a prediction of the bundle deformation that is consistent with the available experimental data. However, limitations to the predictive capabilities of the developed simulation methodology were identified. These are mainly associated to the available swelling laws, which is why using this new coupled simulation methodology for the redefinition of the swelling laws is one of the main future outlooks of this work.

The second application case is a numerical benchmark based on the simulation of a Joyo subassembly, and on the comparison of the obtained results to results computed with a preexisting coupled approach. The results of this benchmark showed a very good agreement in the prediction of the EOL bundle deformation between the two coupled simulation approaches, and a good agreement in the prediction of the coolant temperature distribution. Local temperature differences were observed between the two approaches, which are likely explained by the simplified thermal-hydraulic code employed in the preexisting coupling. Consequence of the geometric and thermal-hydraulic characteristics of the Joyo subassembly, the helical flexion of the pins was shown to significantly affect its temperature distribution. Finally, the deformation-induced coolant mass flow rate reduction, neglected in the preexisting coupling, was also shown to lead to a significant coolant temperature increase.

8. Conclusions and outlooks

This PhD work has been conducted in the framework of the R&D activities of the CEA on an advanced SFR, with the main goal of developing a new simulation methodology for the prediction of the evolution of the thermomechanical and thermal-hydraulic characteristics of SFR subassemblies resulting from their irradiation under nominal operating conditions. A central aspect of this methodology is that it allows taking into account the coupling between the thermomechanical and thermal-hydraulic phenomena, which arises from the significant deformation that SFR fuel bundles undergo in the reactor as a result of the irradiation damage. The subassembly deformation affects the coolant flow and thus the temperature distribution, but it also depends on temperature, since two important irradiation damage mechanisms, the fuel cladding swelling and irradiation creep, are temperature dependent. Gaining insight on the impact of these coupling effects on the evolution of SFR subassemblies is also one of the purposes of this work.

Traditionally, the coupling effects have been neglected in the numerical simulations of SFR subassemblies, and a conservative approach, in which the bundle deformation is not considered in the thermal-hydraulic simulations, has been rather favored. In this work, we have developed a more accurate approach based on the operator split coupling between a detailed CFD-RANS model, implemented in STAR-CCM+, and DOMAJEUR2, a finite element based simulation tool developed at the CEA for the thermomechanical evolution of SFR subassemblies under irradiation. In this approach, DOMAJEUR2 computes the deformation of the fuel bundle resulting from the irradiation, while the cladding temperature distribution in the deformed geometry—one of the main inputs of DOMAJEUR2—is computed with STAR-CCM+. To the best of our knowledge, this is the first time a bundle thermomechanical code has been coupled with a CFD model that considers the irradiation-induced deformation. The use of a CFD model of the fuel bundle allows to provide a much higher detail on the temperature and flow distribution of the coolant than what would have been possible with other simpler methods such as the subchannel analysis. To represent the deformation of the fuel bundle in the CFD simulations, a novel CAD generation algorithm has been developed. This algorithm uses as input the cladding diametral strain distribution and the helical flexion of the fuel pins, both calculated by DOMAJEUR2. The cladding diametral strain is mainly caused by the cladding swelling and irradiation creep, while the helical flexion is primarily caused by the mechanical contacts between fuel pins and between the pins and the hexcan.

In the proposed approach, the evolution of the temperature distribution (or temperature history) of the fuel claddings, necessary for the thermomechanical calculations with DOMAJEUR2, is provided at the start of the simulation of the entire irradiation of the fuel bundle being evaluated, which constitutes a global iteration. At the end of this simulation, the cladding temperature history is updated, and the thermomechanical calculation is restarted. This process is iteratively repeated until convergence, modifying the temperature history, in each global iteration, by considering the effects of the last computed bundle deformation. Different methods were developed for computing the cladding temperature history. They are based on the interpolation of the results of CFD simulations in deformed bundle geometries predicted by DOMAJEUR2 at different instants during the irradiation, the choice of which renders the developed methodology very flexible. The retained method employs two CFD simulations in the non-deformed geometry (which allow to consider the evolution of the power distribution with the fuel utilization), and, in each global iteration, one CFD simulation in the deformed geometry obtained at End Of Life (EOL) in the previous iteration. This method also considers the last calculated time evolution of the deformation in order to perform a part-wise linear interpolation of the CFD-computed temperature distributions. Additionally, unlike in the preexisting coupled approaches, the coolant mass flow rate is calculated considering the effects of the deformation of the fuel bundle, for which a subassembly pressure drop model was developed.

Neutronic simulations, in which the diametral deformation of the fuel claddings was explicitly represented, allowed to confirm that the neutronic feedbacks caused by the subassembly deformation have a minor effect, and that it is therefore not necessary to take them into account in the numerical simulations. Additionally, a conjugate heat transfer simulation including the heat conduction in the cladding and the convection in the coolant showed that considering the first does not significantly affect the temperature distribution of the coolant, nor the heat flux distribution at the external surface of the cladding. Therefore, in order to reduce the computational burden and without introducing a significant error, a 1D radial heat conduction model applied as a post-treatment of the CFD simulations is employed, and it was found to be sufficient to determine the temperature distribution inside the cladding. The conjugate heat transfer simulation also showed that, for the purposes of this work, the spacer wires can be considered adiabatic.

To gain insight on the effects of the coupling, fuel bundles of 7 and 19 pins, with characteristics similar to those of advanced SFR designs, were studied using the proposed methodology. These numerical simulations showed that, for irradiation doses close to the maximal level reached in Phenix reactor (which are still below the objective dose levels for GEN IV SFR), the diametral deformation of the fuel claddings leads to a significant increase in the temperature distribution within the

fuel bundle, mainly due to a large reduction of the coolant mass flow rate, also caused by the deformation. The diametral strain of the claddings was also shown to increase the temperature gradients in their circumference, because it reduces the gaps between pins and between the pins and the hexcan. For high bundle deformation levels, the closing of these gaps was found to cause an important flow redistribution within the fuel bundle. Additionally, these contacts produce hot spots on the cladding. Their quantification requires a very fine spatial discretization in the CFD simulations and it was not amongst the goals of this work, which was focused on the development of the simulation methodology. *However, in the future, this methodology could be employed to contribute to the determination of the cladding hot spots caused by the contacts between pins.* Contrary to the results obtained for highly irradiated fuel bundles, for lower irradiation doses (close to the current design limit of GEN IV SFR), the bundle deformation was shown to induce only a small coolant bulk temperature increase.

The detailed coupled simulations of small fuel bundles also showed that, for high irradiation doses, the deformation-induced temperature increase leads to a significant reduction of the cladding diametral deformation, caused by the temperature dependence of swelling and of irradiation creep. In the axially heterogeneous fuel concepts envisaged for advanced SFR, which have a fuel column that includes a fertile blanket between two fissile ones, the deformation reduction is concentrated in the upper fissile blanket, where the deformation has a local maximum. This is explained by the temperature increase caused by the deformation, which is maximal at the upper part of the fuel column and, for the high operating temperature in this region, leads to a reduction of swelling and of irradiation creep. For axially homogeneous fuel bundles, which present a maximal deformation near the core mid-plane and a low deformation in the upper part of the fuel column, the deformation reduction due to the temperature increase is expected to be lower. In this case, the temperature increase induced by the deformation would also be maximal at the upper part of the fuel column, where the deformation is low. Consequently, the deformation reduction would be low in absolute terms.

The numerical simulations of the small fuel bundles were also used to study the convergence of the coupled temperature and the deformation fields in the subassembly. As mentioned above, the deformation leads to a significant temperature increase with respect to the temperature distribution in the non-deformed bundle. This temperature increase leads to a large reduction of the bundle deformation, which is concentrated in the upper part of the fuel column. This reduction, however, does not greatly affect the global temperature distribution, so the subsequent feedback on the bundle deformation is relatively low. For this reason, a prompt convergence between the thermal and deformation fields was observed.

Additionally, consequence of the reduction of the deformation associated to

the coupling, the contacts between pins and between the pins and the hexcan were shown to be delayed with respect to the non-coupled approach, and thus the predicted mechanical stresses at EOL are lower. This difference is explained by a delay in the initiation of the third phase of the bundle deformation. This third phase is characterized by a large cladding ovalisation that is associated with high cladding stresses. It is important to note that, for simplicity, the ovalisation of the claddings was not modeled in the CFD simulations performed in this work. To evaluate its effect on the thermal-hydraulics of the bundle, a model of the fuel pellet and its interaction with the cladding—not considered in DOMAJEUR2—would need to be incorporated to the coupling methodology. *Evaluating the impact of the fuel pellet and cladding ovalisation on the thermal-hydraulic characteristics of the fuel bundle is part of the future outlook of the present work, and it could be done without major modification to other aspects of the methodology here developed.*

The detail in the cladding temperature field computed by the CFD simulations allowed to quantify—to the best of our knowledge for the first time under conditions representative of SFR operation—the swelling gradients in the circumference of the cladding, induced by the high temperature gradients. Out of the two finite element models available in DOMAJEUR2 (a beam-based 1D model and one based on the use of 3D volumetric elements) only the 3D model can capture these swelling gradients, which cause secondary stresses in the cladding. *The quantification of these secondary stresses using the developed coupling methodology, which would require a very fine spatial discretization in the thermomechanical model, is another important outlook of this work.* The 3D and 1D models were nevertheless found to be in very good agreement in the computation of the diametral strain of the cladding, averaged in its circumference, in spite of the 1D model not being able to consider the circumferential cladding temperature gradients. This is explained by the minor impact of these temperature gradients on the cladding strain averaged in its circumference.

The developed simulation methodology was also applied to a 217-pin subassembly irradiated in Phenix SFR. The simulation of this experimental irradiation yielded a maximal cladding deformation and a deformation gradient that are in good agreement with the measured values. Some limitations related to the empirical laws employed in DOMAJEUR2 to compute the swelling were identified in the analysis. These empirical laws were originally determined based on experimental data obtained from fuel subassembly irradiations, including measurements of the diametral strain of the fuel claddings. The measured cladding deformation was then correlated to the estimated cladding irradiation dose and temperature, which was obtained with very simplified thermal-hydraulic models. *The reformulation of the empirical swelling laws using the developed coupled simulation methodology would allow profiting from the high temperature detail provided by the CFD simulations and from considering the coupling effects, and it is therefore an important future*

application of this work.

Finally, a numerical benchmark against a different coupled approach was conducted by simulating a subassembly of Joyo SFR (127-pin bundle). The EOL deformation computed by both numerical approaches was found to be in very good agreement. The computed temperature distribution also showed a good general agreement, although local temperature differences were observed. These differences are likely a consequence of the effect of the spacer wires, explicitly considered in the CFD model implemented in this work but represented by means of empirical correlations in the subchannel model used in the preexisting approach. In the conditions of this numerical benchmark, the helical flexion of the fuel pins was found to have a great impact on the temperature distribution of the coolant, caused by the reduction of the cross section of the peripheral subchannels. This led to a flow redistribution towards the center of the bundle, thus yielding a flatter temperature distribution at its outlet. Additionally, the coolant mass flow reduction caused by the deformation, not considered in the preexisting approach, was shown to lead to a very large increase of the outlet temperature of the coolant.

The results obtained in this work allowed to gain significant insight on the effects of the coupling on the thermomechanical and thermal-hydraulic evolution of SFR subassemblies. However, these results are very dependent of the characteristics of the design being studied, which include the properties of the materials used, its geometrical parameters, the operational temperature range, etc. The developed simulation methodology is easily adaptable to different SFR subassembly designs, and could be even employed to study subassemblies of different advanced reactors, such as the lead-cooled fast reactor. *In future work, this methodology could be employed to study and compare the behavior under irradiation of different subassembly designs, thus providing a best estimate approach that takes into account the coupling between the bundle deformation and its thermal-hydraulics.*

Bibliography

[Aco17] Francisco Acosta. *CEA internal document*. 2017 (cit. on p. 112).

[AGP17] Ronald Adamson, Malcolm Griffiths, and Charles Patterson. *Irradiation Growth of Zirconium Alloys A Review*. A.N.C International, 2017 (cit. on p. 43).

[And12] Bengt Andersson, ed. *Computational fluid dynamics for engineers*. OCLC: ocn751752493. Cambridge ; New York: Cambridge University Press, 2012. 189 pp. ISBN: 978-1-107-01895-2 (cit. on p. 77).

[BFS14] E. Baglietto, J.W. Fricano, and E. Sosnovsky. "CFD Activities in Support of Thermal-hydraulic Modeling of SFR Fuel Bundles". In: *Proceddings of the 10th International Topical Meeting on Nuclear Thermal-Hydraulics, Operation and Safety (NUTHOS-10)*. The 10th International Topical Meeting on Nuclear Thermal-Hydraulics, Operation and Safety (NUTHOS-10). Japan, Dec. 15, 2014 (cit. on pp. 14, 85, 108).

[BNM06] E. Baglietto, H. Ninokata, and Takeharu Misawa. "CFD and DNS methodologies development for fuel bundle simulations". In: *Nuclear Engineering and Design*. 13th International Conference on Nuclear Energy 236.14 (Aug. 1, 2006), pp. 1503–1510. ISSN: 0029-5493. DOI: 10.1016/j.nucengdes.2006.03.045. URL: http://www.sciencedirect.com/science/article/pii/S0029549306003359 (visited on 05/15/2019) (cit. on p. 77).

[Bai99] Henri Bailly. *The nuclear fuel of pressurized water reactors and fast neutron reactors design and behaviour*. Paris Seacaucus, N.J. Andover, Hampshire, U.K: Lavoisier Pub. Intercept, 1999. ISBN: 2-7272-0198-2 (cit. on pp. 33, 41–43, 48, 49).

[Bec+17] Thierry Beck, Victor Blanc, Jean-Michel Escleine, et al. "Conceptual design of ASTRID fuel sub-assemblies". In: *Nuclear Engineering and Design* 315 (Apr. 15, 2017), pp. 51–60. ISSN: 0029-5493. DOI: 10.1016/j.nucengdes.2017.02.027. URL: http://www.sciencedirect.com/science/article/pii/S0029549317300857 (cit. on pp. 7, 9, 57).

[Bej93] A. Bejan. *Heat transfer*. John Wiley & Sons, Inc., 1993. ISBN: 978-0-471-50290-6. URL: https://books.google.fr/books?id=TgtRAAAAMAAJ (cit. on p. 25).

[BL12] J. S. Bell and B. J. Lewis. “CANDU fuel bundle deformation modelling with COMSOL multiphysics”. In: *Nuclear Engineering and Design* 250 (Sept. 1, 2012), pp. 134–141. ISSN: 0029-5493. DOI: 10.1016/j.nucengdes.2012.05.015. URL: http://www.sciencedirect.com/science/article/pii/S0029549312002671 (visited on 09/24/2018) (cit. on p. 96).

[Bor+14] Vladimir Borodin, Jia-Chao Chen, Maxime Sauzay, et al. *Analysis and assessment of mechanisms of irradiation creep*. KIT, 2014. URL: http://www.fp7-matisse.eu/wp-content/uploads/2018/01/MatISSE-D2.41_Analysis-and-assessment-of-mechanisms-of-irradiation-creep_rev1.1.pdf (visited on 04/17/2019) (cit. on p. 49).

[Bro+17] Landon Brockmeyer, Lane B. Carasik, Elia Merzari, et al. “Numerical simulations for determination of minimum representative bundle size in wire wrapped tube bundles”. In: *Nuclear Engineering and Design* 322 (Oct. 2017), pp. 577–590. ISSN: 00295493. DOI: 10.1016/j.nucengdes.2017.06.038. URL: https://linkinghub.elsevier.com/retrieve/pii/S0029549317303084 (visited on 04/18/2019) (cit. on pp. 28, 85).

[Bro+14] Barry W. Brook, Agustin Alonso, Daniel A. Meneley, et al. “Why nuclear energy is sustainable and has to be part of the energy mix”. In: *Sustainable Materials and Technologies* 1-2 (2014), pp. 8–16. ISSN: 2214-9937. DOI: https://doi.org/10.1016/j.susmat.2014.11.001. URL: http://www.sciencedirect.com/science/article/pii/S2214993714000050 (cit. on p. 1).

[Bru+07] GB Bruna, F Fouquet, F Dubois, et al. “HEMERA: a 3D coupled core-plant system for accidental reactor transient simulation”. In: (2007), p. 10 (cit. on p. 12).

[Cac10] D.G. Cacuci. *Handbook of Nuclear Engineering: Vol. 1: Nuclear Engineering Fundamentals; Vol. 2: Reactor Design; Vol. 3: Reactor Analysis; Vol. 4: Reactors of Generations III and IV; Vol. 5: Fuel Cycles, Decommissioning, Waste Disposal and Safeguards*. Handbook of Nuclear Engineering vol. 1. Springer, 2010. ISBN: 978-0-387-98130-7. URL: https://books.google.de/books?id=pu9BWuf2gdkC (cit. on pp. 6, 37, 53).

[CA18] Thierry Cadiou and Francisco Acosta. “The impact of the fuel pin bundle deformation on the thermal-hydraulics of ASTRID sub-assembly”. In: 12th International Topical Meeting on Nuclear Reactor Thermal-Hydraulics, Operation and Safety (NUTHOS-12). Qingdao, China, 2018 (cit. on p. 58).

[CS15] Thierry Cadiou and Aakanksha Saxena. “Thermal–hydraulic numerical simulation of fuel sub-assembly using a dedicated meshing tool”. In: *Nuclear Engineering and Design* 295 (Dec. 15, 2015), pp. 162–172. ISSN: 0029-5493. DOI: 10.1016/j.nucengdes.2015.10.001. URL: http://www.sciencedirect.com/science/article/pii/S0029549315004434 (visited on 09/24/2018) (cit. on pp. 27, 35).

[CEA81] CEA. *CEA internal document*. 1981 (cit. on pp. 68, 136).

[CEA94] CEA. *CEA internal document*. 1994 (cit. on p. 7).

[Cha+09] Laltu Chandra, Ferry Roelofs, Michiel Houkema, et al. “A stepwise development and validation of a RANS based CFD modelling approach for the hydraulic and thermal-hydraulic analyses of liquid metal flow in a fuel assembly”. In: *Nuclear Engineering and Design* 239.10 (Oct. 1, 2009), pp. 1988–2003. ISSN: 0029-5493. DOI: 10.1016/j.nucengdes.2009.05.022. URL: http://www.sciencedirect.com/science/article/pii/S002954930900260X (visited on 09/24/2018) (cit. on p. 86).

[CD11] T. Charras and F. Di Paola. *La procedure PASAPAS, Documentation Cast3M*. 2011. URL: www-cast3m.cea.fr/html/Documentation_Cast3M/Pasapas.pdf (cit. on p. 96).

[Cha+11] Christian Chauliac, José-Maria Aragonés, Dominique Bestion, et al. “NURESIM – A European simulation platform for nuclear reactor safety: Multi-scale and multi-physics calculations, sensitivity and uncertainty analysis”. In: *Nuclear Engineering and Design* 241.9 (2011), pp. 3416–3426. ISSN: 0029-5493. DOI: https://doi.org/10.1016/j.nucengdes.2010.09.040. URL: http://www.sciencedirect.com/science/article/pii/S0029549311001713 (cit. on p. 12).

[CCT18] S. K. Chen, Y. M. Chen, and N. E. Todreas. “The upgraded Cheng and Todreas correlation for pressure drop in hexagonal wire-wrapped rod bundles”. In: *Nuclear Engineering and Design* 335 (Aug. 15, 2018), pp. 356–373. ISSN: 0029-5493. DOI: 10.1016/j.nucengdes.2018.05.010. URL: http://www.sciencedirect.com/science/article/pii/S0029549318301389 (visited on 01/11/2020) (cit. on pp. 29, 137).

[CTN14] S.K. Chen, N.E. Todreas, and N.T. Nguyen. “Evaluation of existing correlations for the prediction of pressure drop in wire-wrapped hexagonal array pin bundles”. In: *Nuclear Engineering and Design* 267 (Feb. 2014), pp. 109–131. ISSN: 0029-5493. DOI: 10.1016/j.nucengdes.2013.12.003. URL: http://www.sciencedirect.com/science/article/pii/S002954931300678X (cit. on pp. 29, 137).

[CT86] Shih-Kuei Cheng and Neil E. Todreas. "Hydrodynamic models and correlations for bare and wire-wrapped hexagonal rod bundles — Bundle friction factors, subchannel friction factors and mixing parameters". In: *Nuclear Engineering and Design* 92.2 (Apr. 1, 1986), pp. 227–251. ISSN: 0029-5493. DOI: 10.1016/0029-5493(86)90249-9. URL: http://www.sciencedirect.com/science/article/pii/0029549386902499 (visited on 04/15/2019) (cit. on p. 21).

[CM12] Haecheon Choi and Parviz Moin. "Grid-point requirements for large eddy simulation: Chapman's estimates revisited". In: *Physics of Fluids* 24.1 (Jan. 1, 2012), p. 011702. ISSN: 1070-6631. DOI: 10.1063/1.3676783. URL: https://aip.scitation.org/doi/10.1063/1.3676783 (visited on 05/10/2019) (cit. on p. 78).

[CB17] Simon A. Clément and Philippe M. Bardet. "Surrogates for Single-Phase Conjugate Heat Transfer Validation Experiments at Light Water Reactor Prototypical Conditions". In: *Nuclear Technology* 199.2 (Aug. 3, 2017), pp. 151–173. ISSN: 0029-5450. DOI: 10.1080/00295450.2017.1327254. URL: https://doi.org/10.1080/00295450.2017.1327254 (visited on 04/30/2019) (cit. on p. 22).

[CHP82] A. Combescure, A. Hoffman, and P. Pasquet. "The CASTEM Finite Element System". In: *Finite Element Systems*. Berlin: Springer, 1982 (cit. on p. 95).

[Coq+17] C Coquelet-Pascal, C Venard, P Sciora, et al. *CEA internal document*. 2017 (cit. on p. 65).

[DB85] F. W. Dittus and L. M. K. Boelter. "Heat transfer in automobile radiators of the tubular type". In: *International Communications in Heat and Mass Transfer* 12.1 (Jan. 1, 1985), pp. 3–22. ISSN: 0735-1933. DOI: 10.1016/0735-1933(85)90003-X. URL: http://www.sciencedirect.com/science/article/pii/073519338590003X (visited on 04/15/2019) (cit. on p. 25).

[Dol+17] Xavier Doligez, Sandra Bouneau, Sylvain David, et al. "Fundamentals of reactor physics with a view to the (possible) futures of nuclear energy". In: *Comptes Rendus Physique*. Demain l'énergie 18.7 (Sept. 1, 2017), pp. 372–380. ISSN: 1631-0705. DOI: 10.1016/j.crhy.2017.10.004. URL: http://www.sciencedirect.com/science/article/pii/S1631070517300725 (visited on 04/21/2019) (cit. on p. 66).

[EJE14] Emilio Baglietto, Joseph William Fricano, and Eugeny Sosnovsky. "CFD Activities in Support of Thermal-hydraulic Modeling of SFR Fuel Bundles". In: *Proceddings of the 10th International Topical Meeting on Nuclear Thermal-Hydraulics, Operation and Safety (NUTHOS-10)*. The 10th International Topical Meeting on Nuclear Thermal-Hydraulics,

Operation and Safety (NUTHOS-10). Japan, Dec. 15, 2014 (cit. on p. 74).

[FPT09] T. H. Fanning, W. D. Pointer, and J. W. Thomas. "Multi-resolution modeling of subassembly pin bundles for advanced fast reactor safety simulations". In: International Conference on Mathematics, Computational Methods & Reactor Physics. United States: American Nuclear Society - ANS, 2009. ISBN: 978-0-89448-069-0. URL: http://inis.iaea.org/search/search.aspx?orig_q=RN:42064753 (cit. on pp. 14, 73, 108).

[Fio+15] Carlo Fiorina, Ivor Clifford, Manuele Aufiero, et al. "GeN-Foam: a novel OpenFOAM® based multi-physics solver for 2D/3D transient analysis of nuclear reactors". In: *Nuclear Engineering and Design* 294 (2015), pp. 24–37. ISSN: 0029-5493. DOI: https://doi.org/10.1016/j.nucengdes.2015.05.035. URL: http://www.sciencedirect.com/science/article/pii/S0029549315003829 (cit. on p. 12).

[Fis+90] Antoine Fissolo, Richard Cauvin, Jean-Pierre Hugot, et al. *Influence of Swelling on Irradiated CW Titanium Modified 316 Embrittlement*. Ed. by N. Packan, R. Stoller, and A. Kumar. West Conshohocken, PA: ASTM International, Jan. 1, 1990. 700 pp. ISBN: 978-0-8031-8887-7. DOI: 10.1520/STP49485S. URL: https://www.astm.org/DIGITAL_LIBRARY/STP/PAGES/STP49485S.htm (cit. on p. 45).

[Fra57] F. C. Frank. "Dislocations and point defects". In: *Discussions of the Faraday Society* 23.0 (Jan. 1, 1957), pp. 122–127. ISSN: 0366-9033. DOI: 10.1039/DF9572300122. URL: https://pubs.rsc.org/en/content/articlelanding/1957/df/df9572300122 (visited on 05/02/2019) (cit. on p. 41).

[FB14] J.W. Fricano and E. Baglietto. "A quantitative CFD benchmark for Sodium Fast Reactor fuel assembly modeling". In: *Annals of Nuclear Energy* 64 (Feb. 2014), pp. 32–42. ISSN: 0306-4549. DOI: 10.1016/j.anucene.2013.09.019. URL: http://www.sciencedirect.com/science/article/pii/S0306454913004891 (cit. on p. 86).

[GV16] R. Gajapathy and K. Velusamy. "CFD investigations of helical wire-wrap fuel pin bundle and its comparison with straight wire bundle". In: *Progress in Nuclear Energy* 89 (May 2016), pp. 57–68. ISSN: 0149-1970. DOI: 10.1016/j.pnucene.2016.01.014. URL: http://www.sciencedirect.com/science/article/pii/S0149197016300142 (cit. on p. 28).

[Gaj+15] R. Gajapathy, K. Velusamy, P. Selvaraj, et al. "CFD investigation of effect of helical wire-wrap parameters on the thermal hydraulic performance of 217 fuel pin bundle". In: *Annals of Nuclear Energy* 77 (Mar. 2015), pp. 498–513. ISSN: 0306-4549. DOI: 10.1016/j.anucene.

2014.10.038. URL: http://www.sciencedirect.com/science/article/pii/S0306454914005775 (cit. on p. 28).

[Gar04] Francis A. Garner. *Survey of Recent Developments Concerning the Understanding of Radiation Effects on Stainless Steels Used in the LWR Power Industry*. PNWD-SA–6274. United States, Aug. 2004, p. v. URL: http://inis.iaea.org/search/search.aspx?orig_q=RN:37004563;%20American%20Nuclear%20Society,%20La%20Grange%20Park,%20IL%20(US) (cit. on p. 42).

[Gar06] Frank Garner. "Irradiation Performance of Cladding and Structural Steels in Liquid Metal Reactors". In: *Materials Science and Technology*. American Cancer Society, 2006. ISBN: 978-3-527-60397-8. DOI: 10.1002/9783527603978.mst0110. URL: https://onlinelibrary.wiley.com/doi/abs/10.1002/9783527603978.mst0110 (cit. on pp. 8, 44, 49, 52).

[Gar12] Frank Garner. "Radiation Damage in Austenitic Steels". In: *Comprehensive Nuclear Materials*. Vol. 4. Konings R.J.M, Jan. 1, 2012, pp. 33–95 (cit. on pp. 42, 44, 49, 50).

[Gar07] Gary S. Was. *Fundamentals of Radiation Materials Science. Metals and Alloys*. Berlin: Springer, 2007. ISBN: 978-3-540-49471-3 (cit. on pp. 40, 41, 48, 49).

[GR11] F. Gauche and J. Rouault. "French SFR R&D Program and Design Activities for SFR Prototype ASTRID". In: *Energy Procedia*. Asian Nuclear Prospects 2010 7 (Jan. 1, 2011), pp. 314–316. ISSN: 1876-6102. DOI: 10.1016/j.egypro.2011.06.040. URL: http://www.sciencedirect.com/science/article/pii/S1876610211015499 (visited on 04/06/2019) (cit. on p. 2).

[Gou+15] H D Gougar, R A Bari, T K Kim, et al. "Assessment of the Technical Maturity of Generation IV Concepts for Test or Demonstration Reactor Applications". In: (2015), p. 33 (cit. on p. 2).

[Grö13] G. Grötzbach. "Challenges in low-Prandtl number heat transfer simulation and modelling". In: *Nuclear Engineering and Design*. SI:NURETH-14 264 (Nov. 1, 2013), pp. 41–55. ISSN: 0029-5493. DOI: 10.1016/j.nucengdes.2012.09.039. URL: http://www.sciencedirect.com/science/article/pii/S0029549313000952 (visited on 04/14/2019) (cit. on pp. 25, 87).

[Grö81] Günther Grötzbach. "Numerical simulation of turbulent temperature fluctuations in liquid metals". In: *International Journal of Heat and Mass Transfer* 24.3 (Mar. 1, 1981), pp. 475–490. ISSN: 0017-9310. DOI: 10.1016/0017-9310(81)90055-7. URL: http://www.sciencedirect.com/science/article/pii/0017931081900557 (visited on 05/18/2019) (cit. on p. 87).

[GM87] J Guidez and L Martin. *CEA internal document*. 1987 (cit. on p. 214).

[GB14] Joël Guidez and Bernard Bonin. *Réacteurs nucléaires à caloporteur sodium*. E-den, Une monographie de la Direction de l'énergie nucléaire. CEA Saclay; Groupe Moniteur, June 2014. URL: https://hal-cea.archives-ouvertes.fr/cea-01152795 (cit. on pp. 4, 5).

[HB10] Kurt D. Hamman and Ray A. Berry. "A CFD simulation process for fast reactor fuel assemblies". In: *Nuclear Engineering and Design* 240.9 (Sept. 2010), pp. 2304–2312. ISSN: 00295493. DOI: 10.1016/j.nucengdes.2009.11.007. URL: https://linkinghub.elsevier.com/retrieve/pii/S0029549309005664 (visited on 05/15/2019) (cit. on p. 85).

[Hil98] R. Hill. *The Mathematical Theory of Plasticity*. Oxford classic texts in the physical sciences. Clarendon Press, 1998. ISBN: 978-0-19-850367-5. URL: https://books.google.fr/books?id=Wy_kuQZzfdIC (cit. on p. 38).

[IAE12] IAEA. *Structural Materials for Liquid Metal Cooled Fast Reactor Fuel Assemblies — Operational Behaviour*. 2012 (cit. on pp. 9, 66).

[Inc07] F.P. Incropera. *Fundamentals of heat and mass transfer*. Fundamentals of Heat and Mass Transfer v. 1. John Wiley, 2007. ISBN: 978-0-471-45728-2. URL: https://books.google.fr/books?id=_P9QAAAAMAAJ (cit. on p. 33).

[IKM94] K. Itoh, H. Kinjo, and Y. Mimura. "Development of a 3-D FBR fuel bundle-to-duct interaction analysis code marse". In: *Nuclear Engineering and Design* 148.1 (June 1, 1994), pp. 53–69. ISSN: 0029-5493. DOI: 10.1016/0029-5493(94)90241-0. URL: http://www.sciencedirect.com/science/article/pii/0029549394902410 (visited on 07/01/2019) (cit. on p. 96).

[Jeo+07] Hae-Yong Jeong, Kwi-Seok Ha, Young-Min Kwon, et al. "A dominant geometrical parameter affecting the turbulent mixing rate in rod bundles". In: *International Journal of Heat and Mass Transfer* 50.5 (Mar. 1, 2007), pp. 908–918. ISSN: 0017-9310. DOI: 10.1016/j.ijheatmasstransfer.2006.08.023. URL: http://www.sciencedirect.com/science/article/pii/S0017931006004984 (visited on 05/17/2019) (cit. on p. 73).

[JSL17a] Jae-Ho Jeong, Min-Seop Song, and Kwi-Lim Lee. "CFD investigation of three-dimensional flow phenomena in a JAEA 127-pin wire-wrapped fuel assembly". In: *Nuclear Engineering and Design* 323 (Nov. 2017), pp. 166–184. ISSN: 0029-5493. DOI: 10.1016/j.nucengdes.2017.08.008. URL: http://www.sciencedirect.com/science/article/pii/S0029549317303825 (cit. on pp. 28, 91).

[JSL17b] Jae-Ho Jeong, Min-Seop Song, and Kwi-Lim Lee. "Thermal-hydraulic effect of wire spacer in a wire-wrapped fuel bundles for SFR". In: *Nuclear Engineering and Design* 320 (Aug. 15, 2017), pp. 28–43. ISSN: 0029-5493. DOI: 10.1016/j.nucengdes.2017.05.019. URL: http://www.sciencedirect.com/science/article/pii/S0029549317302480 (cit. on p. 27).

[Jia11] Ziying Jiang. "Nuclear Power Development for Greenhouse Gas Emission Reduction in China". In: *Advances in Climate Change Research* 2.2 (2011), pp. 75–78. ISSN: 1674-9278. DOI: https://doi.org/10.3724/SP.J.1248.2011.00075. URL: http://www.sciencedirect.com/science/article/pii/S1674927811500188 (cit. on p. 1).

[Kad81] B. A. Kader. "Temperature and concentration profiles in fully turbulent boundary layers". In: *International Journal of Heat and Mass Transfer* 24.9 (Sept. 1, 1981), pp. 1541–1544. ISSN: 0017-9310. DOI: 10.1016/0017-9310(81)90220-9. URL: http://www.sciencedirect.com/science/article/pii/0017931081902209 (visited on 05/15/2019) (cit. on p. 87).

[Kal+05] Georgi Kalitzin, Gorazd Medic, Gianluca Iaccarino, et al. "Near-wall Behavior of RANS Turbulence Models and Implications for Wall Functions". In: *J. Comput. Phys.* 204.1 (Mar. 2005), pp. 265–291. ISSN: 0021-9991. DOI: 10.1016/j.jcp.2004.10.018. URL: http://dx.doi.org/10.1016/j.jcp.2004.10.018 (visited on 02/22/2019) (cit. on p. 84).

[Kár31] Th von Kármán. *Mechanical similitude and turbulence*. 1931. URL: http://resolver.caltech.edu/CaltechAUTHORS:20140804-121813080 (visited on 05/12/2019) (cit. on p. 83).

[Kel95] C. Kelley. *Iterative Methods for Linear and Nonlinear Equations*. Frontiers in Applied Mathematics. Society for Industrial and Applied Mathematics, Jan. 1, 1995. 169 pp. ISBN: 978-0-89871-352-7. DOI: 10.1137/1.9781611970944. URL: https://epubs.siam.org/doi/book/10.1137/1.9781611970944 (visited on 05/26/2019) (cit. on p. 112).

[Key+13] David E Keyes, Lois C McInnes, Carol Woodward, et al. "Multiphysics simulations: Challenges and opportunities". In: *The International Journal of High Performance Computing Applications* 27.1 (Feb. 1, 2013), pp. 4–83. ISSN: 1094-3420. DOI: 10.1177/1094342012468181. URL: https://doi.org/10.1177/1094342012468181 (visited on 05/24/2019) (cit. on p. 110).

[Kik+16] Norihiro Kikuchi, Hiroyuki Ohshima, Masaaki Tanaka, et al. "Development of thermal hydraulics analysis code ASFRE for fuel assembly of sodium-cooled fast reactor Modification of distributed resistance model and validation analysis". In: The 21st national symposium on power and energy systems (SPES 2016). 2016, p. 506. URL: http://inis.iaea.org/search/search.aspx?orig_q=RN:48057379;%20Power%20and%20Energy%20System%20Division,%20Japan%20Society%20of%20Mechanical%20Engineers,%2035%20Shinanomachi,%20Shinjuku-ku,%20Tokyo%20160-0016%20Japan (cit. on p. 108).

[Kol41] A. Kolmogorov. "The Local Structure of Turbulence in Incompressible Viscous Fluid for Very Large Reynolds' Numbers". In: *Akademiia Nauk SSSR Doklady* 30 (1941), pp. 301–305. ISSN: 0002-3264. URL: http://adsabs.harvard.edu/abs/1941DoSSR..30..301K (visited on 05/10/2019) (cit. on p. 76).

[KCH01] P.K. Kundu, I.M. Cohen, and H. Hu. *Fluid Mechanics*. Elsevier Science, 2001. ISBN: 978-0-08-054558-5. URL: https://books.google.fr/books?id=AFVnbQqCJSQC (cit. on p. 29).

[Lah+88] J.P. Lahaye, G. Cognet, L. Mertens, et al. *Etude l'écoulement dans des faisceaux d'assemblages RNR à 7 aiguilles déformées*. 1988 (cit. on p. 69).

[Lai+19] Marc Lainet, Bruno Michel, Jean-Christophe Dumas, et al. "GERMINAL, a fuel performance code of the PLEIADES platform to simulate the in-pile behaviour of mixed oxide fuel pins for sodium-cooled fast reactors". In: *Journal of Nuclear Materials* 516 (Apr. 1, 2019), pp. 30–53. ISSN: 0022-3115. DOI: 10.1016/j.jnucmat.2018.12.030. URL: http://www.sciencedirect.com/science/article/pii/S0022311518312601 (visited on 04/21/2019) (cit. on pp. 70, 95).

[Lau82] L Laubin. *CEA internal document*. 1982 (cit. on p. 14).

[LWW69] T. Lauritzen, A. Withop, and U. E. Wolff. "Swelling of austenitic stainless steels under fast neutron irradiation at elevated temperatures". In: *Nuclear Engineering and Design* 9.2 (Feb. 1, 1969), pp. 265–268. ISSN: 0029-5493. DOI: 10.1016/0029-5493(69)90063-6. URL: http://www.sciencedirect.com/science/article/pii/0029549369900636 (visited on 05/02/2019) (cit. on p. 43).

[Le 11] E. Le Fichoux. *Presentation et utilisation de Cast3M*. 2011. URL: www-cast3m.cea.fr (cit. on p. 95).

[Lec83] J Leclere. *CEA internal document*. 1983 (cit. on p. 8).

[LMD16] B Leturcq, J. B. Minne, and F. Di Paola. "A new structural behavior to perform efficient nonlinear SFR fuel bundle thermomechanical analysis". Club Cast3M 2016. 2016. URL: http://www-cast3m.cea.fr/index.php?xml=clubcast3m2016 (cit. on p. 104).

[LMD17] B Leturcq, J. B. Minne, and F. Di Paola. "Nouvel élément de structure pour les calculs d'interaction dans les faisceaux d'aiguilles combustibles des RNR". In: 13ème Colloque National en Calcul des Structures. Var, France, 2017 (cit. on pp. 103, 104).

[LS15] X.J. Liu and N. Scarpelli. "Development of a sub-channel code for liquid metal cooled fuel assembly". In: *Annals of Nuclear Energy* 77 (Mar. 2015), pp. 425–435. ISSN: 0306-4549. DOI: 10.1016/j.anucene.2014.10.030. URL: http://www.sciencedirect.com/science/article/pii/S0306454914005696 (cit. on p. 73).

[Loc+16] T. Locatelli, F. Di Paola, B Leturcq, et al. *CEA internal document*. 2016 (cit. on p. 99).

[Mah+14] Vijay S. Mahadevan, Elia Merzari, Timothy Tautges, et al. "High-resolution coupled physics solvers for analysing fine-scale nuclear reactor design problems". In: *Philosophical Transactions. Series A, Mathematical, Physical, and Engineering Sciences* 372.2021 (Aug. 6, 2014). ISSN: 1364-503X. DOI: 10.1098/rsta.2013.0381 (cit. on pp. 12, 110, 112).

[Mai+92] A Maillard, R Touron, J L Séran, et al. "Swelling and irradiation creep of neutron irradiated 316Ti and 15-15Ti steels". In: 16th Symposium on Effects of Radiation on Materials. Denver, 1992, p. 17 (cit. on p. 50).

[Mas16] P Masoni. *CEA internal document*. 2016 (cit. on pp. 13, 69, 101, 230).

[McC10] Ryan G. McClarren. "Theoretical Aspects of the Simplified P_n Equations". In: *Transport Theory and Statistical Physics* 39.2 (Mar. 2010), pp. 73–109. ISSN: 0041-1450, 1532-2424. DOI: 10.1080/00411450.2010.535088. URL: http://www.tandfonline.com/doi/abs/10.1080/00411450.2010.535088 (visited on 06/27/2019) (cit. on p. 165).

[Mer+16] E. Merzari, P. Fischer, H. Yuan, et al. "Benchmark exercise for fluid flow simulations in a liquid metal fast reactor fuel assembly". In: *Nuclear Engineering and Design* 298 (2016), pp. 218–228. ISSN: 00295493 (ISSN). DOI: 10.1016/j.nucengdes.2015.11.002. URL: https://www.scopus.com/inward/record.uri?eid=2-s2.0-84954219621&doi=10.1016%2fj.nucengdes.2015.11.002&partnerID=40&md5=73fbd57db8dcf061444c57b035a5cbb0 (cit. on pp. 85, 86, 92).

[Mer+15] E. Merzari, E. R. Shemon, Y. Yu, et al. *Full Core Multiphysics Simulation with Offline Mesh Deformation*. 2015. URL: https://publications.anl.gov/anlpubs/2016/01/124532.pdf (cit. on p. 12).

[Mik79] Kazuyoshi Miki. "Deformation analysis of fuel pins within the wire-wrap assembly of an LMFBR". In: *Nuclear Engineering and Design* 52.3 (May 1, 1979), pp. 371–384. ISSN: 0029-5493. DOI: 10.1016/0029-5493(79)90028-1. URL: http://www.sciencedirect.com/science/article/pii/0029549379900281 (visited on 04/10/2019) (cit. on pp. 14, 108, 109).

[MIT18] MIT. "The Future of Nuclear Energy in a Carbon-Constrained World". In: (2018), p. 275 (cit. on pp. 1, 15).

[MMD16] F. Moukalled, L. Mangani, and M. Darwish. *The Finite Volume Method in Computational Fluid Dynamics*. Vol. 113. Fluid Mechanics and Its Applications. Cham: Springer International Publishing, 2016. ISBN: 978-3-319-16873-9 978-3-319-16874-6. DOI: 10.1007/978-3-319-16874-6. URL: http://link.springer.com/10.1007/978-3-319-16874-6 (visited on 05/11/2019) (cit. on p. 74).

[Mou12] "4 - Strengthening of metal alloys". In: *Introduction to Aerospace Materials*. Ed. by Adrian P. Mouritz. Woodhead Publishing, Jan. 1, 2012, pp. 57–90. ISBN: 978-1-85573-946-8. DOI: 10.1533/9780857095152.57. URL: http://www.sciencedirect.com/science/article/pii/B9781855739468500042 (visited on 04/22/2019) (cit. on p. 41).

[NT90] Masatoshi Nakagawa and Yasusi Tsuboi. "Étoile: A Three-Dimensional Finite Element Code for LMFBR Fuel Bundle Analysis". In: *Nuclear Technology* 91.3 (Sept. 1, 1990), pp. 345–360. ISSN: 0029-5450. DOI: 10.13182/NT90-A34456. URL: https://doi.org/10.13182/NT90-A34456 (visited on 07/01/2019) (cit. on p. 95).

[Nat+10] K. Natesan, T. Sundararajan, Arunn Narasimhan, et al. "Turbulent flow simulation in a wire-wrap rod bundle of an LMFBR". In: *Nuclear Engineering and Design* 240.5 (May 2010), pp. 1063–1072. ISSN: 0029-5493. DOI: 10.1016/j.nucengdes.2009.12.025. URL: http://www.sciencedirect.com/science/article/pii/S0029549310000117 (cit. on pp. 28, 86, 91).

[NM90] Neil E. Todreas and Mujid S. Kazimi. *Nuclear Systems II: Elements of Thermal Hydraulic design*. 1990. ISBN: 1-56032-079-6 (cit. on pp. 25, 28).

[NS72] R. H. Notter and C. A. Sleicher. “A solution to the turbulent Graetz problem—III Fully developed and entry region heat transfer rates”. In: *Chemical Engineering Science* 27.11 (Jan. 1, 1972), pp. 2073–2093. ISSN: 0009-2509. DOI: 10.1016/0009-2509(72)87065-9. URL: http://www.sciencedirect.com/science/article/pii/0009250972870659 (visited on 04/15/2019) (cit. on p. 25).

[OEC14] OECD/NEA. “Technology Roadmap Update for Generation IV Nuclear Energy Systems”. In: (2014), p. 66 (cit. on pp. 2, 6).

[OEC15] OECD/NEA. “Handbook on Lead-bismuth Eutectic Alloy and Lead Properties, Materials Compatibility, Thermal-hydraulics and Technologies”. In: (2015), p. 950 (cit. on p. 24).

[OEC18] OECD/NEA. “Preparing the Future through Innovative Nuclear Technology: Outlook for Generation IV Technologies”. In: (2018), p. 18 (cit. on pp. 2, 3, 15, 41).

[Ohm+72] Kenichi Ohmae, Akikazu Morino, Noboru Nakao, et al. “Channel deformation analysis for fast reactor fuel assemblies undergoing swelling and thermal bowing”. In: *Nuclear Engineering and Design* 23.3 (Dec. 1, 1972), pp. 309–320. ISSN: 0029-5493. DOI: 10.1016/0029-5493(72)90152-5. URL: http://www.sciencedirect.com/science/article/pii/0029549372901525 (visited on 10/02/2018) (cit. on pp. 14, 108, 109).

[OK16] H. Ohshima and S. Kubo. “5 - Sodium-cooled fast reactor”. In: *Handbook of Generation IV Nuclear Reactors*. Ed. by Igor L. Pioro. Woodhead Publishing Series in Energy. Woodhead Publishing, Jan. 1, 2016, pp. 97–118. ISBN: 978-0-08-100149-3. DOI: 10.1016/B978-0-08-100149-3.00005-7. URL: http://www.sciencedirect.com/science/article/pii/B9780081001493000057 (visited on 04/07/2019) (cit. on pp. 3, 5).

[Pac+17] J. Pacio, T. Wetzel, H. Doolaard, et al. “Thermal-hydraulic study of the LBE-cooled fuel assembly in the MYRRHA reactor: Experiments and simulations”. In: *Nuclear Engineering and Design*. 16th International Topical Meeting on Nuclear Reactor Thermal Hydraulics 312 (Feb. 1, 2017), pp. 327–337. ISSN: 0029-5493. DOI: 10.1016/j.nucengdes.2016.08.023. URL: http://www.sciencedirect.com/science/article/pii/S0029549316302837 (visited on 04/18/2019) (cit. on pp. 85, 89).

[PS72] S. V Patankar and D. B Spalding. “A calculation procedure for heat, mass and momentum transfer in three-dimensional parabolic flows”. In: *International Journal of Heat and Mass Transfer* 15.10 (Oct. 1, 1972), pp. 1787–1806. ISSN: 0017-9310. DOI: 10.1016/0017-9310(72)90054-

3. URL: http://www.sciencedirect.com/science/article/pii/0017931072900543 (visited on 05/13/2019) (cit. on p. 86).

[Pel18] Michel Pelletier. *CEA internal document*. 2018 (cit. on pp. 34, 40, 53, 54, 70, 155).

[PD06] J. B. Perot and S. M. De Bruyn Kops. "Modeling turbulent dissipation at low and moderate Reynolds numbers". In: *Journal of Turbulence* 7 (Jan. 2006), N69. ISSN: 1468-5248. DOI: 10.1080/14685240600907310. URL: http://www.tandfonline.com/doi/abs/10.1080/14685240600907310 (visited on 05/15/2019) (cit. on p. 81).

[PB78] A. Pol and P. Bourdot. *CEA internal document*. 1978 (cit. on pp. 14, 109).

[PB79] A. Pol and P. Bourdot. *CEA internal document*. 1979 (cit. on pp. 109, 136).

[Pop00] Stephen B. Pope. *Turbulent Flows*. Cambridge: Cambridge University Press, 2000. ISBN: 978-0-521-59886-6. URL: https://www.cambridge.org/core/books/turbulent-flows/69322053C06F73F7EB7124915F9256BD (cit. on p. 76).

[RPF10] R. Ranjan, C. Pantano, and P. Fischer. "Direct simulation of turbulent swept flow over a wire in a channel". In: *Journal of Fluid Mechanics* 651 (May 1, 2010), p. 165. ISSN: 0022-1120. DOI: 10.1017/S0022112009993958. URL: http://adsabs.harvard.edu/abs/2010JFM...651..165R (visited on 07/24/2019) (cit. on p. 77).

[Reh73] Klaus Rehme. "Pressure Drop Correlations for Fuel Element Spacers". In: *Nuclear Technology* 17.1 (Jan. 1, 1973), pp. 15–23. ISSN: 0029-5450. DOI: 10.13182/NT73-A31250. URL: https://doi.org/10.13182/NT73-A31250 (visited on 07/10/2019) (cit. on p. 29).

[Rei51] H. Reichardt. "Vollständige Darstellung der turbulenten Geschwindigkeitsverteilung in glatten Leitungen". In: *ZAMM - Journal of Applied Mathematics and Mechanics / Zeitschrift für Angewandte Mathematik und Mechanik* 31.7 (Jan. 1, 1951), pp. 208–219. ISSN: 1521-4001. URL: https://onlinelibrary.wiley.com/doi/abs/10.1002/zamm.19510310704 (visited on 05/17/2019) (cit. on p. 87).

[Reu08] P. Reuss. *Neutron Physics*. Nuclear engineering. EDP Sciences, 2008. ISBN: 978-2-7598-0041-4. URL: https://books.google.fr/books?id=2FajZzx0jy0C (cit. on p. 62).

[RC83] C. M. Rhie and W. L. Chow. “Numerical study of the turbulent flow past an airfoil with trailing edge separation”. In: *AIAA Journal* 21.11 (Nov. 1983), pp. 1525–1532. ISSN: 0001-1452, 1533-385X. DOI: 10.2514/3.8284. URL: http://arc.aiaa.org/doi/10.2514/3.8284 (visited on 07/25/2019) (cit. on p. 86).

[Roe+18] Ferry Roelofs, Daniele Dovizio, H Uitslag-Doolaard, et al. “Core Thermal Hydraulic CFD Support for Liquid Metal Reactors”. In: Aug. 28, 2018 (cit. on pp. 78, 86).

[Roe+13] Ferry Roelofs, Vinay R. Gopala, Santhosh Jayaraju, et al. “Review of fuel assembly and pool thermal hydraulics for fast reactors”. In: *Nuclear Engineering and Design* 265 (Dec. 2013), pp. 1205–1222. ISSN: 0029-5493. DOI: 10.1016/j.nucengdes.2013.07.018. URL: //www.sciencedirect.com/science/article/pii/S0029549313004524 (cit. on pp. 72, 78).

[Rol+12] Stefano Rolfo, Christophe Péniguel, Matthieu Guillaud, et al. “Thermal-hydraulic study of a wire spacer fuel assembly”. In: *Nuclear Engineering and Design* 243 (Feb. 2012), pp. 251–262. ISSN: 0029-5493. DOI: 10.1016/j.nucengdes.2011.11.021. URL: http://www.sciencedirect.com/science/article/pii/S0029549311009940 (cit. on pp. 28, 86, 87).

[Rug+06] J M Ruggieri, J Tommasi, J F Lebrat, et al. “ERANOS 2.1 : International Code System for GEN IV Fast Reactor Analysis”. In: *Proceedings of ICAPP ’06*. Reno, NV USA, 2006, p. 9 (cit. on p. 165).

[SOH78] Katsuhiro Sakai, Yoshiyuki Okubo, and Hisashi Hishida. “Three-dimensional deflection analyses of wire-spaced fuel pin bundles under temperature and hydrodynamic force fields with irradiation effects”. In: *Nuclear Engineering and Design* 48.2 (Aug. 1, 1978), pp. 595–610. ISSN: 0029-5493. DOI: 10.1016/0029-5493(78)90101-2. URL: http://www.sciencedirect.com/science/article/pii/0029549378901012 (visited on 04/10/2019) (cit. on pp. 14, 108).

[Sax14] Aakanksha Saxena. *Thermal-hydraulic numerical simulation of fuel subassembly for Sodium-cooled Fast Reactor*. FRCEA-TH–7430. France, Oct. 2014, p. 273. URL: http://inis.iaea.org/search/search.aspx?orig_q=RN:47082333 (cit. on pp. 8, 26, 27, 84, 87).

[Sch92] Nicolas Schmidt. “Endommagement de la gaine des éléments combustibles du réacteur à neutrons rapides PHENIX. Réalisation et analyse d’expériences de chargement limite. Validation et optimisation de la méthodologie de dimensionnement RAMSES 2”. C.N.A.M, 1992 (cit. on p. 45).

[Sch09] Mycle Schneider. "Fast Breeder Reactors in France". In: *Science & Global Security* 17.1 (June 26, 2009), pp. 36–53. ISSN: 0892-9882. DOI: 10.1080/08929880902953013. URL: https://doi.org/10.1080/08929880902953013 (visited on 07/09/2019) (cit. on p. 7).

[Sér+92] J. L. Séran, V. Lévy, D. Gilbon, et al. "Behavior under Neutron Irradiation of the 15-15Ti and EM10 Steels Used as Standard Materials of the Phénix Fuel Subassembly". In: *Effects of Radiation on Materials: 15th International Symposium* (Jan. 1992). DOI: 10.1520/STP17941S. URL: http://www.astm.org/DIGITAL_LIBRARY/STP/PAGES/STP17941S.htm (visited on 09/25/2018) (cit. on pp. 48, 53).

[Sha18] Afaque Shams. "The importance of turbulent heat transfer modelling in low-Prandtl fluids". In: Advances in Thermal Hydraulics (ATH 2018), ANS Winter Meeting Embedded. Orlando, USA, Nov. 14, 2018 (cit. on p. 87).

[Smi+08] Jeffrey G. Smith, Bruce R. Babin, W. David Pointer, et al. "Effects of Mesh Density and Flow Conditioning in Simulating 7-Pin Wire Wrapped Fuel Pins". In: 48159 (2008), pp. 755–763. DOI: 10.1115/ICONE16-48306. URL: http://dx.doi.org/10.1115/ICONE16-48306 (cit. on p. 86).

[Smi+09] Jeffrey G. Smith, Akira Tokuhiro, W. David Pointer, et al. "Predictions in CFD simulations of wire-wrapped SFR fuel assemblies". In: Proceedings of 2009 international congress on advances in nuclear power plants. 2009, p. 2572. URL: http://inis.iaea.org/search/search.aspx?orig_q=RN:43084110 (cit. on pp. 86, 90).

[SM13] Alexander J. Smits and Ivan Marusic. "Wall-bounded turbulence". In: *Physics Today* 66.9 (Sept. 2013), pp. 25–30. ISSN: 0031-9228, 1945-0699. DOI: 10.1063/PT.3.2114. URL: http://physicstoday.scitation.org/doi/10.1063/PT.3.2114 (visited on 04/13/2019) (cit. on p. 22).

[Sob11] V. Sobolev. *Database of thermophysical properties of liquid metal coolants for GEN-IV*. 1379-2407. BLG–1069. Belgium: Belgian Nuclear Research Center SCK-CEN Belgium, 2011, p. 175. URL: http://inis.iaea.org/search/search.aspx?orig_q=RN:43095088 (cit. on pp. 22, 23, 85).

[Sog+09] Tomonori Soga, Chikara Ito, Takafumi Aoyama, et al. *Fuels and materials research under the high neutron fluence using a fast reactor Joyo and post-irradiation examination facilities*. INIS-XA–09N2038. International Atomic Energy Agency (IAEA), 2009, p. 40. URL: http://inis.iaea.org/search/search.aspx?orig_q=RN:41028108 (cit. on p. 209).

[Sos+15] E. Sosnovsky, E. Baglietto, S. Keijers, et al. “CFD simulations to determine the effects of deformations on liquid metal cooled wire wrapped fuel assemblies”. In: Proceedings of the 16th International Topical Meeting on Nuclear Reactor Thermalhydraulics (NURETH-16). Chicago, USA, 2015. URL: http://glc.ans.org/nureth-16/data/papers/13595.pdf (visited on 02/21/2018) (cit. on p. 14).

[Spa00] P. R Spalart. “Strategies for turbulence modelling and simulations”. In: *International Journal of Heat and Fluid Flow* 21.3 (June 1, 2000), pp. 252–263. ISSN: 0142-727X. DOI: 10.1016/S0142-727X(00)00007-2. URL: http://www.sciencedirect.com/science/article/pii/S0142727X00000072 (visited on 07/28/2019) (cit. on p. 78).

[Sta07] W.M. Stacey. *Nuclear Reactor Physics*. John Wiley & Sons, 2007. ISBN: 978-3-527-40679-1. URL: https://books.google.fr/books?id=y1UgcgVSXSkC (cit. on p. 63).

[SA83] R.J.J. Stamm’ler and M.J. Abbate. *Methods of Steady-state Reactor Physics in Nuclear Design*. Academic Press, 1983. ISBN: 978-0-12-663320-7. URL: https://books.google.fr/books?id=Ot1xQgAACAAJ (cit. on p. 165).

[17] *STAR-CCM+ v12.02 Users Manual*. 2017 (cit. on pp. 84, 86, 90, 264).

[SZ17] Janez Sušnik and Pieter van der Zaag. “Correlation and causation between the UN Human Development Index and national and personal wealth and resource exploitation”. In: *Economic Research-Ekonomska Istraživanja* 30.1 (Jan. 1, 2017), pp. 1705–1723. ISSN: 1331-677X. DOI: 10.1080/1331677X.2017.1383175. URL: https://doi.org/10.1080/1331677X.2017.1383175 (visited on 04/06/2019) (cit. on p. 1).

[TY56] S. Timoshenko and D.H. Young. *Engineering Mechanics ... Fourth Edition*. McGraw-Hill Book Company, 1956. URL: https://books.google.fr/books?id=VNjzMgEACAAJ (cit. on p. 102).

[Tou88] H Touron. *CEA internal document*. 1988 (cit. on p. 46).

[Ulr+10] Ulrich Bieder, Valérie Barthel, Frederic Ducros, et al. “CFD calculations of wire wrapped fuel bundles: modeling and validation strategies”. In: *Workshop Proceedings of Computational Fluid Dynamics for Nuclear Reactor Safety Applications (CFD4NRS-3)*. Bethesda, USA, 2010 (cit. on pp. 90, 92).

[UKB04] E. Uspuras, A. Kaliatka, and E. Bubelis. “Validation of coupled neutronic/thermal-hydraulic code RELAP5-3D for RBMK-1500 reactor analysis application”. In: *Annals of Nuclear Energy* 31.15 (2004), pp. 1667–1708. ISSN: 0306-4549. DOI: https://doi.org/10.1016/j.anucene.2004.06.002. URL: http://www.sciencedirect.com/science/article/pii/S0306454904001124 (cit. on p. 12).

[UIM11] Tomoyuki Uwaba, Masahiro Ito, and Koji Maeda. "Diametral strain of fast reactor MOX fuel pins with austenitic stainless steel cladding irradiated to high burnup". In: *Journal of Nuclear Materials* 416.3 (Sept. 30, 2011), pp. 350–357. ISSN: 0022-3115. DOI: 10.1016/j.jnucmat.2011.06.033. URL: http://www.sciencedirect.com/science/article/pii/S0022311511005976 (visited on 11/21/2018) (cit. on p. 54).

[Uwa+05] Tomoyuki Uwaba, Masahiro Ito, Shigeharu Ukai, et al. "Development of a FBR Fuel Bundle-duct Interaction Analysis Code-BAMBOO". In: *Journal of Nuclear Science and Technology* 42.7 (July 1, 2005), pp. 608–617. ISSN: 0022-3131. DOI: 10.1080/18811248.2004.9726428. URL: https://doi.org/10.1080/18811248.2004.9726428 (visited on 09/24/2018) (cit. on pp. 95, 108).

[UOI17] Tomoyuki Uwaba, Hiroyuki Ohshima, and Masahiro Ito. "Analyses of deformation and thermal-hydraulics within a wire-wrapped fuel subassembly in a liquid metal fast reactor by the coupled code system". In: *Nuclear Engineering and Design* 317 (June 2017), pp. 133–145. ISSN: 0029-5493. DOI: 10.1016/j.nucengdes.2017.03.026. URL: http://www.sciencedirect.com/science/article/pii/S0029549317301395 (cit. on pp. 14, 108, 109, 156, 220–226, 236).

[UT01] Tomoyuki Uwaba and Kosuke Tanaka. "Development of a Fast Breeder Reactor Fuel Bundle-Duct Interaction Analysis Code—BAMBOO: Analysis Model and Validation by the Out-of-Pile Compression Test". In: *Nuclear Technology* (2001). DOI: 10.13182/NT01-A3225. URL: http://www.tandfonline.com/doi/abs/10.13182/NT01-A3225 (visited on 02/22/2018) (cit. on p. 55).

[UT17] Tomoyuki Uwaba and Kosuke Tanaka. "Development of a Fast Breeder Reactor Fuel Bundle-Duct Interaction Analysis Code—BAMBOO: Analysis Model and Validation by the Out-of-Pile Compression Test". In: *Nuclear Technology* (May 10, 2017). DOI: 10.13182/NT01-A3225. URL: http://www.tandfonline.com/doi/abs/10.13182/NT01-A3225 (visited on 02/22/2018) (cit. on p. 108).

[UU02] Tomoyuki Uwaba and Shigeharu Ukai. "The secondary stress analyses in the fuel pin cladding due to the swelling gradient across the wall thickness". In: *Journal of Nuclear Materials* 305.1 (Sept. 1, 2002), pp. 21–28. ISSN: 0022-3115. DOI: 10.1016/S0022-3115(02)00909-1. URL: http://www.sciencedirect.com/science/article/pii/S0022311502009091 (visited on 03/01/2019) (cit. on pp. 95, 188).

[Vaz+12] Miriam Vazquez, Haileyesus Tsige-Tamirat, Luca Ammirabile, et al. "Coupled neutronics thermal-hydraulics analysis using Monte Carlo and sub-channel codes". In: *Nuclear Engineering and Design* 250 (2012),

pp. 403–411. ISSN: 0029-5493. DOI: https://doi.org/10.1016/j.nucengdes.2012.06.007. URL: http://www.sciencedirect.com/science/article/pii/S0029549312003251 (cit. on p. 12).

[WTT12] Alan E. Waltar, Donald R. Todd, and Pavel V. Tsvetkov, eds. *Fast spectrum reactors*. New York: Springer, 2012. 720 pp. ISBN: 978-1-4419-9571-1 (cit. on pp. 38, 54, 61, 63, 65).

[Web+04] D.P. Weber, T. Sofu, W.S. Yang, et al. "Coupled calculations using the numerical nuclear reactor for integrated simulation of neutronic and thermal-hydraulic phenomena". In: Proceedings of the PHYSOR 2004: The Physics of Fuel Cycles and Advanced Nuclear Systems - Global Developments. 2004, pp. 69–78. ISBN: 978-0-89448-683-8 (cit. on p. 12).

[Wol69] M. Wolfshtein. "The velocity and temperature distribution in one-dimensional flow with turbulence augmentation and pressure gradient". In: *International Journal of Heat and Mass Transfer* 12.3 (Mar. 1, 1969), pp. 301–318. ISSN: 0017-9310. DOI: 10.1016/0017-9310(69)90012-X. URL: http://www.sciencedirect.com/science/article/pii/001793106990012X (visited on 09/20/2019) (cit. on p. 86).

[Wu+13] Y.W. Wu, Xin Li, Xiaolei Yu, et al. "Subchannel thermal-hydraulic analysis of the fuel assembly for liquid sodium cooled fast reactor". In: *Progress in Nuclear Energy* 68 (Sept. 2013), pp. 65–78. ISSN: 0149-1970. DOI: 10.1016/j.pnucene.2013.05.001. URL: http://www.sciencedirect.com/science/article/pii/S0149197013001017 (cit. on p. 73).

[Xu+09] Yunlin Xu, Thomas Downar, R. Walls, et al. "Application of TRACE/PARCS to BWR stability analysis". In: *Annals of Nuclear Energy* 36.3 (2009), pp. 317–323. ISSN: 0306-4549. DOI: https://doi.org/10.1016/j.anucene.2008.12.022. URL: http://www.sciencedirect.com/science/article/pii/S030645490800340X (cit. on p. 12).

[Yan12] W.S. Yang. "FAST REACTOR PHYSICS AND COMPUTATIONAL METHODS". In: *Nuclear Engineering and Technology* 44.2 (2012), pp. 177–198 (cit. on pp. 4, 36, 54, 61).

[Yvo+15] Pascal Yvon, Marion Le Flem, Céline Cabet, et al. "Structural materials for next generation nuclear systems: Challenges and the path forward". In: *Nuclear Engineering and Design* 294 (Dec. 1, 2015), pp. 161–169. ISSN: 0029-5493. DOI: 10.1016/j.nucengdes.2015.09.015. URL: http://www.sciencedirect.com/science/article/pii/S0029549315004173 (visited on 07/11/2019) (cit. on p. 57).

[Zha+17] Pinghui Zhao, Jiaming Liu, Zhihao Ge, et al. “CFD analysis of transverse flow in a wire-wrapped hexagonal seven-pin bundle”. In: *Nuclear Engineering and Design* 317 (June 2017), pp. 146–157. ISSN: 0029-5493. DOI: 10.1016/j.nucengdes.2017.03.038. URL: http://www.sciencedirect.com/science/article/pii/S0029549317301504 (cit. on pp. 27, 91).

Appendices

A. CFD mesh and mesh dependency

In this Appendix, we evaluate the CFD mesh parameters employed in the simulations of chapters 6 and 7, based on the results obtained in the 7-pin fuel bundle described in Section 6.1.

The procedure outlined in Section 3.3.5 was employed to generate the meshes for the CFD simulations. The target base size of the mesh was set to 1 mm, and the target thickness of the prism layer to 0.45 mm. This resulted in a cell count of between 2.0 and 2.3 million, depending on the deformation level. As an example, a comparison of the nominal mesh and the mesh in the deformed bundle is presented in Figure A.1, for a region within a highly deformed compact plane (plane in which the centers of the wires are aligned with the centers of the fuel pins, following the direction of one of the diagonals of the hexagonal tube). In this figure, some cells might appear incorrectly distorted since the observed cell cross section depends on the distance of the cell centroid from the plane used to intersect the volume mesh. All the cells intersected by this plane were verified to have a volume change, defined as the ratio of a cell volume to the volume of its largest neighbor, superior to 0.1, which is the lower limit of what is considered a good quality cell (*STAR-CCM+ v12.02 Users Manual* 2017). It can be observed in Figure A.1 that roughly the same number of cells are present in the smallest gap between fuel claddings in the nominal and deformed conditions. This is due to a parameter of the meshing tool that allows to prescribe the minimum number of cells between two close surfaces, which leads to a reduction of the cell size in the smaller gaps of the deformed geometry. Also, even in the nominal geometry, this leads to a mesh refinement in the areas where a spacer wire becomes closest to a neighboring cladding.

In order to select the cell target base size to be employed in this work, which allows the automatic generation of the different meshes needed for a coupled simulation, four different meshes were analyzed. The number of cells, pressure drop and average sodium outlet temperature obtained with each of them, which differ only in their target base size, are presented in Table A.1. In all cases, the target thickness of the prism layer was kept constant at 0.45 mm, so that a change in the base size would not affect the y^+ of the near wall cells, which could lead to finer meshes introducing more physical modeling error. It can be noted that, as expected from the global energy balance, the average outlet sodium temperature was not significantly affected by the mesh refining. Additionally, the two finest meshes present a cell count percentage difference of 28%, while the difference in the pressure drop is less than 2%. In view of this, a target base size of 1 mm was pre-selected to be employed in this work for all the CFD simulations. This choice, based on global results, was confirmed by an evaluation of the impact of the mesh refinement on local variables, discussed below.

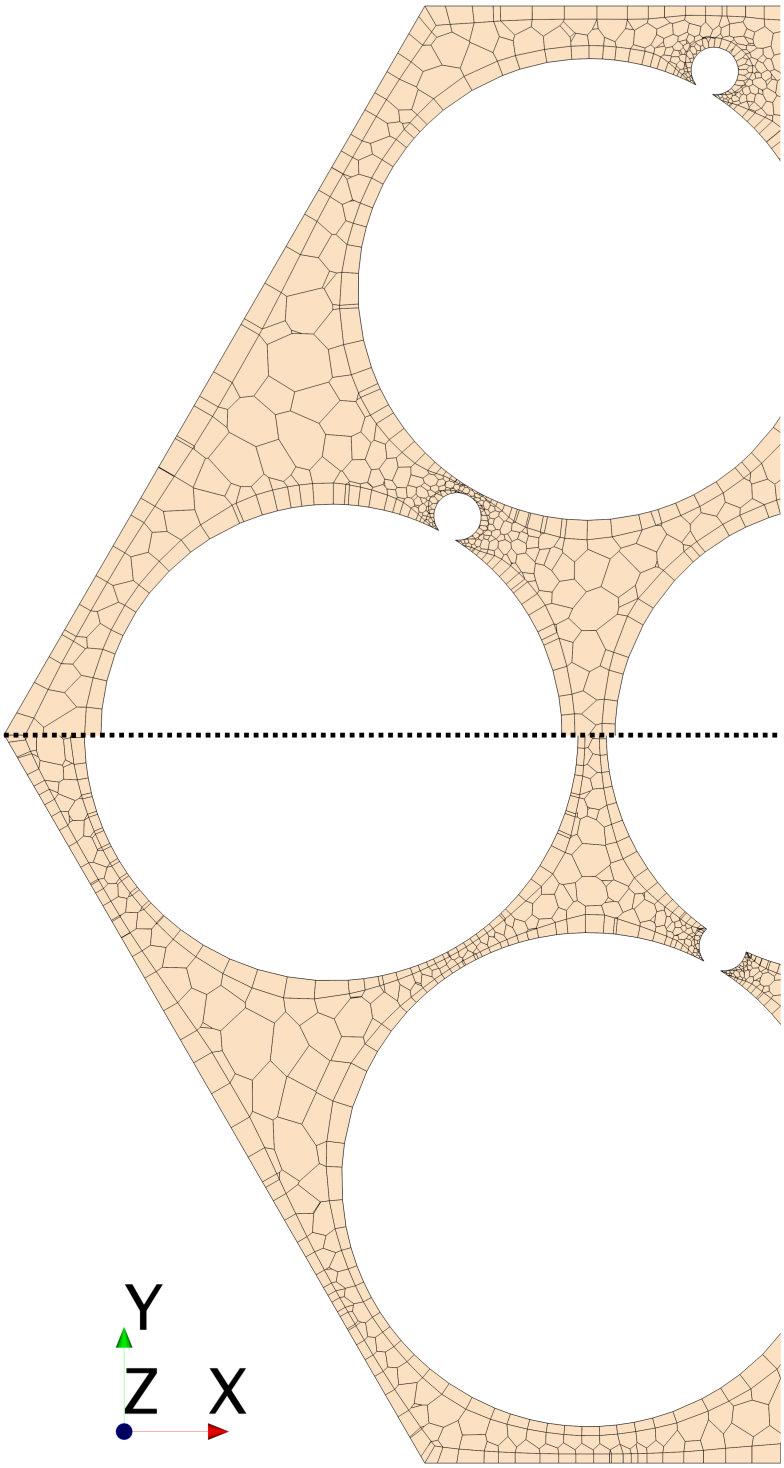

Figure A.1.: Close-up comparison of the nominal (up) and a deformed (down) mesh in a highly deformed compact plane.

Base size [mm]	Number of cells [x10^6]	Pressure drop [Bar]	Avg. sodium outlet T [°C]
0.8	2.9	0.538	547.9
1.0	2.1	0.539	547.9
1.3	1.6	0.541	547.9
1.8	1.1	0.545	547.8

Table A.1.: Mesh parameters and global results obtained with them.

Since the axial temperature profiles on the surface of the claddings are exported from the CFD calculations to be later used as input for the thermomechanical calculations, it is important to quantify the impact that refining the mesh has on them. Ideally, the temperature discretization error should be significantly smaller than the temperature variation induced by the deformation.

Therefore, the temperature difference induced by the mesh refinement was compared to the temperature difference induced by the deformation. To do so, the results obtained with the finest mesh (target base size of 0.8 mm) were taken as a reference, and the variation of temperature observed with the mesh retained in this work (target base size of 1 mm) was compared to the temperature increase computed in the deformed geometries calculated with DOMAJEUR2 for both dose levels essayed, results that are detailed in Section 6.5. This comparison is presented in Figure A.2 for an axial temperature profile on the surface of the central pin of the bundle, where the temperature difference induced by the mesh refinement in both the nominal and a deformed mesh are presented. It can be noted that the temperature variation due to the deformation induced by the highest irradiation dose is significantly larger than the variation found between the meshes. For the lowest dose essayed, the discretization error is low enough to be able to capture the relatively small temperature variations induced by the bundle deformation. The discontinuities in the profiles presented in Figure A.2 correspond to the points where the line used to probe the cladding temperature intersects the spacer wire (see Section 5.3.4).

The all y^+ wall treatment adopted provides more accurate results when the non-dimensional wall distance, y^+, lies outside the buffer layer (that is, $5 < y^+ < 30$ approximately), even though a blending approach between high y^+ and low y^+ treatments creates reasonable solutions in these intermediate cells. In the simulations here evaluated, including the ones conducted in deformed geometries, less than 20% of the near wall cells present wall y^+ values between 5 and 30 and, since they are concentrated around the contact lines between the fuel pins and their spacer wires, they account for less than 2% of the surface of the claddings. The average wall y^+ of the different meshes employed in this work ranges from 110 to 130, values

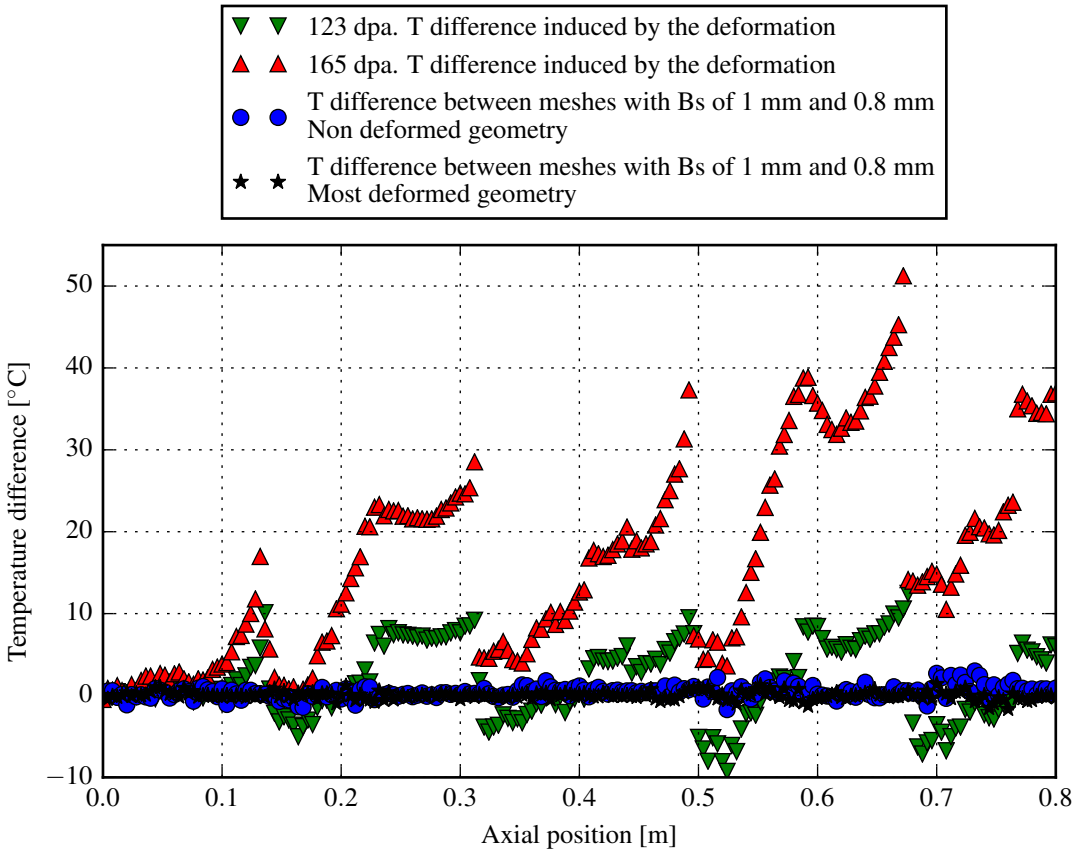

Figure A.2.: Axial distribution of the temperature (T) differences obtained, along a vertical line on the surface of the central pin of the bundle, with meshes of base size (Bs) 1 mm and 0.8 mm, compared to the temperature increase induced by the deformation associated to irradiation dose distributions with a maximum of 123 dpa and 165 dpa.

well within the recommended range for the employed wall treatment. This was judged to be adequate for our purposes, which are the development and evaluation of a coupled simulation methodology for SFR subassemblies. Nevertheless, without modifying the underlying methodology, further optimization of the mesh parameters could be conducted if, for example, a more precise determination of the cladding hot spots—which is not the goal of the simulations here described—was desired.